POLISH ACADEMY OF SCIENCES
COMMITTEE OF METALLURGY
INSTITUTE OF METALLURGY
AND MATERIALS SCIENCE

ARCHIVES OF METALLURGY AND MATERIALS

QUARTERLY

Volume 49 · Issue 1

WARSZAWA — KRAKÓW 2004

The Archives of Metallurgy and Materials is covered in the following Institute for Scientific Information® products: SciSearch (the Science Citation Index® — Expanded), Research Alert®, Materials Science Citation Index®, and Current Contents® / Engineering, Computing and Technology. Articles published in the Archives of Metallurgy and Materials are also indexed or abstracted by Cambridge Scientific Abstracts.

EDITORIAL ADDRESS
M. Bitner, al. Mickiewicza 30, AGH, paw. A-4, III p., pok. 312b
30-059 Kraków, Poland
Tel. +48 (12) 6173425
e-mail: archives@imim-pan.krakow.pl

Skład, łamanie druk i oprawa: Warszawska Drukarnia Naukowa PAN
Warszawa, ul. Śniadeckich 8, tel./fax 628-87-77

Ark. wyd. 11,5 Ark. druk. 14,25
Nakład: 170 egz.
Druk ukończono w kwietniu 2004 r.

This issue is devoted to the memory of
Professor Wojciech Truszkowski

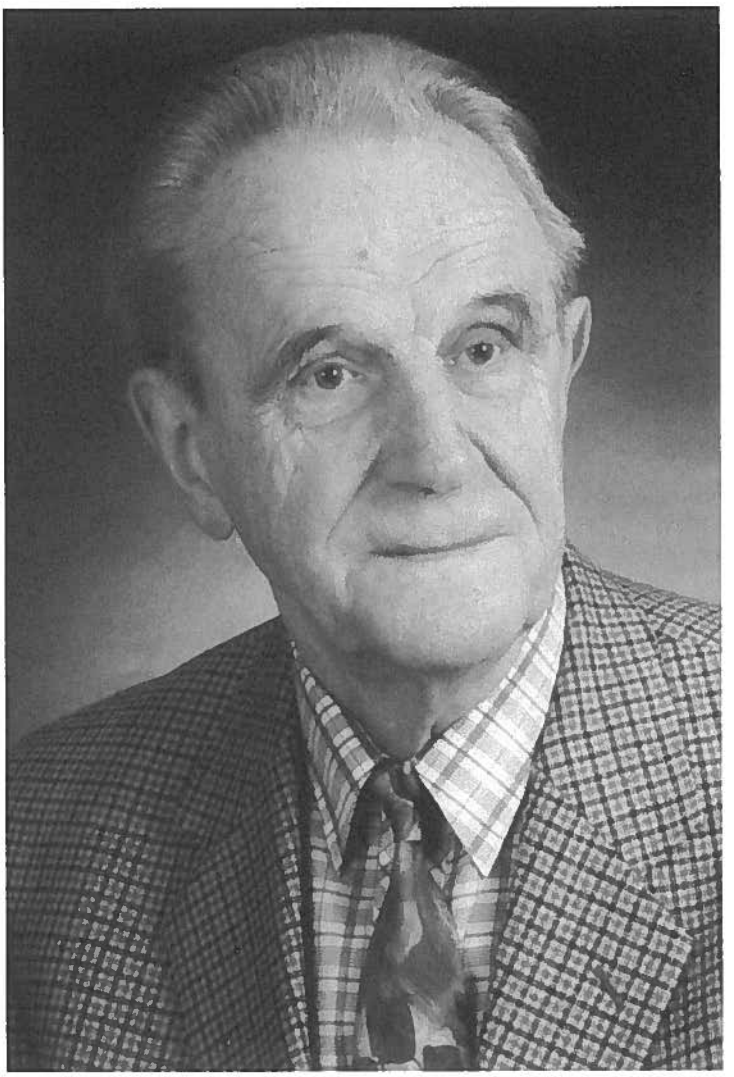

From the Editor

Only a short time ago, in the 2/2002 issue of "Archives of Metallurgy" the 80th birthday anniversary of Professor Truszkowski was celebrated by an article presenting the main directions of his activity, and at that time nobody thought that very soon he would be no longer among us. It was the idea of persons who had known him well to dedicate 1/2004 issue of our Quarterly to the memory of this eminent man.

In this issue, in a number of short presentations, the various fields of Professor Truszkowski's activity are described, his relations with the Academy of Mining and Metallurgy (now AGH-University of Science and Technology), with the Institute of Metallurgy and Materials Science as well as with the Polish Academy of Sciences (PAS), the Polish Academy of Art and Sciences – not neglecting his passion for mountaineering and, in the later years, long walks in the country.

Professor Truszkowski had excellent psycho-physical conditions for climbing mountains. In the years 1948–1953, in the High Tatra, in the vicinity of Hala Gąsienicowa and Morskie Oko, he climbed several high peaks. However, as he was greatly engaged in his scientific work, he could not devote much time to sport.

Professor Truszkowski as a member of the Editorial Board of our Quarterly participated in the preparation of almost every issue and spent much time correcting several apparently unimportant details which distinguish a scientific journal of a high rank from others. We discussed with him the problem of changing the name of "Archives of Metallurgy" into "Archives of Metallurgy and Materials" as in the recent years the subject matter of the published articles was directed to materials science, as well as to the problem of including the reports from conferences and workshops. The latter problem became rather urgent after our Quarterly had been covered by the Institute of Scientific Information in USA in the year 1998. This fact opened new possibilities of publishing materials from important international cyclic conferences, organized in Poland, which until then were published only abroad.

I should like to add some personal reflections from my memories of a long friendship with Wojtek (as he was usually called) since the year 1956. The many years during which he was the director of our Institute were marked not only by his great concern about the development of his specialization, but also by promoting other research directions represented in the Institute. I owe much to him as regards the development of the theory of metallurgical processes, which is now the field of my current research carried out together with my team, and which was initiated in the post-war years by Professor Krupkowski and Professor Ptak. It was his initiative that I became the editor of "Archives of Metallurgy"; I was promoted by him as a candidate to the Polish Academy of Art and Sciences and also to become the Head of the Institute in the years 1999-2003. Especially during the period when I served as the director of the Institute I had often an opportunity to make extensive use of

his experience and valuable advice. Wojtek was unwearying in his discussions on the development of our Institute and he was always friendly and helpful towards all workers of the Institute.

Zbigniew Moser
Editor
Archives of Metallurgy and Materials

Activity of Professor Wojciech Truszkowski in the Committee of Metallurgy of the Polish Academy of Science

Professor Wojciech Truszkowski, Ph.D., D.Sc., Eng, passed away at a time when the Committee of Metallurgy of the Polish Academy of Sciences (PAS) celebrated 50 years of its existence. He was closely connected with the activity of the Committee since the moment of its establishment. As a young, but already a mature scientist, he took active part in the work of the Committee of Metallurgy, at that time under the direction of Professor Alexander Krupkowski, Nestor of Polish Metallurgy.

In the years 1981–1990 he was chairman of the Committee of Metallurgy of PAS. During the whole period of his work in the Committee Professor Truszkowski was an unwearying protector of scientific meetings integrating the environment interested in the problems of metallurgy.

He thought it very important to organize the Reporting Conferences of the Committee of Metallurgy of PAS at which the achievements of each past term were discussed and evaluated. I remember how much Professor Truszkowski was satisfied when after a break of about 11 years, in which due to the transformations in our Committee, the Reporting Conferences were not organized, in the year 1998 the XII Reporting Conference of the Committee of Metallurgy of PAS was opened in Krynica.

In the current activity of the Committee of Metallurgy Professor Truszkowski preferred monothematic meetings at which specialists exchanged their opinions on a special problem. He enjoyed participating in scientific discussions.

A very important aspect characterizing the work of the Committee of Metallurgy, which from its beginning was closely connected with the Institute of Metallurgy and Materials Science of PAS were the publications. Professor Truszkowski co-operated for many years with the journal "Archives of Metallurgy", which due to its high scientific rank is covered by the Institute of Scientific Information from USA.

The present activity of the Committee of Metallurgy of PAS is based on the fundamentals and achievements to which Professor Truszkowski has greatly contributed.

Józef Zasadziński
Chairman of the Committee of Metallurgy of
The Polish Academy of Sciences

Professor Wojciech Truszkowski

Director of the Aleksander Krupkowski
Institute of Metallurgy and Materials Science
of the Polish Academy of Sciences

Professor Truszkowski belonged to this group of professor Krupkowski's pupils, who defined the directions of development of Polish metallurgy in the first years after the second world war. He focused his interest in plastic anisotropy and crystallographic texture, for which the original input was offered by W.M. Baldwin Jr., already in 1946, who observed the differentiated strain rates in three mutually perpendicular directions of the sample subjected to static tensile test. A further and expanded analysis of the problem was undertaken by Lankford, Hill, Gensamer, Jackson, Low and Smith. However, the breakthrough in analytical approach to this problem was made by Krupkowski and Kawiński, as well as Lankford, Snyder and Bauscher, who proposed a quantitative method to define the strain ratio as the measure of plastic anisotropy. In the 60s, as a student of Non-ferrous Metals Department, AGH- University of Science and Technology in Cracow, I had the pleasure to listen to professor Truszkowski's lectures on physical metallurgy and metal physics. Later, as a researcher in the institute headed by the professor, I saw his excitement, whenever he talked about quantitative approach to static tension test description, plastic anisotropy and preferred crystallographic orientation. His career started and continued to develop at the AGH- University of Science and Technology. He graduated here and obtained all the scientific degrees, up to professorship. It was at the AGH-University of Science and Technology in Cracow, where he educated and tutored a numerous group of Polish specialists in physical metallurgy. However, he realized his research passion primarily at the Institute of the Polish Academy od Sciences, established in 1953 by professor Krupkowski. Numerous scientists obtained their successive university degrees under his tutorship. I have the pleasure to count myself among them.

The quantitative definition of crystallographic texture and its relation to plastic anisotropy was the goal aimed at by the Professor. It was reflected in his numerous publications in this field. I had the honour to co-author some of the papers focused on the inhomogeneity of deformation and recrystallization texture. His scientific activity and passion found a sort of culmination in the monograph book "The Plastic Anisotropy in Single Crystals and Polycrystalline Metals" published by Kluwer Academic Publishers in 2001. Professor Truszkowski always wanted his quantitative solutions in the domains of plastic anisotropy and crystallographic texture, and especially for single crystals, to be remembered. He coined the notion of "texture of f.c.c. single crystals", understood as the degree of their imperfection, and analyzed the impact of this real crystalline structure on the behaviour of materials during deformation tests.

While delivering numerous papers at international conferences, professor Truszkowski was tireless in his struggle to assure the deserved rank is granted to Polish scientific thought. He always emphasised Polish contribution into science, especially in the physical basis of the description of plastic anisotropy. He will remain in our memory as a man of wide horizons of thought and a passionate scientist devoted to our Institute to the last days of his life.

Bogusław Major
Director of the Aleksander Krupkowski
Institute of Metallurgy and Materials Science
of the Polish Academy of Sciences

Co-operation of Professor Wojciech Truszkowski with the IVth Department of the Technical Sciences of the Polish Academy of Sciences

Professor Wojciech Truszkowski became a corresponding member of the Polish Academy of Sciences (PAS) in the year 1965. However he was already connected with the Academy and the IVth Department earlier, and since the moment the Department of Metals was established at the Institute of Fundamental Technological Research of PAS he was concerned about the development of this institution. In the year 1965 he was appointed its vice-director.

He supervised the organization of scientific work, cared about modern equipment and apparatus, was engaged also in designing and construction of new buildings for the Department. From 1971 to 1988, and later again in the years 1990–1992, he was director at first of the Department of Metals of the Institute of the Fundamental Technological Reseach of PAS, and next of the independent Institute of the Basic Problems of Metallurgy of PAS. At the same time he willingly shared his knowledge with others carrying out didactic work. When functioning as director of the institution, he did not restrict his activity to his scientific specialization. He had many concepts concerning other directions of research. He initiated many actions and helped to continue them. It is worth to note that during his term of office and as a results of his efforts the Department acquired a new, high position – it was transformed into the Institute of the Basic Problems of Metallurgy, which since the year 1994 is known as the Alexander Krupkowski Institute of Metallurgy and Materials Science. Till the end of his life Professor Truszkowski was an active member of the Scientific Council of the Institute, and in years 1958–1983 he was also member of the Scientific Council of the Institute of Fundamental Technological Research.

Professor Truszkowski was greatly concerned about the development of the area of science in which he specialized. He participated for many years in the activities of the Committee of Metallurgy of PAS, serving as a chairman for nine years (1981–1990). Until the year 2000 he was also a member of the Prize Commission of the IVth Department. Ready to give

advice, having both experience and knowledge, he helped in suggesting the proper candidates for the prize in the field of metallurgy and materials science, chemical engineering, as well as in a thorough evaluation of the candidates.
In the year 1980 Professor Truszkowski became full member of PAS. For many years he worked for the Department of PAS Cracow. In the years 1958–1961 he performed the function of a scientific secretary of the Commission for Technical Sciences. Since 1966 he was a member of the Committee for Metallurgical and Foundry Engineering, and for about 20 years he represented the IVth Departmenr of PAS in the Editorial Commission of the Department.
In the nineteen-nineties (from 1993 to 1998) he was vice-president of the Department, and in the years 1999–2002 he was a member of its Presidium. At that time he supervised 35 Scientific Commissions of the Department and reorganized their activity carried out until then. Following his proposal, several valuable initiatives were undertaken by the Presidium, intended to activate the work of the Commissions and to raise their rank in science. It was decided that members would be elected for some definite term of office and their number in the particular commissions would be limited.
When remembering Professor Truszkowski I cannot forget about my personal contacts in the course of our joint work in the Prize Commission, and later on, during the sessions of the Scientific Council of the Metallurgy and Materials Science. In the conversations with Professor Truszkowski one could notice not only his friendliness but also his concern about the Institute, its activities and the level of scientific research carried out there. A characteristic feature of his character was also his true interest in the young candidates for the scientific careers.
I feel deeply moved when remembering my last meeting with Professor Truszkowski, when at the moment I was elected chairman of the Department of Technical Sciences he congratulated me heartily and advised what was the most important thing to be done about the Department. I shall always remember him as a friendly man, concerned about the future of the Institute, the Department and science.

Władysław Włosiński
Chairman of the IV th Department of the Technical Sciences
of the Polish Academy of Sciences

Professor Wojciech Truszkowski a member of the Polish Academy of Art and Sciences

Professor Wojciech Truszkowski, an outstanding scientist and a great teacher, was a true Cracovian: Born in a Cracow family, he spent here practically all his life. Equally important, the family owned a house in town and therefore he had a honour to be a *Citizen of the City of Cracow*. All this gave a special flavour to his great professional and personal achievements.

Although our professional interest were rather remote, I have known Professor Truszkowski for many years, mostly from common trips to Warsaw which we undertook to attend the meetings of the Polish Academy of Sciences. Sitting with him in the same compartment was considered a real good luck, as he was a great *causeur* and had many interesting stories to tell (this was particularly important at the old days when the trip to Warsaw lasted close to 5 hours). His views about the Polish political system were rather negative and, being closer than most of us to the industrial and economic reality (due to his scientific work in material sciences and metallurgy), he could present a number of really juicy examples of the nonsense and waste in the so-called "socialist economy".

I was therefore not surprized that he turned out to be an ardent enthusiast of the idea to bring the Polish Academy of Arts and Sciences – after 47 years of nonexistence during the communist regime – back to life. I know that he considered this as an important step forward on the road to the independence of our country and our nation, and thus treated this task as a patriotic obligation. In fact, his influence and support were extremely valuable from the very beginning: being a long-time member of the Polish Academy of Sciences, his voice weighted heavily in the discussions which preceded the historical meeting of 16 November 1989, at which the Polish Academy of Arts and Sciences was declared active and ready to work.

Since then he very actively participated in construction and organization of the Faculty of Mathematics, Physics and Chemistry. His activity was particularly crucial in the first, difficult days, when his enthusiasm and experience greatly helped to form and shape the Faculty as it is now. He remained active until his last illness, and I always considered him one of the most valuable advisors. Apart from the great sorrow, his death leaves a terrible gap in our society, a gap which will not be easy to fill.

Andrzej Białas
President of the Polish Academy
of Art and Sciences

A R C H I V E S O F M E T A L L U R G Y A N D M A T E R I A L S
Volume 49 2004 Issue 1

ZDZISŁAW JASIEŃSKI*, JAN POSPIECH*, ANDRZEJ PIĄTKOWSKI*, ROBERT SCHWARZER**, ALINA LITWORA*, MARIA OSTAFIN**

TEXTURAL AND STRUCTURAL EFFECTS OF THE CHANGE OF DEFORMATION PATH IN COPPER SINGLE CRYSTALS IN A CHANNEL-DIE TEST

TEKSTUROWE I STRUKTURALNE EFEKTY ZMIANY DROGI ODKSZTAŁCENIA W NIESWOBODNIE ŚCISKANYCH MONOKRYSZTAŁACH MIEDZI

The microtextural and microstructural effects caused by the change of the deformation path in the cold rolling process of fcc metals of medium SFE have been studied by individual grain orientation measurement in the SEM (ACOM, "Automated EBSD") and by X-ray pole figure measurement. The choice of the (112)[11$\bar{1}$] and the (112)[1$\bar{1}$0] orientations and channel-die compression for the investigation of copper single crystals enabled a more detailed characteristic of these effects. These investigations aim to elucidate the crystallographic conditions of the strong texture and structure changes which were observed in cold rolled polycrystalline copper after the change of the rolling direction. It has been found that the main textural effects is the destabilization of the {112}<110> orientation which leads to the appearance of the {110}<112> components of texture in pre-deformed crystals as well as in not pre-deformed (112)[1$\bar{1}$0] single crystals. However, in the former case in which the deformation path was changed, the transformation proceeds much faster and more dynamic in comparison with the latter. The fragmentation of the pre-deformed single crystal structure in the form of non-regular blocks and/or compact clusters of layers is the origin of the development of two {110}<112> complementary components of texture. It has been shown that the formation of two sets of layer with complementary {110}<112> components of texture in these banded structures of pre-deformed samples is rather similar to deformation band, which differ from the typical copper-type shear bands.

Mikroteksturowe i mikrostrukturalne efekty zmiany drogi odkształcenia w procesie walcowania metali o sieci Al i średniej energii błędu ułożenia badano przez pomiar pojedynczych orientacji przy użyciu SEM (ACOM, „Automated EBSD") oraz rentgenowski pomiar figur biegunowych. Wybór monokryształów miedzi orientacji (112)[11$\bar{1}$] i (112)[1$\bar{1}$0] oraz metody nieswobodnego ściskania umożliwił bardziej szczegółową charakterystykę tych efektów.

Badania miały na celu wyjaśnienie krystalograficznych uwarunkowań silnych zmian tekstury i struktury, które obserwuje się w przypadku wstępnie walcowanej polikrystalicznej miedzi po

* INSTITUTE OF METALLURGY AND MATERIALS SCIENCE POLISH ACADEMY OF SCIENCES, REYMONTA 25, KRAKÓW, POLAND
** INSTITUT FÜR PHYSIK UND PHYSIKALISCHE TECHNOLOGIEN, TU CLAUSTHAL, GERMANY

zmianie drogi odkształcenia przez obrót 90° wokół ND. Stwierdzono, że głównym efektem teksturowym jest destabilizacja orientacji {112}<110>, która powoduje wystąpienie składowych tekstury {110}<112> we wstępnie walcowanych próbkach monokrystalicznych jak również w monokryształach idealnej orientacji (112)[1$\bar{1}$0] nie poddanych wstępnemu odkształceniu. Jednakże w pierwszym przypadku, transformacja tekstury jest bardziej dynamiczna. Fragmentacja struktury odkształconych monokryształów w formie nieregularnych bloków a zwłaszcza w formie zwartych pakietów warstw, występujących głównie we wstępnie odkształconych próbkach, jest przyczyną rozwoju dwóch komplementarnych składowych tekstury {110}<112>. Wykazano, że powstanie dwóch zbiorów warstw charakteryzujących się alternatywnie jedną z dwóch komplementarnych składowych tekstury {110}<112> we wstępnie walcowanych próbkach jest podobne raczej do procesu tworzenia pasm odkształcenia znacznie różniących się od struktury typowych pasm ścinania w miedzi.

1. Introduction

The microstructural, textural and energetic effects induced by the change of the deformation path are widely utilized in practice in the deformation processing of metals; they enable to impart definite functional properties to the product of a given geometrical form in a controlled way. One of the typical methods of changing the deformation path in order to optimize the properties of deep-drawn metal sheets, is cross rolling which consists in the change of the rolling direction in the successive pass by a 90° rotation about the normal direction (ND) to the sheet plane.

In cold rolled polycrystalline materials of face-centered cubic (FCC) lattice two types of the rolling texture are distinguished. Metals of medium stacking fault energy (SFE) are characterized by the rolling texture of "copper" type (pure metal) described by a series of orientations C{112}<111>, S{123}<634> and B{011}<112> lying along the so-called β fibre. The B{011}<112> orientation with scattering towards {011}<100> (α fibre) is the main component of the rolling texture of "brass" type, i.e. of metals of small SFE, in which the phenomenon of mechanical twinning plays a fundamental role.

In most published studies the textural effects induced by the change of the deformation path have been discussed in relation to the structure and/or texture of polycrystalline metals [1], where the influence of various forms of deformation inhomogeneities on the texture transformation is relatively difficult to identify.

Investigation of rolled polycrystalline copper [2] and of some of its alloys [3] have shown that after the change of the rolling direction a relatively small amount of additional deformation introduces significant changes in the previously formed structure and rolling texture. This phenomenon is illustrated in Fig. 1 on which the rolling texture of copper is characterized by densities of orientation distribution along the texture skeleton lines running from the orientation C{112}<111> to the orientation B{011}<211>, and after the change of the rolling direction (by rotation 90° around the normal direction) into the transverse direction (which refers to Fig.1) from the orientation C90{112}<110> to the orientation B90{011}<111>. A strong decay of the orientation density in the whole range of the skeleton line is visible, except a narrow area near the component B90, in which the orientation density increases.

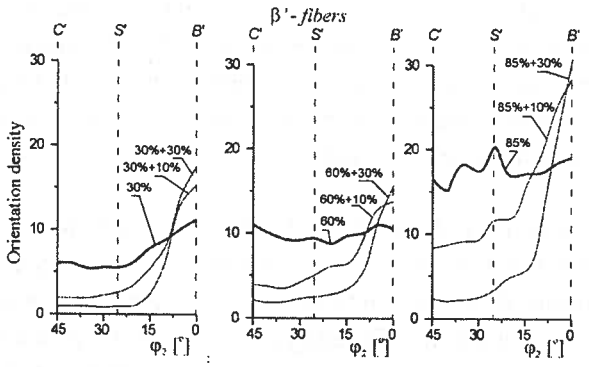

Fig. 1. Orientation densities along β-fibre in Cu. The specimens have been cold rolled up to 30%, 60% and 85% reduction and subsequently cross rolled to 10% and 30% reduction

The change of the deformation path leads to destabilization of the structure and texture in the deformed material. An elementary explanation of the reason of the disintegration of some texture components is the instability of these components with respect to the changed rolling geometry. The results show that significant texture changes appear at relatively small amount of additional deformation (up to 10%) when the material is deformed before the rolling direction is changed. The observed changes in the microstructure and texture appears as a sudden event which corresponds to the character of destabilization and reorganization of the substructure after the change of the deformation path. The structure and the texture alterations are slow when the primary deformation is absent.

Previous investigations were based on observations of the global textures obtained from *X*-ray measurements and on observations of the microstructure in a light microscope. However, for a detailed elucidation of the observed effects of the inhomogeneous deformation further systematic investigations are needed which have been undertaken in the present paper. First of all, the crystallographic conditions of the observed texture and microstructure alterations should be considered.

For a clear exposition of the phenomenon, a single crystal of copper with the initial orientation of C{112}<111> was chosen. This orientation is the dominant stable component of texture of cold rolled polycrystalline copper and according to the previous investigations [4–8], it favours localization of deformation in form of macroscopic shear band (MSB). The change of the rolling direction into the primary transverse direction change the orientation C{112}<111> into the C90{112}<110> orientation. Accepting the assumption of homogeneous slip, the numerical simulation [10] has shown that the orientation {112}<110> is not stable and turns over to the B{011}<112> position during rolling transformation.

The aim of this study is to explain the controversial opinion concerning the role of MSB [3] in the evolution of texture after the change of the deformation path and to give a detailed characteristics of the nature of the occurring deformation inhomogeneities depending on the orientation of the deformed single crystal.

In this investigation rolling has been replaced by a channel-die compression test, modelling the plane state of strain and on this account representing an approach to the

rolling process [11], which enable a more precise control of the development of some definite strain inhomogeneities. A detailed crystallographic characteristics of deformation inhomogeneities was possible through the measurements of local orientations by ACOM/EBSD. The results of measurements have the form of orientation map in which the crystallographic orientations are subordinated to coordinates of points in the sample cross-section.

This method provides not only detailed information of local character (e.g. geometry of the grain boundaries), but it enables also an extensive global analysis of the texture and microstructure by means of distribution function of orientation or orientation differences as well as of other statistical quantities. The analysis have been completed by *X*-ray pole figure measurements and optical microscope observation of the microstructure.

2. Methods of investigation

The investigations were carried out on copper single crystals (99.99%Cu) obtained by a modified Bridgman method at the Department of Structure and Mechanics of Solid Body of AGH – University of Science and Technology. Cubic samples have been used with the edge length 10mm, cut with a wire saw from the supplied prisms 10.2mm by 10.2mm by 100mm in size. The sample walls were chemically and electrolitically polished and then covered with a Teflon foil to reduce the effects of friction in the channel-die test.

The samples were channel-die compressed with an INSTRON 6025 tensile testing machine. The value of the load and the change of the sample thickness (distance covered by the traverse of the testing machine) were recorded. In the case of a change of the deformation path, the front and the back parts of the sample were cut off perpendicular to ED; the distance between the parts was 10mm. In the next step, the sample was turned around the axis ND by an angle of 90° such that the planes perpendicular to the extension direction took the position of the side planes perpendicular to TD_2. Taking into consideration the typical rolling texture of copper, where the component C{112}<111> is dominating, the investigations comprised single crystals of the following orientations:

1. (112)[11$\bar{1}$] (the so-called "copper" orientation *C*) which was subjected to channel-die compression without the change of the extension direction (ED) to a reduction of $z = 21.7\%$, determining the occurrence of one family of macroscopic shear bands (MBS).
2. C90 – obtained by pre-deformation of a single crystal of the orientation *C* to $z_1 = 21.1\%$ (with formed shear band), and next additionally channel-die compressed to $z_2 = 28.7\%$ after the change of the extension direction by 90° rotation about ND (where $ND_1 = ND_2$; $ED_2 = TD_1$; $TD_2 = ED_1$).
3. (112)[$\bar{1}$10] – corresponding to the case of rolling in the transverse direction ($TD_1 = ED_2$), not pre-deformed, ideal orientation *C*. The single crystals of this orientation were deformed up to the reductions: 20.3%, 41.9% and 66.0%.

In the plane state of strain, induced by the conditions of the channel-die test, where ε_{33}||ED = $-\varepsilon_{11}$||ND and ε_{22}||TD = ε_{21} = 0, the shears $\varepsilon_{31} \neq 0$ and $\varepsilon_{32} \neq 0$ are allowed. Schmid's factor of the operating slip system {111}<110> for selected orientations was calculated from Tucker's expression

$$\mathrm{Ws} = \tau/\sigma = \cos\alpha_c \cos\beta_c - \cos\alpha_e \cos\beta_e$$

based on the assumption that channel-die compression (or rolling) is a superposition of the elementary processes of compression or tension, where α_c and β_c as well as α_e and β_e are the angles contained between the normal to the slip plane and the direction of slip and the axes of compression and tension, respectively.

In the case of C(112)[11$\bar{1}$] orientation a specific configuration of four equally privileged slip systems (W_s = 0.544, see Table 1) occur, favouring the development of shear bands in the range of large reductions [4–7]. As it follows from Fig. 2a, a pair of co-planar slip systems (CP), BIV and BII, (S c h m i d convention or a_1 and a_2 in B i s h o p - H i l l convention) occurs that operates on a common (111) plane parallel to TD, and another pair of co-linear slip systems (CD), AVI and DVI, (c_3 and d_3 in B i s h o p - H i l l convention) having a common slip direction [110] slip direction perpendicular to TD. The pairs of the systems CP and CD are situated asymmetrically with respect to the main deformation axes, in the plane (ND-ED). The trace of the (111) plane of the CP slips lies along the [$\bar{1}\bar{1}$2] direction (resultant of the directions [$\bar{1}$01] and [0$\bar{1}$1]) and forms the angle 19.5° with ED, whereas the [110] direction of CD slip (corresponding to the trace of the (001) plane) is inclined by 35° with respect to ED.

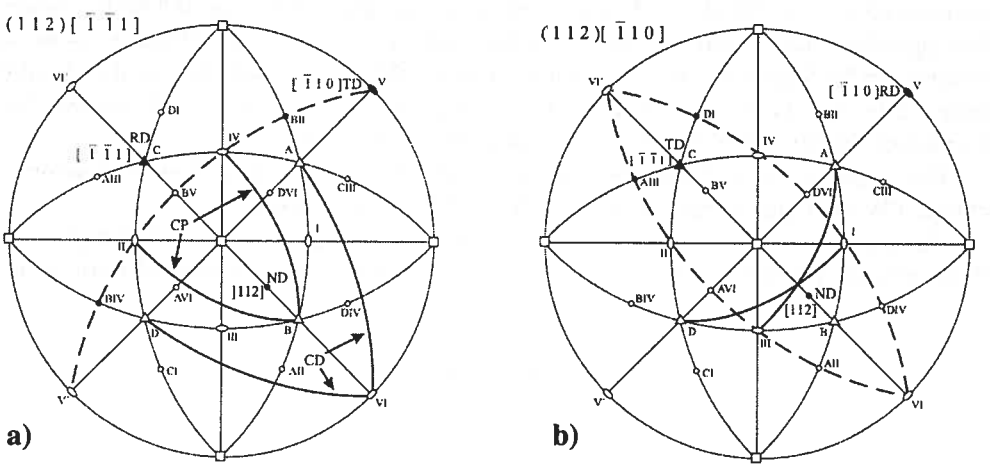

Fig. 2. Stereographic (001) projection showing the active slip systems in channel-die compressed single crystals.
a) (112)[$\bar{1}\bar{1}$1] orientation – the co-planar systems: BII, BIV, and co-linear systems: AVI, DVI.
b) (112)[$\bar{1}$10] orientation – single slip systems: AIII and DI

TABLE 1

Schmid factor values of the slip systems in the (112)[11$\bar{1}$] single crystals deformed by channel-die compression

Orientation	Angle between CP(111) plane and ED [°]	$\tau/\sigma = \cos\alpha_c \cos\beta_c - \cos\alpha_e \cos\beta_e$							
		BII	BIV	AVI	DVI	AIII	DI	CI	CIII
C(112)[11$\bar{1}$]	19.5	0.544	0.544	0.544	0.544	0.408	0.408	0.000	0.000
D(4 4 11)[$\bar{1}\bar{1}$ $\bar{1}\bar{1}$ 8]	27.4	0.710	0.710	0.470	0.470	0.472	0.472	0.240	0.240
(114)[$\bar{2}$ $\bar{2}$ 1]	35.5	0.816	0.816	0.363	0.363	0.499	0.499	0.454	0.454
(116)[$\bar{3}$ $\bar{3}$ 1]	42.0	0.859	0.859	0.258	0.258	0.494	0.494	0.602	0.602
(118)[$\bar{4}$ $\bar{4}$ 1]	45.0	0.866	0.866	0.198	0.198	0.482	0.482	0.668	0.662
(1 1 11)[$\bar{1}\bar{1}$ $\bar{1}\bar{1}$ 2]	48.0	0.863	0.863	0.146	0.146	0.468	0.468	0.717	0.717
(001)[110]	55.0	0.816	0.816	0.000	0.000	0.408	0.408	0.816	0.816

In the case of the initial orientation (112)[1$\bar{1}$0] two equally privileged single slip systems AIII and DI (W_s = 0.816), occur in which the operating slip directions [101] and [011], respectively are situated symmetrically in the plane (ND-ED) and form equal angles of 30° with the direction ED (Fig. 2b). This symmetrical arrangement of active slip systems is disadvantageous for the development of MPS.

The microtexture within the local areas of heterogeneity (MSB, transition bands) and the neighbouring matrix, the sections of deformed samples (perpendicular to the transverse direction) were investigated by the ACOM (Automated Crystal Orientation Measurement from Backscatter Kikuchi patterns, also known as "Automated EBSD") on a JEOL JSM 6400 scanning micoscope (SEM) [9]. Local orientations data obtained by this ACOM technique in the longitudinal planes were transformed to the standard ED(or RD)-TD reference system, and presented in the form of Crystal Orientation Maps (COM), inverse pole figures of ND and ED respectively and {111} pole figures. In the analysis misorientations and misorientation distribution functions (MDF) have been calculated in addition.

The global textures of deformed samples were measured using an *X*-ray diffractometer Philips PW1830 and presented in the form of {111} pole figures.

On the optical microscope (OM) scale, the longitudinal sections of samples were characterized in some cases using an etching technique with concentrated nitric acid.

3. Results

3.1. Optical microscopy

Optical microscopy observation shows a typical macroscopic shear band on the side plane (perpendicular to TD_1) of the (112)[11$\bar{1}$] oriented sample and deformed by 21.7%

(Fig. 3a). This one family set of the straight MSB forms an angle of 35° with respect to ED and the plane of MSB is parallel to the transverse direction. The observations on the samples C90 (i.e. single crystals of C orientation deformed 21.1% and, after a rotation of 90° about ND, additionally compressed 28.7%) were conducted on the section perpendicular to TD_2 after etching with concentrated nitric acid to reveal the trace of the local inhomogeneities. As can be seen on Fig. 3b, the observed bands are more wavy and form the angles from 26° to 42° with respect to ED_2. The transverse direction is inclined at a small angle with respect to the plane of these bands. It should be noted that the structure of bands is composed of packets of thin laminae (~ 50μm) which significantly differ from that of the "copper" type shear bands.

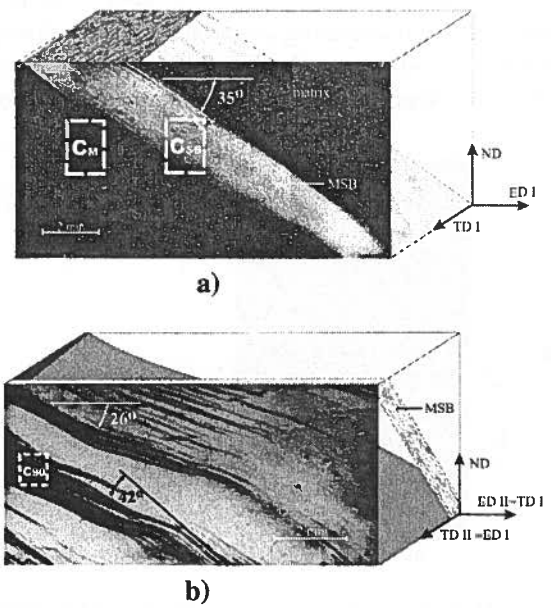

Fig. 3. Optical microscopy in a plane perpendicular to TD of Cu single crystals after channel-die compression. a) C(112)[$\bar{1}\,\bar{1}$1] orientation 21.7% reduction. One set of MSB is shown. b) C90 orientation after the second 28.7% reduction (the initial C oriented crystal was pre-deformed 21.1% and then ND rotated by 90°). The specific "deformation" bands are shown after etching with concentrated nitric acid

3.2. Local orientations measurements by ACOM in the SEM

Measurements of individual orientations by ACOM in the SEM were performed in selected fields on longitudinal sections (perpendicular to TD) of deformed samples, point by point with the distance about 0.2μm.

The results are presented in the form of crystal orientation maps and in the form of continuous {111} pole figures and inverse pole figures where the positions of the ND and ED axes are referred to the standard stereographic triangle.

3.2.1. Single crystals of the C(112)[11$\bar{1}$] orientation

Two sets of single orientations data contained in two fields ~ 650μm by 650μm wide are analyzed. One set is placed in the area of the matrix (field C_M in Fig. 3a), and the other in the area containing a macroscopic shear band (field C_{SB} in Fig. 3b).

In the area of the matrix (field C_M), a distinct destabilization of the initial orientation *C* occurs with a tendency of scattering towards Dillamore position D(4 4 11)[11 11 $\bar{8}$] ($\varphi_1 = 90°$, $\Phi = 27.4°$, $\varphi_2 = 45°$), corresponding to the rotation (+)7.9° about TD||[1$\bar{1}$0] (Fig. 4a). In the range of deformation preceding the development of a single family of shear bands, the adjustment of the asymmetric configuration of pairs of the co-planar BII and BIV and co-linear AVI and DVI privileged slip systems take place to the symmetry of deformation which is induced by the channel-die test (Table 1). In the position *D*, the [$\bar{1}\bar{1}$2] direction (the resultant of the two operating co-planar slip directions [$\bar{1}$01] and [0$\bar{1}$1]) and the [110] direction of the two co-directional slip systems are symmetrical with respect to the (ND_1-TD_1) plane and are inclined at 27.4° to the extension direction.

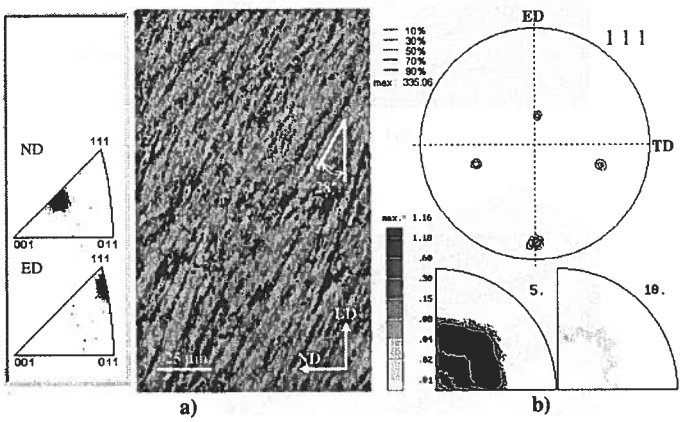

Fig. 4. A (112)[11$\bar{1}$] single crystal after 21.7% reduction by channel-die compression.
a) Pattern Quality Map (PQ) imaging the microstructure of the matrix (Field C_M in Fig. 3a) in the plane of the ND-ED section and the inverse pole figures of the ND and ED axes.
b) The {111} pole figure and the distribution of the axes and misorientation angles (MDF)

When the orientation changes in the matrix, the angle between the common [110] slip direction of the CD system and the ED direction decreases, whereas the angle between the (111) plane of the CP systems and the compression plane increases. Accordingly, the value of the τ/σ ratio in the pair of the systems AVI and DVI diminishes from 0.544 to 0.470, and increases in the pair of the systems BII and BIV from 0.544 to 0.710 (Table 1), which leads to an increase of the reduced shear stress τ in the CP systems. It is worth nothing that in the (ND-ED) plane the shears along the symmetrically arranged [$\bar{1}\bar{1}$2] and [110] directions are of different values ($\gamma_{CD} > \gamma_{CP}$). In this case the accommodation of the unbalanced bending moments, caused by the reactions of the anvils by a rotation of (+)$\alpha°$ about the axis parallel to

TD_1, takes place by way of local lattice kinking. The newly formed kink-band is a precursor of the occurrence of a macroscopic shear band. In the plane perpendicular to TD_1 (see Fig. 3a) it forms a greater angle (35°–48°) with ED_1 than is the angle of ~ 28° contained between ED_1 and the trace of the CP slip plane (direction $[\bar{1}\bar{1}2]$) in the matrix. The observed difference between the inclination angles with respect to ED_1 is the origin of controversial opinions presented in literature on the non-crystallographic nature of shear bands.

The results of measurements of single orientations in the area of shear bands (field C_{SB}) (Fig. 5b) do not confirm this hypothesis. A characteristic feature of shear bands is a local step–by–step change of orientation towards the $(001)[\bar{1}\bar{1}0]$ position, in general corresponding to the lattice rotation of (+)10°–15° about the $TD \| [1\bar{1}0]$ axis. The range of orientation from D through $(114)[\bar{2}\bar{2}1]$ to $(118)[\bar{4}\bar{4}1]$ in the MSB (Table 1) determines the change of the inclination angle of the plane of CP systems with respect to the compression plane. The values of this angle increase from 27.4° through 35.5° to ~45°. It must be stressed that in the case of the $(114)[\bar{2}\bar{2}1]$ orientation a coincidence of the plane of CP systems is found with the shear plane lying in the analyzed MSB at an angle of ~35° to ED (Fig. 3a). The increase of the Schmid factor of the CP slip systems (Table 1) from 0.710 through 0.816 to 0.866 (maximum), is related to the changes in the inclination of the (111) plane as described above. This newly formed kink-band causes a local increase of the reduced shear stress in the co-planar systems belonging to the range of orientations cumulated in MSB, which determines the preferential localization of shear in the CP slip planes.

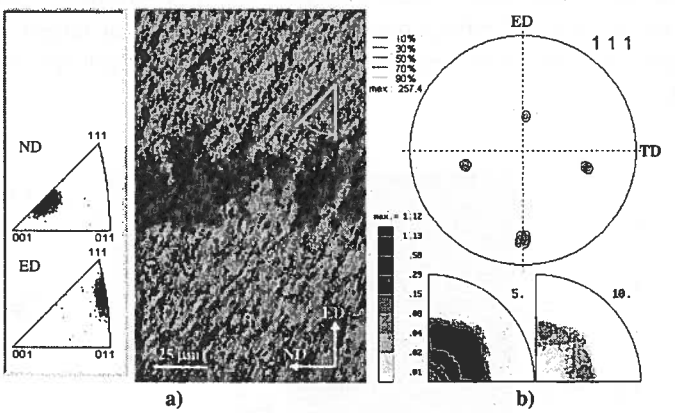

Fig. 5. The microtexture of a macroscopic shear band formed in $(112)[11\bar{1}]$ single crystal after 21.7% reduction (Field C_{SB} in Fig. 3a). a) Pattern Quality Map imaging the microstructure in the plane of the (ND-ED) section and the inverse pole figures of the ND and ED axes. b) The {111} pole figure and the distribution of the axes and misorientation angles (MDF)

The continuous {111} pole figures and the distributions of the axis and the rotation angle (orientation differences) calculated from the sets of single orientations in the fields C_M and C_{SB} (Fig. 3a) give evidence of the crystallographic character of the analyzed "copper type" shear bands. The orientation of a homogeneously deformed matrix is well described by the position *D*, which corresponds to the orientation difference limited to 10° (Fig. 4b)

and to the distribution of the rotation axis from the surroundings of <112> to <210> which is connected with the axes of rotation of the operating single slip systems. The (114)[$\bar{2}\bar{2}$1] orientation dominates within the shear band (Fig. 5b) whereby the plane of the pair of CP slips forms the angle 35.26° with the extension direction, ED_1. As shown in Figure 5b, the progressive rotation not exceed 10°, and the preferential concentration of the rotation axes in the surroundings of the <110> direction are in agreement with the privileged activity of the pair of CP slip systems.

3.2.2. Orientation C90(112)[1$\bar{1}$0] of a single crystal pre-deformed in the position C(112)[$\bar{1}\bar{1}$1]

Prior to the change of the extension direction, a single crystal in the position *C* was pre-deformed to 21.1% reduction. In the course of deformation (in accordance with description given in the preceding chapter), the (112)[11$\bar{1}$] orientation undergoes destabilization and becomes displaced towards the direction of the D i l l a m o r e position (4 4 11)[11 11 $\bar{8}$]. The sample is next rotated by 90° about ND. The extension direction ED_2 is then along the former transverse direction TD_1 which causes that the D i l l a m o r e orientation passes into the unstable orientation D90(4 4 11)[1$\bar{1}$0]. This change of the deformation geometry leads to privileged position of the two systems AIII and DI, that is ($\bar{1}$11)[[101] and (1$\bar{1}$1)[011] which are situated symmetrically to the plane perpendicular to ED_2[1$\bar{1}$0] (Fig. 3b). Operation of these systems, which according to Table 2 possess high S c h m i d factors (Ws = 0.849), creates new possibilities for single slips. Slip may be realized in both slip systems alternately or simultaneously, however in different fragments of the sample.

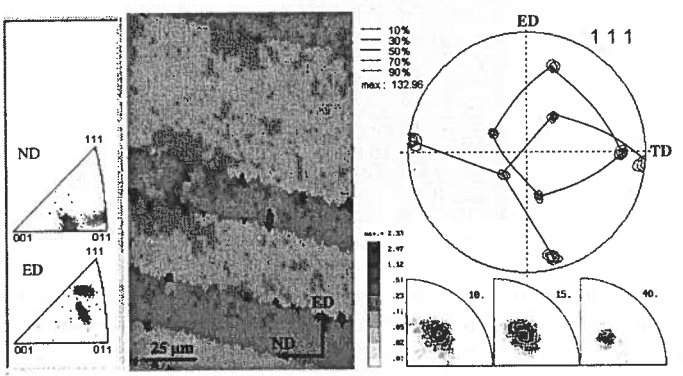

Fig. 6. The microtexture of a deformation band in the C90 sample (Field C90 in Fig. 3b) after 90° rotation about the ND axis and an additional reduction to 28.7% of the pre-deformed (112)[11$\bar{1}$] single crystal. a) Pattern Quality Map imaging the microstructure in the plane of the (ND – ED_2 = TD_1) section and the inverse pole figures of the ND and ED_2 axes. b) The {111} pole figure and the distribution of the axes and misorientation angles (MDF)

TABLE 2

Schmid factor values of the slip systems in the pre-deformed C90 single crystals

Orientation	$\tau/\sigma = \cos\alpha_c \cos\beta_c - \cos\alpha_e \cos\beta_e$							
	AIII	DI	AII	DIV	BII	BIV	CI	CIII
C90°(112)[1$\bar{1}$0]	0.816	0.816	0.544	0.544	0.272	0.272	0.000	0.000
D90°(4 4 11)[1$\bar{1}$0]	0.849	0.849	0.614	0.614	0.355	0.355	0.120	0.120
(114)[1$\bar{1}$0]	0.862	0.862	0.680	0.680	0.408	0.408	0.227	0.227
(116)[1$\bar{1}$0]	0.859	0.859	0.731	0.731	0.430	0.430	0.301	0.301
(118)[1$\bar{1}$0]	0.854	0.854	0.755	0.755	0.433	0.433	0.334	0.334
(1 1 11)[1$\bar{1}$0]	0.846	0.846	0.733	0.733	0.431	0.431	0.328	0.323

It should be noted that during the pre-deformation of the C-oriented sample, the slip planes of the systems AIII and DI are the cross-slip planes of the operating dislocations $\bar{b}$ IV = 1/2[$\bar{1}$01] and $\bar{b}$ II = 1/2[0$\bar{1}$1] in the CP systems BIV and BII, respectively. Thus, the cross-slip debris and their density on the planes A and D can act as obstacles which restrict the dislocation motion in the single slip systems AIII or DI. Moreover, the components (114)[1$\bar{1}$0] to (118)[1$\bar{1}$0], which describe the internal MSB microstructure in pre-deformed C90-oriented sample, lead locally to higher S c h m i d factors. With respect to the matrix orientations, they range from 0.862 to 0.854 in the systems AIII and DI and from 0.680 to 0.755, in the systems AII and DIV (Table 2). In the author's opinion, these initial conditions drastically restrict the ability of the pre-deformed and C90 oriented single crystals to accommodate deformation by homogeneous double slip.

An important feature of the micro-mechanical behaviour of the C90 sample during additional deformation of 28.7% ($ED_2 = TD_1$) is the appearance of a specific fragmentation of the structure in the form of wavy bands (black in Fig. 3b). The measurements of individual orientations from area marked C90 in Fig. 3b show that the microstructure of these bands consists of a set of laminae 20–60μm thick (Fig. 6a).

The boundary plane of the lamina is inclined by about 10° to TD_2 and makes an angle of 26° to 28° with the ED_2 axis. Figure 6a shows that the microtexture of each lamina can be described by one of the two components (1 11 11)[11 $\bar{7}$ 6] and (035)[10 5 $\bar{3}$] which are almost complementary. These orientations are close to the complementary components (011)[2$\bar{1}$1] and (011)[21$\bar{1}$] of the brass type rolling texture. The {111} pole figure (Fig. 6b) show that the decomposition of the initial orientation of the C90 sample results from the rotations of opposite sign about an axis approximately parallel to the TD_2 direction. The formation, of two sets of orientations by plastic strain is rather similar to the deformation banding observed in fcc single crystals with initial {100}<011> orientation. These deformation bands, with two alternating orientations separated by transition bands, correspond qualitatively to the banded structures observed here. The crystallographic mechanism responsible for the formation of the observed compact clusters of layers oriented alternatively differs from that of MSB, as characterised in the preceding chapter.

Namely, the alternating changes of orientation, occurring almost simultaneously in the particular layers, are induced by selected activity of only one of the privileged slip systems AIII or DI. As a consequence, the axes of 20°–30° rotations in each layer are the directions $[\bar{2}\bar{1}1]$ and $[\bar{1}\bar{2}1]$, respectively, situated near the $TD_2 \| [\bar{1}\bar{1}1]$ direction. In the case of MSB of copper type, on the other hand, the local laminar structure of the band can be described only by one component. In these bands, a co-planar slip {111} plane tends towards a position parallel to the shear plane and a "resultant" <112> slip direction consequently adopts a position parallel to the shear direction, as a result of the local change in orientation by rotation about TD||<110>.

3.2.3. Single crystals of the (112)[1$\bar{1}$0] orientation

The deformation behaviour of the ideal (112)[1$\bar{1}$0] oriented single crystals is significantly different from that of more inhomogeneous C90-oriented, pre-deformed samples. The not pre-deformed single crystals have restricted ability to accommodate deformation by heterogeneous slip which is localised in the banded structures of the compact clusters of layers oriented alternatively, as characterized in Figs 3b and 6a. The deformed crystals become divided into larger fragments in which only either one of the two privileged slip systems AIII or D1 operates.

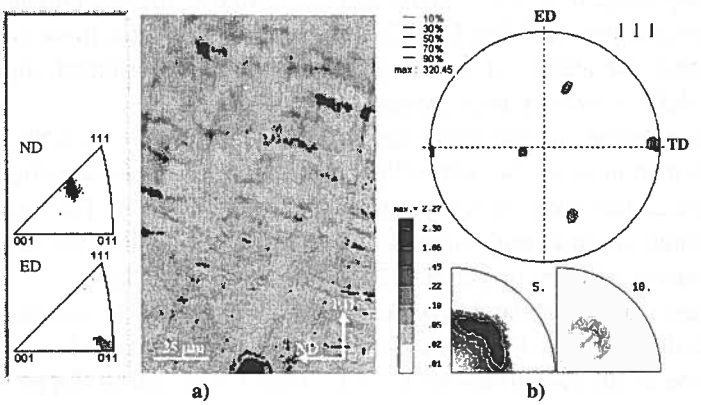

Fig. 7. The microtexture of the (112)[1$\bar{1}$0] single crystals a reduction 20.3% by channel-die compression. a) Pattern Quality Map imaging the microstructure in the section (ND-ED_2) and the inverse pole figures of the ND and ED_2 axes. b) The {111} pole figure and the distribution of the axes and misorientation angles (MDF)

In the range of small reductions below 20% the changes of the initial orientation are rather small, although a distinct tendency of rotation towards the main component B{110}<112> of the brass type texture can be observed (see the inverse pole figures in Fig. 7a). Such a behaviour gives evidence of a relatively uniform activity of two privileged slip systems (Fig. 7b). The orientation changes become particularly intense above 20% reduction (Figs 8a and 8b). In particular, a sample deformed to 41.9% attains an orientation

close to the (011)[$\bar{2}$11] position, corresponding to one of the complementary components of the microstructure of a pre-deformed C90 sample. This means that in the analysed fragment of the sample the ($\bar{1}$11)[101] single slip system is predominantly operating. As a consequence, the progressive change of orientation inside this selected area occurs by rotation of 20°–30° about the [$\bar{1}\bar{2}$1] AIII axis close to the TD$_2$||[$\bar{1}\bar{1}$1] direction. This interpretation is supported by the results of calculations of the misorientation distribution function (MDF) presented in Fig. 8b.

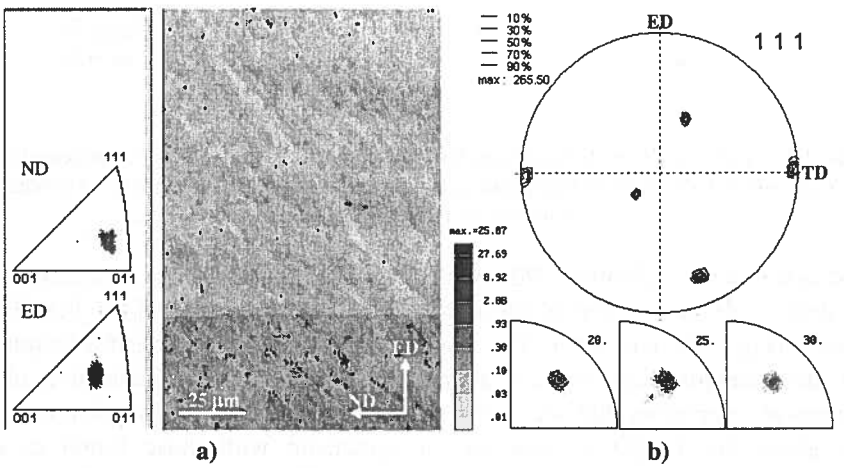

Fig. 8. The microtexture of the (112)[1$\bar{1}$0] single crystals after a reduction 41.9% reduction.
a) Pattern Quality Map imaging the microstructure in the section (ND–ED$_2$) and the inverse pole figures of the ND and ED axes. b) The {111} pole figure and the distribution of the axes and misorientation angles (MDF)

3.3. Evolution of the global textures

The analysis of the effect of the changes of local orientation on the global texture of the examined single crystals was carried out on the basis of {111} pole figures obtained by X-ray diffraction measurements using the reflection method.

The orientation changes (Fig. 9a and 9b) that occur in the single crystal of the (112)[11$\bar{1}$] orientation after a reduction of 21.7% are in agreement with the local textures as characterized by the EBSD method. The initial orientation is scattered toward the D matrix orientation by the TD$_1$||[1$\bar{1}$0] rotation, resulting from the non-equilibrium operation of the CP and CD slip systems (Fig. 9a). In the area containing the MSB (Fig. 9b, projection on the ND-TD plane), a further increase of scattering toward (001)[$\bar{1}\bar{1}$0] is observed. This step–by–step, progressive rotation of (+)14° about the TD$_1$ axis is considered responsible for the lattice bending in the form of kink-band, which brings the CP slip plane inside the MSB into a position parallel to the shear plane.

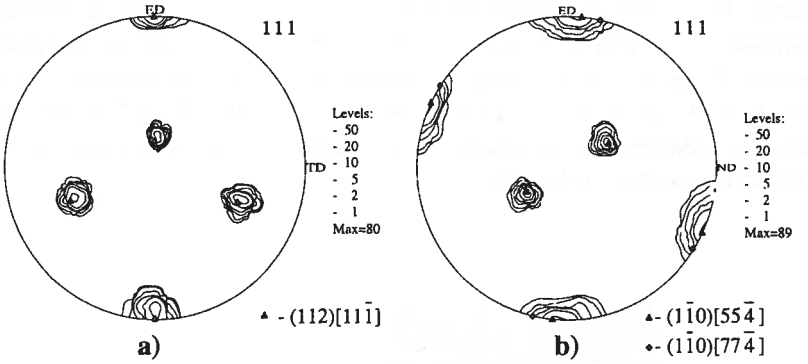

Fig. 9. The {111} pole figures recalculated from ODF for the (112)[11$\bar{1}$] single crystal deformed to 21.7% reduction. X-ray diffraction method. a) Orientation in the matrix area. b) Orientation in the area containing MSB. Projection on the (ND-ED) plane

In the case of a pre-deformed C90 sample (Fig. 10a), the additional reduction of 28.7% leads to distinct decomposition of the initial (112)[1$\bar{1}$0] and/or D90(4 4 11)[1$\bar{1}$0] main components (Fig. 10b and 10c). The general tendency of the transformation of the {112}<110> orientation into two complementary {110}<112> components is observed. The changes of orientation that occur as a result of two alternating (positive or negative) rotations about the TD_2||[$\bar{1}\bar{1}$1] axis are in agreement with those found in specific deformation bands, as characterized in Figure 6. Hence, the preponderance of the orientations in the surroundings of the (011)[2$\bar{1}$1] complementary component seems to be associated with non-equilibrium operation of one of the two preferred single slip systems AIII and DI. Namely in this case, the single system ($\bar{1}$11)[101] with the axis of rotation [$\bar{1}\bar{2}$1] near the TD_2||[$\bar{1}\bar{1}$1] is more active in the particular fragments of the sample.

The evolution of initial orientation in the channel-die compressed single crystals of the ideal (112)[1$\bar{1}$0] orientation is shown in Figure 11. This orientation after the reductions of 35.3%, 42.0% and 65.9% is transformed towards the (011)[$\bar{2}$11] position. The presence of the second, complementary component is strongly restricted in these samples (Fig. 11b and 11d). The preponderance of only one of the two complementary components coincides with a rather sporadic occurrence of the banded structures, as it is observed in the pre-deformed samples C90 (Fig. 6a).

4. Concluding remarks

The choice of the (112)[111] orientation and the use of the channel-die compression method in the investigation of copper single crystals enabled a more transparent exposition of effects caused by the change of the deformation path in the cold rolling process of fcc metals of medium SFE and a more detailed characterization of these effects.

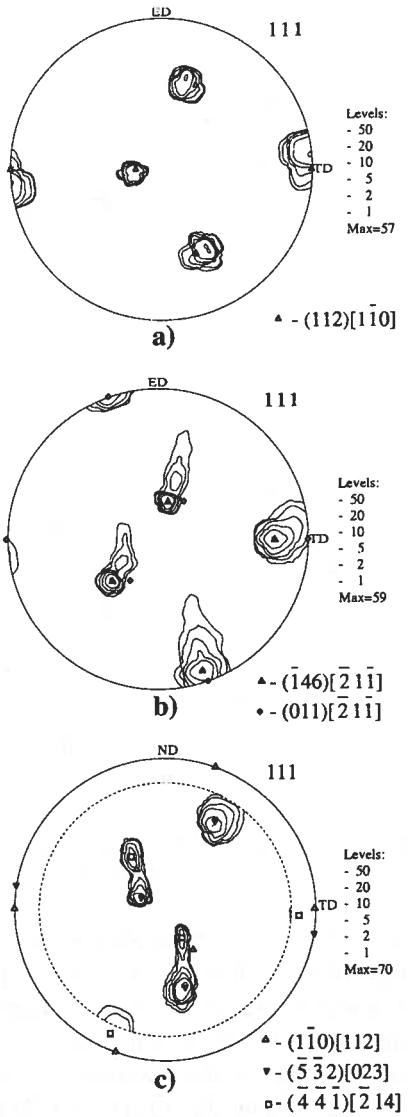

Fig. 10. The {111} pole figures for the C90 single crystal recalculated from X-ray pole figures. a) The {111} pole figure after pre-deformation to 21.1% in the (112)[11$\bar{1}$] position and then at the beginning of the second deformation after 90° rotation about the ND axis. b) The {111} pole figure of C90 sample after an additional reduction of 28.7%. c) Experimental {111} pole figure. Projection on the (ND-ED_2) plane. Additional reduction to 28.7%

It has been shown that the changes of texture and microstructure caused by additional deformation in the transverse direction of pre-deformed samples correspond with those observed in cold rolled polycrystalline copper with respect to the preferred C{112}<111> orientation.

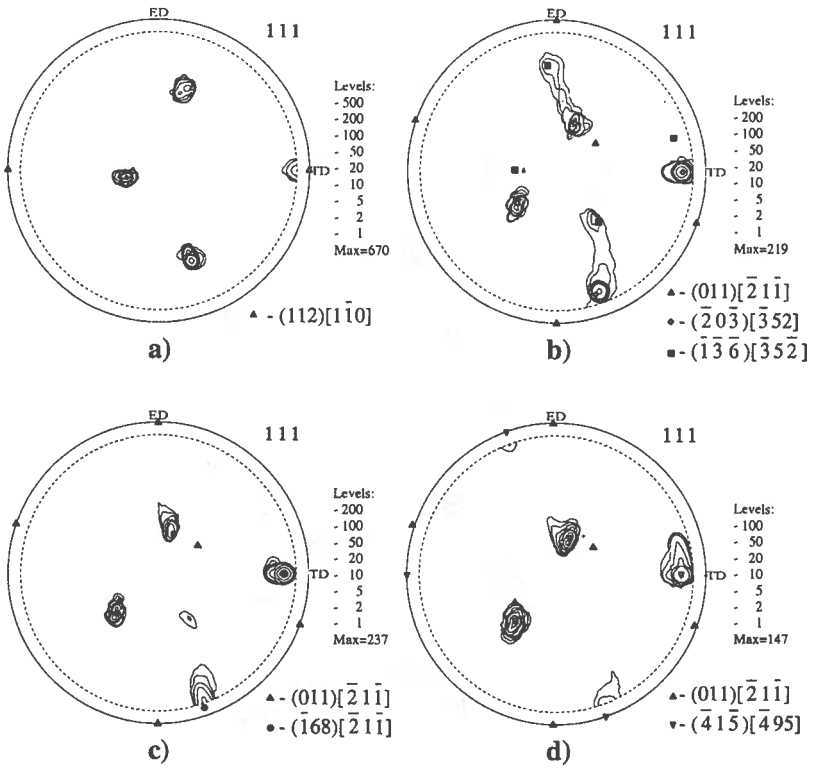

Fig. 11. The {111} pole figures of the (112)[1$\bar{1}$0] single crystals. a) Initial orientation. b) Reduction of 35.3%. c) Reduction of 42.0%. d) Reduction of 65.9%

1. The main findings of these studies is the evidence that the destabilisation of the {112}<110> orientation during rolling leads to the {110}<112> preferred orientation. It has been shown that this type of transformation occurs in pre-deformed C90 samples as well as in single crystals with the ideal {112}<110> orientation.

Pre-deformation, however, influences the dynamics of this transformation which is realized by a rotation of ~30° about the [$\bar{2}\bar{1}$1] or [$\bar{1}\bar{2}$1] axis lying in the (1$\bar{1}$1) or ($\bar{1}$11) slip plane of the two preferred glide systems DI and AIII. They are inclined at small angles to the [$\bar{1}\bar{1}$1] direction parallel to TD_2. Orientation changes are less dynamic in the case of homogeneous double slip in the whole volume of the crystal (initial stage of deformation of the (112)[1$\bar{1}$0] sample). However, these changes are faster in the case of simultaneous but non-homogeneous operations in single slip systems in different fragments of the deformed single crystal. As a consequence, the fragmentation of the sample microstructure in the form of non-regular blocks (sample (112)[1$\bar{1}$0]) and/or deformation bands (sample C90) is the origin of the development of two {110}<112> complementary components of deformation texture.

2. The structural effect of the change of the deformation path, occurring in samples C90 in a specific form of a banded structure, has often been attributed erroneously in the literature to the development of the copper-type MSB. The substructure within the MSB consists of very fine microbands, slightly elongated in the <211> shear direction on the {111} co-planar slip plane. The microtexture of these MSB is formed by progressive, step–by–step change of orientations from the position *D* in the matrix to the {114}<221> position within the band. On the other hand, the formation of two sets of layers (20–60μm thick) with two complementary orientations of {110}<112> in these banded structures of the C90 sample is rather similar to deformation banding observed in single crystals of {100}<011> initial orientation. These deformation bands, with two alternating orientations separated by transition bands with a {100} plane perpendicular to ND, correspond qualitatively to the compact clusters of layers observed here. In the case of a deformed C90 sample, the planes of the preferred slip systems DI and AIII are situated symmetrically relative to the (001) plane. Its trace in the section perpendicular to TD_2 creates the angle of ~30° with ED, which approximately corresponds to the inclination angle of the layers inside the observed banded structures.

The performed analysis specify the conclusion that the localization of deformation in the form of typical shear bands or deformation bands depends on the initial orientation of the single crystal. The lattice orientation with respect to the deformation field determinines a defined configuration of the preferred slip systems.

Acknowledgements

The study has been carried out within the research project No 7T08A06221 supported by the Polish State Committee for Scientific Research.

Financial support by the German Research Foundation (DFG) is gratefully acknowledged: One of us (M.O.) has received a grant (DFG project SCHW 403/13-1). The JOEL JSM 6400 SEM has been provided in the framework of the DFG Research Group "Textur und anisotropie kristalliner Stoffe".

REFERENCES

[1] J. Pospiech, Z. Jasieński, A. Litwora, A. Piątkowski, J. Gryziecki, Proceed. of the 12th Int. Conf. on Texture of Materials (ICOTOM), Montreal, ed. Jerzy A.Szpunar, NRC Research Press **1**, 581-586 (1999).

[2] J. Pospiech, M. Wróbel, J. Bonarski, M. Blicharski, Mat. Science Forum **408-412** 613-618 (2002).

[3] A. Korbel, Advances in Crystal Plasticity, A Symposium in Honour of Professor Z. S. Basiński, ed. by D.S. Wilkinson and J.D. Embury, Kingston, Ontario (1992).

[4] K. Mori, H. Mecking, Y. Nakayama, Acta Metall. **33**, 379 (1985).

[5] Z. Jasieński, A. Piątkowski, Proceed. of the 8th Int. Conf. on Strength of Metals and Alloys (ICMA), ed. P.O.Kettunen et al., Pergamon Press **1**, 367 (1988).

[6] Z. Jasieński, T. Baudin, A. Piątkowski, R. Penelle, Scripta Mater. **35**, 397 (1996).

[7] P. Wagner, O. Engler, K. Lücke, Acta Metal. Mater. **43**, 3799 (1995).

[8] Z. Jasieński, H. Paul, A. Piątkowski, A. Litwora, Journ. of Materials Processing. Technology **53**, 187 (1995).

[9] R. Schwarzer Micron **28**, 249-265 (1997).
[10] K. Wierzbanowski, Z. Jasieński, Bull. Acad. Polon. Sci., Serie sci. techn. **25**, 67 (1977).
[11] S. Nourbakhsh, D. Vujič, Acta Metall. **34**, 1083 (1986).

REVIEWED BY: JAN KUŚNIERZ
Received: 2 December 2003.

ARCHIVES OF METALLURGY AND MATERIALS
Volume 49 2004 Issue 1

WŁODZIMIERZ BOGDANOWICZ*, ZBIGNIEW BOJARSKI*

SUBGRAIN AND DOMAIN STRUCTURE OF Al-Cu-Co SINGLE QUASICRYSTALS

BLOKOWA I DOMENOWA STRUKTURA MONOKWAZIKRYSZTAŁÓW STOPU Al-Cu-Co

The influence of low-temperature (100°C) and high-temperature (900°C) thermal treatment on the subgrain and domain structure of two-subgrain single quasicrystals of Al-Cu-Co alloy was studied. The low-temperature treatment causes the fragmentation of the domains, and increases their boundaries density. The high-temperature thermal treatment causes some broadening of the domains which is connected with the partial disappearance of their boundaries. The treatment also causes the rotation of the subgrains in relation to one another.
Keywords: Al-Cu-Co single quasicrystals; Mosaic structure; Domain structure

Badano wpływ niskotemperaturowej (100°C) i wysokotemperaturowej (900°C) obróbki termicznej na strukturę blokową i domenową dwublokowych monokwazikryształów stopu Al-Cu-Co. Niskotemperaturowa obróbka powoduje rozdrobnienie domen i zwiększenie gęstości ich granic. Obróbka termiczna przy 900°C powoduje poszerzenie domen, wynikające z zanikania części ich granic, oraz wzajemny obrót bloków.

1. Introduction

The subgrains of the mosaic can be studied by methods of *X*-ray topography in a simple way [1–8]. These methods enable a determination of the shape, dimensions, arrangement, strain field and angles of misorientation of subgrains. The defects, appearing in quasicrystals, such as phasons, dislocations or vacancies may interact with the subgrain boundaries. It is an interaction of the atomic scale defects with the macroscopic defects. For example, the authors in [9] report an interaction between the domain (domains of a size ranged from 10 to 100 nm) containing considerable phason-deformations and the grain boundaries (about 1 mm in a size) of an icosahedral phase of the Al-Li-Cu alloy.

It was shown in [1, 4], that Al-Pd-Mn single quasicrystals have the subgrain boundaries and faceted voids surrounded by the strain fields. Annealing of the single quasicrystal for

* INSTYTUT NAUKI O MATERIAŁACH, UNIWERSYSTET ŚLĄSKI, 40-007 KATOWICE, UL. BANKOWA 12

96 h at temperature of 750°C and subsequent slow cooling down to room temperature significantly influences the size and the concentration voids. The concentration of voids also depends on their distance from the subgrain boundaries [8].

In [2] it was asserted from the *X*-ray topograms that inside the subgrains of ikosahedral Zn-Mg-Y (Y = Ho, Tb) single quasicrystals there exist five sets of contrast bands, coming from the area of the nucleation. Whereas in [3] it was proved that the ikosahedral Al-Pd-Mn single quasicrystals have the subgrain structure of the disorientation angle between several arc minutes to several degrees.

The aim of this paper is to examine relation between the subgrain and domain structure of two-subgrain single quasicrystals of the Al-Cu-Co alloy after low-temperature (100°C) and high-temperature (900°C) thermal treatment.

2. Material and experimental procedures

Using a modified horizontal static B r i d g m a n method, the so called inclined front crystallization (IFC) method [7], two-subgrain plate-like single quasicrystals of the decagonal phase of Al-Cu-Co alloy were obtained. The average chemical composition of the single quasicrystals, determined by *X*-ray microanalyser, was found to be Al-17.7Cu-16.8Co [at.%].

One sample was prepared from each of the single quasicrystals. Samples have the form of plates of $15 \times 3 \times 0.5$ mm^3 size (Fig.1 (a)). The areas of the samples, in which the solidification process had begun, were marked ***B*** and their terminal areas were marked ***E***.

In the *X*-ray topograms of all the samples, diffraction images of two subgrains, $\boldsymbol{Q_1}$ and $\boldsymbol{Q_2}$ were observed (Fig. 1(b)). The subgrain boundary is placed along the ***X*** axis. Reflection *X*-ray topograms were obtained from the top surface of the samples by the modified Auleytner oscillation method [6]. In the topogram shown in Fig. 1(b), the images of subgrains $\boldsymbol{Q_1}$ and $\boldsymbol{Q_2}$ are displaced in relation to one another. This is due to a relative rotation of the subgrains the angle of which is called an angle of subgrains' disorientation. This angle varied between 0.1 and 0.7 degrees for the samples examined. The orientation of all the samples were examined by L a u e diffraction.

An *X*-ray phase analysis of powder, which was obtained by grinding of the lower surface of the samples, proved that all the samples consisted only of decagonal phase of Al-Cu-Co alloy. Diffraction pattern showed only those reflections which were previously reported to occur from the decagonal phase [7, 10, 11].

The single quasicrystals were examined by the differential thermal analysis (DTA) method. In Fig. 2, the DTA heating curve, which is typical for the samples in their initial (as grown) state, is shown. The material for this examination was obtained from the sample by cutting off a small part near ***E*** surface (Fig. 1(a)). The characteristic peak at a temperature of 1040°C to 1060°C corresponds with the well-known reversed peritectic reaction of the

decagonal phase [7]. However, the change in the slope of the basic line at about 600°C, may relate to a transformation of the order – disorder type. This corresponds to the results of [12]. In [12] it was shown, by transmission electron microscopy (TEM) investigation, that in $Al_{65}Cu_{15}Co_{20}$ alloy, below a temperature about 600°C, a decagonal phase with space group $P\bar{1}0$ m2 occurs, whereas at high temperature, a decagonal phase with space group $P10_5/mmc$ occurs [12]. A possible order-disorder type transformation in $Al_{65.5}Cu_{18.5}Co_{17}$ alloy is reported in [12, 13]. On the basis of high resolution *X*-ray diffraction as a function of annealing temperature, it was asserted in [14] that in the $Al_{63}Cu_{17.5}Co_{17.5}Si_2$ alloy the transformation of phason order occurs at a temperature 770°C.

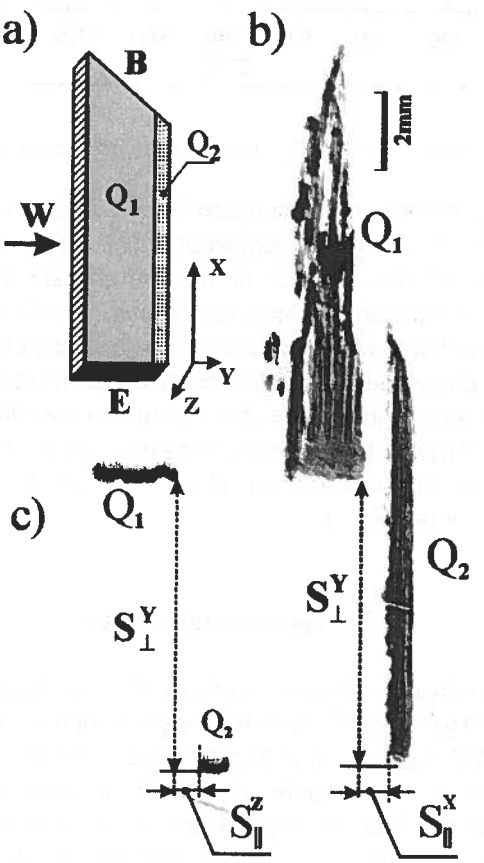

Fig. 1. (a) Shape of the single qusicrystals and the prepared samples. Examples of X-ray topograms obtained for the sample in the initial state (b, c). Topograms (b) – top surface of the sample. Topogram (c) – surface *E* of the sample, the plane of which is parallel to plane *YZ*.
Radiation $Cu_{K\alpha 1}$. Reflection $23\bar{1}0$

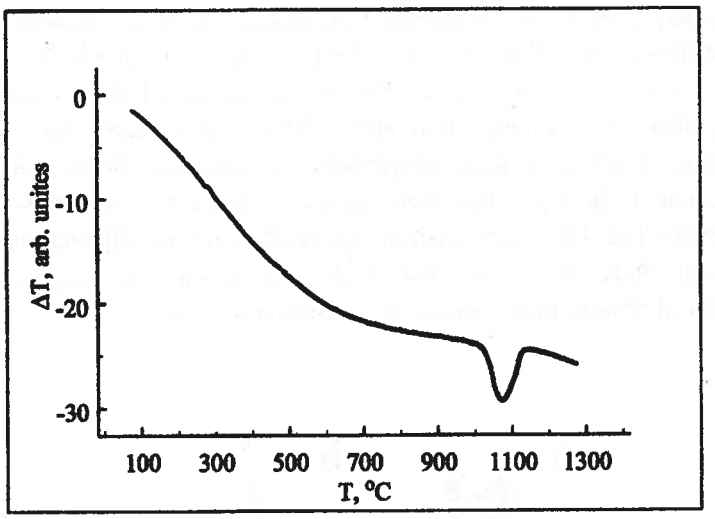

Fig. 2. DTA heating curves of the $Al_{65.5}Cu_{17.7}Co_{16.8}$ alloy in initial state. Heating rate – 4°C/min

The last stage of the process of single quasicrystals obtaining was rapid cooling from temperature about 600°C down to room temperature [7]. This caused a situation in which the real microstructure of the samples in the initial state was not an equilibrium microstructure at room temperature. These single quasicrystals were annealed at 100°C (8 h) and subsequently cooled down in the furnace. The treatment was aimed at stabilization of the low-temperature phase and making the thermodynamic state of the samples close to the equilibrium state at room temperature. Next treatment was the annealing of the single quasicrystals at 900°C (8 h) and subsequent cooling down in ice-water. This treatment was aimed at stabilization of high-temperature phase. The whole treatment took place in a helium atmosphere of a purity 5N.

3. Experimental results

Metallographic examination of lateral surfaces W of the samples (Fig. 1(a)) revealed bands of contrast parallel to vector R_{XZ} which is the projection of the ten-fold symmetry axis onto surface W (plane XZ, Fig. 1(a), 3(a). Similar bands were discovered on the top surface of the samples. The direction of the bands tallied with the direction of the projection of the ten-fold symmetry axis (R_{XY}) on the top surface of the samples (plane XY, Fig. 1(a)). Therefore, it was concluded that in the samples there exists a band structure which is set along the ten-fold axis.

In Fig. 3(b) and 3(c) the typical optical micrographs are shown, which were obtained after the treatments at 100°C and 900°C, respectively. The treatment at 100°C has caused a decrease in the widths of the bands and an increase in their density, which is related to the appearance of additional boundaries of the bands (Fig. 3 (b)). However, the treatment at

900°C, in contrast, caused a widening of the part of the bands and a decreasing of their density which means the disappearance of some of the boundaries (Fig. 3 (c)).

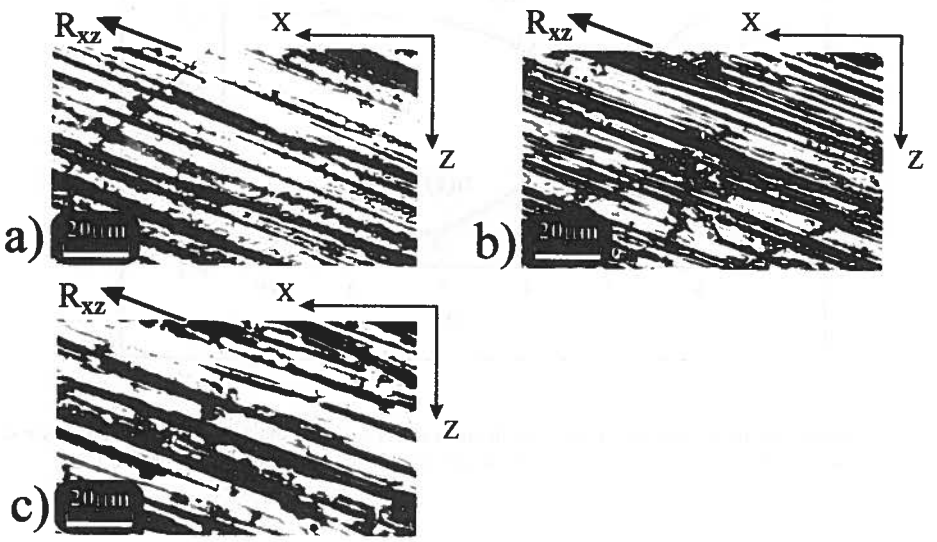

Fig. 3. (a) Optical micrographs obtained from the lateral surface *W* (Fig. 1(a)) for the samples in the initial state; (b) after thermal treatment at 100°C; (c) after thermal treatment at 900°C.
R_{XZ} – projection of the ten-fold symmetry axis on plane *XZ*

Each of the topograms shown in Figs. 1(b), (c) (indices of the reflections are marked according to the convention used in [15]) contains the images of two subgraines Q_1 and Q_2 displaced in relation to one another. Thermal treatment at 100°C did not cause any change in the displacement but treatment at 900°C increased the amount of displacement. This means that, in the last case, the rotation of subgrain Q_2 in relation to Q_1 had occurred.

In the topograms shown in Fig. 1(b) the bands of contrast parallel to axis *X*, that is, the axis of the single quasicrystal growth, can be seen. The occurrence of such bands of the growth origin was discovered in [2] for the Zn-Mg-Y (Y = Ho, Tb) single quasicrystals. These bands can be related to a slight heterogeneous chemical composition.

After each thermal treatment of the samples, part of the material was ground from their lower surfaces and then examined by *X*-ray phase powder analysis. In all cases neither a change of the peak pattern nor a splitting of the peaks of the decagonal phase was noted. The only noticeable change was a slight broadening of the weak peaks after thermal treatment at 100°C and a narrowing after the treatment at 900°C.

For additional five single quasicrystals the density of bands of microstructure (Fig. 3) and the angle of subgrain rotation as the functions of annealing time at temperature of 900°C were determined (Fig. 4).

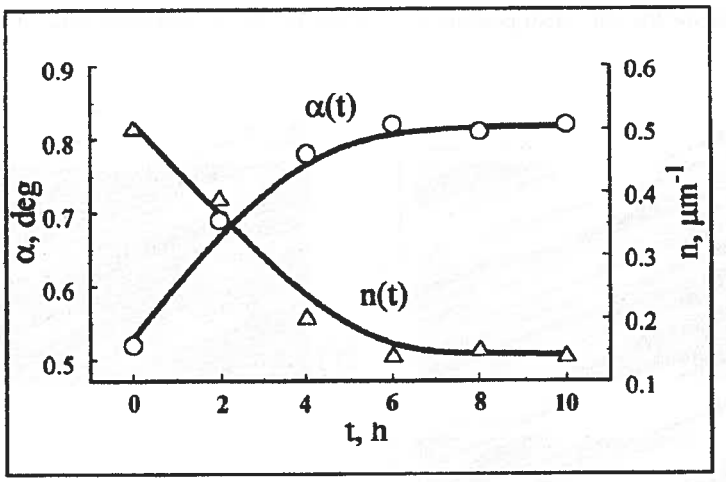

Fig. 4. Relationship of the density of the band of microstructure n(t) and the subgrains' rotation angle $\alpha(t)$ versus period of annealing time of the single quasicrystals at temperature of 900°C

4. Discussion of the results

The band microstructure along the direction of ten-fold symmetry axis shown in Fig. 3 may correspond to the domain structure of the low-temperature decagonal phase (space group $P\bar{1}0$ m2). This matches the result of the TEM investigations presented in [12]. Additionally, in [12] it was concluded that above 600°C domains disappear and high-temperature decagonal phase (space group $P10_5/mmc$) occurs. The building elements of both phases are polyatomic cylindrical clusters. The low-temperature phase consists of domains with sizes of about 30–100 nm [12]. Each of the domains contains the clusters with the same sense of polarity [12]. However, in neighboring domains the sense of polarity is opposite. In the high-temperature phase no domains occur and sense of polarity of all clusters is completely random.

Band structures can often be observed in single quasicrystals. For example, band structures elongated along ten-fold symmetry axes were observed by atomic force microscopy [16] in polished sections of decagonal phase of Al-Ni-Co and Al-Ni-Fe alloys annealed at 900°C. The width of the bands was found to be about 0.06 μm.

Thermal treatment of samples at temperature 100°C causes a narrowing of the domains (Fig. 3a, b) which is connected with the fragmentation of the domains into smaller ones. The annealing at 900°C causes disappearance of some of the domains. This caused the formation of the wider areas of the "disordered" high-temperature phase. Cooling down in ice-water stabilizes this phase in ambient temperature. This is visible in the optical micrograph by widening of the part of the bands (Fig. 3(c)).

Widening of domains after treatment at 900°C implies a decrease of a number of domain boundaries parallel to the direction of the ten-fold axis. Mechanical stresses which are accumulated on the boundaries, are unloaded through rotation of the subgrains in relation to one another.

The presented results show the dependence between the domain and subgrain structure in the decagonal single quasicrystals of Al-Cu-Co alloy. This is confirmed by the correlation between the following functions: (i) $\alpha(t)$ – the subgrains' rotation angle as a function of annealing time at 900°C and (ii) n(t) – the concentration of the domains as a function of the time of annealing at 900°C (Fig. 4). While annealing the single quasicrystals in the time period 6h shorter the increase of the value of function $\alpha(t)$ takes place simultaneously with the decrease of the value of the function $n(t)$. While annealing the single quasicrystals in the time period 6h longer the value of both functions ceases to be dependent on the time of annealing simultaneously.

Similar dependence between grains boundaries of quasicrystal alloys and their domain microstructure was also revealed in [9]. There the authors emphasize the fact that the boundaries are formed together with a domain microstructure during slow solidification of a quasicrystal alloy. High temperature annealing causes displacements of the grain boundaries and a reduction of phason stresses. However, their experiments were carried out on polyquasicrystal samples containing great numbers of grain boundaries [9]. Interactions of many boundaries makes the analysis of the phenomenon more difficult. In the present case of a single quasicrystal with only one subgrain boundary, the situation is much easier to analyze. Therefore such two-subgrain single quasicrystals are a very good model material for the study of the interaction of macroscopic subgrain boundaries with microstructural defects.

5. Summary

1. In two-subgrain single quasicrystals $Al_{65.5}Cu_{17.7}Co_{16.8}$, obtained by the IFC method, the band microstructure parallel to the ten-fold symmetry axis was discovered by use of metallography methods. This structure is probably connected with antiphase domains of a low-temperature decagonal phase of space group $P\bar{1}0$ m2.
2. Annealing of single quasicrystals in the "as grown" state at 100°C causes fragmentation of the band microstructure which consists in appearance of narrower bands and increase of their boundaries density.
3. The annealing of single quasicrystals at 900°C, and rapid cooling down afterwards, causes widening of the bands and a decrease of the density of their boundaries. Concomitantly rotation of the subgrains in relation to one another occur.
4. It is assumed that in the sample, after its treatment at 900°C, the mixture of two decagonal phases appears, which differ in respect to cluster ordering. The low-temperature phase (space group $P\bar{1}0$ m2) contains antiphase domains, which vanish in the high-tempereture phase (space group $P10_5/mmc$). Disappearance of the part of the domains' boundaries at 900°C treatment causes the rotation of the subgrains in relation to one another and an unloading of the internal stresses accumulated in the boundaries.

REFERENCES

[1] L. Mancini, A. Létoublon, S. Agliozzo, J. Wang, J. Gastaldi, M. de Boissieu, J. Härtwig, H. Klein, Mater. Sci. Eng. **294-296**, 57 (2000).

[2] A. Létoublon, I. R. Fisher, T. J. Sato, M. de Boissieu, M. Boudard, S. Agliozzo, L. Mancini, J. Gastaldi, P. C. Canfield, A. I. Goldman, A.-P. Tsai, Mater. Sci. Eng. **294-296**, 127 (2000).

[3] J. Gwóźdź, B. Grushko, M. Surowiec, Mater. Sci. Eng. **294-296**, 49 (2000).

[4] E. Reinier, L. Mancini, J. Gastaldi, N. Baluc, J. Härtwig, J. Baruchel, Phys. **B 253**, 61 (1998).

[5] W. Bogdanowicz, Mater. Sci. Eng. **A280**, 247 (2000).

[6] W. Bogdanowicz, Scripta Mater. **37**, 829 (1997).

[7] W. Bogdanowicz, J. Cryst. Growth **240**, 255 (2002).

[8] J. Härtwig, S. Agliozzo, J, Baruchel, M. de Boissieu, J. Gastaldi, H. Klein, L. Mancini, in: J. Wolny, R. Wawszczak (Eds.), Aperiodic Structures 2001, Proceedings of Intenational Conference, Faculty of Physics and Nuclear Techniques University of Mining and Metallurgy, Kraków, p. 56, 2001.

[9] K. Wang, P. Donnadieu, P. Garoche, Eur. Phys. Journal **B13**, 279 (2000).

[10] B. Grushko, R. Wittmann, K. Urban, J. Mater. Res. **7**, 2713 (1992).

[11] K. Edawaga, K. Kajiyama, R. Tamura, S. Takeuchi, Mater. Sci. Eng. **A 312**, 239 (2001).

[12] K. Saitoh, K. Tsuda, M. Tanaka, A.-P. Tsai, A, Inoue, T. Masumoto, Phil. Mag. **A 73**, 387 (1996).

[13] K. Edagawa, K. Kajiyama, Mater. Sci. Eng. **294-296**, 646 (2000).

[14] F. Dénoyer, R. Reich, J. P. Lauriat, Mater. Sci. Eng. **294-296**, 287 (2000).

[15] A. Yamamoto, K. N. Ishihara, Acta Crystallogr. Sect. **A44**, 707 (1988).

[16] T. Drobek, W. M. Heckl, Mater. Sci. Eng. **294-296**, 878 (2000).

REVIEWED BY: JANUSZ WOLNY

Received: 20 November 2003.

A R C H I V E S O F M E T A L L U R G Y A N D M A T E R I A L S
Volume 49 2004 Issue 1

BORYS MIKUŁOWSKI*, GRZEGORZ BOCZKAL*

INFLUENCE OF THE 0.01 at.% Ti ADDITION ON Zn SINGLE CRYSTALS HARDENING IN THE (0001)<11-20> SYSTEM

WPŁYW DODATKU 0.01 at.% Ti NA UMOCNIENIE MONOKRYSZTAŁÓW Zn ODKSZTAŁCANYCH W SYSTEMIE (0001)<11-20>

Zn and ZnTi0,01at.% single crystals were deformed in a compression test in the (0001)<11-20> system up to a $\gamma = 0.2$ range at temperatures 77K, 150K, 293K, 373K, 473K. Two deforming rates were used; 10^{-4} s^{-1} and 10^{-3} s^{-1}. On the base of obtained compression curves of the critical resolved shear stress CRSS, the hardening coefficient within the range of easy slip Θ_A and activation volume V^* were determined. A substantial impact of small additions of Ti (0.01at%) on the process of crystals strengthening was established. The CRSS value single crystals of pure Zn was changing within a range of 0.46MPa at 77K to 0.27MPa at 473K, wheras for ZnTi0.01 at.% it amounted respectively 1.96MPa i 0.87MPa.

The hardening coefficient Θ_A was changing respectively from 11.1 MPa to 0.97 MPa for Zn, and from 80.4 MPa to 7.2 MPa for ZnTi0.01 at.%. The activation volume V^* was rising monotonically with temperature inside a range of 12.7 to 46×10^{-20} cm^3 for ZnTi0.01 at.% and 2.1 to 9.8×10^{-20} cm^3 for Zn.

Keywords: Zn and ZnTi0.01 at.% single crystals, precipitation hardening, critical resolved shear stress, activation volume.

Monokryształy Zn oraz ZnTi0.01 at% odkształcano w próbie ściskania w systemie (0001) <11-20> do zakresu $\gamma = 0.2$ w temperaturach 77K, 150K, 293K, 373K, 473K. Stosowano dwie prędkości odkształcenia; 10^{-4} s^{-1} oraz 10^{-3} s^{-1}. Na podstawie uzyskanych krzywych ściskania wyznaczano krytyczne naprężenie ścinające KNS, współczynnik umocnienia w zakresie łatwego poślizgu Θ_A oraz objętość aktywowaną V^*. Stwierdzono silny wpływ niewielkich ilości dodatku Ti (0.01% at.) na proces umocnienia monokryształów Zn. Wielkość KNS dla monokryształów czystego Zn zmieniała się od 0.46 MPa w 77K do 0.27 MPa w 473K, natomiast dla monokryształów ZnTi0.01 at.% wynosiła 1.96 MPa i 0.87 MPa.

Współczynnik umocnienia Θ_A zmieniał się odpowiednio 11.1 MPa do 0.97 MPa dla Zn oraz 80.4 MPa do 7.2 MPa dla ZnTi0.01 at.%. Objętość aktywowana V^* wzrastała monotonicznie wraz z temperaturą w zakresie 12.7 do 46×10^{-20} cm^3 dla ZnTi0.01 at.% oraz 2.1 do 9.8×10^{-20} cm^3 dla Zn.

* WYDZIAŁ METALI NIEŻELAZNYCH, KATEDRA STRUKTURY I MECHANIKI CIAŁA STAŁEGO
AKADEMIA GÓRNICZO-HUTNICZA, 30-059 KRAKÓW, Al. MICKIEWICZA 30

Słowa kluczowe: monokryształy Zn i ZnTi0.01 at.%, umocnienie wydzieleniowe, krytyczne naprężenie ścinające, współczynnik umocnienia, objętość aktywowana.

1. Introduction

A hardening with $Zn_{15}Ti$-second-phase particles [9] is mainly responsible for the hardening mechanism of Zn-Ti alloys. As Ti solves in Zn with difficulty, it causes the contribution of solution hardening to be very small. The investigation into hexagonally structured ZnTi single crystals of an orientation of a preference for basal slip system allow to observe the mechanism of precipitate hardening within a wide range of deformation inside one slip system [11].

The research on hardening metal single crystals with second phases particles (included as a second phase or developed as a result of an effect of secondary precipitation process out of the solution), were concerned mainly with the single crystals hardening of a regular lattice. These are the works of E b e l i n g and A s h b y [1] who conducted research on Cu single crystals with an additive of 0.3–1% SiO_2 phase, and of D e w - H u g e s and R o b e r t s o n [2] who carried out research on AlCu3–5 at.% single crystals hardened with Al_2Cu phase, B y r n e , F i n e and K e l l y [3] who conducted research on AlCu1.7 at.% single crystals hardened with Θ', GP I, GP II phases.

The theoretical calculations of the CRSS value conducted with the aid of formulations established by O r o w a n [4] and A s h b y [4,5] substantiate their good consistence with experimental results [1–3].

The precipitation hardening depends also on the stability of the hardening phase.

A research into such dependence carried out by G u p t a et al. [6] on Al-Mg-Si alloys demonstrated that upon exceeding some critical temperature, at which the hardening phase loses its thermal stability and is partially dissolves in the matrix, a vigorous decrease in microhardening occurs.

The purpose of the conducted research was to examine the impact of the $Zn_{15}Ti$ phase precipitates on the properties of ZnTi0.01 at.% single crystals within a wide temperature range and to compare the obtained results with the properties for pure Zn single crystals.

2. Investigation method

The investigation was conducted on ZnTi0.01 at.% single crystals produced by the modified B r i g m a n ' s method. [7] Samples measuring 5×5×10 mm and having an $\lambda_o = 43°; \theta_o = 44°$ orientation were deformed in a compression test over an easy slip system (0001)<11-20> operating range.

The tests was carried out at temperatures 77K, 150K, 293K, 373K and 473K. Two deformation rates were applied; 10^{-4} s^{-1} and 10^{-3} s^{-1}. In order to maintain identical friction factors throughout the compression test, investigation washers of buffered Al_2O_3

covered with teflon were used. On the basis of compression characteristics values for CRSS and θ_A were established. The value of the activation volume V^* was obtained from the change of strain rate in a constant strain rate test.

3. Results and discussion

As the analysis of the Zn-Ti phase system indicates, below a 0.02 at.% Ti contents the predominating hardening mechanism is that of hardening with particles of the secondary precipitates of the $Zn_{15}Ti$ [8] intermetallic phase from the α solution (Fig. 2). Fig. 1 presents the structure of precipitates on the (0001) plane of a ZnTi0.01 at% single crystal immediately upon producing single crystals. After an analysis of the chemical composition (TEM) these precipitates were found to be $Zn_{15}Ti$.[11]

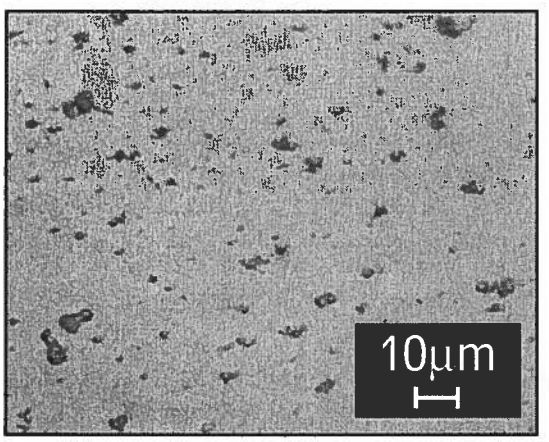

Fig. 1. Structure of the $Zn_{15}Ti$ precipitates on the plane (0001) of the ZnTi0.01 at.% single crystals

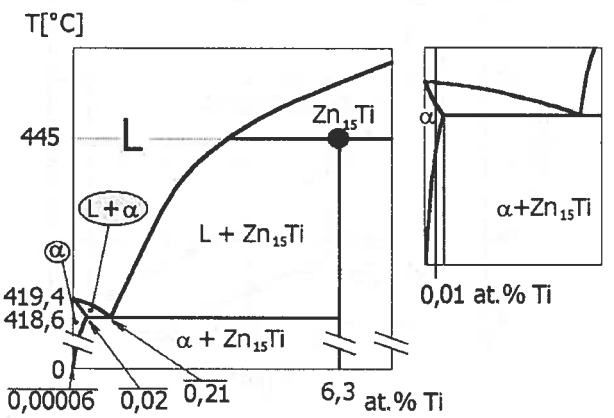

Fig. 2. The part of Zn-Ti phase diagram. [9]

The results of mechanical testing are shown in Fig. 3 and 4. ZnTi0.01 at.% single crystals have substantially higher CRSS and Θ_A values than the examined single crystals of pure Zn. With rising temperature, the mechanical properties of both examined kind of single crystals being deformed in the same system (0001)<11-20> rapidly decreases. An increase of hardening coefficient Θ_A for Zn can be observed a temperature of 150K, afterwards its value decreases (Fig. 3). As the research [7] demonstrates this phenomenon is due to an anomaly of the hardening coefficient. This phenomenon was not recorded for ZnTi0.01 at% single crystals. For Zn deformed at high temperatures (>373K) the hardening coefficient Θ_A remains fairly low.

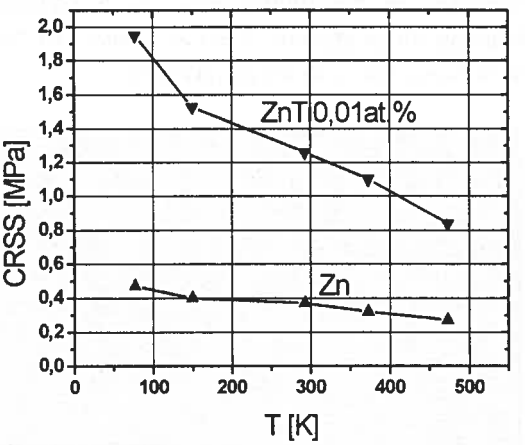

Fig. 3. Critical resolved shear stress CRSS of the Zn and ZnTi0.01 at.% single crystals as a function of the temperature

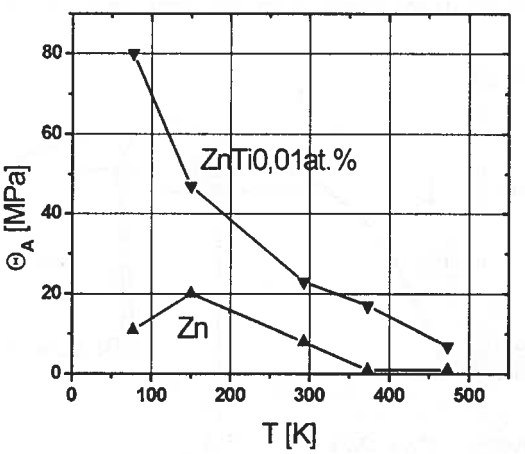

Fig. 4. Hardening coefficient of the Zn and ZnTi0.01 at.% single crystals as a function of the temperature

For pure Zn single crystals the main lattice obstacles on the plane of easy slip (0001) are the forest dislocations. The investigations [7, 10] demonstrated that their quantity during deformation within an easy slip interval ($\gamma < 0.2$) does not change.

At temperatures above 293K a steady decrease in hardening coefficient Θ_A was recorded, thus revealing a occurring conversion of the precipitate structure. As an examination of ZnTi0.1 at.% single crystals shows the structure of precipitations can be altered by means of thermal treatment. [11] Fine $Zn_{15}Ti$ phase precipitates undergo a partial or complete dissolution, whereas great precipitates change size and shape [6, 11].

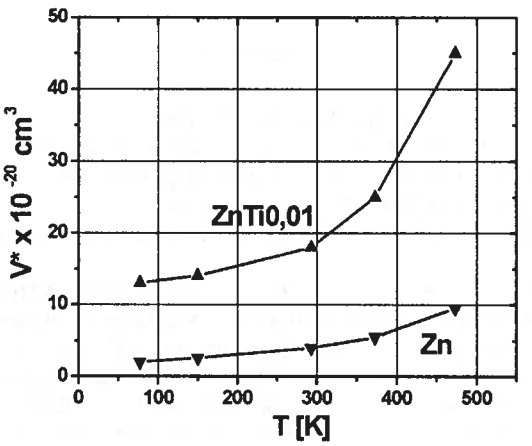

Fig. 5. The influence of the temperature on the activation volume V^*;
– for Zn single crystals – V^* determined by stress relaxation method (relaxation after strain $\gamma = 0.1$),
– for ZnTi0.01 at.% single crystals – V^* determined on the basis change strain rate in constant strain rate test (after $\gamma = 0.1$)

Conducted examinations of the activation volume demonstrate that when temperature rises, the V^* value increases. A monotonic shape of $V^* = f(T)$ curves for ZnTi0.01 and Zn single crystals points to the action of similar hardening mechanisms over the entire interval of deformation under investigation.

4. Conclusions

- Ti alloy additives of an 0.01 at.% order significantly affect the hardening process of Zn single crystals.
- In ZnTi0.01 at.% single crystals a prevailing mechanism of hardening phenomenon is that of precipitate hardening with $Zn_{15}Ti$ – phase precipitates.
- As the temperature rises the mechanical properties of the examined single crystals strongly diminish.

- The reason for a strongly decline of hardening above the temperature of 373K is the partial dissolution of secondary $Zn_{15}Ti$ – phase precipitates.
- Within the deformation range of ZnTi0.01 at.% single crystals under investigation the hardening mechanism does not change.

Acknowledgment

The authors acknowledge the support of the Polish Committee for Scientific Research, Grant No. 11.11.180.255.

REFERENCES

[1] R. Ebeling, M. F. Ashby, Phil. Mag. **13**, 805 (1966).
[2] D. Dew-Hughes, W. D. Robertson, Act. Metall. **8**, 147 (1960).
[3] J. G. Byrne, M. E. Fine, A. Kelly, Phil. Mag. 1119 (1961).
[4] T. Gladman, Mat. Sci. and Tech. **15**, 30-36, Jan. (1999).
[5] M. F. Ashby OXIDE DISPERSION STRENGTHENING, (ed. G.S.Ansell et al.) 143 (1958), New York, Gordon and Breach.
[6] A. K. Gupta, D. J. Lloyd, S. A. Court, Mat. Sci. Eng. **A316**, 11 (2001).
[7] B. Mikulowski, Zeszyty Naukowe AGH nr. 96 – Metalurgia i Odlewnictwo, Kraków (1982).
[8] M. Sailard, G. Develey, C. Becle, Acta Cryst. **B37**, 224-226 (1981).
[9] J. L. Murray, Ti-Zn (1987) (in Massalski Binary Alloys Phase Diagrams).
[10] G. Boczkal, B. Mikulowski, Arch. of Metall. **48**, 11-19 (2003).
[11] G. Boczkal, B. Mikulowski, Journ. of Com. and Met. (2003) (in print).

REVIEWED BY: ANDRZEJ ŁATKOWSKI
Received: 20 January 2003.

A R C H I V E S O F M E T A L L U R G Y A N D M A T E R I A L S
Volume 49 2004 Issue 1

JAN KUŚNIERZ*

ON TRANSIENT RANGE OF STRAIN HARDENING AND PLASTIC ANISOTROPY AT TENSILE DEFORMATIONS

PRZEJŚCIOWY ZAKRES UMOCNIENIA ODKSZTAŁCENIOWEGO I ANIZOTROPII PLASTYCZNEJ W PRÓBKACH ROZCIĄGANYCH

The stress-strain relation, exemplified on tensile test measurement of CuZn37 brass, copper and aluminium, is considered according to L u d w i g s o n model, and values of transient ε_l limit elongation are calculated. That concept is compared to the dependence of r-value on elongation ε and an analogue transient ε_{rl} limit is defined. Both values are of the same order and considerably greater than the ε_r elongation defined earlier by the author, below which the r-value is non-real, i.e. has negative value.

Zależność naprężenia od odkształcenia, rozważana zgodnie z modelem L u d w i g s o n a na przykładzie wybranych wyników z rozciągania wyciętych z blachy próbek mosiężnych, miedzianych i aluminiowych, posłużyła do wyznaczenia wydłużenia ε_l, ograniczającego zakres przejściowy. Ta koncepcja została porównana z zależnością od wydłużenia współczynnika anizotropii plastycznej r, gdzie definiowana jest analogiczna wartość granicznego wydłużenia ε_{rl}. Obydwie wartości są tego samego rzędu i znacznie większe niż określane przez autora wcześniej wydłużenie ε_r, poniżej którego współczynnik anizotropii plastycznej r przyjmuje wartości ujemne czyli nierzeczywiste.

1. Introduction

The effect of change of deformation path on properties and structure of materials after pre-deformation has been recently intensively studied. It relates in particular to mechanical properties, crystallographic texture and microstructure changes under shearing in pre-deformed by rolling Cu and its alloys [1, 2], Al [3] and steel [4]. In all investigated samples an influence of pre-deformation on mechanical behaviour was observed and consequently changes in texture and microstructure were noted especially in initial range of deformation, with intensity dependent on material and pre-deformation reduction of area. That

* INSTYTUT METALURGII I INŻYNIERII MATERIAŁOWEJ IM. A. KRUPKOWSKIEGO, PAN, 30-059 KRAKÓW, UL. REYMONTA 25

phenomenon suggests that the change of deformation path has an general aspect and the behaviour in a last state of loads is connected with the history of deformation or at least just penultimate treatment mode.

In the paper, the small deformation behaviour under tension will be considered with respect to strain hardening (deduced from $\sigma - \varepsilon$ relation) and to anisotropy coefficient (r-value) which relates the partial elongation in the width direction to the partial elongation in the thickness direction.

2. Stress – strain relation according to Ludwigson model

The dependence of stress on strain under plastic deformation is commonly interpreted as the power law formulae

$$\sigma = K\ \varepsilon^n \tag{1}$$

$$\sigma = \sigma_o + K\ \varepsilon^n \tag{2a}$$

$$\sigma = K\ (\varepsilon + \varepsilon_o)^n \tag{2b}$$

with σ as true stress, ε as true plastic strain and n, σ_o, ε_o as constants accountable for strain hardening (n) or elastic limit of the material (σ_o or ε_o). Formula (1) was already proposed by B u l l f i n g e r in the year 1729 [5], as it was noticed by Coulomb [6] (it is also known as H o l l o m o n formula [7]); formula (2a) is considered as L u d w i k [8] one, while (2b) as the formula of S w i f t [9]. The graphical representation of formula (1) in log–log scale gives a straight line, where n represents the slop of a straight line log σ in respect to log ε axis. The lack of linearity inspired many research workers to invent other formulae, and among others K r u p k o w s k i [10] with his latent hardening z_1

$$\sigma = k\ z_i^m, \tag{3}$$

where z_i is ideal cold work and $z_i = z_1 + (1 - z_1)\ z$, while z is interpreted as actual cold work ($z = 1 - A_o/A$, where A_o and A denote the initial and the actual cross section). T r u s z k o w s k i [11] had largely discussed the problem of linearity verifying different measures of deformation and formulae, introducing his heterogeneity parameter s_o, which did not provide satisfactory results either. In the course of experimental collecting of the data in the stress – strain relation a minimum of two different ranges in $\sigma - \varepsilon$ relation were distinguished [12, 13].

L u d w i g s o n [14] admitted to interpret the stress – strain relation as composed of two ranges i.e.:

(i) stabilised with a linearity of the expression $\ln \sigma - \ln \varepsilon$, which implicates a power law $\sigma - \varepsilon$ relation in the whole range of straining by tension (strain or work hardening range)

$$\sigma_1 = K_1\ \varepsilon^{n1}, \tag{4}$$

where it is supposed: K_1 is a "strength factor" n_1 is a "strain hardening exponent",
(ii) initial range in $\sigma - \varepsilon$ relation as a transient range with $\Delta = \sigma - \sigma_1$, where (with introduced corrections [15])

$$\Delta = K_e \exp(n_t * \varepsilon) \tag{5}$$

is founded on admission of the fact that the beginning part of the stress – strain relation is the passage from the initial state ($\sigma = \sigma_1 + \Delta$) to the stabilized plastic flow under tension ($\sigma = \sigma_1$); although not necessarily caused by planar flow of dislocations favoured by low stacking fault energy (SFE) as was suggested by L u d w i g s o n [14]; because that type of behaviour was observed independently on SFE [7, 11–13], which suggests that the phenomenon is rather a general one. Thus we obtain the $\sigma - \varepsilon$ relation valid in the whole range of straining:

$$\sigma = K_1 \varepsilon^{n1} + K_e \exp(n_t * \varepsilon) \tag{6}$$

where K_1 is a "strength factor", K_e is a stress at which plastic flow begins; it corresponds to proportional limit, n_1 is a "strain hardening exponent", n_t is a "transient sensitivity exponent".

The meaning of K_1 and n_1 conform to L u d w i k [8] law, while K_e is equal to the value of stress at $\varepsilon = 0$, which corresponds to the proportional limit of $\sigma - \varepsilon$ relation. The introduction of the constants K_1 and K_e in the postulated formula (6) enables to avoid troubles when one changes the stress units from one set to another one (compare Appendix).

3. Anisotropy coefficient (*r*-value)

The result of anisotropic plastic flow can be observed visibly during deep drawing of sheets as ears in a drawn cup and at the localisation of a groove in flat samples undergoing tension (compare the author's paper [15]). There are two properties of metal, one expressed by the strain hardening exponent n1 described in Chapter 2 and the other, considered here coefficient of plastic anisotropy (*r*-value), which control the ability of sheet metal to deep drawing operation [16].

Recently T r u s z k o w s k i [17] had re-evoked his method of estimation of $r_o = r(\varepsilon = 0)$ from the maximal error limit of integral *r*-value on tensile elongation in opposition to the initial suggestion of the determination of the *r*-value at the limit of uniform elongation [16]. He also called over the author's paper [18], where $r = r(\varepsilon)$ dependence was deduced from linear dependences of partial strains on ε. According to definition [16, 19] *r*-value is calculated as the ratio of partial strains ε_w in the width direction ($\varepsilon_w = \ln(w/w_o)$, where w_o and w correspond to the width initial and after elongation, respectively to partial strains ε_t in the thickness direction ($\varepsilon_t = \ln(t/t_o)$, where t_o and t correspond to thickness initial and after elongation, respectively, namely

$$r = \varepsilon_w / \varepsilon_t. \tag{7}$$

In the author's papers [15, 18] linear relations were postulated (similar were re-evoked recently by L i u [20])

$$\varepsilon_w = \ln (w_o / w) = A + \alpha * \varepsilon \tag{8}$$

$$\varepsilon_t = \ln (t_o / t) = B + \beta * \varepsilon \tag{9}$$

with limit conditions

$$\alpha + \beta = 1 \tag{10}$$

$$A + B = 0 \tag{11}$$

and where in (7) the numerator (8) and denominator of (9) were multiplied by (– 1) for comfort.
The expression (10) enables to postulate the *r*-value independent of ε, as was proposed already [15, 18]

$$r_k = \alpha / (1 - \alpha). \tag{12}$$

The constants *A* and *B* account for the run of *r*-value in the vicinity of $\varepsilon = 0$ and in consequence of (11) only one is independent, suppose A; when A is negative then r tends to 0 when $\varepsilon \rightarrow 0$, and when A is positive then *r* tends to ∞ when $\varepsilon \rightarrow 0$. The formulae (8) and (9) determine directly the limit elongation ε_r

$$\varepsilon_r = |A/\alpha| \text{ when } A < 0 \text{ or } |B/\beta| \text{ when } B < 0, \tag{13}$$

such that for $\varepsilon < \varepsilon_r$ the *r*-values are negative and do not have any physical meaning. The expressions (8), (9) and (12) giving the constant r_k value resolve also the problem of the difference between the differential $r^H = d\varepsilon_w / d\varepsilon_t$ and the integral *r*-value [16, 17, 20].

4. Experimental results and discussion

In the following, re-examinations of certain author's results [18], according to L u d w i g s o n [14] model, are presented. In Fig. 1 there are demonstrated the stress – strain relations of a M2-90 sample, cut out of a sheet at 90 degrees to the rolling direction (in Fig. 2 for Al-0 cut out in the rolling direction and in Fig. 3 for Cu1-45 cut out of a sheet at 45° degrees to the rolling direction are illustrated), and subjected to tension, when natural

logarithm scaling is applied. The total assembly of experimental points for M2-90 brass (Fig. 1a) can be described by the formula $\sigma = \sigma_1 + \Delta$, while the linearity description comprises

$$\ln \sigma_1 = 4.264 + 0.525 \ln \varepsilon \tag{14}$$

and $K_1 = e^{4.264} = 71.094$ MPa, and $n1 = 0.525$. The difference $\Delta = \sigma - \sigma_1$, between σ measured and σ_1 recalculated is presented in Fig. 1b. and may be described as a straight line when semi-logarithm scaling is applied

$$\Delta = 95.692 \exp(-0.226 * \varepsilon), \tag{15}$$

where $\varepsilon = \varepsilon$ [%] and $K_\varepsilon = 95.692$ Mpa, n2 = −0.226 according to hypothesis postulated by Ludwigson [14].

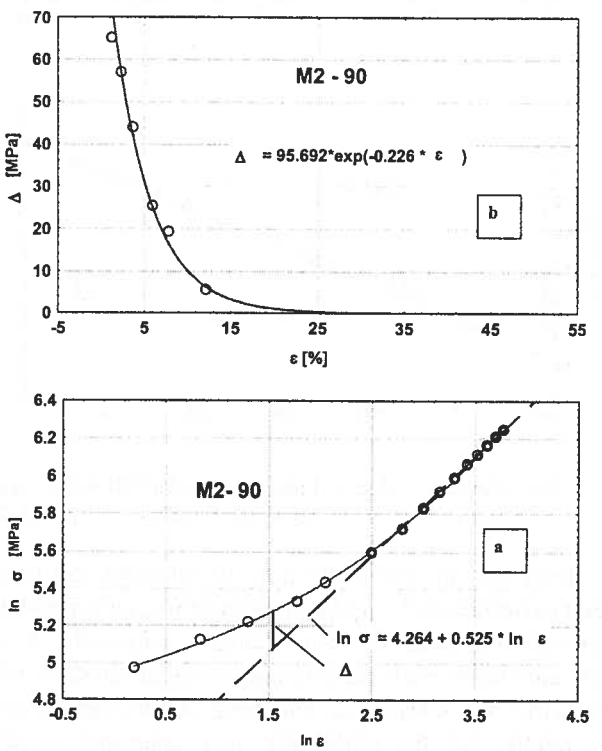

Fig. 1. Stress – strain relation according to Ludwigson model [14] for CuZn37 sample M2-90: a) $\sigma = \sigma_1 + \Delta$, b) $\Delta = K_\varepsilon \exp(n_1 * \varepsilon)$. (compare constants for ε [%] in Table 1)

The material constants of Al, Cu and CuZn37 brass according to Ludwigson formula are presented in Table 1 (constants for ε [dimensionless] and ε [%] are compared in the Appendix). The strength constant K_1 and the strength hardening exponent n1 can be compared with the previously obtained results according to Ludwik formula [8].

For all cases considered we observe a satisfactory approximation conformity according to L u d w i k and L u d w i g s o n formulae (Table 1). In Table 1 there is also presented the limiting value ε_l (formula 16) above which the Δ/σ_l relation is below ± 0.02:

$$|\Delta(\varepsilon)/\sigma_l| < 0.02 \quad \text{for} \quad \varepsilon > \varepsilon_l. \tag{16}$$

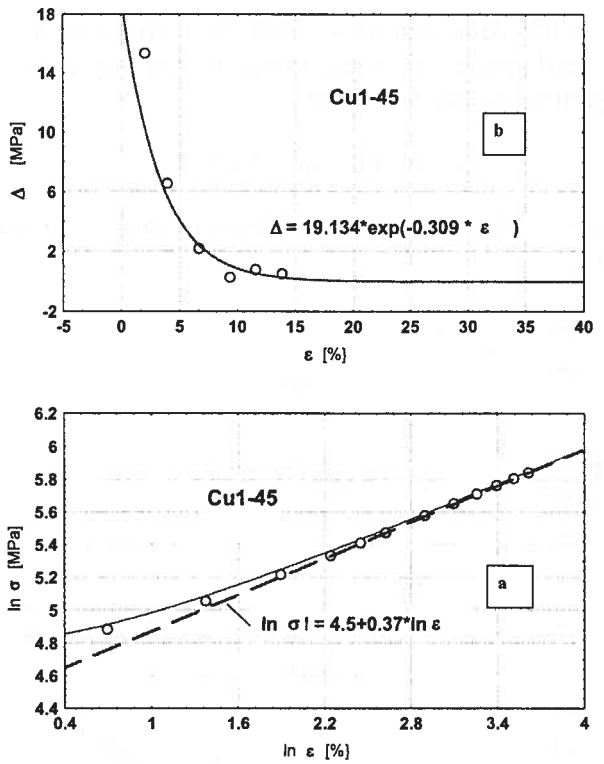

Fig. 2. Stress – strain relation according to Ludwigson model [14] for Cu sample Cu1-45: a) $\sigma = \sigma_l + \Delta$, b) $\Delta = K_r \exp(n_r * \varepsilon)$. (compare constants for ε [%] in Table 1)

In the Table 2 there are presented the data to interpret the coefficient of plastic anisotropy r according to formulae (7) – (13). In the last three columns there are gathered the coefficients to interpret the $r(\varepsilon)$ function in an analogous way as the $\sigma - \varepsilon$ relation. We had received the constant anisotropy coefficient r_k supposing the linearity of partial elongation as was demonstrated in Fig. 4b for brass M2-90, in Fig. 5b for copper Cu1-45 and Fig. 6b for Al-0. Now we can admit, that the initial part is a consequence of material as well experimental parameters influencing the measured values of partial elongation, and as in the prior $\sigma - \varepsilon$ relation the initial part is a transient one responding to the deformation of cross-section, constrained by tension acting in tensile axis. We can suppose

$$r = r_k + r_t \tag{17}$$

$$r_t = r_{0l} * \exp(n_{tr} * \varepsilon) \tag{18}$$

$$r(0) = r_k + r_{01}, \tag{19}$$

n_{tr} – is the exponent for transient behaviour of $r_t(\varepsilon)$ in the range of near zero deformation, r_k, r_{01} are constants.

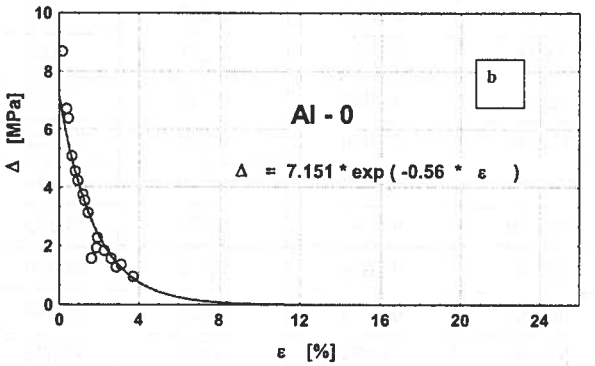

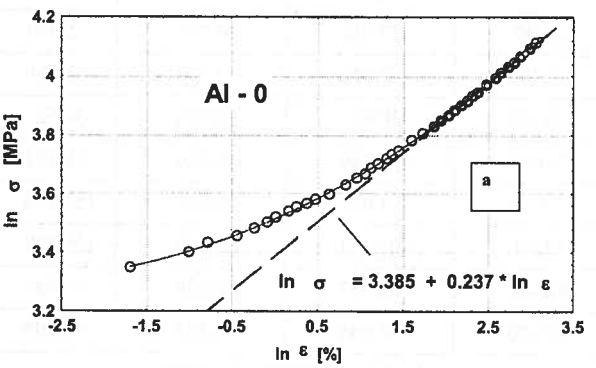

Fig. 3. Stress – strain relation according to Ludwigson model [14] for Al sample Al-0:
a) $\sigma = \sigma_1 + \Delta$, b) $\Delta = K_r \exp(n_r * \varepsilon)$. (compare constants for ε [%] in Table 1)

The expressions (17) and (18) are illustrated in Fig. 4a and 4b for M2-90, in Fig. 5a and 5b for Cu1-45 and in Fig. 6a and 6b for Al-0; particularly, the r_t obtained according to (18) makes us sure that the degree of deviation $r(0)$ from r_k may be significant (Table 2) and depends upon the case as it was demonstrated elsewhere [15, 18]. That mode of reasoning approves the mode of determination of r-value proposed by the author [18]; in the last but one column of the Table 2 there is given the elongation ε_{rt} above which the measured r value is charged by experiment with error smaller than c (it differs from the constant r_k by the chosen admitted small $c = 0.02$ value), namely

$$|(r(\varepsilon) - r_k)/r_k| < 0.02 \quad \text{for} \quad \varepsilon > \varepsilon_{rt}. \tag{20}$$

TABLE 1

Parameters of stress – strain curves of Al, Cu and CuZn37 brass (M2)

No	Sample	K_1 [MPa]	n1	K_e [MPa]	nt	ε_1
Ludwigson [10], ε [%]						
1	Al-0	29.518	0.237	7.151	−0.560	3.8
2	Al-45	33.78	0.281	5.101	−0.724	2.5
3	Al-90	30.054	0.210	8.459	−1.713	2.2
4	Cu1-0	88.850	0.388	38.521	−0.539	4.5
5	Cu1-45	90.017	0.370	19.134	−0.309	6.0
6	Cu1-90	94.16	0.350	159.153	−0.343	3.0
7	M2-0	73.626	0.519	108.399	−0.305	10.2
8	M2-45	68.717	0.529	96.886	−1.357	12.5
9	M2-90	71.094	0.525	95.692	−0.226	12.7
Ludwigson [10], ε [dimensionless]						
10	Al-0	87.920	0.237	7.151	−56.0	0.038
11	Al-45	123.214	0.281	5.101	−72.4	0.025
12	Al-90	79.050	0.210	8.459	−171.3	0.022
13	Cu1-0	530.466	0.388	38.52	−539	0.045
14	Cu1-45	494.680	0.370	19.134	−30.9	0.060
15	Cu1-90	471.918	0.350	159.153	−343	0.030
16	M2-0	803.584	0.519	108.399	−30.5	0.102
17	M2-45	785.352	0.529	96.886	−23.6	0.125
18	M2-90	797.688	0.525	95.692	−22.6	0.127
Ludwik [4], ε [dimensionless]						
		K_1 [MPa]	n1	σ_o [MPa]		
19	Al-0	74.65	0.40	21.62	–	
20	Al-45	92.00	0.33	7.53	–	
21	Al-90	67.72	0.37	20.15	–	
22	Cu1-0	529.66	0.41	13.95	–	
23	Cu1-45	493.52	0.41	19.39	–	
24	Cu1-90	456.55	0.40	30.97	–	
25	M2-0	735.78	0.73	120.96	–	
26	M2-45	727.37	0.70	101.82	–	
27	M2-90	760.49	0.70	100.11	–	

TABLE 2

Coefficient of plastic anisotropy (r-value) for Al, Cu and CuZn37 (M2)

Sample	A	α	B	r_k	r_{01}	$-n_{tr}$	r(0)	ε_{rt} [%]	ε_r [%]
				ε [%]					
Al-0	+0.024	0.325	−0.024	0.480	0.047	0.325	0.527	4.89	0.04
Al-45	−0.071	0.830	−0.123	0.200	0.300	0.430	0.500	10.04	0.72
Al-90	−0.133	0.587	+0.004	0.705	0.092	0.137	0.797	13.69	0.23
Cu1-0	−0.013	0.409	−0.001	0.752	−0.493	0.437	0.259	7.98	0.03
Cu1-45	+0.033	0.630	−0.033	0.600	−0.258	0.203	0.342	15.11	0.09
Cu1-90	−0.280	0.480	+0.287	0.863	−0.202	0.174	0.661	14.14	0.58
M2-0	−0.132	0.432	+0.132	0.750	−0.523	0.414	0.227	8.58	0.31
M2-45	+0.077	0.398	−0.077	0.650	+0.255	0.343	0.905	15.39	0.13
M2-90	+0.128	0.386	−0.128	0.610	+0.913	0.256	1.523	16.86	0.02

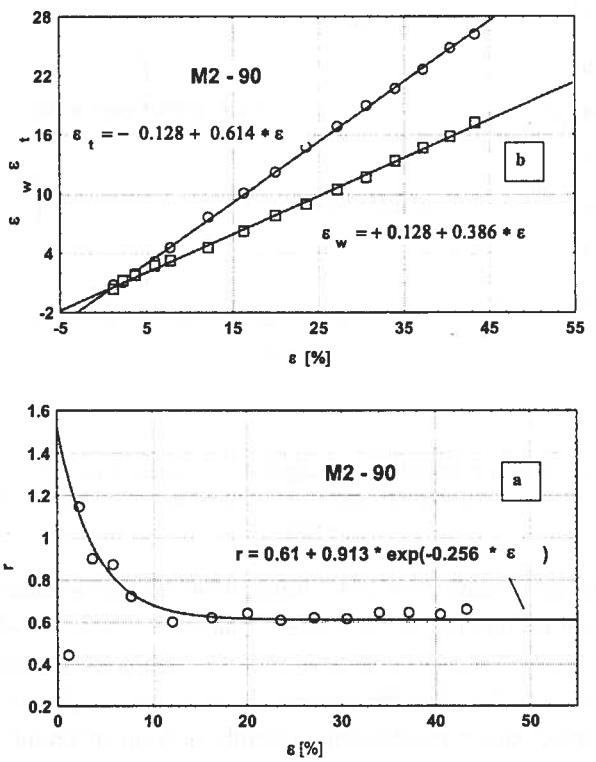

Fig. 4. Anisotropy coefficient r depending on elongation for CuZn37 sample (M2-90) cut out of a sheet at 90° to the rolling direction RD [18]: a) partial strains ε_w and ε_t, b) r-value versus ε[%]

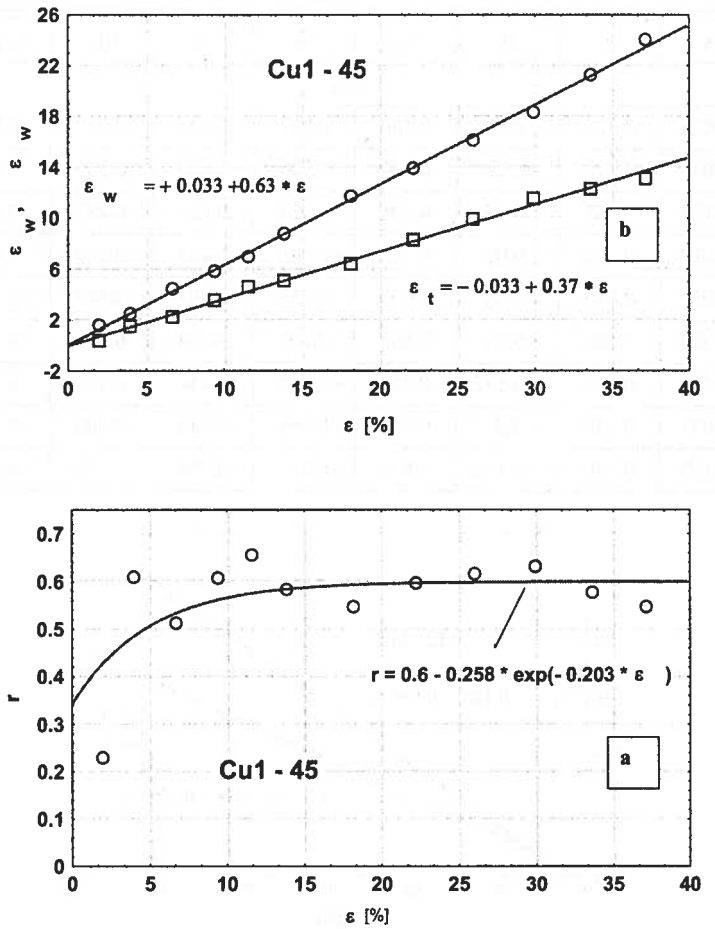

Fig. 5. Anisotropy coefficient r depending on elongation for copper sample (Cu1-45) cut out of a sheet at 45° to the rolling direction RD [18]: a) partial strains ε_w and ε_t, b) r-value versus ε [%]

The transient range obtained from $\sigma - \varepsilon$ relation or r(ε) dependence define similar limits of transient range of elongation (ε_1 in Table 1 and ε_{rt} in Table 2) which is considerably greater than ε_r in Table 2, the limit of non-real, i. e. negative r-value [15, 18]. The most convincing reason is the fact that the passage from elastic to plastic deformation, where different plastic deformation mechanisms (mainly slip on different active slip systems, activity of cross-slip or partial dislocations and twinning) become active and the constrains resulting from interactions of grains inevitably influence the initial course of $\sigma - \varepsilon$ and $r(\varepsilon)$ relations in the form of transient range.

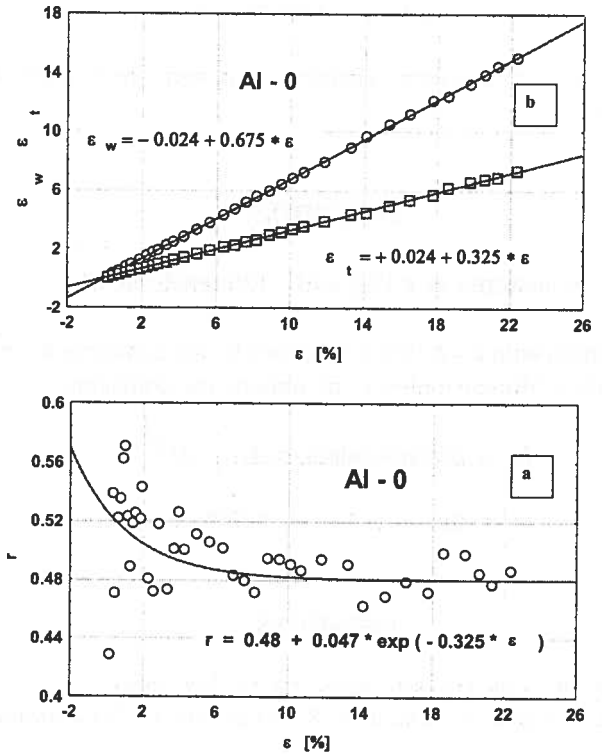

Fig. 6. Anisotropy coefficient r depending on elongation for Al sample (Al-0) cut out of a sheet in the rolling direction RD [18]: a) partial strains ε_w and ε_t, b) r-value versus ε [%]

5. Conclusions

The stress strain relation modified by L u d w i g s o n seems to describe correctly the experimental data for metals independently of SFE values with transient up to ε_1 limit elongation.

Taking into account the mathematical correctness it is postulated to use the formula $\sigma - \varepsilon$ in whole range

$$\sigma = K_1\, \varepsilon^{n1} + K_e \exp\,(nt * \varepsilon), \tag{21}$$

where K_1 is a "strength factor", K_e is a stress at which plastic flow begins; it corresponds to proportional (elastic) limit, $n1$ is a "strain hardening exponent", nt is a "transient sensitivity exponent".

In a similar manner the r-value can be presented as the sum $r = r_k + r_t$ with transient up to ε_{rt} limit elongation

$$\mathbf{r = r_k + r_{01} * \exp(n_{tr} * \varepsilon)}, \tag{22}$$

where r_k is constant, n_{tr} is a transient sensitivity exponent for r-value. Both ε_1 and ε_{rt} are of the same order.

APPENDIX:

Constants at ε [%] and ε [dimensionless]

Suppose the $\sigma - \varepsilon$ relation with $\varepsilon = \varepsilon$ [%] is described by the constants K_1, $n1$, K_e and nt then for $\sigma - \varepsilon$ relation with ε [dimensionless] one obtains the constants:

$$K_1\ (\varepsilon \text{ dimensionless}) = \mathrm{K_1} * 10^{2*\mathrm{n1}} \tag{A1}$$

$$nt\ (\varepsilon \text{ dimensionless}) = 100 * \mathrm{nt} \tag{A2}$$

REFERENCES

[1] J. Kuśnierz, E. Rauch, Mat. Scie. Forum 273-275, 339 (1998).
[2] J. Kuśnierz, E. Rauch, T. Baudin, R. Penelle, J. Jura, Archives of Metallurgy **44**, 23 (1999).
[3] M. Gasperini, C. Pinna, W. Świątnicki, Acta Mater. **44**, 4195 (1996).
[4] E. Rauch, C. G'Sell, Mat. Scie. Eng. **A111**, 71 (1989).
[5] G. B. Bulffinger, Commentarii Academiae Scientiarum Imperialis Petropolitanae **4**, 164 (1729).
[6] P. Coulomb, Les textures dans les metaux de resaux cubique, Dunod, Paris (1972), 175.
[7] J. H. Hollomon, Trans AIME **162**, 268 (1945).
[8] P. Ludwik, Elemente der technologischen Mechanik, Berlin (1909) 32.
[9] H. W. Swift, J. Mech. Phys. Solids **1**, 1 (1952).
[10] A. Krupkowski, Annales de l'Acad. Polon. Scie. Tech. **7**, 113 (1946).
[11] W. Truszkowski, Archiwum Hutnictwa **4**, 283 (1959).
[12] A. Krupkowski, A. Dańda, Archiwum Hutnictwa **14**, 25 (1969).
[13] Z. Jasieński, S. Wierzbiński, Archiwum Hutnictwa **15**, 27 (1970).
[14] D. C. Ludwigson, Metallurgical Transactions **2A**, 2825 (1971).
[15] J. Kusnierz, Archives of Metallurgy **37**, 203 (1992).
[16] W. T. Lankford, S. C. Snyder, J. A. Bauscher, Trans. ASM **42**, 1197 (1950).
[17] W. Truszkowski, The plastic Anisotropy in Single Crystals and Polycrystalline Metals, Kluver Acad. Publ., Dordrecht 2001.
[18] J. Kuśnierz, Z. Jasieński, Mem. Sci. Rev. Metallurg. **73**, 485 (1976).
[19] A. Krupkowski, S. J. Kawiński, Inst. Metals **75**, 869 (1949).
[20] Y. C. Liu, L. K. Johnson, Metallurgical Transactions **16A**, 1531 (1985).

REVIEWED BY: ZDZISŁAW JASIEŃSKI
Received: 20 November 2003.

A R C H I V E S O F M E T A L L U R G Y A N D M A T E R I A L S
Volume 49 2004 Issue 1

MACIEJ SUŁOWSKI*, ANDRZEJ CIAŚ*

MECHANICAL PROPERTIES OF Fe-(3-4)%Mn-0.8%C PM STEELS

WŁASNOŚCI MECHANICZNE SPIEKANYCH KONSTRUKCYJNYCH STALI MANGANOWYCH Fe-(3-4)%Mn-0,8%C

The powder metallurgy route may allow sintered manganese steels to be made based on pure iron powder and ferromanganese powder with control over alloy microstructure. The factors that contribute to the mechanical properties of sintered Fe-(3-4)%Mn-0.8%C manganese steels, such as the basic powder grade, sintering temperature, sintering atmosphere dew point and cooling rate are summarised. The paper shows the influence of these parameters on the tensile strength, yield strength, transverse rupture strength, impact strength and hardness of the investigated steels. It is showed that tensile high strength level higher than those of many conventional steels can be obtained already in the as-sintered condition.

W artykule przedstawiono wpływ parametrów wytwarzania na własności mechaniczne spiekanych konstrukcyjnych stali manganowych o zawartości manganu wynoszącej 3% mas. i 4% mas. oraz stałej zawartości 0,8% węgla. Powyższy skład spiekanej stali wybrano w oparciu o wyniki dotychczasowych badań prowadzonych zarówno w kraju jak i zagranicą. Jako parametry wpływające w znaczny sposób na przebieg spiekania, a tym samym na własności spieków, wyodrębniono: rodzaj zastosowanych proszków żelaza i żelazomanganu, temperaturę spiekania, temperaturę punktu rosy atmosfery spiekania oraz szybkość chłodzenia materiału po spiekaniu. Przeprowadzone badania miały na celu określenie:

- wpływu rodzaju proszków żelaza i żelazomanganu na własności wytrzymałościowe i plastyczne spieków,
- wpływu temperatury spiekania, temperatury punktu rosy atmosfery spiekania i szybkości chłodzenia od temperatury spiekania na własności fizyczne i mechaniczne spieków,
- odpowiednich warunków wytwarzania spiekanych stali manganowych.

Z przeprowadzonych prac i uzyskanych rezultatów badań wynika, że zmiany wymiarowe badanych spieków są głównie zależne od temperatury spiekania, a własności wytrzymałościowe i plastyczne badanych spieków są funkcją następujących parametrów wytwarzania: temperatury

* WYDZIAŁ METALURGII I INŻNIERII MATERIAŁOWEJ, AKADEMIA GÓRNICZO-HUTNICZA, 30-059 KRAKÓW, AL. MICKIEWICZA 30

punktu rosy atmosfery spiekania, temperatury spiekania oraz szybkości chłodzenia po spiekaniu. Stwierdzono również, że własności mechaniczne spiekanych stali manganowych w istotnym stopniu zależą od rodzaju zastosowanych proszków żelaza i żelazomanganu.

1. Introduction

Most powder metallurgy (PM) steels differ significantly from their wrought counterparts. Nickel and cooper, and in some cases molybdenum, are the alloying elements which have traditionally been used in high-strength sintered structural steels. Manganese has a significant influence on hardenability but its use is restricted because of its strong affinity for oxygen. Consideration of Ellingham-Richardson diagrams indicates that sintering of manganese steels is not practicable in endogas and, even in pure hydrogen, the dew point requirements for sintering temperatures of 1120 and 1250°C are –60°C and –50°C, respectively. While Ni, Cu, and particularly Mo additions cost more than additions of Mn, their oxides are reducible during sintering in standard industrial conditions (1120°C, dissociated ammonia atmosphere, –30°C dew point). However, the powder metallurgy industry follows possibilities in order to develop nickel-free sintered steels, which render as high mechanical properties as diffusion alloyed nickel-containing sintered steels and further fulfil the requirements of health protection.

The first fully commercial PM steel with Mn in excess of 1% was patented in 1996 and produced by Canadian company Stockpole. Commercial exploitation of PM Mn ferrous alloys appears restricted to < 1.5% manganese at sintering temperatures < 1300°C. However, even these Mn contents require special processing procedures, e.g. comminuting ferromanganese under nitrogen to a mean particle size of 8μm to minimise the oxygen level of the starting powders and facilitate manganese diffusion and sintering at 1280°C in a relatively dry atmosphere of hydrogen/nitrogen with dew point –40°C. With tensile strength of 600 MPa, and acceptable dimensional stability, manganese PM steels with ~7g/cm^3 density find applications in automotive powertrain components, e.g. clutch backing and apply plates, synchroniser components, transmission sprockets and helical gears. In Europe, in recent years manganese have been introduced as alloying element in iron-based structural parts on laboratory scale [1–5] and for pilot scale production [6], primarily in Germany, Slovakia, Poland and Bulgaria. Manganese is added as an alloying element to sintered steels to provide solid solution strengthening of ferrite, cause precipitation of alloy carbides $(Fe, Mn)_3C$, $(Mn, Fe)_7C_3$ and $(Mn, Fe)_2C$ rather then cementite, and improve the hardenability. Manganese has a significant influence on hardenability, but it must be in solution in order to contribute to hardenability. The focus of alloy development should be to utilise Mn alloying addition and carbon in combinations that optimise the synergistic effect of their presence on the hardenability of the alloy. Such steels as Fe-(3-4)%Mn-0.8%C are referred to as being ''sinter-hardenable", since sintering furnaces equipped with enhanced cooling capacity have been produced for many years. There are a number of benefits of the sinter-hardening process. First of all the need for the secondary quench-hardening treatment is eliminated.

This study is an attempt to evaluate common manufacturing techniques and sintering in semi-closed container, determine their significance on the PM steel thermal history, and introduce an efficient approach to the generation of sintering process specifications based on actual material behaviour properties.

The different demands of a furnace-cooled material targeted for high strength and tensile elongation will be compared with those of convective-cooled material where the need is for a combination of hardness, strength, and ductility.

In this study, the data will be treated in two groups. The first group will pertain to the influence of iron and ferromanganese powders grades on the mechanical properties of steels. The second group will have to do with observed variations in mechanical properties caused by changes in sintering temperature and dew point of the sintering atmosphere.

2. Experimental procedure

2.1. Powder used

Eight PM steels based on Höganäs iron powders were manufactured and examined. Two iron powders have been used in these investigations: NC 100.24 sponge iron powder and ABC 100.30 atomised iron powder. The manganese was added in the form of ferromanganese powders. Two types of ferromanganese powders were used: HP III ferromanganese powder, prepared from high-carbon ferromanganese grit produced in Huta Pokój then milled in nitrogen atmosphere in ZM Trzebinia, and Elkem low-carbon ferromanganese provided as a fine powder by Huta Baildon.

Elemental carbon was added to both iron powders in the form of ultra fine graphite (Höganäs C-UF). The content of ash in graphite powder was 3.3% and content of sulphur was 0.08%.

2.2 Powder characterisation and testing

The investigated properties of the iron and ferromanganese powders were chemical compositions, hydrogen loss, particle size and distribution, apparent density, tap density, flowability and compressibility. The results of the chemical analysis (Leco CS 125, Leco TC 336 and conventional wet analysis) of iron and ferromanganese powders are given in Tables 1÷2.

TABLE 1

Hydrogen loss and chemical analysis for NC 100.24 and ABC 100.30 iron powder – LECO CS 125 and TC 336 analysis

Powder	Hydrogen loss ISO 4491	Element, wt. %			
		C	S	O	N
NC 100.24	0.16	0.008	<0.001	0.268	<0.001
ABC 100.30	0.06	0.001	<0.001	0.054	<0.001

TABLE 2

Chemical composition – 40 μm HP III and ELKEM ferromanganese powders

Powder	Density, g/cm³	Chemical composition, wt. %					
		Nn	C	Si	O	N	S
HP III	7.18	79.04	6.35	0.67	0.08	0.02	<0.001
ELKEM	7.36	89.31	1.18	0.41	2.28	0.13	<0.001

The density of the ferromanganese powder was determined using pyknometer. Two main methods were used to determine the particle size: sieve analysis and sedimentation method based on S t o k e ' s law. Table 3 shows the results of sieve analysis for NC 100.24 and for ABC 100.30 iron powders; Table 4 presents the results of sedimentation analysis of ELKEM and HP III ferromanganese powders.

TABLE 3

NC 100.24 and ABC 100.30 iron powders particles size distribution

Size range, μm	Particle size weight distribution, %	Cumulative, %	Particle size weight distribution, %	Cumulative, %
	NC 100.24 iron powder		ABC 100.30 iron powder	
0–40	9	9	10	10
40–80	28	37	30	40
80–120	39	76	35	75
120–160	23	99	23	78
160–200	1	100	2	100

TABLE 4

Elkem and HP III ferromanganese powders particles size distribution

Stokes' diameter, μm	Weight distribution, %	Cumulative, %	Weight distribution, %	Cumulative, %
	Elkem ferromanganese powder		HP III ferromanganese powder	
0–10	16	16	7	7
10–20	63	79	4	11
20–30	10	89	13	24
30–40	4	93	15	39
40–50	3	96	17	56
50–60	3	99	23	79
60–70	1	100	21	100

The results of apparent and tap density, flowability and compactibility of iron powers and ferromanganese powders are listed in Tables 5÷6.

TABLE 5

Physical properties of NC 100.24 and ABC 100.30 iron powders

Property	NC 100.24 iron powder		ABC 100.30 iron powder	
	AGH measured values	Höganäs certificate data	AGH measured values	Höganäs certificate data
Flowability, s – ISO 4490	27.90	31.50	21.10	24.00
Apparent density, g/cm^3 – ISO 3923	2.64	2.43	3.25	3.05
Tap density, g/cm^3 – ISO 3953	3.16	–	3.79	–
Compactibility (600 MPa), g/cm^3 – ISO 3927	–	6.92	–	7.27

TABLE 6

Physical properties of ELKEM and HP III ferromanganese powders

Property	measured values	
	ELKEM ferromanganese powder	HP III ferromanganese powder
Flowability, s – ISO 4490	do not flow	do not flow
Apparent density, g/cm^3 – ISO 3923	2.00	3.13
Tap density, g/cm^3 – ISO 3953	3.23	3.97

2.3. Mixing

Mixtures of powders were prepared by blending iron, ferromanganese and graphite powders. The powders were mixed in a double cone laboratory mixer (60 min, 50 rev./min) to produce mixtures of the required uniform ferromanganese and graphite particles distribution. No lubricant was added to the powders before mixing. Table 7 shows chemical compositions of the powder mixtures.

TABLE 7

Summary of chemical composition, powder mixtures and specimens type

No	Iron powder	Ferromanganese powder	Chemical composition, wt. %			Specimen type	
	Fe	Fe-Mn-C	Mn	C	Si	Rectangular	ISO
1.	NC 100.24	ELKEM	3	0.8	0.056	A, B, C, D	I, J, K, L
2.	NC 100.24	ELKEM	4	0.8	0.074	E, F, G, H	M, N, O, P
3.	NC 100.24	HP III	3	0.8	0.025	HP-a	HP-c
4.	NC 100.24	HP III	4	0.8	0.034	HP-b	HP-d
5.	ABC 100.30	ELKEM	3	0.8	0.056	R	AA
6.	ABC 100.30	ELKEM	4	0.8	0.074	U	AB
7.	ABC 100.30	HP III	3	0.8	0.025	T	AC
8.	ABC 100.30	HP III	4	0.8	0.034	S	AD

2.4. Compacting

The blended powders were compacted in steel dies with zinc stearate lubricated walls. Unaxial, single-action compacting with a stationary lower punch was used. Two types of compacts were pressed: rectangular 55x10x5mm transverse rupture test bars and tensile strength test bars. Dogbone tensile test pieces were prepared according to ISO 2740 standard. Bars were pressed under pressure of 700 MPa.

2.5. Sintering

Sintering was carried out in dry hydrogen atmosphere in a horizontal laboratory furnace. The heat resisting steel tube furnace was equipped with water jacketed rapid convective cooling zone. The dew point of the hydrogen atmosphere was controlled from –40 to –60°C. The compacts were heated to the sintering temperature at heating rate of

75°C/min. The temperature control was ± 2°C. Sintering was performed at 1120, 1150, 1180 and 1200°C for 60 minutes employing rapid (convective) and slow furnace cooling. The convective cooling rate in the temperature range of 1100÷500°C was approximately 60°C/min. The furnace cooling rate in the temperature range 1100÷500°C was approximately 3.5°C/min. To improve both the local dew point (self-gettering) and to minimise the loss of manganese due to volatilisation, the specimens were sintered in a stainless steel semi-closed container. Following specimen preparation, density was determined on representative samples using the immersion technique. Summary of sintering temperatures for different types of powder mixtures is presented in table 8.

TABLE 8

Summary of Fe-(3-4)%Mn-0.8%C sintering temperatures of specimens prepared from NC 100.24+ELKEM, NC 100.24+HP III, ABC 100.30+ELKEM and ABC 100.30+HP III powder mixtures

Type of mixture	Sintering temperature											
	1120°C			1150°C			1180°C			1200°C		
	−40°C	−50°C	−60°C	−40°C	−50°C	−60°C	−40°C	−50°C	−60°C	−40°C	−50°C	−60°C
M1	x	x	x	x	x	x	x	x	x	x	x	x
M2	–	–	–	–	–	–	–	–	–	–	–	x
M3, M4	–	–	–	–	–	–	–	–	x	–	–	–

M1 – NC 100.24+ELKEM, M2 – NC 100.24+HPIII, M3 – ABC 100.30+ELKEM, M4 – ABC 100.30+HPIII

3. Testing of sintered specimens

3.1. Tensile test

The tensile properties were ascertained for as-sintered steels on dogbone tensile specimens according to PN–EN 10002–1 standard. Tensile test was carried out with MTS 810 testing machine at a crosshead speed of 0.5 mm/min. Elongation was measured with a 10 mm MTS 632.13C-23 extensometer. The load applied and strain were recorded continuously throughout the test. The resulting stress-strain curves were analysed to identify the 0.2% offset yield strength, tensile strength and tensile elongation at fracture. In addition to the tensile and elongation testing, failed specimens underwent metallographic examination. Testing was performed on between 10 and 20 specimens per material.

Figures 1÷4 and Table 9 present the results of the tensile test.

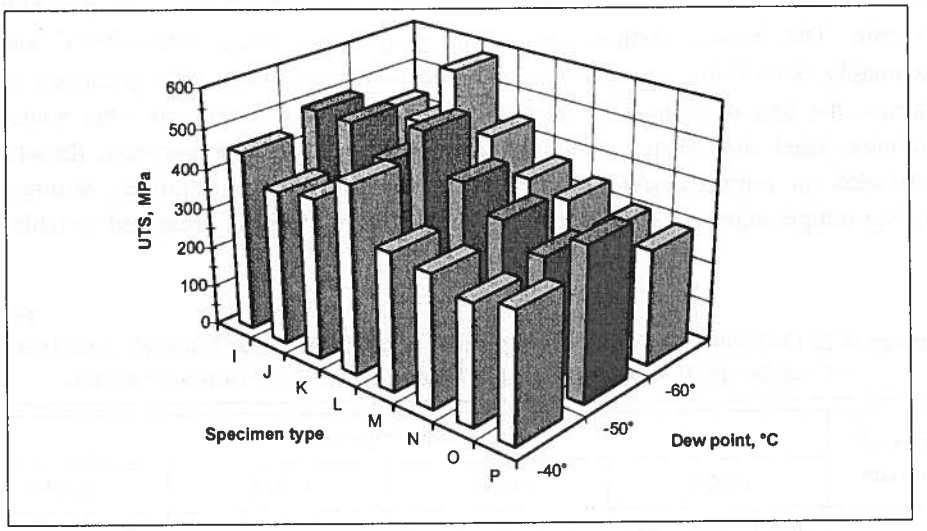

Fig. 1. Tensile strength of Fe-(3-4)%Mn-0.8%C specimens made of M1 powder mixture and sintered at different temperatures in the atmosphere with different dew point. Mean values for ISO 2740 samples

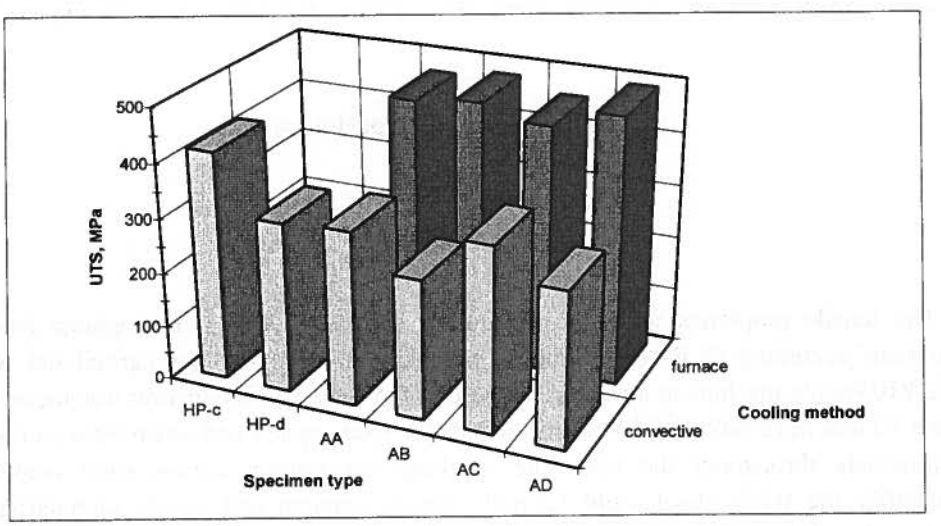

Fig. 2. Tensile strength of Fe-(3-4)%Mn-0.8%C specimens made of M2, M3 and M4 powder mixtures and sintered at different temperatures in the atmosphere with –60°C dew point. Mean values for ISO 2740 samples

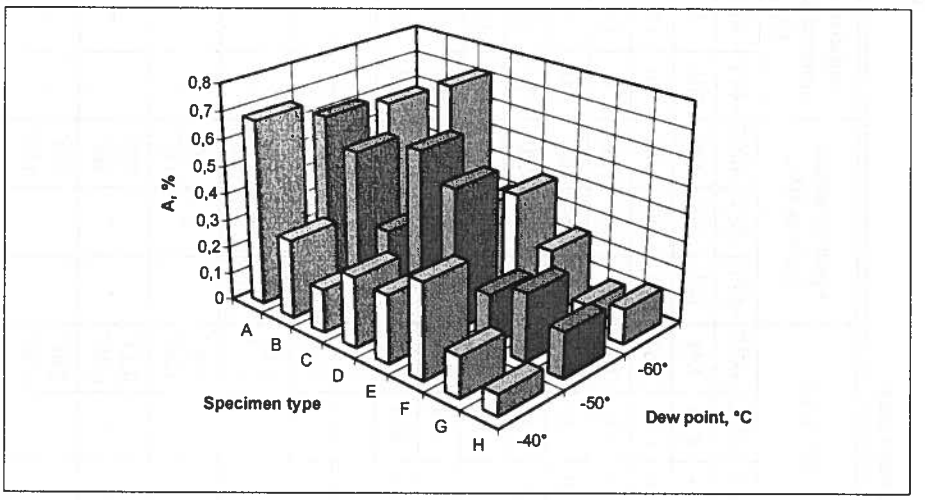

Fig. 3. Elongation of Fe-(3-4)%Mn-0.8%C specimens made of M1 powder mixture and sintered at different temperatures in the atmosphere with different dew point. Mean values for ISO 2740 samples

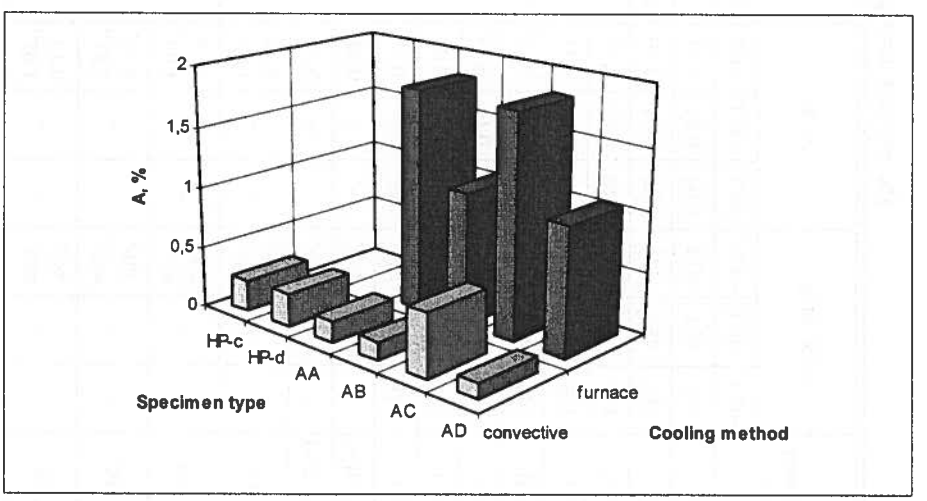

Fig. 4. Elongation of Fe-(3-4)%Mn-0.8%C specimens made of M2, M3 and M4 powder mixtures and sintered at different temperatures in the atmosphere with –60°C dew point. Mean values for ISO 2740 samples

TABLE 9

The results of investigations of sintered manganese steels

Sintering temperature, °C	Specimen type	UTS, MPa			A, %			TRS, MPa			KC, J/cm²			Apparent surface hardness HV_{10}			Apparent cross-sectional hardness HV_{10}		
		–40°C	–50°C	–60°C	–40°C	–50°C	–60°C	–40°C	–50°C	–60°C	–40°C	–50°C	–60°C	–40°C	–50°C	–60°C	–40°C	–50°C	–60°C
1120	A, I	451	491	432	0.68	0.61	0.58	976	1127	1242	8.34	8.18	7.94	147	153	172	203	147	214
1150	B, J	384	489	427	0.29	0.52	0.29	1236	1139	1254	6.09	8.81	7.62	193	142	168	216	132	183
1180	C, K	400	423	583	0.16	0.27	0.72	832	1006	1253	3.72	4.42	7.22	112	165	168	132	169	196
1200	D, L	486	526	445	0.26	0.61	0.31	1240	1091	1015	3.49	5.57	5.45	268	239	193	351	185	266
1120	E, M	340	432	368	0.25	0.52	0.40	1124	1134	968	3.09	6.24	3.63	169	162	202	284	230	222
1150	F, N	328	373	345	0.35	0.19	0.24	884	814	840	2.31	3.6	3.17	180	251	261	264	251	298
1800	G, O	298	319	306	0.15	0.25	0.09	811	709	771	2.43	2.48	2.17	219	277	380	331	318	351
1200	H, P	321	384	289	0.08	0.17	0.13	789	928	745	2.52	3.68	2.21	243	188	250	288	327	372
1200	HP-a, HP-c	–	–	420*	–	–	0.26*	–	–	835*	–	–	4.89*	–	–	165*	–	–	211*
1200	HP-b, HP-d	–	–	312*	–	–	0.27*	–	–	590*	–	–	3.93*	–	–	219*	–	–	160*
1180	R, AA	–	–	319* 467**	–	–	0.18* 1.82**	–	–	719* 1079**	–	–	2.85* 9.25**	–	–	250* 125**	–	–	289* 134**
1180	U, AB	–	–	256* 479**	–	–	0.15* 1.09**	–	–	415* 865**	–	–	3.06* 3.06**	–	–	269* 117**	–	–	183* 147**
1180	T, AC	–	–	339* 455**	–	–	0.52* 1.82**	–	–	741* 868**	–	–	4.43* 6.20**	–	–	232* 169**	–	–	205* 134**
1180	S, AD	–	–	285* 490**	–	–	0.12* 1.05**	–	–	598* 1021**	–	–	2.08* 6.36**	–	–	393* 152**	–	–	233* 163**

* convective cooling; ** furnace cooling

3.2. Bend test

Transverse rupture strength was determined by three-point bend testing with stress at fracture evaluated used simple beam theory, i.e. assuming elastic behaviour, according to PN-EN ISO 3325 standard. The fixture had two support cylinders mounted parallel with the 28.6 mm distance between the centres. The load cylinder was mounted midway between the support cylinders. The testing equipment provided a static condition of loading. The value at which the load suddenly dropped to the first crack was recorded. The transverse rupture strength, in MPa, was calculated from the Navier formula:

$$TRS = \frac{3Fl}{2bh^2}$$

where: F – is a load, in N e w t o n s, required for structure, measured at the moment of breakdown of the piece; l – is the distance, in mm, between supports; b – is the width, in mm, of the test piece at right angels to its height; h – is the height (thickness), in mm, of the test piece parallel to the direction of the test load application

The results of bend test are shown in Table 9 and Figs. 5÷6.

This procedure is only truly applicable to brittle specimens. It was used in this study as a routine measure to quickly distinguish between the apparent bend strength of the investigated alloys. However, some specimens involved in this study were optically found capable of being bent and an attempt was made to take into account plasticity and to convert some results to true bend strength [7-12].

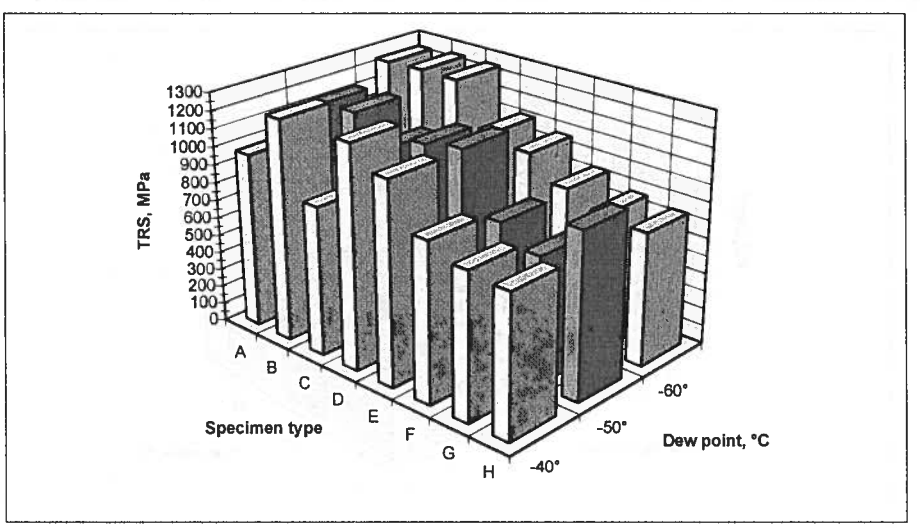

Fig. 5. Transverse rupture strength of Fe-(3-4)%Mn-0.8%C specimens made of M1 powder mixture, sintered at different temperatures in the atmosphere with different dew point. Mean values

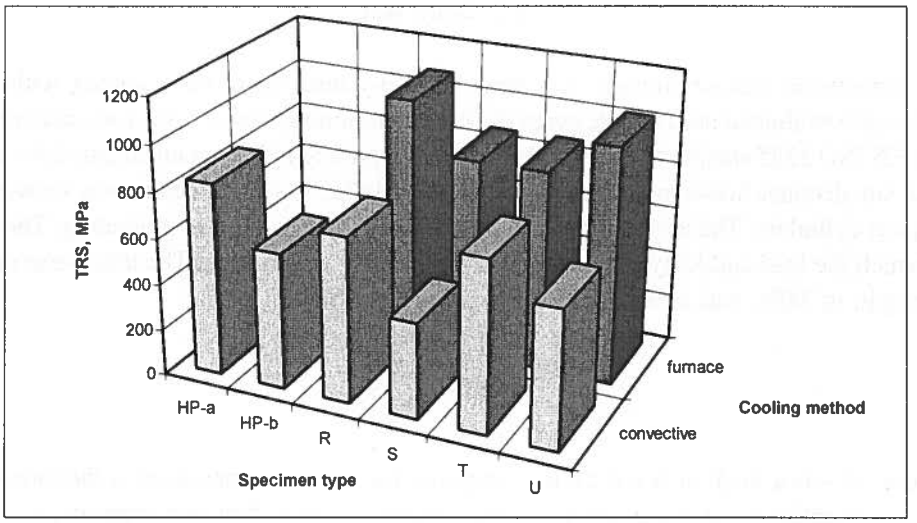

Fig. 6. Transverse rupture strength of Fe-(3-4)%Mn-0.8%C specimens made of M2, M3 and M4 powder mixtures, sintered at different temperatures in the atmosphere with –60°C dew point. Mean values for rectangular specimens

3.3. Impact test

Impact test (KC) was carried out using 55×10×5 mm specimens and a 15 J Charpy bar impact tester according to the PN–EN 10045–1 standard. Samples were placed on supports with a distance of 25 mm. Table 9 and Figs. 7÷8 present the results of impact test.

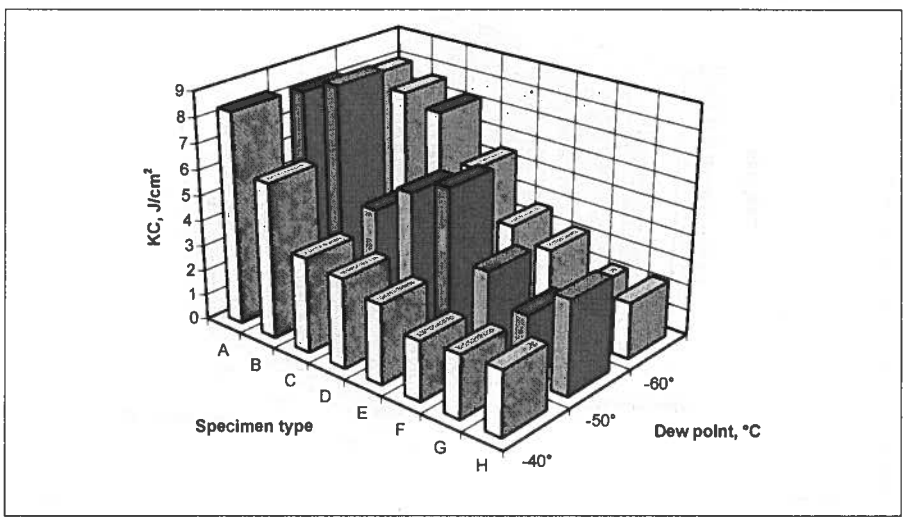

Fig. 7. Impact energy of Fe-(3-4)%Mn-0.8%C specimens made of the M1 powder mixture, sintered at different temperatures in the atmosphere with different dew point. Mean values

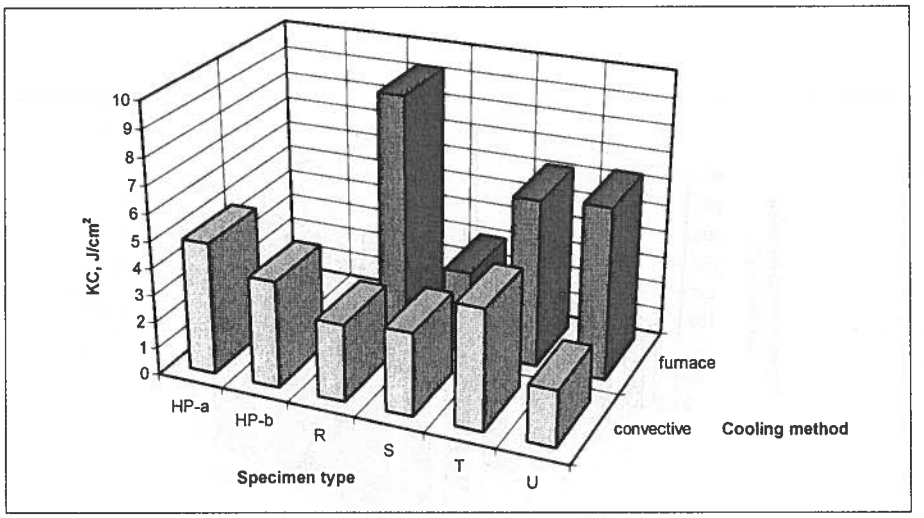

Fig. 8. Impact energy of Fe-(3-4)%Mn-0.8%C specimens made of M2, M3 and M4 powder mixtures, sintered at different temperatures in the atmosphere with –60°C dew point. Mean values

3.4. Apparent surface and cross-sectional hardness

The apparent hardness, as well as cross-sectional hardness of the test specimens (HV_{10}), was determined by means of Vickers hardness tester according to the PN–EN ISO 3878. Table 9 and Figs. 9÷12 show the results of hardness tests.

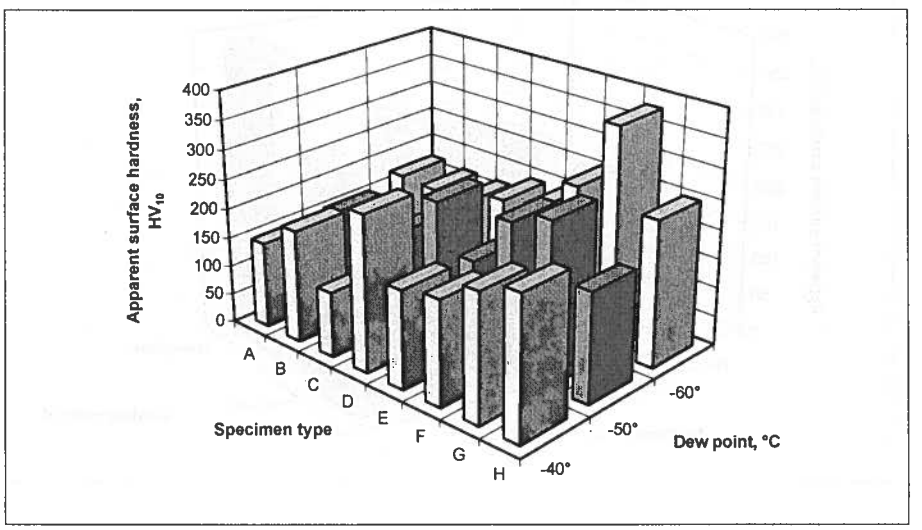

Fig. 9. Apparent surface hardness of Fe-(3-4)%Mn-0.8%C specimens made of M1 powder mixture, sintered at different temperatures in the atmosphere with different dew point. Mean values

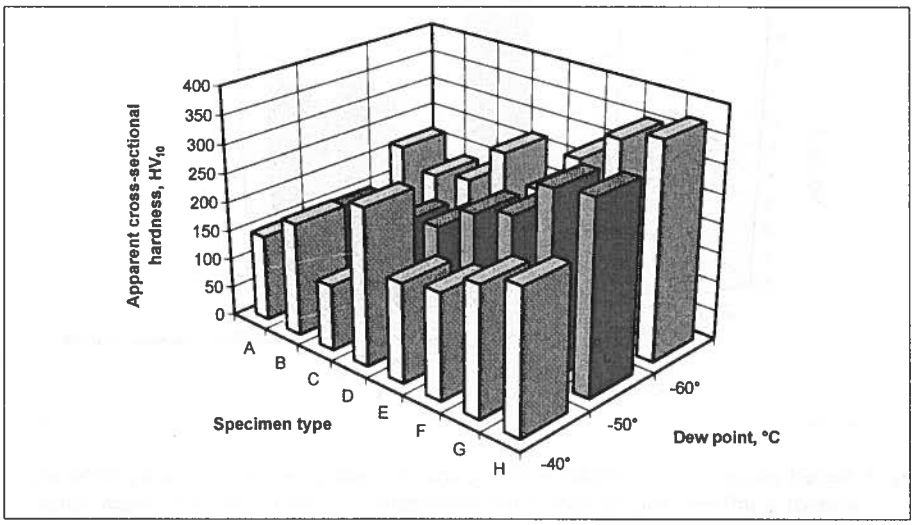

Fig. 10. Apparent cross-sectional hardness of Fe-(3-4)%Mn-0.8%C specimens made of M1 powder mixture, sintered at different temperatures in the atmosphere with different dew point. Mean values

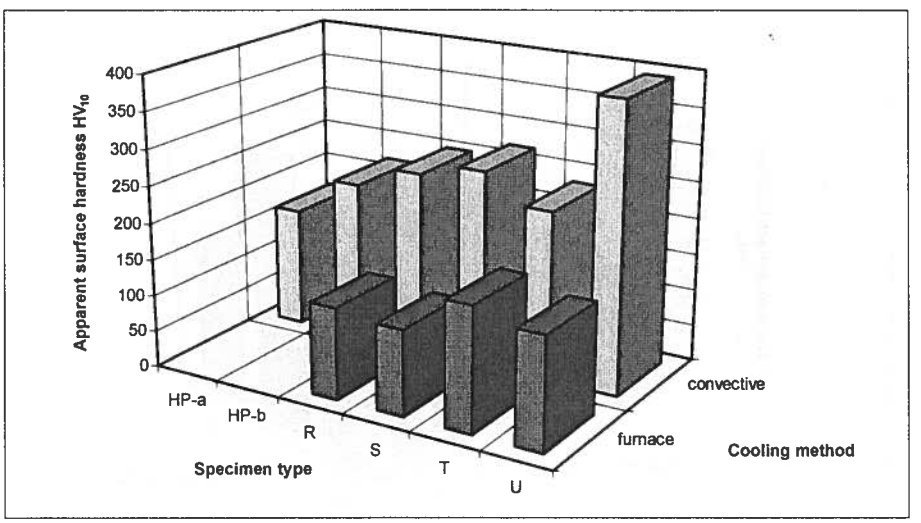

Fig. 11. Apparent surface hardness of Fe-(3-4)%Mn-0.8%C specimens made of M2, M3 and M4 powder mixtures, sintered at different temperatures in the atmosphere with –60°C dew point. Mean values

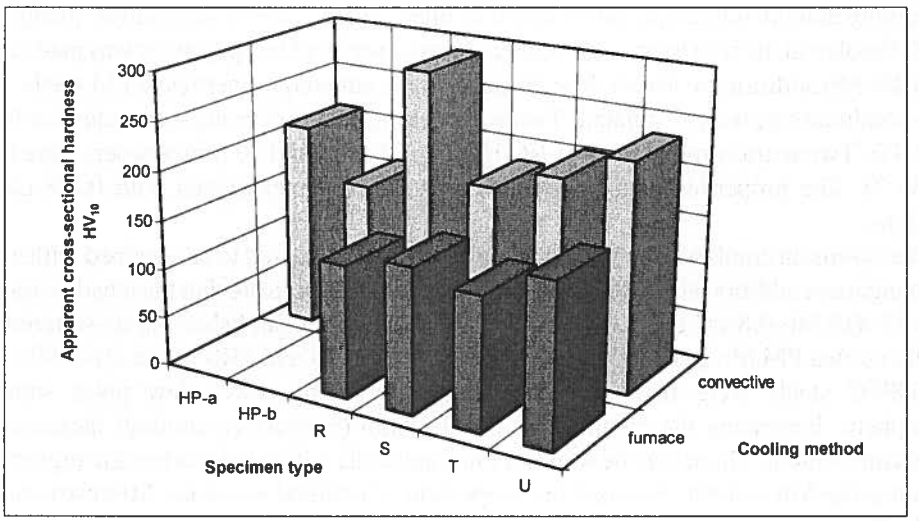

Fig. 12. Apparent cross-sectional hardness of Fe-(3-4)%Mn-0.8%C specimens made of M2, M3 and M4 powder mixtures, sintered at different temperatures in the atmosphere with –60°C dew point. Mean values

4. Experimental results

The following section will compare the effect of the sintering temperature and dew point of the sintering atmosphere on density, hardness, UTS, TRS, tensile elongation, and impact energy with of the various materials (the iron and ferromanganese powders) and processing techniques. The test program examined two principles: alloying with manganese to improve hardenability of the steel and processing to attain high sintered mechanical properties. The analysis was performed by sorting the steels into 14 processing groups (Table 9). Tables 1÷6 show the results of physical testing of iron and ferromanganese powders. It can be noticed that ABC 100.30 iron powder has better compactibility (ISO 3927) than NC 100.24 iron powder. It influenced green density (density before sintering) of the specimens. It appears that low-carbon ferromanganese powder additions favour higher green density. In most cases, the density involved in tensile testing did not exactly match the density of the transverse rupture specimens. When this was the case, the tensile properties reported were extrapolated from the available data to insure that the two set of data (UTS and TRS) were as comparable as possible. The specimens made of ABC 100.30 and ELKEM or HP III powder mixtures reached the green density 7.11 g/cm^3 for rectangular and 6.99 g/cm^3 for ISO specimens. The specimens made of NC 100.24 and ELKEM or HP III powder mixtures had green density not exceeded 6.95 g/cm^3 for rectangular and 6.85 g/cm^3 for dogbone tensile specimens. The dimensional change, from die size, of the investigated steels increase with increasing Mn content and decreasing dew point of the sintering atmosphere.

Having demonstrated that, when added as high– or low-carbon ferroalloys, manganese could dissolve in the iron to increase hardenability, a series of test premixes was made using 3 and 4% Mn additions to assess their influence upon sintered properties of PM steels. Four alloy combinations were evaluated. Two were combinations of manganese added at levels 3 and 4%. Two extra combinations of NC 100.24 and ABC 100.30 iron powders were made (Table 7). The properties of the alloy combinations were examined with 0.8% carbon additions.

The optimum combination of mechanical properties appeared to be obtained with a total 3% manganese addition at 0.8% carbon level. The test data indicate that the tensile strengths of Fe-(3-4)%Mn-0.8%C compare well with those previous published for as-sintered and rapidly cooled PM Mn steels. The results showed that UTS and TRS of the 3%-0.8%C and 4%-0.8%C steels were increased significantly by using lower dew point sintering atmosphere. Increasing the cooling rate to 60°C/min (convective cooling) increases the martensite content. There may be some retained austenite within the martensitic regions and so increasing Mn content increases the proportion of retained austenite. Microstructure of the 4%Mn alloy possesses some lighter etching possibly austenitic areas.

Table 9 and Figs. 1÷12 present the results of mechanical investigations for Fe-3%Mn-0.8%C and Fe-4%Mn-0.8%C steel specimens. In general, the UTS and TRS of the Fe-(3-4)%Mn-0.8%C PM steel slightly increases with decreasing dew point of the sintering atmosphere (Table 9, Figs. 2÷3, and Figs. 5÷6). Decreasing atmosphere sintering dew point increases also impact energy and in some cases apparent surface hardness. The data (Figs. 1÷12) indicate that the effects of manganese, dew point of the sintering atmosphere and cooling rate on the mechanical properties of the investigated alloys are relatively predictable. However, it may be prudent to limit the Mn additions such that dimensional change is close to that of current PM steels.

When considered separately, the data suggest that increasing cooling rate tends to decrease strength the Fe-3%Mn-0.8%C steels. On average, increasing the manganese content by 1% decreases UTS by about 100 MPa. The PM Fe-(3-4)%Mn-0.8%C alloy steels show similar variation in TRS to that observed with UTS. Overall, the TRS of the Mn steels also fell with alloy additions above 3%. However, the differences become less with increasing sintering temperature. The data suggests that a 3% manganese addition is optimal.

Cooling rate has a strong effect on the UTS, TRS, impact energy and apparent surface hardness. Decreasing cooling rate to furnace cooling (3.5°C/min) in some cases increases mechanical properties by factor up to ~ 2. When furnace cooling is employed, plasticity of the specimens increases, and tensile elongation is up to 2%.

The results of tensile and bend tests showed that the TRS/UTS ratio is 1.5÷2.0 and depends on density of sintered manganese steels. It is well recognised that the value of TRS can exceed that of UTS of the same PM steel, identically processed, by factor up to ~ 2, although both these parameters appear relate to the fracture stress in tension by the same mechanism. Taking account of plasticity in bending, the Euler-Bernoulli analysis extended for linear work hardening and by considering the stress distribution in a bending specimen, using Weibull statistics, the tolerated ratio (depend on Weibull modulus) between true

maximum stress in bending and tension was evaluated by Ciaś et al. [7-12] to be in close agreement with the experimental data. This was considered valid as un-notched specimens are sensitive to microstructural feature such as porosity and inclusion size and shape.

The investigated steels possessed relatively low elongation at break given their high strength levels. Elongation increased with increasing sintering temperature and density and decreasing dew point of the sintering atmosphere and cooling rate, so that the furnace cooled steel possessed higher elongation by 0.5÷1.0%. The T and AC furnace cooled specimens (Table 9) possessed an elongation approximately 1.3 % higher than that of the convective cooled specimens for a given density.

The impact properties of these steels are shown in Figs. 7÷8, and it is seen that the toughness is high particularly in view of the strength level involved. As might be expected the impact toughness in furnace cooled condition is superior to that of the convective cooled condition. The impact strength of the –40°C dew point atmosphere sintered specimens is somewhat lower, probably because of oxides introduced during alloy preparation.

5. Summary and conclusions

The results indicate that processing of the Mn alloy steels achieved its objectives. The benefits of improved hardenability are shown if comparing the properties of Fe-3%Mn-0.8%C steels with those of commercial sintered nickel steels. The results indicate that PM steels consisting of the (3-4)% Mn plus 0.8% C possess high mechanical properties. Their properties are explained by the processing parameters in a relatively predictable manner. Thus it should be possible to design Mn steel structural parts to meet strength requirements. This research has considered several processing variables associated with sintering of Fe-(3-4)%Mn-0.8%C steels in semi-closed container in hydrogen atmosphere. Here we found that best overall processing requires manipulation of the variables to control the alloy microstructure formation during heating, sintering and cooling. Optimal processing depends on the green density, heating rate, maximum sintering temperature and sintering atmosphere. It is important to emphasise that for a given chemistry, if cooling rate is such as to produce the bainitic/martensitic structure, the strength is relatively sensitive to powder preparation practice and sintering conditions; however this is not the case for the hardness which is much less structure sensitive. It is quite clear that transformation inducted structure and combination of manganese and carbon in solid solution can together produce a substantial increase in strength of PM steel in the absence of nickel. The decision to give a preference to Mn over Ni was based, among other things, on the fact that Mn has a greater effect on the hardenability of steel than Ni. Produced manganese steel specimens demonstrated satisfactory strength and elongation in the sintered condition and provided good basis for developing in new class of powder metallurgy alloys. We found that sintered in semi-closed container 3%Mn-0.8%C steel has indeed a remarkable combination of strength and toughness. With regard to microstructure the results obtained with produced specimens are encouraging and promise applications for the design of high performance structural application. Finally, it has to be mentioned that post sintering heat treatment can be applied with regard to mechanical properties without a significant loss of dimensional stability [7-11].

The various experimental facts relating to mechanical properties described in the present paper can be summarised as follows.

1. The optimised chemical composition, alloying technique and processing of PM manganese steels result in high mechanical properties of the material, which can be improved by increasing sintering temperature and/or applying sinter-hardening. The need for a secondary quench-hardening treatment is eliminated. Typically, sinter-hardened Mn steels need only low-temperature tempering to relieve stresses and improve toughness. No objections against practical application of Mn steels are obvious, with the stipulation that the hydrogen-reach sintering atmosphere with low dew point and semi-closed container are applied.
2. Improved processing of low alloy steels containing manganese resulted in mechanical properties (UTS 500 MPa and elongation up to 2% for furnace cooled specimens) equal or superior to those of many conventional PM steels. The properties of the investigated PM steels, which were determined following laboratory sintering in semi-closed containers are surprisingly good and belong to the best data available on comparable materials. The characteristics of this new class of steels suggest potential application in areas where high strength and hardness are desired, for example in the construction of sintered gears.

Acknowledgements

The financial support of the Polish Science Research Committee under the contract no 11.11.110.491 is gratefully acknowledged.

REFERENCES

[1] G. Zapf, G. Hoffmann, K. Dalal, Powder Metallurgy **18**, 35, 213 (1975).
[2] A. Šalak, Powder Metallurgy International **12**, 1 (1980).
[3] A. Šalak, Powder Metallurgy International **16**, 6 (1984).
[4] A. Šalak, G. Leitner, W. Hermel, Powder Metallurgy International **13**, 1 (1981).
[5] A. Klein, R. Oberacker, F. Thümmler, Powder Metallurgy International **17**, 2 (1985).
[6] „Tough, Fatigue and Wear Resistance Sintered Gear Wheels" – „Copernicus Join Research Project", Contract No ERB CIPA-CT94-0108.
[7] A. Ciaś, S.C. Mitchell, A. Watts, A.S. Wronski, Powder Metallurgy **42**, 3, 227 (1999).
[8] A. Ciaś, S.C. Mitchell, A.S. Wronski, Proc. of 1998 PM World Congress and Exhibition, Granada, Spain, October 18-22, **3**-PM Steels, 179 (1998).
[9] A. Ciaś, M. Sułowski, S.C. Mitchell, A.S. Wronski, Proc. of European Congress on Powder Metallurgy (EURO PM2001), Nice, October 22-24 2001 **4**, 246 (2001).
[10] A. Ciaś, S.C. Mitchell, K. Pilch, H. Ciaś, M. Sułowski, A. Wronski, Powder Metallurgy **46**, 2, 165 (2003).
[11] A. Ciaś, Development and properties of Fe-Mn-(Mo)-(Cr)-C sintered structural steels. Wyd. AGH. 2004, in press.
[12] A.S. Wronski, A. Ciaś, Powder Metallurgy Progress **3**, 3 (2003).

REVIEWED BY: JAN KUŚNIERZ
Received: 20 November 2003.

A R C H I V E S O F M E T A L L U R G Y A N D M A T E R I A L S
Volume 49 2004 Issue 1

MAREK DZIARMAGOWSKI*

THE ASSESSMENT OF SUITABILITY OF THE NON-METALLIC PHASE OBTAINED FROM THE CONVERTER SLAG FOR SOIL FERTILISATION

OCENA MOŻLIWOŚCI WYKORZYSTANIA FAZY NIEMETALICZNEJ OTRZYMANEJ Z ŻUŻLA KONWERTOROWEGO DO NAWOŻENIA GLEB

The constant search for new products containing Ca and Mg for soil fertilisation was the premise for using to this end material obtained during converter slag reduction in an electric arc furnace. The fraction smaller than 0.5 mm in size is suitable for soil liming. This fraction has a beneficial chemical composition and chemical activity. Using this fraction for fertilisation causes the de-acidification of soils and increases the yields of the cultivated plants.

Stałe poszukiwanie nowych produktów zawierających Ca i Mg do nawożenia gleb stanowiło przesłankę do wykorzystania w tym celu materiału otrzymanego w procesie redukcji żużla konwertorowego w elektrycznym piecu łukowym. Do wapnowania gleb nadaje się frakcja o średnicy mniejszej niż 0,5 mm. Ma ona korzystny skład chemiczny i aktywność chemiczną. Stosowanie tej frakcji do nawożenia powoduje odkwaszenie gleb i zwiększenie plonów uprawianych roślin.

1. Introduction

About 70 percent of soils in the country require liming, and about 60 percent need to be fertilised with magnesium. For this reason, systematic research on products containing Ca or Ca and Mg has been carried out to determine their suitability for liming and fertilising with magnesium.

The constant search for new products containing Ca and Mg for soil fertilisation was the premise for using to this end material obtained during converter slag reduction in an electric arc furnace. The suitability of this material for soil liming was assessed by the Institute of Soil Science and Plant Cultivation (*Instytut Uprawy, Nawożenia i Gleboznawstwa*) in Pulawy, the only institute in the country with the relevant experience.

* WYDZIAŁ METALURGII I INŻNIERII MATERIAŁOWEJ, AKADEMIA GÓRNICZO-HUTNICZA, 30-059 KRAKÓW, AL. MICKIEWICZA 30

2. Research method

Converter slag reduction was carried out in a single-arc furnace described in previous papers [1–3]. The charge material consisted of ground converter slag and ground electrode. The slag mass was 5000 g, and the mass of the reducer – 250 g. The mass of the reducer was 5 percent of the slag mass in order to obtain the self-disintegrating non-metallic phase. The slag mixed with the reducer was added constantly over 40 minutes and processing continued for four minutes after the adding process was completed. As a result of processing, 916.1 g of metal phase and 2476 g of the self-disintegrating non-metallic phase was obtained. The chemical composition of the metal phase was presented in Table 1.

TABLE 1

Chemical composition of metallic phases

mass	chemical composition, %							
	C	Fe	Si	Mn	Al	Cr	P	S
916.1	0.92	91.34	0.75	5.40	0.005	0.11	1.40	0.028

The grain size was determined during the non-metallic phase analysis to assess how the grinding level of the material under study influenced its fertilising suitability. To this end, two samples of 250 g were weighed and screened through screens containing mesh of an adequate diameter. Also, the chemical composition of the non-metallic phase fractions obtained and heavy metal content that can cause soil contamination and worsen the quality characteristics of plant products were determined along with neutralisation power and chemical activity. The neutralisation power was defined as the percentage of CaO dissolved over five minutes in HCl at a temperature of 100°C, and the chemical activity was defined as the percentage of CaO dissolved during five minutes in HCl at a temperature of 20°C related to pure $CaCO_3$. Samples of 1 g mass were used. The results are presented in Table 2–3.

The suitability of the non-metallic phase for fertilisation was tested by carrying out pot experiments on two soils:
– slightly clayey sand of acid reaction and low content of available magnesium
– common dust of acid reaction and very low content of available magnesium
Soil characteristics are listed in Table 4. Nine fertilisation methods were applied according to the following scheme:
1. NPK
2. NPK + limestone acc. to 0.75 Hh
3. NPK + limestone acc. to 1.5 Hh
4. NPK + dolomite acc. to 0.75 Hh
5. NPK + dolomite acc. to 1.5 Hh
6. NPK + non-metallic phase of ϕ 0.5 mm size acc. to 0.75 Hh
7. NPK + non-metallic phase of ϕ 0.5 mm size acc. to 1.5 Hh
8. NPK + non-metallic phase of ϕ 0.5 2.0 mm size acc. to 0.75 Hh
9. NPK + non-metallic phase of ϕ 0.5 2.0 mm size acc. to 1.5 Hh

TABLE 2

Grain size and properties of the non-metallic phase

No.	fraction ϕ mm	fraction share %	neutralisation power % CaO	chemical activity % $CaCO_3$
1.	< 0.08	17.3	65.8	129.4
2.	0.08–0.25	35.9	64.1	120.3
3.	0.25–0.5	16.1	66.9	111.4
4.	0.5–1.0	8.8	63.0	88.7
5.	1.0–2.0	6.3	44.0	51.9
6.	> 2.0	15.6	28.0	29.4

The cultivated plant was maize. White mustard was the aftercrop. NPK components (nitrogen, phosphorus and potassium) were applied as salt in amounts suitable for pot cultures. For a soil mass of 7 kg, 1 g of nitrogen, 0.2 g of phosphorus and 1.5 g of potassium were added. The amounts of limestone, dolomite and non-metallic phase were calculated so that the sum of hydrogen ions, specified by the magnitude of the Hh coefficient, was neutralised in the soil. When cultivation was finished, the amounts of calcium and magnesium and certain metals available to plants and soil were determined. The results of these experiments are listed in Tables 5–7.

TABLE 3

Chemical composition of converter slag and the non-metallic phase

No.	fraction ϕ mm	mass g	chemical composition, %													
			CaO	MgO	SiO_2	MnO	FeO	Cr_1O_3	P_2O_5	ΣS	K_2O	Na_2O	Zn	Cu	Pb	Cd
1.	żużel	5000	44.50	5.26	16.63	5.40	23.19	0.16	1.24	0.11	–	–	–	–	–	–
2.	<0.08	428.35	63.40	2.57	29.20	0.58	0.56	0.016	0.11	0.09	0.05	0.007	0.0052	0.0048	0.0110	0.0008
3.	0.08–0.25	888.88	64.90	2.05	28.20	0.88	2.00	0.037	0.05	0.09	0.05	0.010	0.0028	0.0020	0.0122	0.0013
4.	0.25–0.5	398.64	62.60	2.03	23.00	2.06	5.13	0.064	0.16	0.09	0.05	0.006	0.0026	0.0014	0.0132	0.0015
5.	0.5–1.0	217.89	58.60	2.11	23.56	2.92	10.10	0.469	0.14	0.07	0.05	0.009	0.0020	0.0010	0.0120	0.0009
6.	1.0–2.0	155.99	56.70	2.75	23.20	2.85	9.76	0.435	0.09	0.09	0.05	0.005	0.0014	0.0010	0.0140	0.0011
7.	>2.0	386.25	60.00	2.00	27.30	1.42	4.08	0.039	0.09	0.09	0.05	0.004	0.0010	0.0010	0.0145	0.0012

TABLE 4

Chemical composition of soil

Soil	pH_{KCl}	Hh mmole/100 g of soil	mg/100 g of soil		mmole/100 g of soil				T	V%
			P_2O_5	K_2O	Ca	Mg	K	Na		
soil I	4.2	2.57	20.7	11.5	1.12	0.15	0.18	0.01	4.03	36.2
soil II	5.4	2.55	8.0	6.3	3.59	0.26	0.08	0.04	6.52	60.9

T = Hh + S Hh – sum of hydrogen ions, S – total basic cations

$$\%V = \frac{S}{T} \cdot 100$$

TABLE 5

Plant yield resulting from various fertilisation methods

No.	fertilisation method	crop yield, g/pot							
		maize				white mustard			
		green mass		dry mass		green mass		dry mass	
		soil I	soil II	soil I	soil II	soil I	soil II	soil I	soil II
1.	NPK	474.1	440.6	119.6	116.0	43.4	49.8	4.9	6.9
2.	NPK = limestone acc. to 0.75 Hh	452.8	417.9	120.3	118.9	58.7	31.6	9.1	4.4
3.	NPK + limestone acc. to 1.5 Hh	520.4	469.5	133.5	130.4	45.3	39.3	5.5	6.3
4.	NPK + dolomite acc. to 0.75 Hh	488.2	434.7	134.6	116.6	52.6	29.2	5.9	4.0
5.	NPK + dolomite acc. to 1.5 Hh	525.5	468.3	135.0	122.3	40.0	33.4	5.6	5.4
6.	NPK + non-metallic phase of ϕ 0.5 mm size acc. to 0.75 Hh	484.3	463.1	126.3	122.6	41.0	36.8	5.0	5.3
7.	NPK + non-metallic phase of ϕ 0.5 mm size acc. to 1.5 Hh	578.9	514.1	141.1	136.2	39.9	50.0	5.6	9.1
8.	NPK+non-metallic phase of ϕ 0.5–2.0 mm size acc. to 0.75 Hh	407.5	481.8	118.4	124.3	37.6	46.0	5.4	7.1
9.	NPK+non-metallic phase of ϕ 0.5–2.0 mm size acc. to 1.5 Hh	519.2	484.4	138.9	130.5	50.9	63.0	5.9	10.7

TABLE 6

Component contents in maize dry mass

No.	fertilisation method	soil I									
		chemical composition, %						chemical composition, % × 10^{-4}			
		N	P	K	Ca	Mg	Na	Mn	Zn	Fe	Pb
1.	NPK	1.02	0.17	1.58	0.56	0.16	0.03	96	27.5	46	1.5
2.	NPK + limestone acc. to 0.75 Hh	1.01	0.12	1.38	0.84	0.13	0.03	80	18.5	50	1.8
3.	NPK + limestone acc. to 1.5 Hh	0.98	0.10	1.58	1.16	0.16	0.02	33	15.5	45	1.7
4.	NPK + dolomite acc. to 0.75 Hh	0.95	0.13	1.27	0.56	0.29	0.02	80	18.5	39	1.7
5.	NPK + dolomite acc. to 1.5 Hh	1.01	0.17	1.27	0.78	0.48	0.03	33	15.5	44	1.5
6.	NPK + non-metallic phase of ϕ 0.5 mm size acc. to 0.75 Hh	0.94	0.17	1.33	0.82	0.17	0.03	44	15.5	42	1.0
7.	NPK + non-metallic phase of ϕ 0.5 mm size acc. to 1.5 Hh	1.01	0.15	0.96	0.76	0.14	0.02	24	18.5	42	1.5
8.	NPK + non-metallic phase of ϕ 0.5–2.0 mm size acc. to 0.75 Hh	1.11	0.17	1.33	0.64	0.16	0.02	65	55.0	35	1.7
9.	NPK + non-metallic phase of ϕ 0.5–2.0 mm size acc. to 1.5 Hh	1.06	0.15	0.96	0.76	0.16	0.02	33	12.5	36	0.7
		soil II									
1.	NPK	1.04	0.15	1.31	0.69	0.14	0.02	180	35.0	46	1.0
2.	NPK + limestone acc. to 0.75 Hh	1.12	0.15	0.97	0.73	0.12	0.02	96	45.0	41	1.0
3.	NPK + limestone acc. to 1.5 Hh	1.19	0.14	1.00	0.95	0.12	0.02	75	34.0	38	2.8
4.	NPK + dolomite acc. to 0.75 Hh	1.21	0.15	0.92	0.65	0.23	0.02	96	33.5	40	2.5
5.	NPK + dolomite acc. to 1.5 Hh	0.90	0.10	1.13	0.78	0.38	0.02	96	39.0	39	2.0
6.	NPK + non-metallic phase of ϕ 0.5 mm size acc. to 0.75 Hh	1.25	0.10	1.00	0.84	0.16	0.02	96	18.5	46	2.5
7.	NPK + non-metallic phase of ϕ 0.5 mm size acc. to 1.5 Hh	0.93	0.13	1.23	1.00	0.21	0.02	110	65.0	67	4.5
8.	NPK + non-metallic phase of ϕ 0.5–2.0 mm size acc. to 0.75 Hh	1.12	0.13	1.20	0.71	0.16	0.02	110	47.0	38	3.3
9.	NPK + non-metallic phase of ϕ 0.5–2.0 mm size acc. to 1.5 Hh	1.24	0.12	0.74	0.62	0.13	0.02	94	15.5	39	2.0

TABLE 7

Soil properties following the harvesting of the aftercrop

No.	fertilisation method	soil I													
		pH_{KCl}	Hh mmole/ 100 g of soil	mg/100 g of soil		mmole/100 g of soil				% × 10^{-4}				T	V%
				P_2O_5	K_2O	Ca	Mg	K	Na	Mn	Zn	Fe	Pb		
1.	NPK	4.3	2.89	12.0	3.2	0.95	0.06	0.10	0.03	143	8.0	675	7.2	4.03	28.3
2.	NPK + limestone acc. to 0.75 Hh	5.2	2.03	14.3	5.2	1.75	0.06	0.13	0.03	157	10.4	675	9.3	4.00	49.2
3.	NPK + limestone acc. to 1.5 Hh	6.2	1.48	18.5	4.3	2.84	0.04	0.13	0.03	161	6.0	675	9.8	4.52	67.3
4.	NPK + dolomite acc. to 0.75 Hh	5.1	2.27	13.6	4.3	1.50	0.30	0.10	0.04	152	6.4	655	9.4	4.21	46.1
5.	NPK + dolomite acc. to 1.5 Hh	6.0	1.64	17.7	4.0	1.95	0.57	0.13	0.02	152	10.0	655	10.4	4.31	61.9
6.	NPK + non-metallic phase of ϕ 0.5 mm size acc. to 0.75 Hh	5.6	1.87	20.0	3.9	2.00	0.06	0.10	0.03	167	7.4	675	10.0	4.06	53.9
7.	NPK + non-metallic phase of ϕ 0.5 mm size acc. to 1.5 Hh	6.6	1.01	20.4	5.6	3.39	0.10	0.13	0.01	167	7.4	675	11.1	4.64	78.2
8.	NPK + non-metallic phase of ϕ 0.5–2.0 mm size acc. to 0.75 Hh	5.2	2.11	12.4	3.4	1.65	0.06	0.10	0.03	167	10.4	675	11.3	3.95	46.6
9.	NPK + non-metallic phase of ϕ 0.5–2.0 mm size acc. to 1.5 Hh	6.1	1.01	17.2	4.9	2.89	0.07	0.13	0.03	178	6.0	715	11.1	4.13	75.5
		soil II													
1.	NPK	4.5	3.59	10.0	5.3	2.49	0.08	0.18	0.05	147	6.0	845	4.2	6.34	44.2
2.	NPK + limestone acc. to 0.75 Hh	5.3	2.50	12.7	5.7	3.49	0.07	0.20	0.05	147	6.4	870	4.7	6.31	60.4
3.	NPK + limestone acc. to 1.5 Hh	6.2	2.11	13.1	4.4	4.49	0.06	0.20	0.05	161	5.0	870	5.1	6.91	69.5
4.	NPK + dolomite acc. to 0.75 Hh	5.0	3.05	10.3	5.9	2.74	0.53	0.20	0.07	147	4.6	870	4.9	6.59	53.7
5.	NPK + dolomite acc. to 1.5 Hh	5.8	2.34	11.2	6.0	3.19	0.68	0.23	0.05	157	6.0	845	5.0	6.19	62.2
6.	NPK + non-metallic phase of ϕ 0.5 mm size acc. to 0.75 Hh	5.7	2.27	15.9	6.9	3.94	0.11	0.20	0.05	167	4.6	895	4.9	6.57	65.4
7.	NPK + non-metallic phase of ϕ 0.5 mm size acc. to 1.5 Hh	6.6	1.48	21.9	6.9	4.99	0.16	0.23	0.05	167	5.0	820	5.5	6.91	78.6
8.	NPK + non-metallic phase of ϕ 0.5–2.0 mm size acc. to 0.75 Hh	5.4	2.27	13.9	5.8	3.89	0.12	0.23	0.07	167	6.0	870	4.9	6.58	65.5
9.	NPK + non-metallic phase of ϕ 0.5–2.0 mm size acc. to 1.5 Hh	6.4	1.56	21.4	5.4	4.79	0.14	0.20	0.04	167	7.0	820	5.1	6.73	76.8

3. Assessment of non-metallic phase suitability for soil liming

The non-metallic phase under analysis contained 69 percent particles of a size smaller than 0.5 mm, 9 percent 0.5–1.0 mm in size and about 22 percent larger than 1.0 mm in size. Those fractions smaller than 0.5 mm with their CaO content exceeding 60 percent showed the greatest neutralisation power and chemical activity. Their chemical activity exceeded that of $CaCO_3$.

The FeO content in fractions of sizes not exceeding 0.5 mm was smaller than 6 percent, which shows that introducing these fractions into soil does not pose a threat to it. The FeO content in fractions exceeding 0.5 mm in size increased to over 10 percent. The introduction into soil of a fraction with this amount of iron may have an adverse influence on its properties, especially during subsequent soil acidification. Fractions exceeding 0.5 mm in size also contain a relatively large amount of MnO, an excess of which is also hazardous. These fractions too contain the largest amounts of Cr_2O_3. Zinc, copper, lead and cadmium contents were low in all fractions and did not suggest any problems. The content of sodium, potassium and phosphorus was also low and of practically no importance. The SiO_2 content, which plays no role and is simply ballast, was high in all fractions of the non-metallic phase.

Pot experiments showed that the highest yields of green mass and dry mass of maize were obtained when the non-metallic phase smaller than 0.5 mm in size was applied according to 1.5 Hh. The highest yields of green mass and dry mass of the aftercrop on slightly clayey sand were obtained using limestone according to 0.5 Hh. On dusty soil, the green mass and dry mass of the aftercrop were the highest where the non-metallic phase of size smaller than 0.5 mm and 0.6–2.0 mm was applied. However, it was previously found that the 0.6–2.0 mm non-metallic phases contained too many iron oxides.

Fertilisation influenced the nutrient content in plants. The calcium content in plants cultivated on limed soils was higher than calcium content in plants cultivated on soils solely fertilised with NPK. At the same time, calcium content in plants increased when doses were applied according to 1.5 Hh. This concerns limestone, dolomite and the non-metallic phase to the same extent. The magnesium content in plants was highest when dolomite was applied. In plants cultivated on dusty soils, magnesium content was higher when the non-metallic phase was applied of a size smaller than 0.5 mm than in comparison with that obtained through the application of NPK for reference purposes.

Chemical properties of soils changed beneficially during plant cultivation. The application of calcium carriers caused a clear increase in pHCl and a change of soil qualification from very acid to slightly acid. This means that for slightly clayey sand the further application of calcium carriers is unnecessary while for dusty soil this operation should be limited. It was additionally found that the non-metallic phase did not introduce adverse metals into the soil.

4. Summary

Summarising the above-cited results of the analysis of the chemical composition of the non-metallic phase and its suitability for fertilisation, it can be concluded that fraction

smaller than 0.5 mm in size is suitable for soil liming. The fraction has a beneficial chemical composition and chemical activity. Using this fraction for fertilisation causes the de-acidification of soils and increases the yields of the cultivated plants. The yields of plants obtained when this fraction was used were higher than yields obtained with the application of limestone or dolomite. Non-metallic phase of larger sizes should not be used for soil fertilisation because of excessive amounts of iron oxides. These may be used as an addition to the sinter in the blast-furnace process.

REFERENCES

[1] M. Dziarmagowski, M. Karbowniczek, M. Pyzalski, J. Okoń, Ironmaking and Steelmaking, **19**, 1, 45-49 (1992).
[2] M. Dziarmagowski, Archives of Metallurgy **47**, 3, 287-295 (2002).
[3] M. Dziarmagowski, Archives of Metallurgy **48**, 2, 201-207 (2003).

REVIEWED BY: ANDRZEJ ŁĘDZKI
Received: 25 October 2003.

A R C H I V E S O F M E T A L L U R G Y A N D M A T E R I A L S
Volume 49 2004 Issue 1

BOGUSŁAW MAJOR*, JAN T. BONARSKI*, WOLFGANG WALDHAUSER**,
JURGEN K. LACKNER**, REINHOLD EBNER**

CONTRIBUTION OF PULSED LASER DEPOSITION CONDITIONS TO TEXTURE, MORPHOLOGY AND RESIDUAL STRESSES DEVELOPED IN TiN THIN LAYERS

WPŁYW WARUNKÓW OSADZANIA LASEREM IMPULSOWYM NA TEKSTURĘ, MORFOLOGIĘ I NAPRĘŻENIA WŁASNE W CIENKICH WARSTWACH TiN

Titanium nitride (TiN) thin layers were fabricated by pulsed laser deposition (PLD) by means of a Nd:YAG laser with Q-switch on three types of materials: ferritic steel, metallic titanium and polyurethane. A uniform smooth surface was observed to form in each case. Texture examinations were carried out for both the deposited TiN and the substrate. The application of the position sensitive detection technique in texture examination allowed to draw the pseudo-pole figures of residual stresses, while the X-ray diffraction method ($\sin_2\psi$) made it possible to measure residual stress values for the TiN phase. The substrate surface was positioned parallel (on-axis) and perpendicular (off-axis) to the surface of the target, to simulate deposition on 3D elements. Residual stresses measured in the TiN phase showed compressive values within the range of – 6 to – 8 GPa for the on-axis growth and of about – 2.8 GPa for the off-axis position in case of ferritic steel substrate, while they were within the range of – 8 to – 10 GPa for films fabricated on the metallic titanium substrate and of the order of – 4 to – 5 GPa for the polyurethane substrate (0.5 mm thick). The application of scanning electron microscopy (SEM) for examining materials cross-sections revealed the form of diffusion layers with continuous transfer from the deposited film to the substrate. Transmission electron microscopy (TEM) examinations performed on the thin foils prepared from the cross-section of the metallic titanium covered with the TiN confirmed the diffusion character of the deposited layer. A fine grained microstructure of the deposited TiN phase was stated. The morphology of the surface of the deposited layers was examined by means of the atomic force microscopy (AFM). The results showed that deposition parameters and layer thickness influenced the crystallite sizes and their vertical diameter.

Cienkie warstwy azotku tytanu (TiN) wytwarzane były metoda osadzania laserem impulsowym (PLD) z zastosowaniem lasera typu Nd:YAG z modulacją dobroci. Zastosowano trzy rodzaje podłoża: stal ferrytyczna, tytan oraz poliuretan. Obserwowano tworzenie się jednorodnej, gładkiej powierzchni we wszystkich przypadkach. Przeprowadzono badania tekstury

* INSTYTUT METALURGII I INŻYNIERII MATERIAŁOWEJ IM. A. KRUPKOWSKIEGO PAN, 30-059 KRAKÓW, UL. REYMONTA 25
** JOANNEUM RESEARCH, LASER CENTER LEOBEN STR. 2, A-8712 NIKLASDORF, AUSTRIA

dla osadzonej warstwy TiN oraz stosowanego podłoża. Zastosowano ustawienie podłoża równolegle do tarczy i prostopadle co modelowało osadzanie na elementach 3D. Wykorzystanie pozycyjnie czułej detekcji w badaniach tekstury umożliwiło wykreślenie pseudo-figur bieguno-wych rozkładu naprężeń własnych, zaś stosując rentgenowską metodę pomiaru naprężeń własnych ($\sin^2\psi$) uzyskano dla warstwy TiN wartości w zakresie – 6 do – 8 GPa dla położenia równoległego i 2.8 GPa dla położenia prostopadłego w przypadku podłoża ze stali ferrytycznej, zaś – 8 do – 10GPa dla warstwy TiN osadzonej na tytanie i – 4 do – 5 GPa dla osadzonej na poliuretanie (0.5 mm grubości). Wykorzystując skaningową mikroskopię elektronową (SEM) do analizy przekroju poprzecznego powłok na PU ujawniono dyfuzyjny obszar przejściowy pomiędzy osadzoną warstwą a podłożem. Badania na transmisyjnym mikroskopie elektronowym (TEM) wykonane na cienkich foliach z przekroju poprzecznego tytanu pokrytego TiN potwierdziły i w tym przypadku dyfuzyjny charakter warstwy przejściowej. Stwierdzono nanokrystaliczną mikrostrukturę w osadzonej warstwie TiN. Morfologie powierzchni analizowano mikroskopem sił atomowych (AFM), a uzyskane wyniki wykazały wpływ parametrów osadzania oraz grubości osadzonej warstwy na wielkość krystalitów i nierówność powierzchni.

1. Introduction

Titanium nitride (TiN) is a well known material for its tribological performance, as it increases the lifetime of cutting tools [1, 2]. It is also taken into consideration as a potential biomaterial [3]. TiN films are commonly formed by chemical vapor deposition (CVD) and physical vapor deposition (PVD) techniques [4]. These methods, however, require elevated substrate temperatures – even higher than 500°C – to achieve good adhesion between the film and the substrate and to reach high hardness. The deposition at elevated temperatures limits some applications where the substrate cannot withstand heating. Thus, there is a high demand for developing low-temperature deposition processes for TiN thin films, such as pulsed laser deposition (PLD) [5–9]. Pulsed laser deposition (PLD) belongs to the modern technologies which allow to produce thin layers of the nanostructure type. The possibility of depositing virtually any materials – from pure elements to multicomponent compounds – on various substrates makes PLD a very promising technology in the fabrication of thin layers for a wide range of applications. A typical set-up for the deposition of metallic alloys and multilayers consists of a target holder and a substrate holder housed in a vacuum chamber. In an UVH chamber, ablated targets are struck at the angle of 45° by a pulsed and focused laser beam [5]. The atoms and ions ablated from the target are deposited on substrates mounted on a heater. High-power pulsed lasers with nanosecond pulses are used as an external energy source to vaporize materials by ablation and to deposit thin films. The following three general growth modes have been distinguished in the literature [10] according to characteristic structures observed during the deposition of atoms onto a flat substrate: Frank-van der Merwe (FM), Stranski-Krastanov (SK), and Volmer-Weber (VW). In the FM mode, a crystal growth covers the substrate and is characterized by two-dimensional (2D) nucleation. The 3D nucleation is observed in VW mode, while the SK mode is a combination of the SK and VW growth.

During the early stages of deposition, these three classical morphologies are developed, but the structure should remain approximately similar. These morphologies are continued

as long as the surface diffusion transport is sufficient to allow the film surface to remain close to equilibrium. These later stages lead to the formation of "polycrystalline" or "columnar" growth and kinetic effects based on deposition rates and surface transport rates, which are the determining factors for the developed morphologies. Kinetic effects based on deposition rates and surface transport rates are major determining factors for the mentioned morphologies. The polycrystalline mode corresponds to a dense film, without an appreciable fraction of voids, but containing grain boundaries. The substrate is usually either amorphous, or polycrystalline, but with a large misfit relative to the low index surfaces of the crystalline film material. Columnar growth occurs under conditions similar to those for polycrystalline film, except that the surface diffusion rates are extremely low. Rough columnar crystals are formed, separated from each other by void regions. The transition from the near-equilibrium to kinetic mode occurs when the clusters reach the critical size. The calculation proposed by *Mullins* [10] allows one to estimate the cluster size at which the transition from the classical modes of growth to the kinetic modes occurs. Faceting during deposition is another factor that influences film morphologies and polycrystalline microstructures. The crystallographic orientation of the surface of a thin film may have a large impact on its morphology. It is well known that growth rate depends on orientation, and can produce faceting and other effects. The crystallographic relationships in the inter-phase area strongly influence the adhesion of deposited layers. The fact, that substrate texture is inherited during the deposition process, is one of the factors that have an impact on microstructure and preferred crystallographic orientation of the deposited layers. The problem has been investigated intensively for a few years, especially for a metallic layer deposited on the single-crystals, which imperfection of crystallographic orientation can be characterized by the geometrical and material factors [11].

The aim of this work was to apply the PLD using a Nd-YAG pulsed laser for deposition of TiN on metallic titanium, ferritic steel and polyurethane substrates, in order to study the morphology, texture and residual stress development in the thin layers deposited on various substrate materials with the different roughness.

2. Experimental

2.1. Materials and method of examination

Thin films of titanium nitride were deposited using PLD (pulsed laser deposition) method by means of a Nd:YAG laser, operating at the fundamental harmonics (1064 nm) in nitrogen environment in the reactive chamber (Fig.1). High purity titanium targets were used for ablation, effectuated by the application of energy pulses with the following characteristics: 0.6 J (fluence about 30 J/cm^2), duration: 10 ns, repetition rate: 50 Hz. The deposition on metallic (ferritic steel and pure titanium) and non-metallic (polyurethane) substrates was performed at room temperature. Before deposition, the reactive chamber had been evacuated to the pressure below 2×10^{-3}Pa by means of a pumping unit, consisting of a rotary vane pump and a turbo-molecular pump. During deposition, the flow of the process gases (Ar, N_2) was adjusted by means of electronic mass flow controllers.

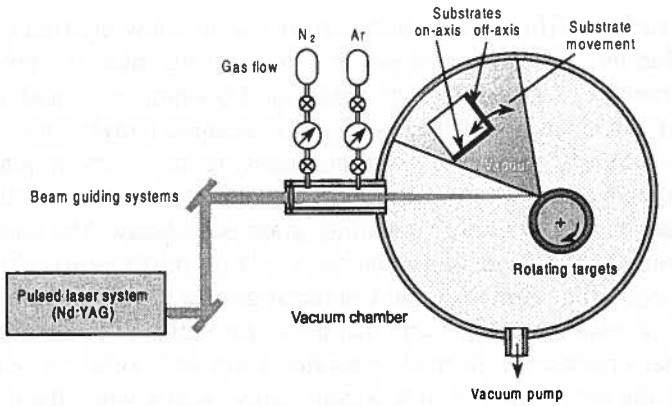

Fig. 1. Schematic view of the PLD system used in experiments

Since the properties of the substrate surface have an important influence on the film growth, this problem was studied on titanium samples used as targets with the following surface preparation:

a. original surface of the substrate, as rolled,
b. mechanically ground surface,
c. mechanically polished surface.

To simulate 3D deposition [12], the experiments on the ferritic steel substrate were performed with the sample mounted in parallel (on-axis) and normal (off-axis) positions with respect to the target surface (Fig.1). Prior to the deposition, all substrates were cleaned in an ultrasonic cleaner with acetone and ethylene. In the case of ferritic steel and titanium, the deposited film thickness was of the order of 1 μm. The nitrogen flow during deposition was at the level of 30 sccm. In order to improve adhesion of TiN to metallic (ferritic steel, titanium) and non-metallic (polyurethane PU) substrates, the onset of the process was triggered by the deposition of metallic titanium. The first step of the deposition process lasted for about 2–3 minutes and led to the formation of a layer about 0.1 μm thick. Different film thickness of the TiN was produced on PU using a prolonged time of exposure (raised number of laser shots). Layers with the following thickness values were fabricated on 1 mm thick PU: 0.5 ; 1.0 and 3 μm.

Structure examinations of the deposited layers were performed by means of scanning electron microscopy (SEM Philips XL30), transmission electron microscopy (TEM Philips CM20), atomic force microscopy (AFM) and X-ray diffraction (XRD Philips PW 1710). Texture examinations by means of the XRD method were performed for the above mentioned TiN layers, produced in different geometries. Three pole figures were measured on the basis of the diffraction lines of the 111, 200 and 220 types in the back-reflection mode. The complete pole figures were obtained by processing of the experimental data, carried out by means of a dedicated program prepared for this purpose, and the LaboTex [15].

2.2. Results and discussion

Atomic force microscopy examinations of the morphology of TiN deposited in on-axis and off-axis geometry showed that a finer structure was produced in the on-axis position, when deposited species had higher energy (Fig.2).

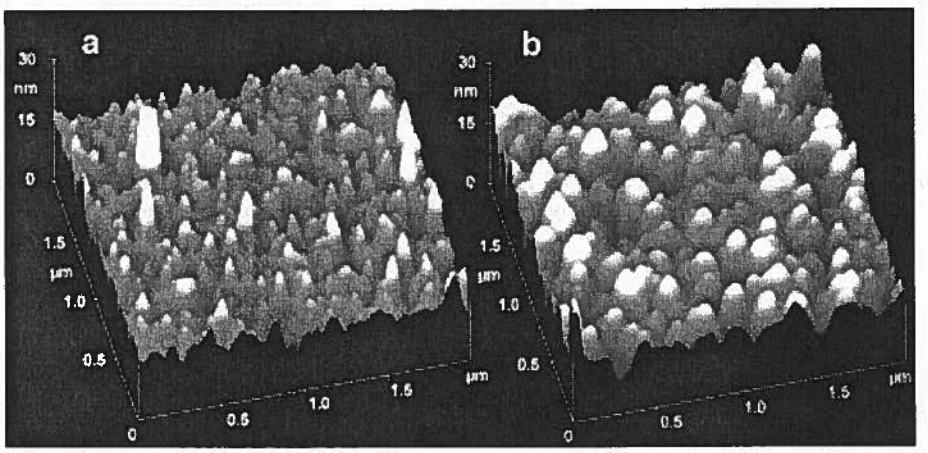

Fig. 2. AFM micrographs of surface layers deposited by means of a Nd:YAG laser in the on-axis (a) and off-axis (b) geometry

Texture examinations performed on the sample surface revealed differences and the results are shown in Figs. 3 and 4. Examinations of the ferritic steel used as a substrate were performed to study a possible contribution of the substrate texture to the preferred orientation developed in the deposited layers. The obtained results are presented in Fig. 5 in the form of complete pole figures. Measurements of residual stresses in the TiN phase, performed by means of the XRD method, showed compressive values within the range of -6 to -8 GPa for the on-axis growth, and of about -2.8 GPa for the off-axis position.

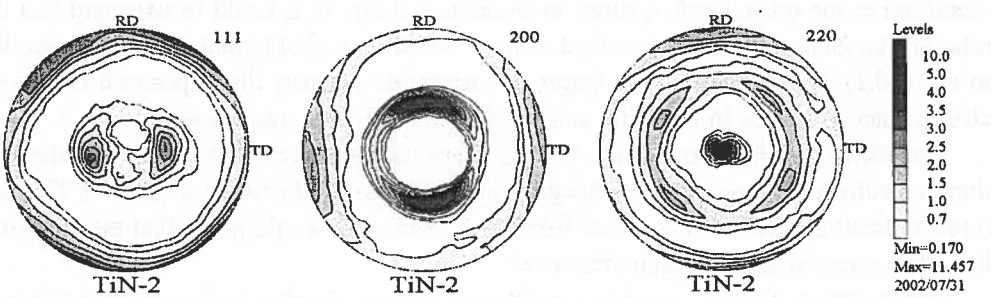

Fig. 3. Pole figures (111), (100) and (110) based on reflections 111, 200 and 220, respectively for TiN deposited in the on-axis geometry by means of a Nd:YAG laser revealing the {110}<011> texture

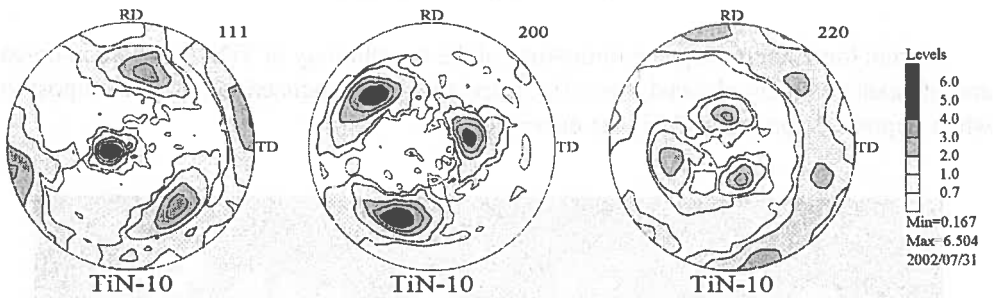

Fig. 4. Pole figures (111), (100) and (110) based on reflections 111, 200 and 220, respectively for TiN deposited in the off-axis geometry by means of a Nd:YAG laser revealing {112}<223> texture

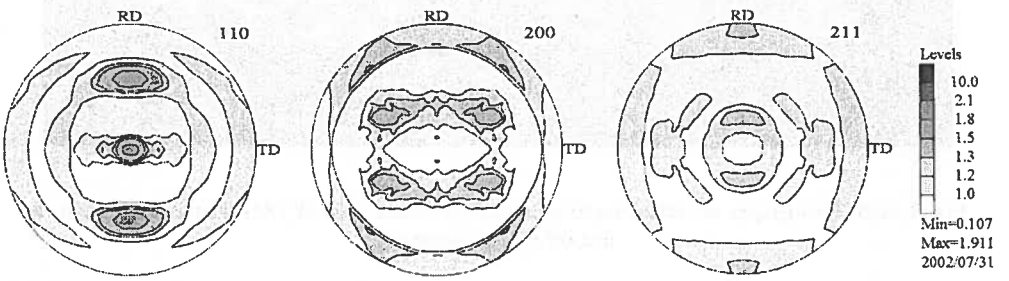

Fig. 5. Pole figures (111), (100) and (110) based on reflections 111, 200 and 220, respectively for the steel sheet used as a substrate, revealing dominant {110}<112> texture which is very characteristic for the annealed ferritic steel sheets subjected to the heat treatment after cold-rolling

The impact of the surface roughness of the metallic substrate (titanium) on the preferred crystallographic orientation of the deposited TiN layer was studied within the framework of texture analysis, performed for: as-rolled, ground and polished samples. Differences were identified in the related pole figures, as presented in Fig. 6. It could be expected that the relationship identified for the as-rolled sample – where the {111} plane in TiN was parallel to the (00.1) Ti – would lead to improved adhesion, because the deposition occurs on closely-packed planes in the cube and hexagonal structures, respectively.

The diffusive character of the boarder between deposited TiN layer and metallic titanium substrate suggests a possible good adhesion of the PLD coating (Fig. 7). The ring type of electron diffraction obtained from the TiN coating would prove that the deposited layer has a character of a nano-structure.

Deposition of the TiN at ambient conditions on non-metallic (polyurethane) substrate revealed in the AFM micrographs that the uniform thin layer and diameter of crystallite were related closely to the thickness of the deposited layer, which is presented in Fig. 8.

Morphology examinations of TiN layers deposited on PU showed a correlation between increasing grain size and layer thickness (Fig. 8). It tends to increase together with an increase of the layer thickness. The increase of layer thickness was obtained by means of a higher number of laser shots, while the other deposition parameters remained unchanged. The measurements – performed by means of the X-ray method – of residual stresses in TiN deposited on PU revealed the following relationship between stresses and layer thickness: – 2.5 GPa was identified for 0.5 μm and – 1.5 and – 1.75GPa for 1.0 and 3.0 μm thickness, respectively. Texture examination of TiN deposited on PU revealed the preferred orientation to be close to random. The TiN layers deposited on polyurethane are of diffusive character, which can be inferred from the diffusive shape of the interface layer/substrate and EDX line scan of Ti through the thickness (Fig. 9).

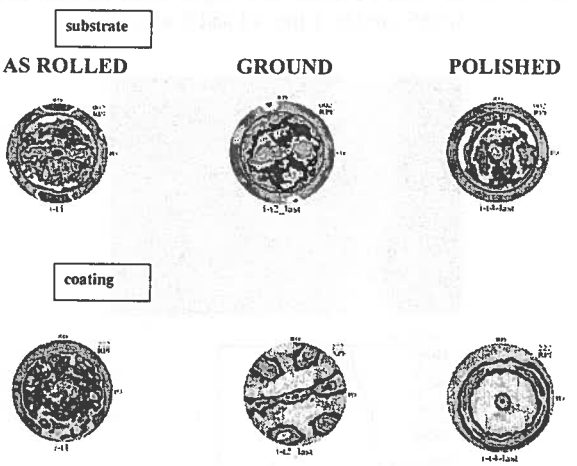

Fig. 6. (00.1) pole figures of metallic titanium substrate measured beneath the deposited TiN layer for different roughness of the substrate (upper part) and {111} pole figures of the deposited TiN layer on the different substrate roughness, respectively (bottom)

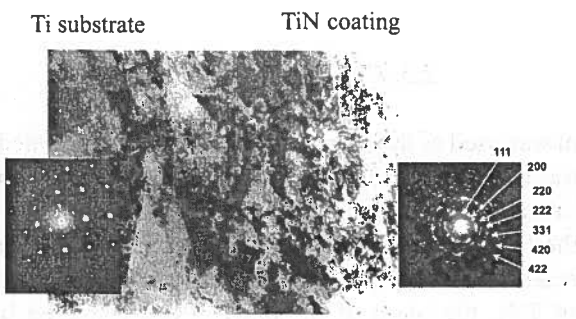

Fig. 7. TEM micrograph of the cross-section of TiN layer deposited on metallic titanium

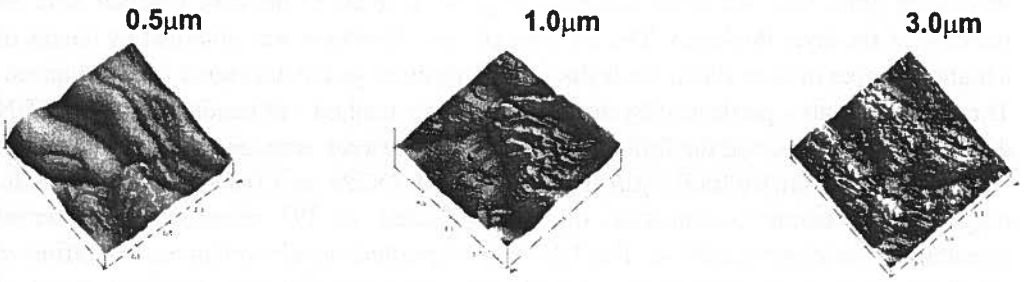

Fig. 8. AFM micrographs of the surface layers deposited on the polyurethane substrate by means of a Nd:YAG laser at the fluence 3 to 50 W/cm^2 in nitrogen environment with the layer thickness of 0.5 μm (a); 1 μm (b) and 3 μm (c)

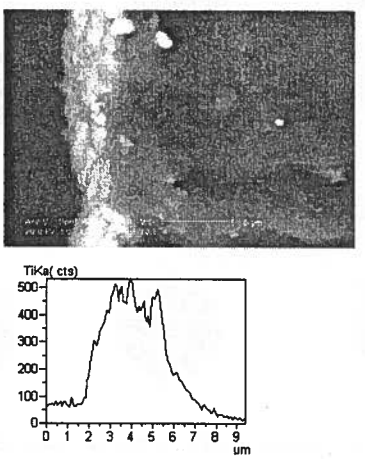

Fig. 9. SEM micrographs of the cross-section of the broken polyurethane samples with the TiN layer deposited by means of a Nd:YAG laser, with the thickness of 1μm (a) and the EDX line scan analysis through the thickness (b)

2.3. Concluding remarks

Metallic titanium was used as the target. Previous results, presented in [13, 14], showed that the TiN phase was formed independently of the nitrogen flow in the reactive chamber. Even deposition of metallic titanium in argon environment led to the formation of a new tetragonal phase of the Ti(N) type [13]. The obtained electron diffraction patterns of the ring type indicated the presence of a very fine grain or even nanostructure in PLD layers [13]. To improve adhesion of TiN, the onset of the process was triggered by the deposition of metallic titanium. This first step of the deposition process lasted for about 2–3 minutes and led to the formation of a layer with the thickness of about 0.1 μm and with grain size slightly

higher than that of the subsequently deposited TiN, which could be inferred from the tendency to form spot-type electron diffraction patterns. Even contrast in darkness may indicate the presence of a variation in nitrogen concentration through the thickness of the deposited layer. AFM micrographs showed that both microstructure and texture were different, depending on the applied geometry of deposition. In the on-axis position – due to higher energy of deposited species, which resulted from hitting the substrate surface at right angle – the probability of nucleation and the activation of diffusion on the surface was higher, which led to finer structure. In the case of the off-axis deposition geometry, however, the ablated species could hit the surface only after scattering, caused by a collision with the other atoms in the deposition chamber. The differences in the deposition mechanism led also to changes in the film thickness, which was about two times smaller in the case of off-axis positioning, compared to the on-axis grown films. The differences in texture were more pronounced (Fig. 3 and 4). The deposition conditions in the off-axis geometry led to the formation of a texture, where a well-developed crystallographic axis was observed beside the preferred crystallographic plane. It could be suggested that there was a correlation between the texture type developed in the deposited layers and the texture of the substrate in the examined samples. The correlation can be described by the relationship (111) TiN parallel to (110) Fe.

The impact of the surface roughness of the metallic substrate (titanium) on the preferred crystallographic orientation of the deposited TiN layer was studied within the framework of texture analysis of the samples subjected to different surface preparation, i.e. as-rolled, ground and polished samples. Certain differences were identified in the measured pole figures (Fig. 6). It could be expected that the relationship identified for the as-rolled sample – where the {111} plane in TiN was parallel to the (00.1) Ti – would lead to improved adhesion, because the deposition occurs on closely-packed planes in the cube and hexagonal structures, respectively.

The examination of the TiN layers fabricated at room temperature on polyurethane substrate showed a correlation between the increase of grain size and of the layer thickness. An increase of the layer thickness was achieved by means of a higher number of laser shots, while the other deposition parameters were constant. Morphology observation of the cross-section of broken samples revealed a possible adhesion which was inferred from the smooth layer/substrate interface, and more evidently from the change of concentration of titanium in line scan.

Acknowledgements

Parts of the present work were supported by the State Committee for Scientific Research of Poland under the Projects No. 4 T08C 028 23 and by the Eureka project E! 2841 decision Nr 62/E-88/SPB/Eureka/T-08DZ 348/2002-2004.

REFERENCES

[1] D. S. Rickerby, A. Matthews, eds., Advanced Surface Coatings: a Handbook of Surface Engineering, Chapman and Hall, New York, (1991).
[2] S. J. Bull, D. S. Rickerby, Amitabhjain, The sliding wear of titanium nitride coatings, Surf.Coat.Technol. **41**, 269 (1990).
[3] B. F. Coll, P. Jacquot, Surface modification of medical implants and surgical devices using TiN layers, Curf.Coat.Technol. **36**, 867 (1988).
[4] T. Burakowski, T. Wierzchoń, Surface engineering of metals – principles, equipment, technology, CRC Press, Boca Raton-London-New York-Washington D.C. (1999).
[5] D. B. Chrisey, G. K. Hubler Eds., Pulsed Laser Deposition of Thin Films, John Wiley and Sons (1994)
[6] H.-G. Rubahn, Laser Applications in Surface Science and Technology; John Wiley, Chichester (1999).
[7] J. C. Miller, R. F. Haglund Jr. Eds., Laser Ablation and Desorption, Academic Press, San Diego **30** (1998).
[8] H.-U. Krebs., International Journal of Non-Equilibrium Processing **10**, 3 (1997).
[9] B. Major, Ablacja i osadzanie laserem impulsowym, Wydawnictwo Naukowo-Techniczne Akapit, Kraków (2002).
[10] J. E. Greene, in: Multicomponenet and Multilayered Thin Films for Advanced Microtechnologies (O. Auciello and J. Engemann, eds.) NATO/ASI Series E 234, Kluver Publ., 39 (1993).
[11] W. Truszkowski, J. Bonarski; On the Imperfection of Crystallographic Orientation in FCC Single Crystals, Z. Metallkd. **91**, 1030 (2000).
[12] R. Ebner, W. Waldhauser, W. Lenz, Pulsed laser deposition: A new technique for coating sheet materials and three-dimensional industrial components, Proc.Materials Week 2001, Munich, 2001.
[13] B. Major, R. Ebner, Laser applications in surface modification and pulsed laser deposition, Journal of Technical Physics, Special Supplement **XL**. 3, 161, Warszawa (1999).
[14] B. Major, R. Ebner, Titanium-based films deposited using a Nd:YAG pulsed laser; Appl.Phys. **A69**, 1-3 921 (1999).
[15] LaboTex, The Texture Analysis Software, by Labasoft S.C. Kraków (2000).

REVIEWED BY: ZDZISŁAW JASIEŃSKI
Received: 7 December 2003.

A R C H I V E S O F M E T A L L U R G Y A N D M A T E R I A L S
Volume 49 2004 Issue 1

EDWARD FRAŚ*, MARCIN GÓRNY*, HUGO F. LOPEZ**

A DEPENDENCY BETWEEN UNDERCOOLING AND EUTECTIC GRAIN DENSITY IN NODULAR CAST IRON – MODELING RESEARCH AND THEIR EXPERIMENTAL VERIFICATION

ZALEŻNOŚĆ MIĘDZY PRZECHŁODZENIEM A GĘSTOŚCIĄ ZIAREN EUTEKTYCZNYCH W ŻELIWIE SFEROIDALNYM – BADANIA MODELOWE I ICH WERYFIKACJA DOŚWIADCZALNA

In this work, analytical expressions for grain density were derived for the globular eutectic transformation that occurs during the solidification of nodular cast iron. The model incorporates heat and mass balance equations in considering nucleation and growth of nodular eutectic grains. In particular, an expression in proposed to correlate the volumetric density of nodular eutectic grain to the maximum degree of undercooling. The proposed expression avoids the use of fitting parameters, frequently employed to correlate the experimental outcome with the relevant nucleation mechanisms involved. Experimentally, 0.6 cm, 1.0 cm, 1.6 cm and 2.2 cm thick plates, respectively were used in this work. The plates were made of nodular graphite cast iron of hypereutectic composition. Measurements of the degree of undercooling versus the eutectic grain density were carried out and good agreement was found to exist between the experimental and predicted data.

W pracy wyprowadzono analityczną zależność na gęstość ziaren eutektyki kulkowej, która powstaje podczas krystalizacji żeliwa sferoidalnego. Gęstość ziaren eutektyki kulkowej i prędkość jej wzrostu zgodnie z opracowanym modelem wynika z bilansu masy i ciepła. W szczególności, zaproponowany model teoretyczny pozwala otrzymać zależność między maksymalnym stopniem przechłodzenia żeliwa sferoidalnego a objętościową gęstością ziaren. W zależności tej nie występują, tzw. parametry dopasowania, stosowane w innych pracach, celem uzyskania zgodności wyników badań doświadczalnych z opracowanymi modelami teoretycznymi. Otrzymaną zależność zweryfikowano doświadczalnie na przykładzie odlewów płyt o grubości ścianki: 0.6 cm, 1.0 cm, 1.6 cm i 2.2 cm. Płyty wykonano z żeliwa sferoidalnego o składzie nadeutektycznym. Pomiary stopnia przechłodzenia żeliwa sferoidalnego oraz gęstości ziaren eutektyki kulkowej potwierdziły dość dobrą ich zgodność z wynikami obliczeń według opracowanego modelu.

* KATEDRA ODLEWNICTWA ŻELIWA, AKADEMIA GÓRNICZO-HUTNICZA, 30-059 KRAKÓW, UL. REYMONTA 23
** MATERIALS DEPARTMENT, UNIVERSITY OF WISCONSIN-MILWAUKEE, P.O. BOX 784, MILWAUKEE, USA

1. Introduction

Nodular cast iron is modern engineering material which production constantly increasing. Including austempered ductile iron (ADI) one may say that, with lover expense of production properties of nodular cast iron are now in range of the field of cast made of cast steel and some grade of steel. It has been made a lot of papers in the field of production nodular cast iron [1–4]. Some of them with fundamental meaning are connected with solidification kinetics, which depends on two processes, that is nucleation and growth of graphite eutectic grain. Nucleation is the dominant process at the beginning of solidification and lead rapidly to establishment of the final grains population. Grain density is very significant structural parameter of the cast iron, which has important influence on:

- Microsegregation of alloying elements [5, 6], degree of segregation and in consequence increasing in microstructure homogeneity decreases with increasing grain density. Redistribution of alloying elements during solidification partially determines kind of eutectics transformation (stable or matastable). Chemical inhomogeneity has also influence on further transformation in solid state [7].
- Chilling tendency of cast iron, chilling tendency decreases with increasing grain density [8].
- Pre-shrinkage expansion, pre-shrinkage expansion increases with increasing grain density [9].
- Formation of the open and closed contraction cavity, contraction cavity volume increases with increasing grain density [10].
- Type of metallic matrix, fraction of ferrite in microstructure of nodular cast iron increases with increasing grain density (decreasing mean grain radius at constant volume fraction of graphite), at identical chemical composition and equal cooling condition [11].

Carrying out calculation of the grain density on the basis of classical nucleation theory [12, 13] or dynamic nucleation theory [14–16] is difficult for lack of date regarding so-called fitting parameters [1, 17, 18]. The foregoing difficulty has been removed in work [19], but it concerns only cast iron with eutectic composition.

The aim of this present work is to expand model given in [19] in order to also embrace no eutectic cast iron.

2. Analysis

List of symbols used in present article are presented below.

Symbols their meaning and definition

Symbol	Meaning	Definition	Units
a	Constant	–	$°C^{-1}$
b	Coefficient of heat accumulation of the material of the mould	–	$J/(cm^2\,°C\sqrt{s})$
B, B_1	Temperature parameters	Equations (7), (14)	–

c_{ef}	Effective specific heat of metal	Equation (8)	J/(cm^3 °C)
c_V	Specfic heat of metal	–	J/(cm^3 °C)
C, Si, P	Carbon, silicon and phosphorus content in liquid cast iron	–	wt. %
C_2,	Carbon content in austenite at graphite/austenite interface	Figure 3	wt. %
C_3	Carbon content in austenite at liquid/austenite interface	Figure 3	wt. %
C_e	Carbon content in eutectic	Table 4	wt. %
C_{gr}, C_4	Carbon content in graphite and in liquid	Fig. 3	wt. %
D	Diffusion coefficient of the carbon in austenite	–	cm^2/s
$dR_m/\,dt$	Eutectic grains growth rate at maximum undercooling	Equation (51)	cm/s
$dT/\,dt$	Metal cooling rate	Equation (16)	°C/s
f_p	Volume fraction of pro-eutectic phase	Table 4	–
F_c	Surface area of the casting	–	cm^2
g_{gr}	Graphite fraction	Table 4	–
k	Coefficient	Equation (42)	–
L_e	Latent heat of graphite eutectic	Table 4	J/cm3
L_g	Latent heat of graphite	Table 4	J/cm^3
L_p	Latent heat of pro-eutectic phase	–	J/cm^3
M	Casting modulus	–	cm
m_2, m_3, m_4	The slopes of the E'S', JE' and BC' lines respectively in Fe-C-Si system	Figure 3	cm^3 °C g^{-1}
m_{gr}, m_γ	The mass of the carbon in graphite and austenite envelope, respectively	Equations (34,38)	g
N_A	Planar grain density	–	1/cm^2
N	Volumetric eutectic grain density	Equation (54)	1/cm^3
q_a	Accumulated heat flux in casting	Equation (4)	J/s
q_s	Heat flux generated during solidification	Equation (25)	J/s
q_m	Heat flux extracted from casting into mould casting	Equation (3)	J/s
r	Radial coordinate	–	cm
R_1	Radius of graphite	Figure 3, equation (39)	cm
R_2	Radius of austenite envelope	Figure 3, equation (48)	cm
R_m	Graphite eutectic grain radius at maximum undercooling	Equation (50)	cm
s	Metal colling rate	Equation (16)	°C/s
t	Time	–	s
t_e	Time at onset of graphite eutectic	Figure 1,	

	solidification	equation (11)	s
t_l	Time at onset of pro-eutectic solidification	Figure 1, equation (5)	s
t_m	Time at maximum undercooling	Figure 1	s
T	Temperature	–	°C
T_b	Initial temperature of mould material	–	°C
T_e	Equilibrium temperature of the graphite eutectic	Figure 1, equation (55)	°C
T_i	Initial temperature of metal in mould cavity	Figure 1, table 4	°C
T_l	Liquidus temperature at the onset of pro-eutectic solidification	Figure 1	°C
$T_{l,g}$	Liquidus temperature of pure graphite	3800	°C
$T_{l,p}$	Liquidus temperature of pro-eutectic phase, when its fraction $f_p = 1$	–	°C
T_m	Temperature at maximum undercooling of eutectic	Figure 1	°C
V	Volume of eutectic grain	–	cm^3
V_c	Volume of casting	–	cm^3
V_p	Volume of pro-eutectic phase	–	cm^3
W, W_1	Parameters	Equations (6,12)	$\sqrt{s}/m$
ϕ	Thermo-chemical coefficient	Equation (13)	$J/(cm^3\ °C)$
ω	Frequency	Equation (19)	1/s
φ_1, φ_2	Constant	Equations (28,29)	
ΔT	Degree of undercooling	Equation (18)	°C
ΔT_m	Maximum undercooling	Equation (56)	°C
ρ_{gr}	Graphite density	Table 4	g/cm^3
ρ_γ	Austentie density	Table 4	g/cm^3

Tree stages of cooling and solidification * of the cast iron can be distinguished in present analysis (Fig. 1), that is:

Stage I – Cooling of metal in liquid state from the initial temperature of metal in mould cavity (T_i) to the liquidus temperature (T_l) in the $0 \le t \le t_l$ time range.

Stage II – Cooling and solidification of pro-eutectic phase from the temperature (T_l) to the beginning of graphite eutectic solidification (T_e) in the $t_l \le t \le t_e$ time range.

Stage III – Cooling and solidification of eutectic from the temperature (T_e) to the minimum temperature at the beginning of solidification (T_m) in the $t_e \le t \le t_m$ time range.

In present work it is assumed that castings will be made of sand mould. Therefore Biot number < 0.1 and thermal gradient in the casting can be neglected. Taking it into account equation of heat balance in cast-mould system can be written as:

* In reality one more process of cast iron cooling occurred, that is during pouring into mould but for the sake of its lower meaning it is more often neglected.

$$q_m = q_s + q_a. \tag{1}$$

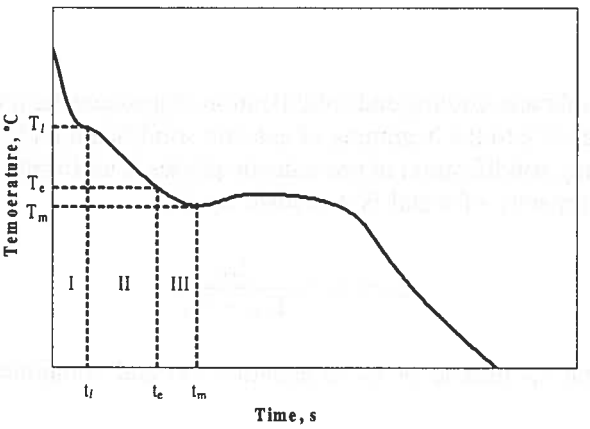

Fig. 1. Cooling curve of no eutectic cast iron

Stage I

In this stage temperature of the melt decreases from the initial one (T_i) to the liquidus (T_l) thus solidification process is impossible. In consequence $q_s = 0$ and equation (1) can be rewritten as:

$$q_m = q_a \tag{2}$$

where:

$$q_m = \frac{bF_c(T - T_b)}{\sqrt{\pi t}}; \tag{3}$$

$$q_a = \frac{c_V V_c d(T_b - T)}{dt}; \tag{4}$$

After solving an equation (2) (for the initial conditions: $T = T_i$ at $t = 0$, and for $T = T_l$ at $t = t_l$) we get the time elapsed during the first cooling stage as [20]

$$t_l = (WBM)^2; \tag{5}$$

where

$$W = \frac{c_V\sqrt{\pi}}{2b}; \tag{6}$$

$$B = \ln\frac{T_i - T_b}{T_l - T_b}. \tag{7}$$

Stage II

The second stage embraces cooling and solidification of pro-eutectic phases in the range of liquidus temperature (T_l) to the beginning of eutectic solidification (T_e). It is assumed that heat generated during solidification of pro-eutectic phases is uniformly released. So-called the effective heat capacity of metal is described by [21].

$$c_{ef} = c_V + \frac{L_p}{T_{l,p} - T_e}. \tag{8}$$

Taking into account c_{ef} instead of c_V in equation (4) and combining it with equation (3) it is obtained

$$\frac{bF_c(T - T_b)}{\sqrt{\pi t}} = \frac{c_{ef} V_o d(T_b - T)}{dt}. \tag{9}$$

After solving the equation (9) (for the initial conditions: $T = T_l$ at $t = t_l$, and for $T = T_e$ at $t = t_e$) we get the temperature during this stage as

$$T = (T_l - T_b)\exp\left[-\frac{\sqrt{t} - \sqrt{t_l}}{W_1 M}\right] + T_b; \tag{10}$$

as well as the time at the beginning of the eutectic solidification

$$t_e = \frac{\pi M^2}{4b^2}\phi^2; \tag{11}$$

where:

$$W_1 = \frac{c_{ef}\sqrt{\pi}}{2b}; \tag{12}$$

$$\phi = c_V B + c_{ef} B_1; \tag{13}$$

$$B_1 = \ln\frac{T_l - T_b}{T_e - T_b}. \tag{14}$$

After differentiation of equation (10) the expression for the cooling rate yields

$$\frac{dT}{dt} = -\frac{(T_l - T_b)}{2W_1 M\sqrt{t}}\exp\left[-\frac{\sqrt{t} - \sqrt{t_l}}{W_1 M}\right]. \tag{15}$$

Essential for the goal of our work is knowledge of metal cooling rate at the end of stage II (when $t = t_e$). It can be calculated by means of equations (5), (11) and (15) and after rearranges

$$\frac{dT}{dt} = s = -\frac{2b^2(T_e - T_b)}{c_{ef}\pi M^2 \phi}. \tag{16}$$

Stage III

As it was mentioned before stage III concerns processes of cooling and solidification of graphite eutectic in in the $t_e \leq t \leq t_m$ time range what replies in the $T_e \leq T \leq T_m$ temperature range. During this stage, the segment of the cooling curve (Fig. 1) where the eutectic reaction takes place can be defined as a function of the degree of undercooling ΔT according to:

$$\Delta T = \Delta T_m \sin[\omega(t - t_e)]; \tag{17}$$

where:

$$\Delta T = T_e - T; \tag{18}$$

$$\omega = \frac{\pi}{2(t_m - t_e)}. \tag{19}$$

From equations (17) and (18) follows that the temperature of cast iron at the beginning of stage III is described by equation:

$$T = T_e - \Delta T_m \sin[\omega(t - t_e)]. \tag{20}$$

Equation (17) has nature of an arbitral assumption and in consequence, equation (20) is also arbitral established. It can be proved that they very good describe experimental facts. As an example it can be figure 2 where it is shown course of real cast iron temperature (continuous curve) in comparisons with course of calculated temperature (dotted line) based on equation (20).

Cooling rate in stage III can be found by differentiating equation (20):

$$\frac{dT}{dt} = -\Delta T_m \omega \cos[\omega(t - t_e)]. \tag{21}$$

Therefore at the beginning of stage III ($t = t_e$) cooling rate yield

$$\frac{dT}{dt} = -\Delta T_m \omega; \tag{22}$$

Combining equations (19) and (22) as well as rearranges it is obtained

$$\frac{\Delta T_m}{(t_m - t_e)} = -\frac{2}{\pi}\frac{dT}{dt}. \tag{23}$$

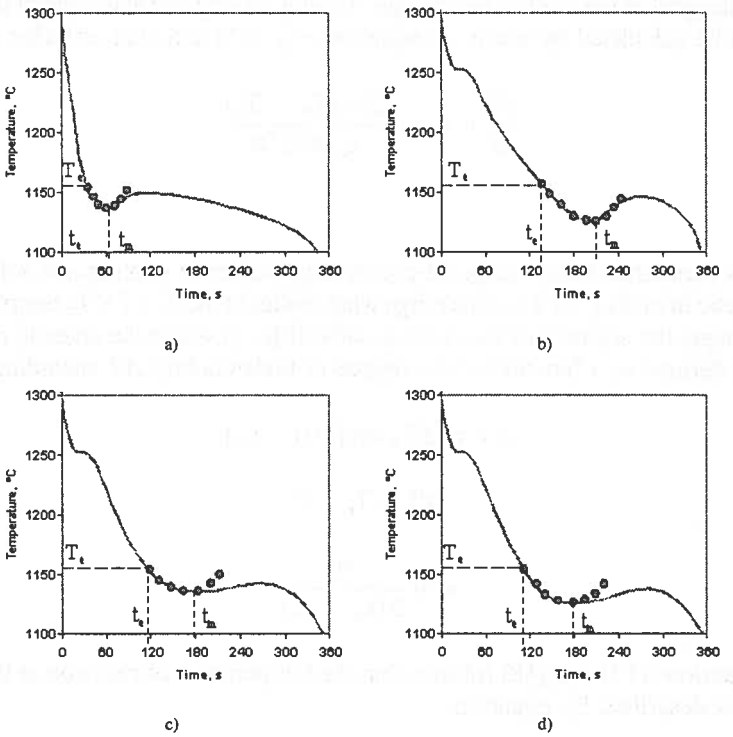

Fig. 2. Comparison between predicted (dotted lines) and experimentally determined (continuous lines) cooling curves for cast iron in the time interval t_e to t_m. (a) Eutectic, (b) hypoeutectic, (c) inoculated after 4 min., and (d) inoculated after 15 min. [8]

This is turn indicates that the maximum undercooling solidification time ratio is directly proportional to the cooling rate, dT/dt (stage II). Moreover, at the onset of eutectic solidification ($t = t_e$), the cooling rates in stages II and III must equal each other. Therefore, using equations (11), (16), and (23), the time for maximum undercooling can be determined from

$$t_m = \frac{M^2 \pi \phi [\phi (T_e - T_b) + \pi \Delta T_m c_{ef}}{4 b^2 (T_e - T_b)}. \tag{24}$$

Let us consider heat generation rate during eutectic solidification in stage III. From description of the sequence of eutectic grain growth in cast iron follows that they are spherical until the moment of bringing together. Volume of eutectic grain amount to $V = 4\pi R^3/3$, where: R – grain radius while increment the volume of grain amount to $dV = 4\pi R^2 dR$. Volume of liquid cast iron amount to $V_c - V_p = V_c(1 - V_p/V_c) = V_c(1 - f_p)$, where: V_p, f_p – volume and volume fraction of pro-eutectic phase, respectively, which is arisen in stage II. It is assumed that

instantaneous nucleation occur i.e. at the beginning of stage III nuclei density (N) amount to grain density. Taking into account foregoing statements and assumptions equation of rate of heat generation during the stage III can be written as

$$q_s = \frac{4\pi L_e N V_c (1 - f_p) R^2 dR}{dt}. \tag{25}$$

In order to establish radius R as well as growth rate dR/dt of grain, eutectic transformation in nodular cast iron will be considered.

Consider a diffusion transformation (fig. 3) and assuming spherical geometry, the steady state solution for carbon diffusion through the austenite shell can be found by solving the equation

$$D\left(\frac{2}{r}\frac{dC}{dr} + \frac{d^2C}{dr^2}\right) = 0. \tag{26}$$

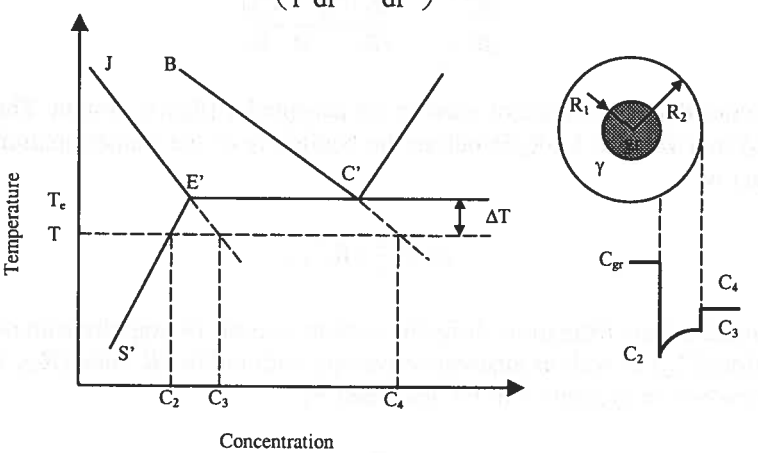

Fig. 3. Schematic representation of a fragment of the phase equilibrium diagram and eutectic grain with the range of carbon content

General solution to the above equation gives

$$C = \varphi_1 + \frac{\varphi_2}{r}, \tag{27}$$

where: r is the radial coordinate, and φ_1 and φ_2 are constants which can be determined from the boundary conditions $C = C_3$, at $r = R_2$ and $C = C_2$ at $r = R_1$. This yields

$$\varphi_1 = C_3 - \frac{R_1 (C_2 - C_3)}{R_2 - R_1}; \tag{28}$$

$$\varphi_2 = \frac{R_1 R_2 (C_2 - C_3)}{R_2 - R_1}. \tag{29}$$

Hence, the solute concentration field in the austenite envelope can be described by:

$$C = C_3 - \frac{R_1(r - R_2)(C_2 - C_3)}{r(R_2 - R_1)}. \tag{30}$$

Moreover, derivation of equation (30) the carbon concentration gradient in the austenite envelope at the liquid – austenite interface amount to

$$\frac{dC}{dr} = \frac{(r - R_2)(C_2 - C_3)R_1}{r^2(R_2 - R_1)} - \frac{(C_2 - C_3)}{r(R_2 - R_1)}. \tag{31}$$

On austenite solidification front that is for $r = R_2$ concentration gradient in the austenite yield:

$$\left.\frac{dC}{dR}\right|_{\gamma} = \frac{R_1(C_3 - C_2)}{(R_2 - R_1)R_2}. \tag{32}$$

Let us consider the balance of mass in the accepted diffusion system. The mass of the carbon (C_4) in a volume $4\pi R_2^3/3$ before the beginning of the transformation (when only liquid exist) is

$$m_l = \frac{4}{3}\pi R_2^3 C_4. \tag{33}$$

After eutectic transformation, diffusion system consists of graphite with radius (R_1) and concentration (C_{gr}) as well as austenite envelope with radius (R_1) and (R_2). Therefore the mass of a carbon in graphite can be described by

$$m_{gr} = \frac{4}{3}\pi R_1^3 C_{gr}. \tag{34}$$

Increment of the volume of the austenite envelope amount to $dV = 4\pi r^2 dr$. Increment the mass of the carbon can be written as

$$dm_\gamma = 4\pi C(r) r^2 dr; \tag{35}$$

while, the mass of the carbon in austenite envelope describe the following equat

$$m_\gamma = 4\pi \int_{R_1}^{R_2} C(r) r^2 dr. \tag{36}$$

Taking into consideration equation (30) and after its solution

$$m_\gamma = \frac{4}{3}\pi \left[C_3 R_2^3 - C_2 R_1^3 - \frac{1}{2} R_2 R_1 (C_3 - C_2)(R_2 + R_1) \right]. \tag{37}$$

Third part in brackets of above equation is neglected for the sake of its small value*. In this connection it can be written:

$$m_\gamma = \frac{4}{3}\pi (C_3 R_2^3 - C_2 R_1^3). \tag{38}$$

From the mass balance, based on equations (33), (34) and (38) we obtain:

$$R_1 = R_2 \left(\frac{C_4 - C_3}{C_{gr} - C_2} \right)^{1/3} \tag{39}$$

The continuity condition across the liquid – austenite interface is given by

$$(C_4 - C_3) \frac{dR_2}{dt} = D \frac{dC}{dR}\bigg|_\gamma . \tag{40}$$

Combining equations (32), (39), and (40) yields:

$$R_2 \, dR_2 = kDdt; \tag{41}$$

where:

$$k = \frac{C_3 - C_2}{(C_4 - C_3)\left(\sqrt[3]{\frac{C_{gr} - C_2}{C_4 - C_3}} - 1 \right)}. \tag{42}$$

Equation (42) can be interrelated with the degree of undercooling (ΔT). After assuming that the JE', E'S' and BC' lines of the Fe-C-X system (Fig. 3) are straight and taking into account the silicon influence on $C_{E'}$ and $C_{C'}$ points of the equilibrium system it can be written

$$C_2 = 10^{-3} \left[(C_{E'} - 0.11Si) \frac{\rho_\gamma}{100} - \frac{\Delta T}{m_2} \right]; \tag{43}$$

$$C_3 = 10^{-3} \left[(C_{E'} - 0.11Si) \frac{\rho_\gamma}{100} + \frac{\Delta T}{m_3} \right]; \tag{44}$$

$$C_4 = 10^{-3} \left[(C_{C'} - 0.3Si) \frac{\rho_c}{100} + \frac{\Delta T}{m_4} \right]; \tag{45}$$

* Error of this simplification not exceed 3%.

Taking into account typical date: $m_2 = 4070$; [cm^3 °C g^{-1}], $m_3 = 2486$; [cm^3 °C g^{-1}], $m_4 = 1655$; [cm^3 °C g^{-1}], $\rho_\gamma = 7.3$; [g cm^{-3}], $\rho_c = 7.0$; [g cm^{-3}] according to equations (42-45) calculations were made. The results of the calculations are shown in Fig. 4, from which it follows that

$k = f(\Delta T)$ is almost linear and it can be presented in simply form

$$k = a\,\Delta T; \tag{46}$$

where: $a = 0.0033$ [$°C^{-1}$].
Combining (17), (41) and (46) we find thet

$$R_2 \int dR_2 = aD\Delta T_m \int \sin[\omega(t - t_e)]\,dt. \tag{47}$$

Upon integration, the integration constant can be found using the limiting conditions $t = t_e$ at $R_2 = 0$, yielding

$$R_2 = \left(\frac{2aD\Delta T_m}{\omega}[1 - \cos[\omega(t - t_e]]\right)^{1/2}; \tag{48}$$

the rate of eutectic grain growth becomes

$$\frac{dR_2}{dt} = \left(\frac{aD\omega\Delta T_m}{2}\right)^{1/2} \frac{\sin[\omega(t - t_e)]}{(1 - \cos[\omega(t - t_e)])^{1/2}}. \tag{49}$$

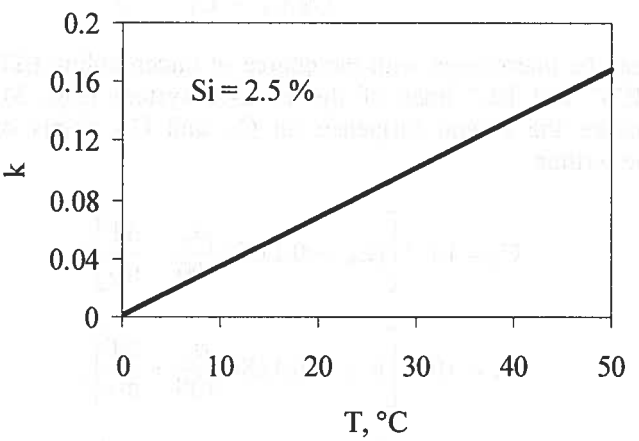

Fig. 4. k coefficient correlated with the undercooling ΔT

At the time of maximum undercooling ($t = t_m$), equations (16), (23), (48) and (49) after rearranges give us grain radius and growth rate of eutectic grain:

$$R_m = \frac{M\Delta T_m}{b}\left(\frac{aDc_{ef}\pi\phi}{(T_e - T_b)}\right)^{1/2}; \tag{50}$$

$$\frac{dR_m}{dt} = \frac{b}{M}\left(\frac{aD(T_e - T_b)}{\pi c_{ef}\phi}\right)^{1/2}. \tag{51}$$

Therefore equation of the heat generation rate equation during eutectic solidification at maximum undercooling after taking into account equations (25), (50) and (51) for $R = R_m$ and $dR/dt = dRm/dt$ can be finally written as:

$$q_s = 4L_eNMV_c(1 - f_p)(\pi aD)^{3/2}\left(\frac{\phi c_{ef}}{T_e - T_b}\right)^{1/2}. \tag{52}$$

At maximum undercooling the cooling rate is zero thus the rate of heat accumulation is zero. In this connection the heat balance yield:

$$q_s = q_m. \tag{53}$$

Taking into account equation (3) for $t = t_m$ as well as equations (52) and (53), after crearranges it is obtained nuclei density numerical identity with eutectic grain density, which has arisen during eutectic solidification.

$$N = \frac{b^3(T_e - T_b)^2}{2\pi^3 c_{ef}L_e(1 - f_{gr})M^3(aD\phi\Delta T_m)^{3/2}[\pi c_{ef}\Delta T_m + \phi(T_e - T_b)]^{1/2}} \tag{54}$$

From equation (54) follows that graphite grain density in cast iron decrease with maximum undercooling increases, as rest of the parameters remains invariable.

3. Experimental procedure

The experimental verification of the model was done on the hyper-eutectic cast iron. The test melts were made in an electric of low frequency (50 Hz) induction furnace and 8000 kg crucible capacity. Charge materials for the furnace consisted of iron scrap, steel scrap and silicon carbide. After melting of the charge and preheating to the temperature of 1485°C cast iron was poured into a casting ladle where spheroidization treatment was made by cored wired injection method. Afterwards process of inoculation was made, see table 1. Four different inoculants in different amounts were used (table 1). The aim of using different type and process of inoculation was to obtain different value of maximum undercooling. Cast iron was poured into mould of plates of the thickness 0.6; 1.0; 1.6 and 2.2 cm. The length and height was 10 cm in the case of 0.6 cm, 1.0 cm and 1.6 cm thick plates; in the case of 2.2 cm it was14 cm. All plates had one common gating system.

The foundry mould was prepared from the quick-hardening moulding sand and was provided with Pt/PtRh10 thermocouples in quartz sleeves of 0.16 cm diameter for plates of

the thickness 0.6 and 1 cm, and 0.3 cm for plates of other thickness values. The terminals of the thermocouples (Pt-Pt10Rh) were placed in the geometrical centre of each mould cavity, perpendicular to the heat transfer direction to improve the reliability of measurements. Additionally, samples were cast for analysis of the chemical composition that enabled calculation of the equilibrium temperature of eutectic transformation which according to the stable Fe-C-Si-P equilibrium diagram [22]

$$T_e = 1154 + 5.22Si - 14.88P; \quad (55)$$

TABLE 1

Type of metalurgical treatment, consumption and type of spheroidizator and inoculants

No. of sample	Type of metallurgical treatment	Consumption, % type of spheroidizator	Consumption, % type of inoculants
1	Cast iron poured into mould after 4 minutes from inoculation (in ladle)	0.91; K102	0.28; Zircinoc
2	Double inoculation (in ladle and in pouring basin)	0.83; K102	0.86; Zircinoc +0.5; RZM55AV
3	Inoculation under down-gate	1; INJECTALLOY	0.28; Foundrysil
4	Double inoculation (in ladle and in pouring basin)	0.87; K102	0.87; Zircinoc +0.3; RZM55AV
5	Inoculation in pouring basin	1.08; INJECTALLOY	0.65; Zircinoc
6	Inoculation in pouring basin	0.94; INJECTALLOY	1; FeSi75
7	Inoculation in pouring basin	0.8; PEM	0.55; RZM55AV

Chemical composition is presented in table 2.

TABLE 2

Results of chemical composition

No. of heat	Chemical composition, [% wt.]					
	C	P	S	Si	Mn	Mg
1	3.62	0.02	0.02	2.68	0.51	0.05
2	3.84	0.03	0.01	2.30	0.28	0.05
3	3.73	0.01	0.02	2.57	0.43	0.04
4	3.62	0.01	0.02	2.65	0.44	0.03
5	3.71	0.02	0.01	2.77	0.44	0.04
6	3.75	0.03	0.01	2.77	0.42	0.03
7	3.61	0.02	0.01	2.67	0.51	0.04
Mean value	3.70	0.02	0.01	2.63	0.04	0.04

The maximum undercooling in the individual plates was determined in the following way:

$$\Delta T_m = T_e - T_m \tag{56}$$

After cooling of castings, from their geometrical centres the specimens for metallographic examinations were taken. An example of structures of heat no. 6 is presented on figures 5.

Photos were made by means of scanning electron microscope (Jeol 5500 LV) with magnification of 50 x. Using scanning electron microscope it can be possible to distinguish graphite from impurities, which would have deformed final experiment results. Planar microstructure is characterised by the grain density (N_A), which gives the average number of grains per unit area. The N_A parameter has been determined by means of the automatic quantitative analyser (Leica Qwin). Planar grain density were recalculated into volumetric grain density by means of Owadano equation [23]:

$$N = \sqrt{\frac{\pi}{6g_{gr}}}(1.2N_A)^{3/2}; \tag{57}$$

Results of experiment are shown in table 3.

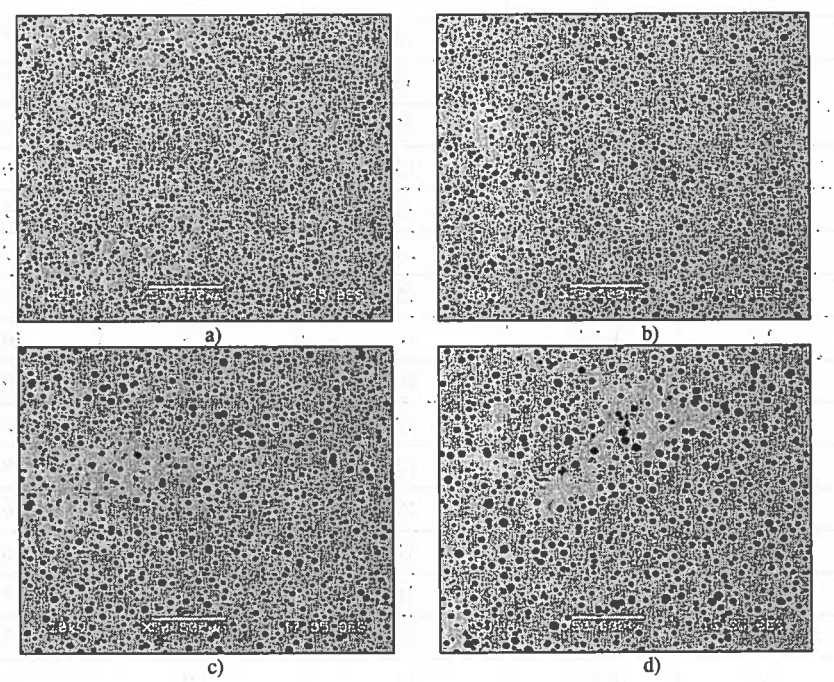

Fig. 5. Structure of nodular cast iron form heat no. 6 in plates thickness of 0.6 cm, a) 1.0 cm, b) 1.6 cm, c) and 2.2 cm, d), respectively

TABLE 3

Results of experiments and numerical calculations

No. of heat	Thickness of plates cm	Modulus cm	Maximum undercooling, ΔT_m	Grain density, N	
				Experiment, $cm^{-3} \times 10^6$	Calculated base on eq. (54) $cm^{-3} \times 10^6$
1	0.6	0.268	45	13.3	13.22
	1.0	0.417	36	5.5	5.84
	1.6	0.606	21	3.3	6.34
	2.2	0.837	18	3.2	3.37
2	0.6	0.268	36	19.7	19.73
	1.0	0.417	31	8.5	7.33
	1.6	0.606	22	5.7	5.11
	2.2	0.837	12	4.8	7.19
3	0.6	0.268	49	17.8	10.13
	1.0	0.417	34	10.1	6.18
	1.6	0.606	26	4.5	3.67
	2.2	0.837	20	4.3	2.48
4	0.6	0.268	43	16.7	14.79
	1.0	0.417	33	10.1	7.17
	1.6	0.606	21	4.7	6.40
	2.2	0.837	13	3.9	6.89
5	0.6	0.268	35	24.1	21.47
	1.0	0.417	24	16.0	13.22
	1.6	0.606	15	12.0	12.01
	2.2	0.837	10	5.5	10.82
6	0.6	0.268	30	27.8	29.43
	1.0	0.417	22	18.6	15.52
	1.6	0.606	12	12.9	18.74
	2.2	0.837	10	5.1	10.47
7	0.6	0.268	41	18.5	16.51
	1.0	0.417	31	9.9	8.26
	1.6	0.606	19	5.8	7.98
	2.2	0.837	16	3.9	4.41

4. Calculations

In order to calculate graphite eutectic grain density, according to equation (54) it was assumed typical date from table 4. Results of calculation are shows in Fig. 6, and in table 3.

TABLE 4

Results of the experiment

Parameter	Value	unit
Latent heat of graphite eutectic [19]	$L_e = 1825.8$	Jcm^{-3}
Latent heat of graphite [8]	$L_g = 3559.7$	Jcm^{-3}
Specific heat of metal [8]	$c_V = 5.95$	$Jcm^{-3}°C^{-1}$
Coefficient of heat accumulation by the material of the mould	$b = 0.12$	$Jcm^{-2}s^{-1/2}°C^{-1}$
Diffucion coefficient of the carbon in austenite *	$D = 3 \times 10^{-6}$	$cm^2 s^{-1}$
Initial temperature of metal in mould cavity **	$T_i = 1280$	°C
Mould initial temperature	$T_b = 20$	°C
Directional coefficient	$a = 0.0033$	$°C^{-1}$
Liquidns temperature	$T_l = \frac{C + 0.31\,Si + 0.33\,P - 1.3}{2.57 \cdot 10^{-3}}$	°C
Volume fraction of pro-eutectic graphite	$f_p = \frac{(C - C_e)\rho_e}{(C - C_e)\rho_e + \rho_{gr}(C_{gr} - C)}$	0
Carbon content in eutectic	$C_e = 4.26 - 0.30\,Si - 0.36\,P$	% wt.
Density of eutectic	$\rho_e = 0.926 \times \rho_\gamma + 0.074 \times \rho_{gr}$	$g\ cm^{-3}$
Density of austenite	$\rho_\gamma = 7.3$	$g\ cm^{-3}$
Density of graphite	$\rho_{gr} = 2.22$	$g\ cm^{-3}$
ΔT_p	2632	°C
Volume fraction of graphite in eutectic ***	$g_{gr} = 0.1$	–

Remark: * For D literature show a range of $8.62 \times 10^{-7} \div 1 \times 10^{-5}$ [24, 25], 3×10^{-6} was used for the calculations.
** Mean value was used from cooling curves for the calculations.
*** Mean value was used from metallographic examinations for the calculations.

Solid line on figure 6 has been calculated for cast iron with averaging chemical composition. In equation (54) the essential parameter, which decided on casting cooling rate is its modulus (M). At constant casting modulus as nuclei density (grain density) increases maximum undercooling decreases as shows result based on equation (54). Figure 6 shows result which concern cast iron with different physicochemical state (different:

spheroidization and modification treatment, time after modification, chemical composition). From figure it follows that results of calculations and experimental measurements good tally.

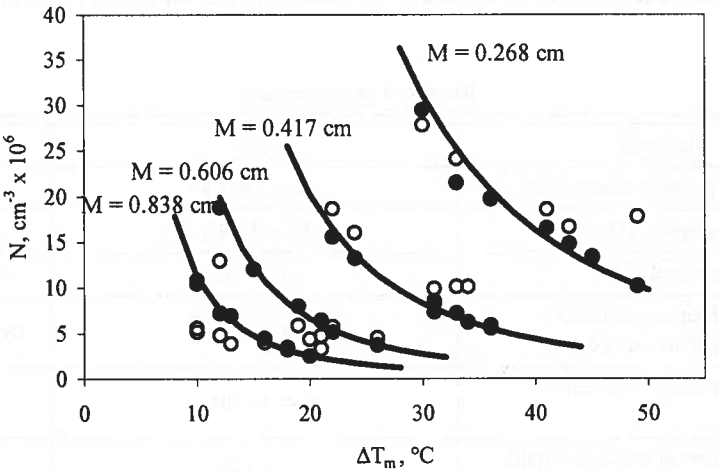

Fig. 6. Eutectic grain density as a function of maximum undercooling and modulus:
o – experimental results
• – results based on eq. (54),
▬ – results based on eq. (54) for averaging chemical composition.

5. Conclusion

1. Heat and mass balance equations were used in considering the nucleation and growth of nodular eutectic grains during the solidification of nodular cast iron.
2. An analytical solution is found that allows predict density of eutectic grain as a function of maximum degree of undercooling. The analytical solution requires only a knowledge of the parameters of metal and mould.
3. The predictions of proposed analytical model are rather in good agreement with experimental measurements of nodular eutectic grain density.

Acknowledgment

The work has been carried out within the framework of statutory research no. 11.11.170.102.

REFERENCES

[1] D. K. Banerjee, D. M. Stefanescu, Structural Transformations and Solidification Kinetics of SG Cast Iron During directional Solidification Experiments. Transactions of the American Foundryman Society **99**, 747-759 (1991).

[2] E. Fraś, Krystalizacja żeliwa. Skrypt AGH, Kraków, 1976.
[3] E. Guzik, Cz. Podrzucki, Nowoczesne metody obróbki uszlachetniającej ciekłego żeliwa. III Seminarium nt. „Prognozy rozwoju odlewnictwa w Polsce na tle tendencji światowych". s. 10.1 Szczyrk, 1996.
[4] G. Lesoult, M. Castro, J. Lacaze, Solidification of Spheroidal Graphite Cast Iron: III Microsegregation related effects. Acta Materialia **47**, 3779-3792 (1999).
[5] M. N. Achmadabadi, E. Niyama, T. Ohide, Structural control of 1% Mn ADI aided by modeling of microsegregation. Transactions of the American Foundrymans Society **97**, 269-278 (1994).
[6] H. Bayati, R. Elliot, A stepped austempering heat treatment for a Mn alloyed ductile cast iron. In: Physical Metallurgy of Cast Iron V. Editors: G. Lesoult and J. Lacaze, Scitec Publication, 399-406, Switzerland (1997).
[7] J. Lacaze, Solidification of Spheroidal Graphite Cast Iron: III. Microsegregation related effects. Acta Materialia **47**, 3779-3792 (1999).
[8] E. Fraś, H. F. Lopez, A theoretical analysis of the chilling susceptibility of hypoeutectic Fe-C alloys, Acta Metalurgica and Materialia **41**, 12, 3575-3583 (1993).
[9] E. Fraś, H. Lopez, Generation of International Pressure During Solidification of Eutectic Cast Iron. Transactions of the American Foundryman Society **102**, 597-601 (1994).
[10] E. Fraś, C. Podrzucki, Żeliwo modyfikowane. Skrypt AGH, wyd. II, Kraków, 1981.
[11] D. Venugopalan, A Kinetic Model of the $\gamma \rightarrow \alpha$ + Gr Eutectoid Transformation in Spheroidal Graphite Cast Iron. Metallurgical and Materials Transactions **21 A**, 913-918 (1990).
[12] D. Turnbull, J. C. Fisher, w: Journal of Chemical Physics **17** (1949).
[13] D. Turnbull, Principals of solidification. Thermodynamics in Physical Metallurgy, American Society for Metals, Cleveland, 1950.
[14] B. Chalmers, Principles of Solidification. New York, John Wiley, 1964.
[15] G. Daves, Solidification and Casting. Applied Science Publishers Ltd. London, 1973.
[16] J. Frayley, W. Childs, Transactions of the Metallurgical Society of AIME **242**, 256 (1969).
[17] W. Oldfield, Quantitative Approach to Casting Solidification. Frazing of Cast Iron., ASM **59**, 945-961 (1966).
[18] D. M. Stefanescu, G. Upadhya, D. Bandyopadhyay, Heat transfer-solidification kinetics modeling of solidification of casting, Metallurgical Transactions A **21 A**, 997-1005 (1990).
[19] E. Fraś, H. F. Lopez, A theoretical and Experimental Study of the Dependence Between Undercooling and Nodular Eutectic Grains Density. Archives of Metallurgy. PWN Kraków **43**, 227-240 (1999).
[20] W. Longa, Krzepnięcie odlewów. Wyd. Śląsk, Katowice, 1985.
[21] W. Longa, General theoretical background of the differential analysis of the casting cooling curves (in Polish). Arch. Metall. **28**, 281 (1983).
[22] B. Lux, W. Kurz, Solidification of Metals, The Iron and Steel Institute, London **110**, 193 (1967).
[23] C. Charbon, M. Rappaz, 3D Stochastic Modeling of Nodular Cast Iron Solidification. Physical Metallurgy of Cast Iron V, Ed. Lesoult G., Lacaze J., Scitec Publication 453-460, Nancy (1994).
[24] W. Kurz, D. J. Fisher, Fundamentals of Solidification. Trans., Tech., Aedermannsdorf, Switzerland, 1986.
[25] Smitells, Metals Reference Books, 6-th edition. London, 1983.

REVIEWED BY: WALDEMAR WOŁCZYŃSKI
Received: 20 December 2003.

A R C H I V E S O F M E T A L L U R G Y A N D M A T E R I A L S
Volume 49 2004 Issue 1

EDWARD FRAŚ*, ANDRZEJ JANAS*, PAWEŁ KURTYKA**,
STANISŁAW WIERZBIŃSKI**

STRUCTURE AND PROPERTIES OF CAST Ni3Al/TiC AND Ni3Al/TiB2 COMPOSITES

PART II. INVESTIGATION OF MECHANICAL AND TRIBOLOGICAL PROPERTIES AND OF CORROSION RESISTANCE OF COMPOSITES BASED ON INTERMETALLIC PHASE Ni_3Al REINFORCED WITH PARTICLES OF TiC AND TiB_2

STRUKTURA I WŁAŚCIWOŚCI KOMPOZYTÓW ODLEWANYCH Ni3Al/TiC ORAZ Ni3Al/TiB2

CZĘŚĆ II. OCENA WŁAŚCIWOŚCI MECHANICZNYCH, TRYBOLOGICZNYCH I ODPORNOŚCI NA KOROZJĘ KOMPOZYTÓW NA OSNOWIE FAZY MIĘDZYMETALICZNEJ Ni_3Al WZMACNIANYCH CZĄSTKAMI TiC i TiB_2

The study gives the results of mechanical tests carried out to determine the characteristics of high-temperature strain response (σ-ε) of composites "in situ" based on intermetallic phase Ni_3Al reinforced with particles of TiC and TiB_2, the volume content of which is 5 and 10%. Basing on these results, the temperature ranges and strain rates were established within which the composites undergo plastic deformation; some selected mechanical properties of composites at high temperatures were determined as well. Tribological tests were conducted on Miller apparatus, evaluating the effect of abrasion time on a relative loss of matrix weight, on overall composite loss of weight, and on change of abrasion wear rate. In a similar way, also the resistance of the investigated composites to electrochemical and gas-induced corrosion was determined.

W pracy przedstawiono wyniki analizy charakterystyk mechanicznych wysokotemperaturowego odkształcania (σ–ε) kompozyów "in situ" na osnowie fazy międzymetalicznej Ni_3Al wzmacnianej cząsteczkami TiC oraz TiB_2, których udział objętościowy wynosił 5 oraz 10%.

Na podstawie wyników badań ustalono zakresy temperatur i prędkości odkształcenia, w których istnieje możliwość plastycznego kształtowania kompozytów, a także określono wybrane własności wytrzymałościowe kopozytu w podwyższonych temperaturach. Przeprowadzono próby trybologiczne na aparaturze Millera oceniając wpływ czasu ścierania na względny ubytek masy osnowy i kompozytów, a także na zmianę prędkości ścierania.

Analizowano również odporność badanych kompozytów na korozję elektrochemiczną oraz gazową.

1. Introduction

The systematically extending range of the available engineering materials, this including also composites, makes us think of their rational selection, based on multi-

* WYDZIAŁ ODLEWNICTWA, AKADEMIA GÓRNICZO-HUTNICZA, 30-059 KRAKÓW, UL. REYMONTA 27
** WYDZIAŁ MATEMATYCZNO-FIZYCZNO-TECHNICZNY, AKADEMIA PEDAGOGICZNA, 30-084 KRAKÓW, UL. PODCHORĄŻYCH 2

criterial optimisation, supported by the methods of computer-aided design (CAD-), computer-aided manufacturing (CAM-), and computer-aided materials selection (CAMS-). Complex use of the above mentioned programmes requires constant updating of our knowledge on the mechanical, tribological and structural properties of composites, determined for a possibly wide range of temperatures.

Mechanical properties of material reflect its response to loading or strain, which is either constant or changing in time, and the time itself can vary from a fraction of second (impact resistance test) up to several years (creep resistance test). As revealed by numerous research studies, composite materials can be loaded and/or shaped over a wide range of temperatures and at different strain rates in the medium of air, gas, or liquid. The response of material to loading is expressed by its strain, which successively assumes the form of elastic strain, plastic strain, and finally a rupture [1].

By now, numerous methods of investigating the mechanical properties have been developed; they enable simulation of loading conditions to which parts of machines and constructions are exposed in service. The results of the tests which enable these properties to be determined are usually applied in practice when parts of constructions are designed, mainly in a comparative analysis of true stresses and stresses calculated from theoretical relationships (models).

Testing of mechanical properties includes technological properties determining the applicability of material in certain types of treatment, and mechanical properties which, to be determined, require prior knowledge of the values of force or of the moment of force, usually considered one of the basic parameters. Thinking of the performance conditions under which the parts of constructions will be operating later, these properties are determined under the following test conditions: static loads (increasing slowly), dynamic loads (increasing rapidly), fatigue response (cycling loading), and creep behaviour tested in creep resistance test (long-term creep, constant load or stress). Here it should be noted that material properties determined by various mechanical tests (tensile, compression, torsion, bending, impact, creep and hardness) are not physical properties, as they depend entirely on the adopted test conditions (shape and dimensions of specimens, rigidity of the testing machine, and rate of load variations) [2].

This study presents some selected results of investigation of the mechanical properties carried out on an intermetallic phase of Ni_3Al and on Ni_3Al/TiC and Ni_3Al/TiB_2 composites "in situ" fabricated by the method of self-propagating high-temperature synthesis in bath (SHBS) in as-cast state. In final analysis of the problem, using the results obtained in compression and tensile tests conducted over a wide range of temperatures and strain rates, the stress-strain curves were plotted and described by *Hollomon and Ludwigson equations*. The results of tribological tests were also presented along with the results obtained in testing of corrosion resistance to the effect of chemical agents and gases.

2. Results and discussion

2.1. Investigation of mechanical properties of NiAlB matrix alloy and of Ni_3Al/TiC and Ni_3Al/TiB_2 composites

The mechanical properties of Ni_3Al/TiC and Ni_3Al/TiB_2 composites were investigated using the results of tangential uniaxial compression and tensile tests, applying constant

temperature (293, 1073 and 1273 K) and travel rate of traverse (0,2 cm/min.). The specimen dimensions used in the tests were ϕ 6 mm, h 9 mm ϕ or the compression test, and ϕ 5 mm, l_o 25 mm for the tensile test.

The initial strain rates computed from relationship $\dot{\varepsilon} = 1/l_0 * dl/dt$ assumed the values of $3{,}7*10^{-3}s^{-1}$ (compression specimens) and $1{,}3*10^{-3}s^{-1}$ (tensile specimens). The static compression and tensile tests were carried out on an INSTRON testing machine provided with computer control, with data recording system (measurement of Δl and P), and a furnace with protective argon atmosphere controlled by OMEGA CN 76000 microprocessor, ensuring the accuracy of temperature measurement in a furnace working zone of ±1 °C.

The investigation also covered an intermetallic compound Ni_3Al with various additions of boron used as a matrix alloy, as well as two composites, i.e. Ni_3Al/TiC and Ni_3Al/TiB_2, containing 5 and 10 vol.% of the reinforcing phase in the form of TiC and TiB_2, respectively.

The analysis of stress-strain curves plotted in a double logarithmic system ($\log\sigma$-$\log\varepsilon$) revealed, both in compression and tensile tests, the occurrence of two ranges of the strain hardening, and therefore in further interpretation of the data it was decided to apply the well-known functions developed by Hollomon (functions 1 and 2) [3] and by Ludwigson (functions 3, 4, 5) [4] in the form of:

$$\sigma = K_1\varepsilon^{n1} \text{ (first range of strain hardening)} \tag{1}$$

$$\sigma = K_2\varepsilon^{n2} \text{ (second range of strain hardening)} \tag{2}$$

where: K_1 and K_2 – strength coefficients, n_1 and n_2 – strain hardening coefficients in the range of low and high deformations, respectively.

$$\sigma = K_1\varepsilon^{n1} \pm \Delta \tag{3}$$

$$\Delta = \varepsilon^{(K2+n2\varepsilon)} \tag{4}$$

$$\sigma = K_1e^{n1} \pm e^{K2}*e^{n2\varepsilon} \text{ (complete curve of strain hardening)} \tag{5}$$

where: K_1 and K_2 – strength coefficients, n_1 and n_2 – strain hardening coefficients in the range of low and high deformations, respectively [4-8].

In further part of analysis, comparing the values of the yield stress σ at different levels of strain ε, the increments of the yield stress were determined for various composites in respect of their matrix, using relationship:

$$\left(\frac{\sigma_k}{\sigma_0 - 1}\right)_{\varepsilon = const} \cdot 100\% \tag{6}$$

where: σ_k and σ_o – values of the yield stress at different strain levels determined for composite and matrix, respectively.

Figure 1 shows the mechanical strain response characteristics obtained in uniaxial compression test carried out on NiAlB matrix alloys with various boron contents : a) change of yield stress σ in function of strain ε and boron content, b) change of proof stress R_{02} and shortening A in function of boron content. The values of temperature and strain rates are given in the drawing.

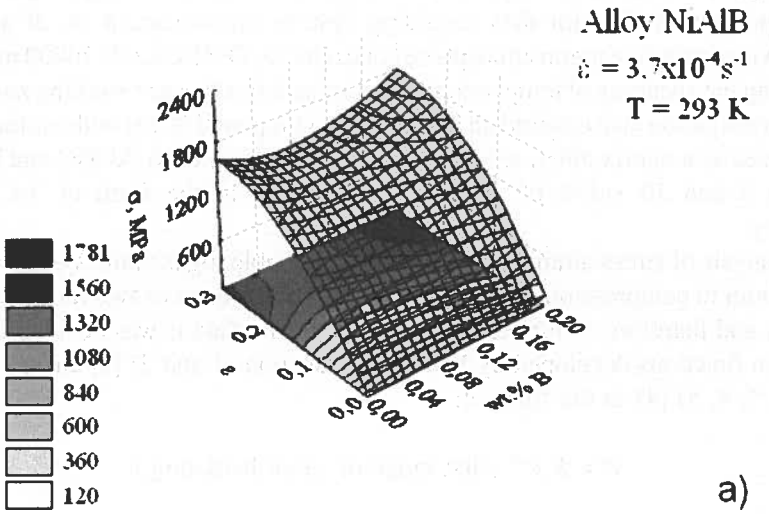

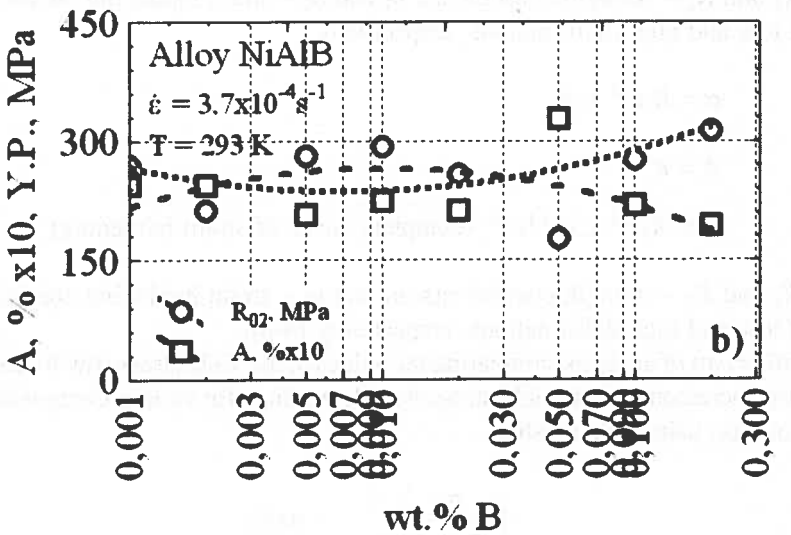

Fig. 1. Mechanical characteristics of NiAlB alloy strain response: a) yield stress σ vs strain ε and boron content, b) proof stress R_{02} and shortening A vs. boron content. The values of temperature and compression rates are given in the drawing

In an analogical system, Figure 2 shows the mechanical strain response characteristics obtained in uniaxial tensile test carried out on NiAlB matrix alloys with various boron contents: a) change of yield stress σ in function of strain ε and boron content, b) change of proof stress R_{02} and elongation A in function of boron content. The values of temperature and strain rates are given in the drawing.

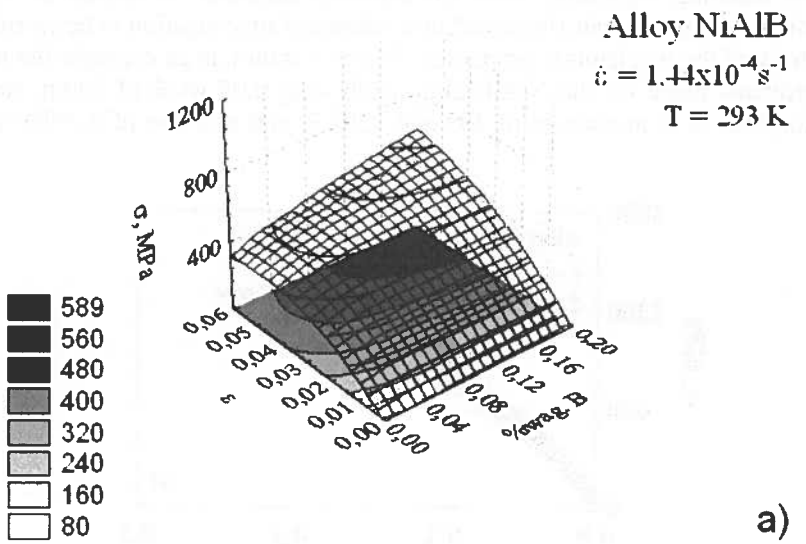

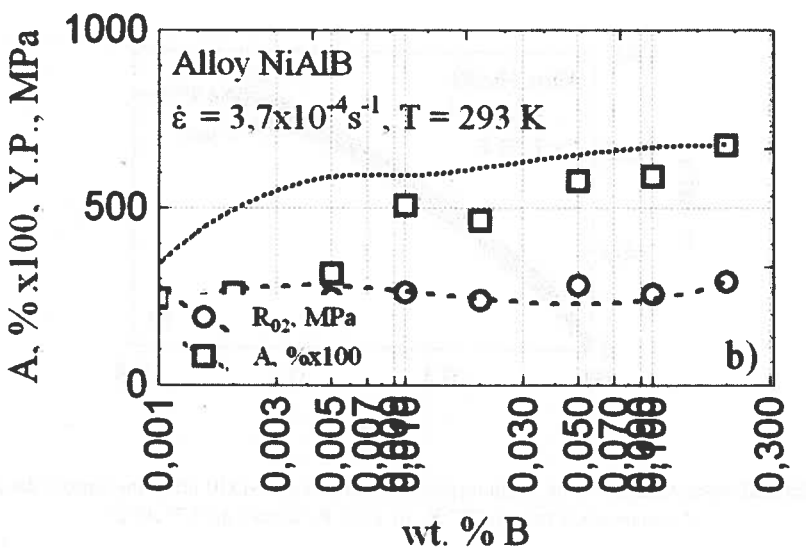

Fig. 2. Mechanical charakteristics of NiAlB alloy strain response: a) yield stress σ vs strain ε and boron content, b) proof stress R_{02} and elongation A vs. boron content. The values of temperature and tension rates are given in the drawing

An analysis of the mechanical strain response characteristics of the NiAlB alloys has revealed that with boron content increasing up to 0-0.05 wt.%, the range of alloy yielding in compression test tends to be gradually extended, but with this value exceded, the formation of structural discontinuities and consequently a drop of deformability are observed.

Parts of machines operating under the effect of different, in respect of value and direction of application, forces (loads) require additional investigation to be carried out on the anisotropy of the mechanical properties. Figure 3 shows as an example the results of such experiments made for the NiAlB alloy containing 0,05 wt.% of boron, strained in compression tests at temperatures of 293 and 1223 K and at a rate of $3{,}7*10^{-4}s^{-1}$.

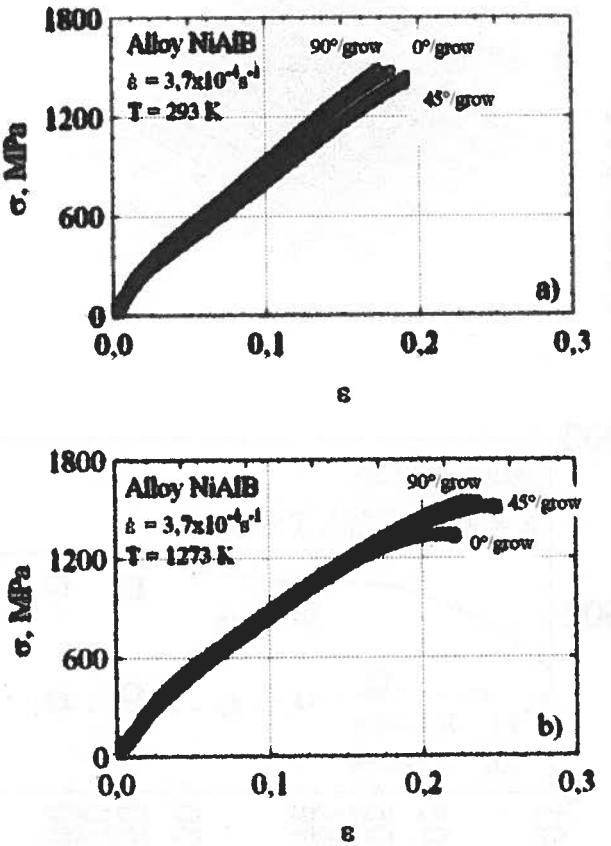

Fig. 3. Mechanical characteristics of the strain response of anisotropic NiAlB alloy specimens; the temperature of compression test: a) 293 K, b) 1223 K, strain rate $3{,}7*10^{-4}s^{-1}$

In the case of specimens tested at high temperatures (1223 K), the anisotropy of the values of the ratio : yield stress σ – to- strain $\varepsilon = 0{,}16$ is quite insignificant, which proves that the matrix alloy is characterised by properties close to the isotropic ones.

Adopting finally for the matrix an Ni_3Al + 0,05 wt.% B alloy, a series of composites b"in situ" reinforced with TiC and TiB_2 particles were made. The compositions and designations of both matrix and composite are given in Table 1.

TABLE 1

Compositions and designations of matrix and composite

Designation of matrix/composite	Composition of matrix/composite
A	Ni_3Al + 0.05B
B	Ni_3Al + 0.05B + 5% TiC
C	Ni_3Al + 0.05B + 10% TiC
D	Ni_3Al + 0.05B + 5% TiB_2
E	Ni_3Al + 0.05B + 10% TiB_2

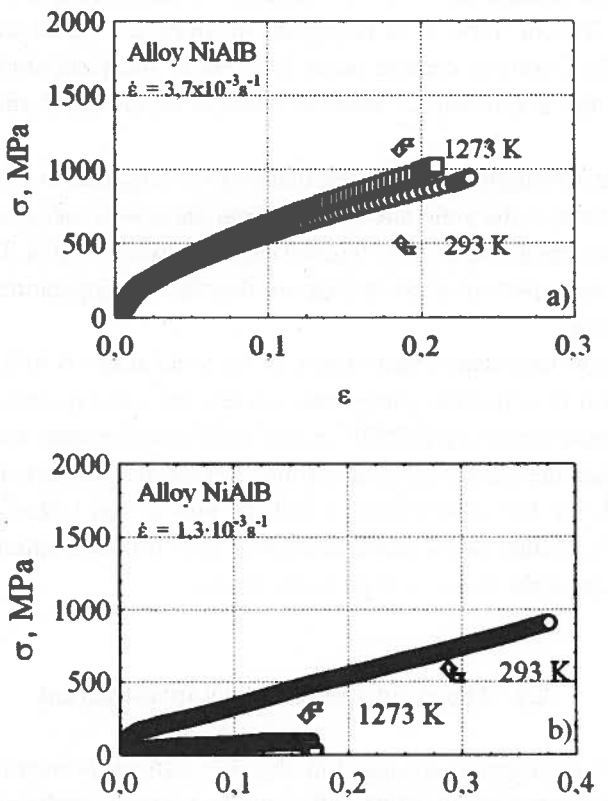

Fig. 4. Strain hardening curves plotted for NiAlB matrix alloy subjected to: a) compression test, b) tensile test, conducted at temperatures of 293 and 1273 K. The values of strain raters are given in the drawing

Figure 4 shows the strain hardening curves plotted in a system of $\sigma = f(\varepsilon)$ for specimens of NiAlB alloy subjected to a) compression test and b) tensile test carried out

at temperatures of 293 and 1273 K, while Figure 5 shows these curves plotted in a system of $\log\sigma = \log(\varepsilon)$ together with the individual strain hardening ranges described by Hollomon equations. The strain hardening curves plotted for both matrix alloy and composite have two ranges; in the second range lower values of the hardening exponent n are observed. In an analogical system, the investigation was made for composites B (Figs.6 and 7), C (Figs.8 and 9), D (Figs.10 and 11) and E (Fig.12). Additionally, for composite B the ranges of strain hardening described by Ludwigson equation were presented (Fig.13), and points obtained experimentally and computed theoretically were compared for their consistency.

The synthesis of results are the strain hardening curves plotted in Figures 14 and 15, which show the course of relationship $\sigma - \varepsilon$ plotted for alloys and composites (excluding composite E) subjected to compression test (Fig.14) and tensile test (Fig.15) carried out at temperatures of 293 and 1273 K.

To evaluate the effectiveness of the process of reinforcing the composite matrix with particles of TiC or TiB_2, it is important to know the effect exerted by the type of particles and their volume content on an increase of the yield stress. This evaluation is possible using the coefficient of relative increase of the yield stress determined by equation (6).

The conducted investigation has proved that in both compression and tensile tests (Figs. 15 and 16, respectively), the yield stress raises from the lowest values obtained for matrix alloy to the highest values obtained for Ni_3Al/TiB_2 composite (5 vol.% TiB_2). The sequence of increments in the values of stress σ does not depend on temperature at which the tests have been conducted.

In a similar way, the relative increments in the yield stress σ follow the sequence of composite B, C and D. Since the composites possess the same matrix and, moreover, are fabricated by the same technique (SHSB "in situ") and have the same volume content of the reinforcing particles, the increase in stress is mainly caused by different values of Young's modulus E, which for TiC is 379 GNm^{-2}, and for TiB_2 is 500 GNm^{-2} [9].

Quite a specific feature of the examined composites is their limited deformability and higher values of the yield stress at high temperatures.

2.2. The results of tribology investigation

The tribology investigation consisted in abrasion tests performed on Miller apparatus equipped with a V-shaped trough filled with water bearing SiC particles of dimensions 4-6 μm. A constant specific pressure exerted on the specimen was 0,07 MPa; the arm with the mounted specimen was driven by electric motor and made reciprocating movements at a frequency of 48 strokes per minute, with path length of one single stroke amounting to 0.2 m. For specimens of matrix (A) and composites (B, C, D, E) tests were performed in

four-hour cycles. Upon completing of each cycle, the specimens were rinsed and dried, and then the weight loss was measured in milligrams; the surface exposed to friction was examined under the light microscope and under the scanning electron microscope. Figure 17a shows the effect of friction time on relative loss of weight in both matrix (A) and composites (B, C, D, E), while Figure 17b shows the effect of abrasion time on changes in abrasion wear rate. The curves plotted and shown in these drawings confirm the role that the reinforcing phase plays in these processes.

The relative loss in weight $\Delta m/m$ in relation to the time of abrasion can be, with some approximation, described by function:

$$\frac{\Delta m}{m}(t) = at^b \tag{7}$$

where a and b are the constants which can be calculated from an analysis of regression and experimental data. For the described materials these relationships assume the following form:

$$\text{Matrix A: } \Delta m/m(t) = (0.0211365)t^{(0.6083907)};\ r=0.997 \tag{8}$$

$$\text{Composite B: } \Delta m/m(t) = (0.0120243)t^{(0.508599)};\ r=0.999 \tag{9}$$

$$\text{Composite C: } \Delta m/m(t) = (0.0093131)t^{(0.5766624)};\ r=0.997 \tag{10}$$

$$\text{Composite D: } \Delta m/m(t) = (0.0093556)t^{(0.7716874)};\ r=0.998 \tag{11}$$

$$\text{Composite E: } \Delta m/m(t) = (0.0038424)t^{(0.6835546)};\ r=0.999 \tag{12}$$

where : r – coefficient of regression

Changes in surface topography of the matrix and of some chosen composites subjected to abrasion tests were also examined (Fig. 18a-c)

An analysis of the surface reliefs on specimens subjected to a 16 hour abrasion test has proved that the depth of the reliefs on the specimens of matrix was relatively the smallest, because the matrix was characterised by the same hardness throughout the entire volume of the specimen, while it assumed the highest values in the specimens of Ni_3Al/TiC (10 vol.%TiC) composite, owing mainly to considerable differences between the hardness of the particles of the reinforcing phase and that of the matrix, similar as in the case of Ni_3Al/TiB_2 (10 vol.% TiB_2) composite specimens. Compared with other engineering materials, the abrasion wear resistance of the examined composites is much higher.

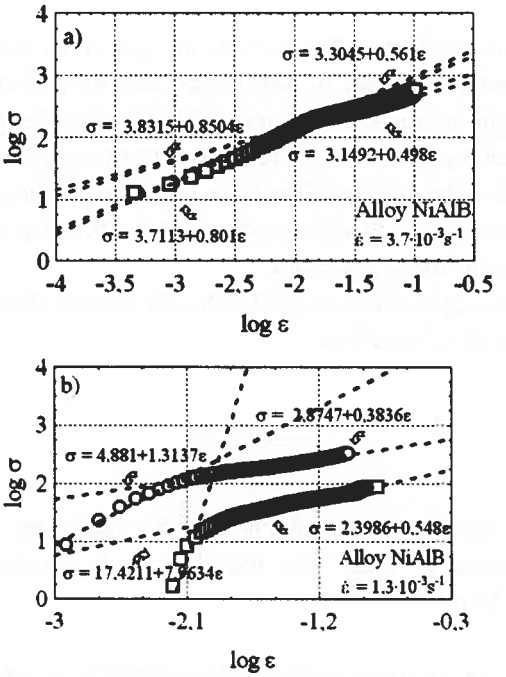

Fig. 5. Strain hardening curves plotted a system of log σ–logε NiAlB matrix alloy subjected to: a) compression test, b) tensile test. Hollomon equations were used to describe the individual ranges of strain hardening

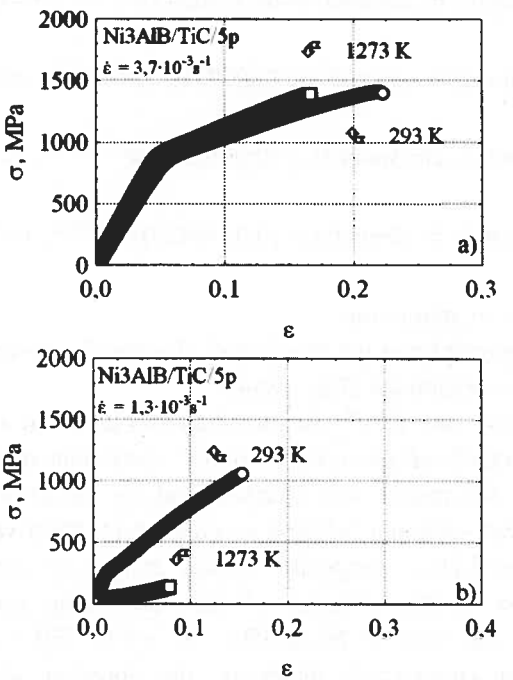

Fig. 6. Strain hardening curves plotted for Ni_3Al/TiC matrix alloy (5 vol% TiC) subjected to: a) compression test, b) tensile test. The values of temperature and strain rates are given in the drawing

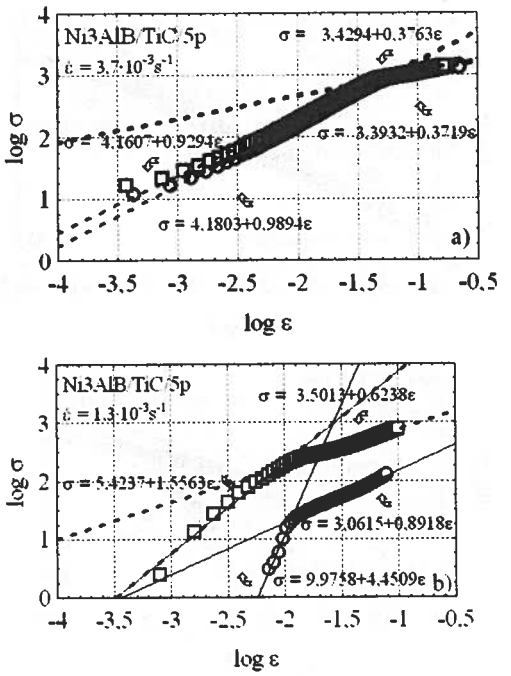

Fig. 7. Strain hardening curves plotted in a system of $\log\sigma - \log\varepsilon$ for composite B subjected to: a) compression test, b) tensile test. Hollomon equations were used to describe the individual ranges of strain hardening

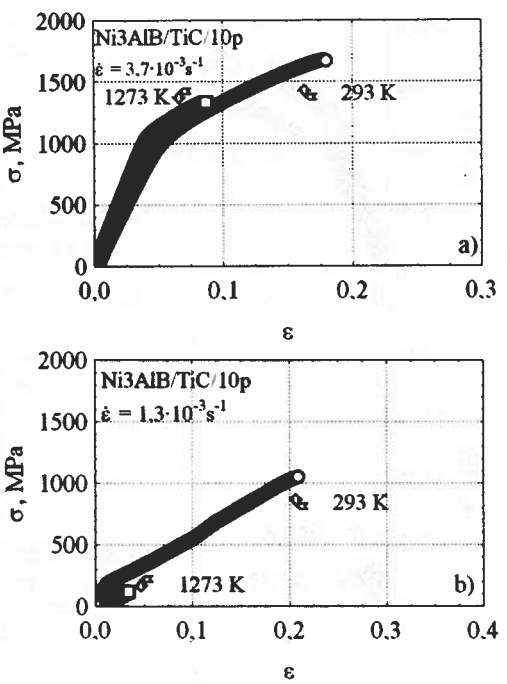

Fig. 8. Strain hardening curves plotted for Ni_3Al/TiC composite (10 vol% TiC) subjected to: a) compression test, b) tensile test. The values of temperature and strain rates are given in the drawing

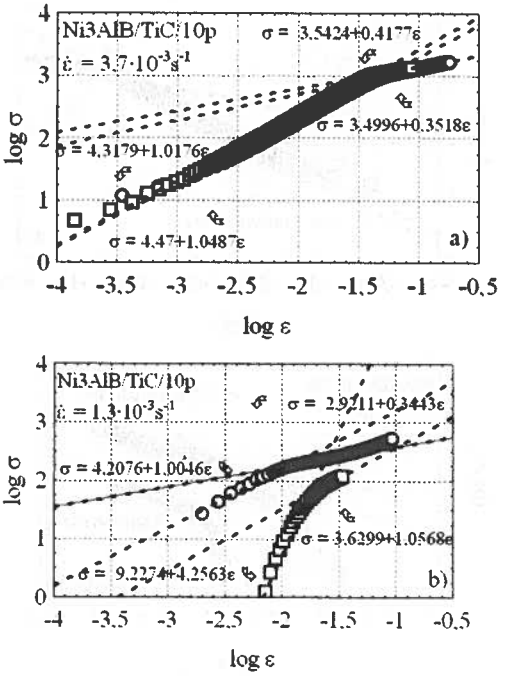

Fig. 9. Strain hardening curves plotted in a system of $\log\sigma - \log\varepsilon$ for composite C subjected to: a) compression test, b) tensile test. Hollomon equations were used to describe the individual ranges of strain hardening

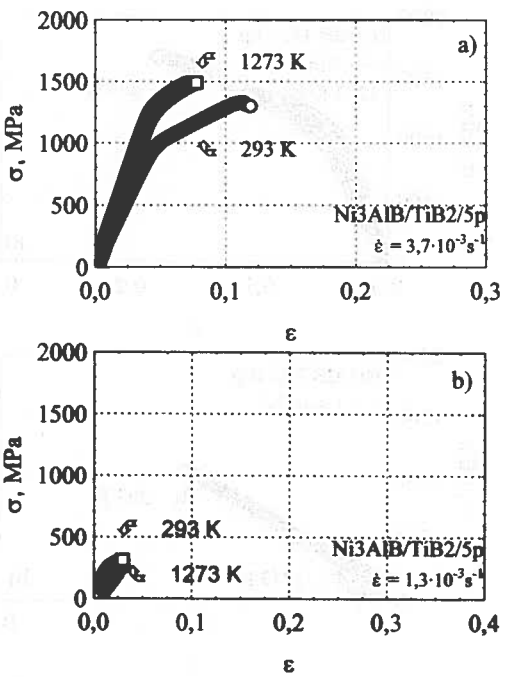

Fig. 10. Strain hardening curves plotted for Ni_3Al/TiB_2 composite (5 vol% TiB_2) subjected to: a) compression test, b) tensile test. The values of temperature and strain rates are given in the drawing

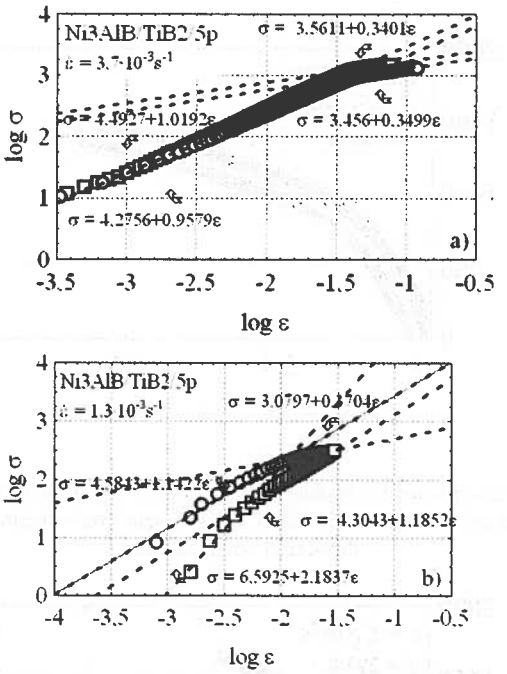

Fig. 11. Strain hardening curves plotted in a system of $\log\sigma - \log\varepsilon$ for composite D subjected to: a) compression test, b) tensile test. Hollomon equations were used to describe the individual ranges of strain hardening

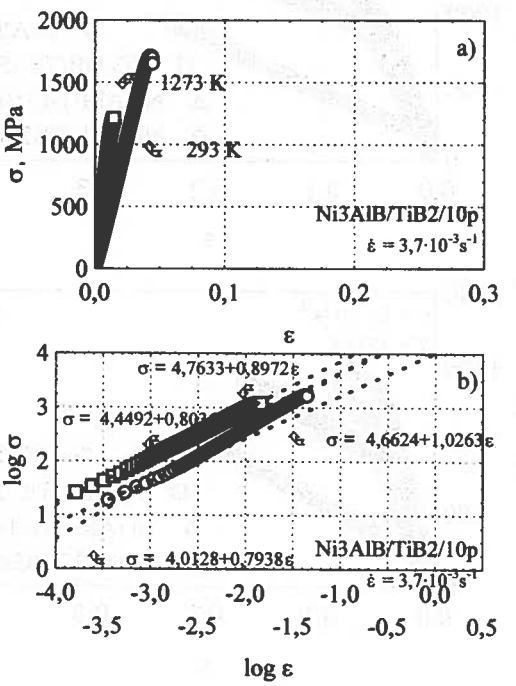

Fig. 12. Strain hardening curves plotted in a system of a) $\sigma - \varepsilon$, b) $\log\sigma - \log\varepsilon$ for composite E subjected to compression test. Hollomon equations were used to describe the individual ranges of strain hardening

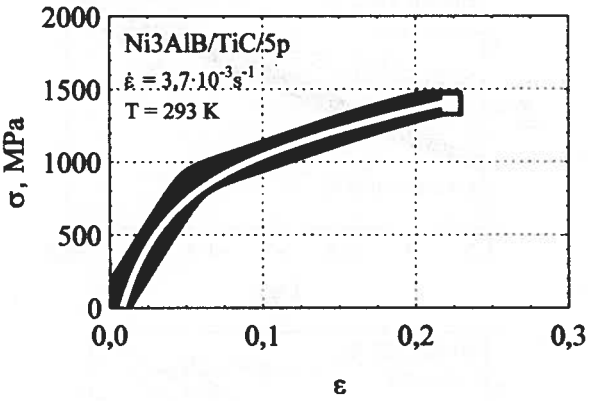

Fig. 13. Strain hardening curve plotted for Ni_3Al/TiC composite (5 vol.% TiC) subjected to compressions test described by Ludwigson equation (Equation 5). Black points – data from experiments, white line – data from theoretical computations

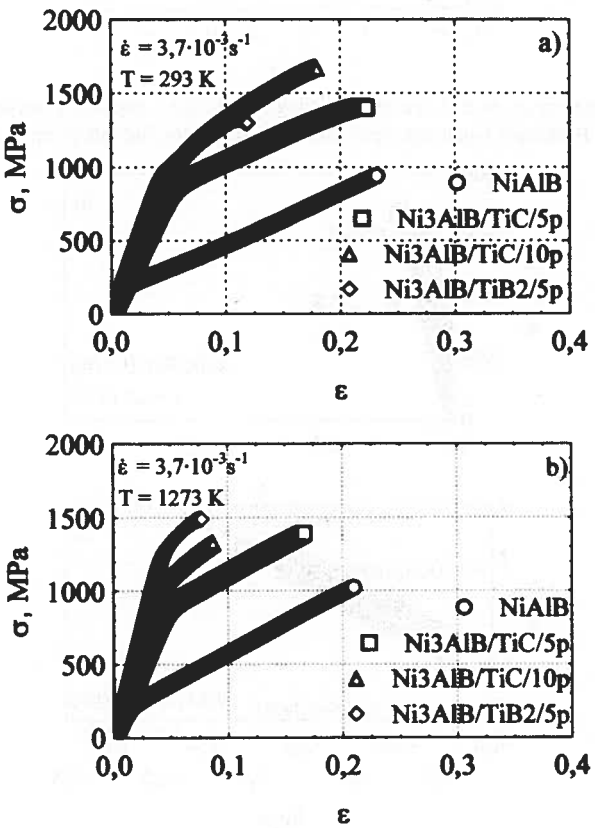

Fig. 14. Cumulative strain hardening curves plotted in a system of $\sigma - \varepsilon$ for specimens subjected to compression test at temperatures of: a) 293 K and b) 1273 K

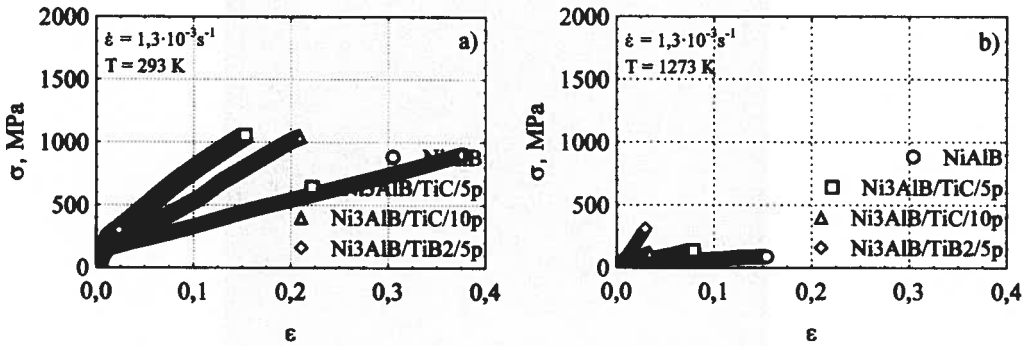

Fig. 15. Cumulative strain hardening curves plotted in a system of $\sigma - \varepsilon$ for specimens subjected to compression test at temperatures of: a) 293 K and b) 1273 K

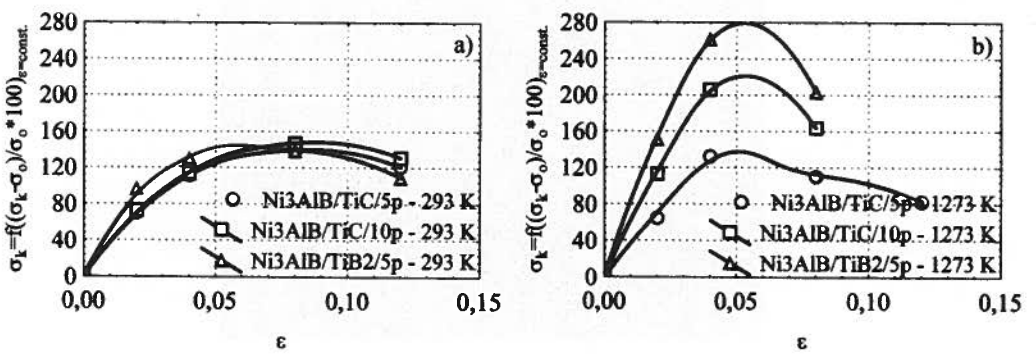

Fig. 16. Relative increase of the yield stress σ in composites B, C and D subjected to compression test at temperatures: a) 293 K and b) 1273 K

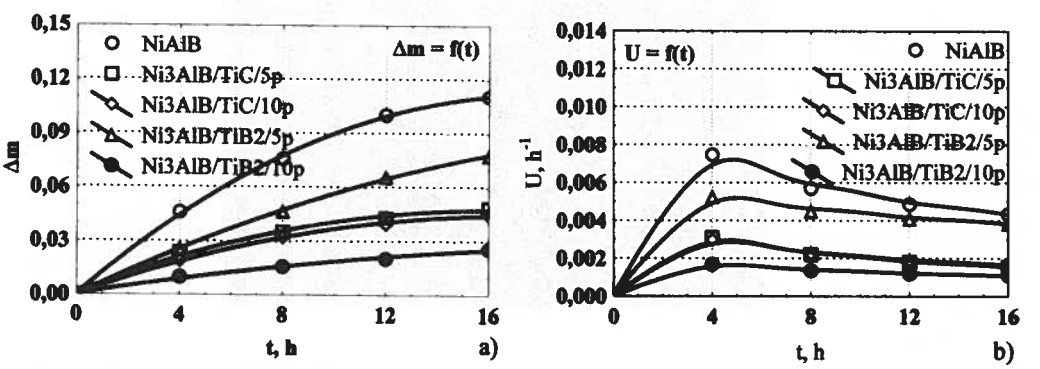

Fig. 17. Effect of time on: (a) weight loss, (b) abrasion wear rate

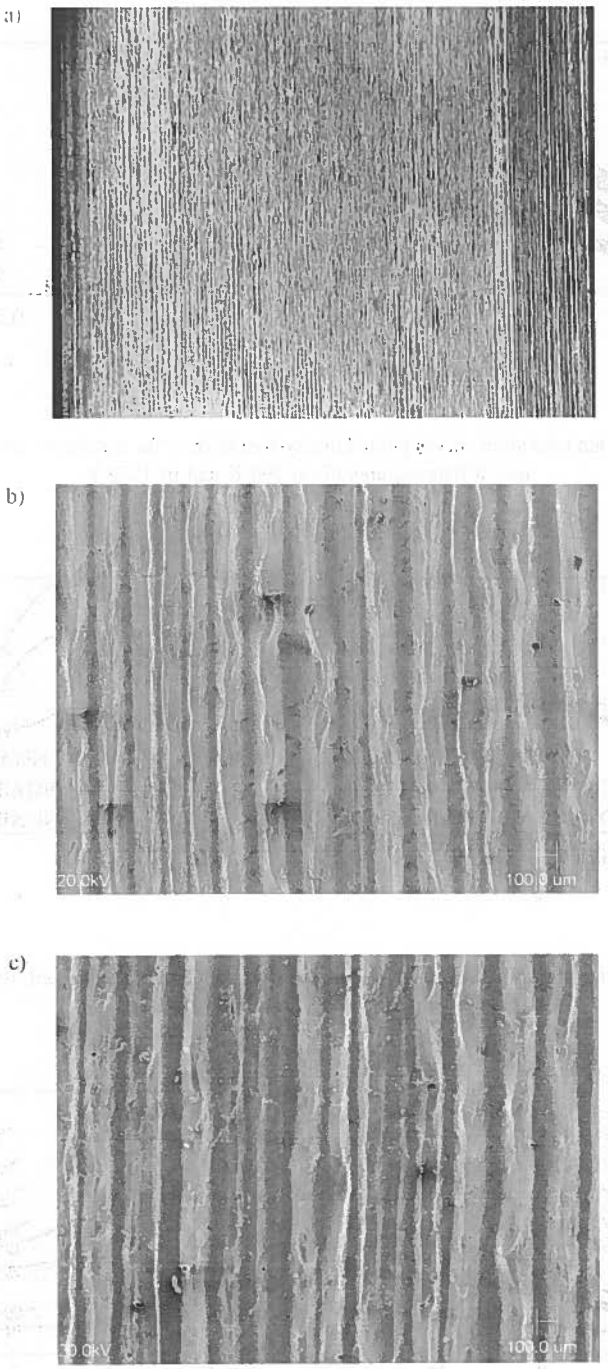

Fig. 18. Images of surface topography after abrasion tests a) Ni_3Al matrix, b) Ni_3Al/TiC composite (10 vol.% TiC) and c) Ni_3Al/TiB_2 composite (10 vol.% TiB, TiB_2)

2.3. Examination of the resistance to electrochemical corrosion

The resistance to chemical corrosion was compared for matrix alloy, which was an intermetallic phase Ni_3Al enriched with an addition of 0,05 wt.% B (sample A), for Ni_3Al/TiC composite (10 vol.% TiC – sample C) and for Ni_3Al/(TiB,TiB_2) composite (10 vol.% TiB,TiB_2 – sample E), using polarisation technique of LSV (linear sweep voltamperometry).

In the studies, an aqueous solution of sulphuric acid (0.1M H_2SO_4) deaerated with argon in a triple-electrode system was used. The reference electrode was chlorine-silver electrode Ag/AgCl, the counter electrode was platinum electrode, while the working electrode was the examined specimen A, C or E. The rate of potential changes during polarisation of the working electrode was 1, 3, 5, 10V/min.

Figure 19 shows reference curves plotted for matrix and composites (A, C, E), while Figure 20 shows polarisation curves plotted for samples A and C. The curves which describe samples A and C are characterised by a similar course; within the area of active digestion two peaks are noted to occur (the first at a potential of ~ -0.25V and the second at a potential of ~ -0.07V) as well as a passive area within the range of potentials from the peak to the transpassive region. Sample A before the peak of active digestion has got a small plateau. The shape of the polarisation curve for sample E (Fig.21) differs from the curve describing samples A and C.

Compared with sample C, sample A shows better corrosion resistance, which is proved by lower density of the current in anodic peak of digestion amounting to ~ 1.2 mA/cm^2, lower density of the current in passive area amounting to ~ 0.9 mA/cm^2, and shifting of transpassive potential towards higher values. The value of corrosion potential (Figs. 20 and 21) is for both samples ~ -0.4V, and it is lying within the area of active digestion in the case of sample C, w hile in the case of sample A it is found within the area of plateau before the peak of active digestion.

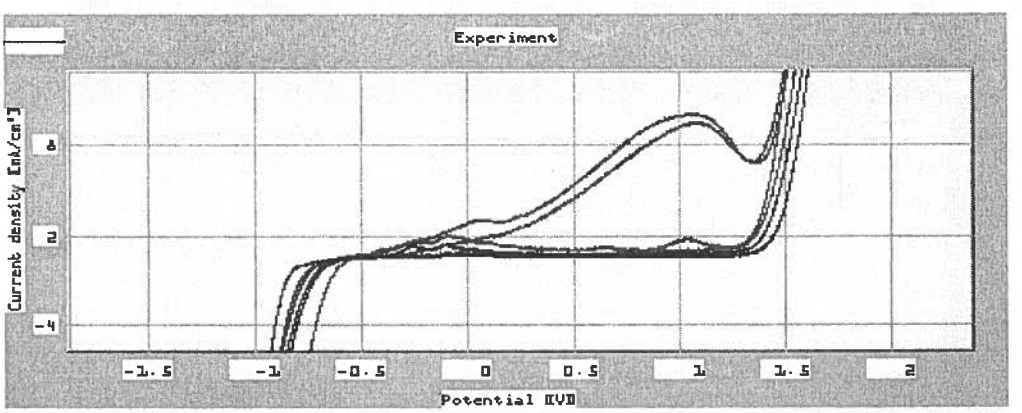

Fig. 19. A comparison of samples: 0.1M H_2SO_4 in H_2O v = 3V/min; red line – Ni_3Al/TiC (sample C), blue line – Ni_3Al (sample A) and green line – Ni_3Al/(TiB, TiB_2) (sample E)

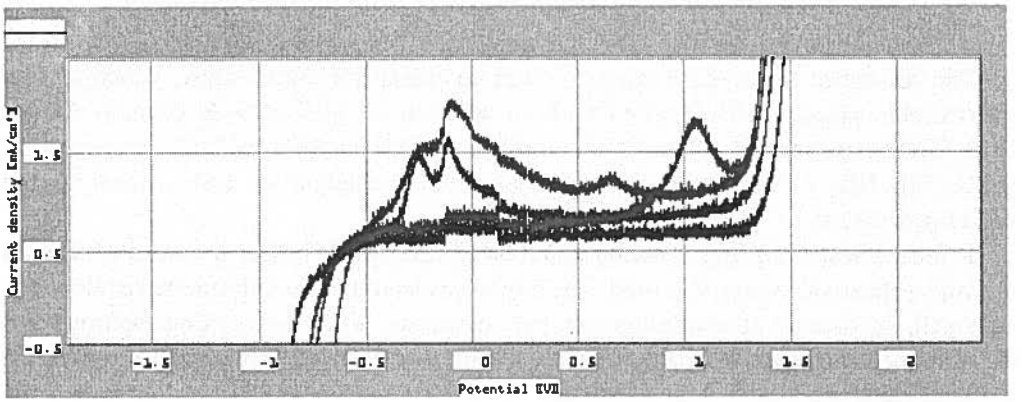

Fig. 20. Polarisation curves plotted for samples A and C in 0.1M H_2SO_4, v = 1V/min, red line – Ni_3Al/TiC (sample C), blue line – Ni_3Al (sample A)

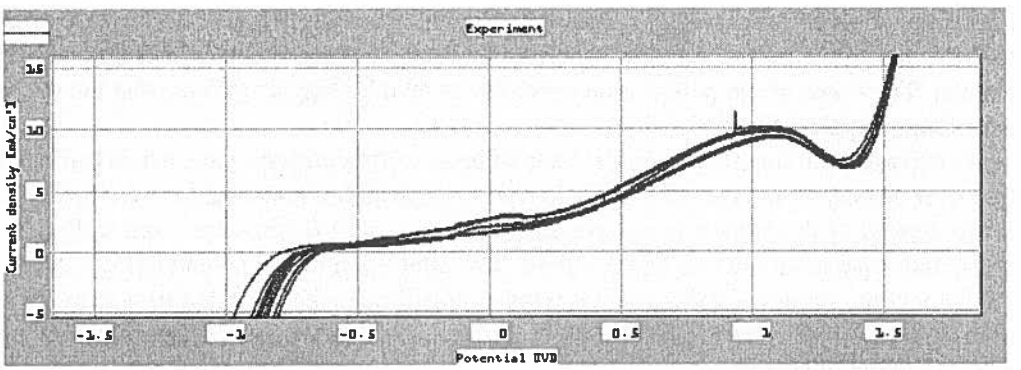

Fig. 21. Polarisation curves plotted for sample of Ni_3Al/ (TiB, TiB_2) (sample E), v = 1V/min

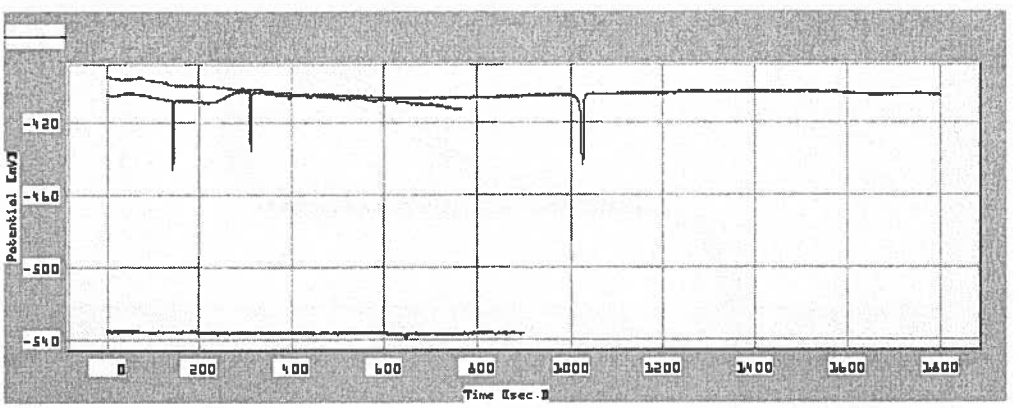

Fig. 22. Corrosion potential curves plotted for samples A, C and E immersed in 0.1M H_2SO_4

Figure 22 obviously indicates that the least resistant to corrosion is sample E, (Ni_3Al/(TiB,TiB_2 composite), which in the medium of 0.1 molar H_2SO_4 undergoes digestion over a wide range of potentials, and where the density of anodic current increases with increasing value of potential. The value of corrosion potential amounting to about 530 mV is lying on a small plateau at the beginning of polarisation curve.

To illustrate the destruction of the surface subjected to electrocorrosion process in 0.1 molar aqueous solution of sulphuric acid, the images of the matrix topography are shown in Figures 23 and 24, and of composites in Figures 25 and 26 (Ni_3Al/TiC composite) and in Figures 27 and 28 (Ni_3Al/(TiB,TiB_2 composite).

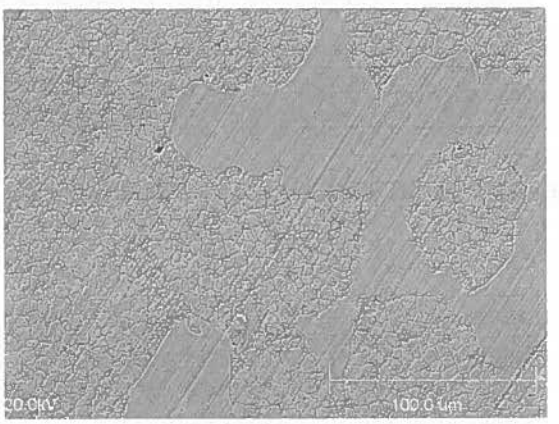

Fig. 23. Surface of Ni_3Al phase subjected to electrocorrosion process; 500x

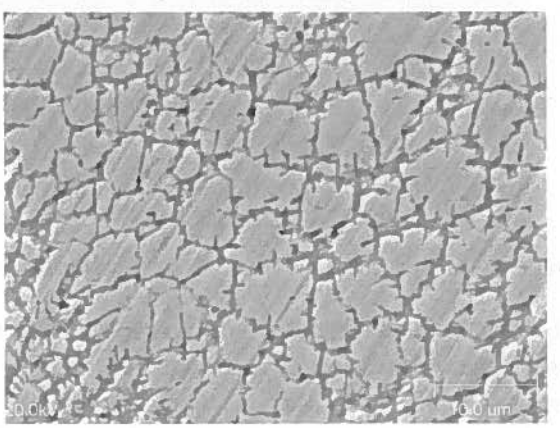

Fig. 24. Surface of Ni_3Al phase subjected to electrocorrosion process; 2500x

The destructive effect of electrocorrosion in 0.1 M H_2SO_4 on the surface of a sample of Ni_3Al/(TiB,TiB_2) composite is well visible. Corrosion degradation mainly affects the zones in the interdendritic spaces as well as titanium borides distributed in the dendrites.

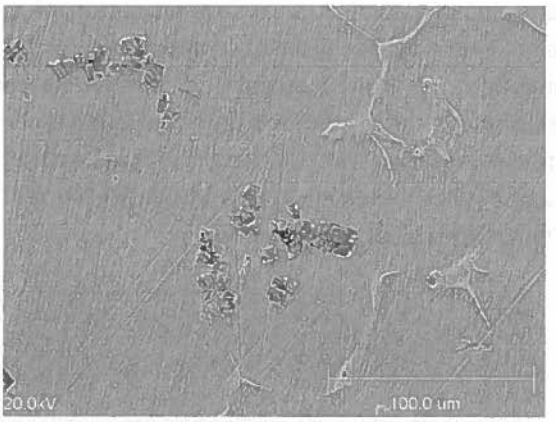

Fig. 25. Surface of Ni_3Al/TiC composite (10 vol.% TiC) subjected to electrocorrosion

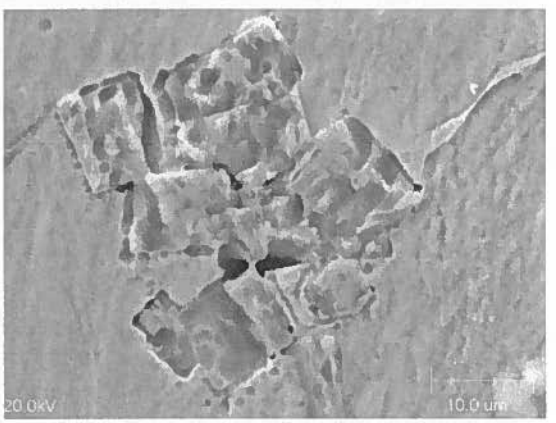

Fig. 26. Surface of Ni_3Al/TiC composite (10 vol.% TiC) subjected to electrocorrosion

The surface of both matrix and composite undergoes some degradation. In the case of matrix, the process of electrocorrosion affects rather the interdendritic spaces. In the composite, the destruction process attacks the titanium carbides which reinforce the composite. On the other hand, corrosion is not proceeding along the matrix-reinforcing phase boundary.

The destructive effect of electrocorrosion in 0.1 M H_2SO_4 on the surface of the sample of Ni_3Al/(TiB,TiB_2) composite is well visible. The corrosion is mainly degrading the zones in the interdendritic spaces and titanium borides distributed in the dendrites.

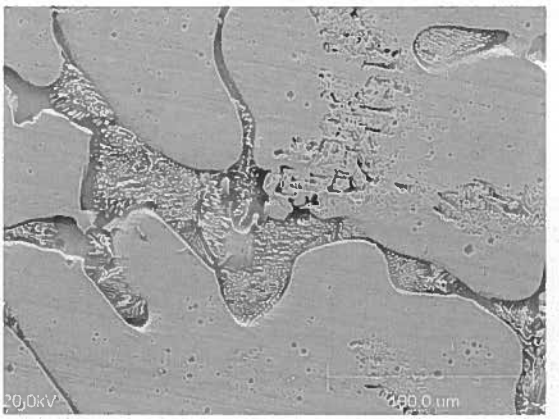

Fig. 27. Surface of $Ni_3Al + 10\%(TiB, TiB_2)$ composite subjected to electrocorrosion process; 500x

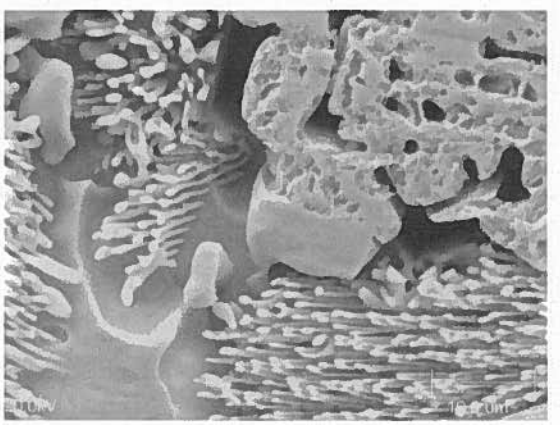

Fig. 28. Surface of $Ni_3Al + 10\%(TiB, TiB_2)$ composite subjected to electrocorrosion process; 2500x

2.4. Studies of gas corrosion resistance

Gas corrosion resistance at a temperature of 1073 K was investigated for non-reinforced matrix and for composites from the Ni_3Al/TiC and $Ni_3Al/(TiB,TiB_2)$ family..

In the studies a thermobalance was used to measure weight increments in samples exposed to the process of corrosion in active gas. The gas composition corresponded to the composition of the waste gas from motor car engines, i.e. steam, carbon monoxide and sulphur oxide. Additionally, composite materials were subjected to tests of corrosion resistance in the medium of hydrogen sulphide.

The results of tests are compiled in Table 2.
= Table 2

TABLE 2

Results of tests on gas corrosion resistance

Process conditions: temp. 800 °C, atmosphere – air, 10% H_2O, 5% CO, 1% SO_2									
Sample of sample	d [cm]	g [cm]	q [cm^2]	m_0 [g]	m_1 [g]	Δm [g]	Δm/q [g/cm^2]	t [s]	A [$g/cm^2 \cdot s$]
Ni_3Al + 0.05% B	1.00	0.08	1.82	0.45300	0.45338	0.00038	0.00021	86400	$2.43 \cdot 10^{-9}$
Ni_3Al + 5% TiC	1.00	0.09	1.85	0.50720	0.50916	0.00196	0.00106	86400	$1.23 \cdot 10^{-8}$
Ni_3Al + 10% TiC	1.12	0.18	2.60	1.27594	1.27876	0.00282	0.00108	86400	$1.25 \cdot 10^{-8}$
Ni_3Al + 5% (TiB, TiB_2)	1.00	0.08	1.82	0.48593	0.48743	0.00150	0.00082	86400	$9,49 \cdot 10^{-9}$
Ni_3Al + 5% (TiB, TiB_2)	0.88	0.11	1.52	0.46904	0.47056	0.00152	0.00100	86400	$1.16 \cdot 10^{-8}$
Process conditions: temp. 800 °C, atmosphere H_2S (p_{S2} = 1 Pa)									
Symbol of sample	d [cm]	g [cm]	q [cm^2]	m_0 [g]	m_1 [g]	Δm [g]	Δm/q [g/cm^2]	t [s]	A [$g/cm^2 \cdot s$]
Ni_3Al + 0.05% B	1.00	0.03	1.66	0.16268	0.16420	0.00152	0.00092	7200	$1.28 \cdot 10^{-7}$
Ni_3Al + 5% TiC	10.00	0.07	1.82	0.69755	0.70916	0.01161	0.00638	86400	$7.38 \cdot 10^{-8}$
Ni_3Al + 10% TiC	1.01	0.12	1.98	0.93600	0.95686	0.02086	0.01050	86400	$1.22 \cdot 10^{-7}$
Ni_3Al + 5% (TiB, TiB_2)	1.01	0.08	1.86	0.80736	0.82667	0.01931	0.01040	86400	$1.20 \cdot 10^{-7}$
Ni_3Al + 5% (TiB, TiB_2)	0.87	0.10	1.46	0.68638	0.66450	0.02188	0.01499	86400	$1.73 \cdot 10^{-7}$

Designations used in the table: d – sample diameter, g – sample thickness, q – total surface of sample, m_0,m^1 – starting and final sample weight, Δm – increments in sample weight, t – time of exposition, A – corrosion constant $\left(\frac{\Delta m}{q}\right) / time$

The corrosion constant in oxides assumes the lowest value in the case of matrix, while for all the composites its values are similar. Compared with Ni_3Al + 0.05%B matrix, introducing alien phase to the matrix decreases the gas corrosion resistance. The corrosion resistance is not decreasing in a more visible way with increasing volume content of the reinforcing phase in composite. The degree of surface degradation due to oxide corrosion is visible on the topography images shown in Figures 29 – 38.

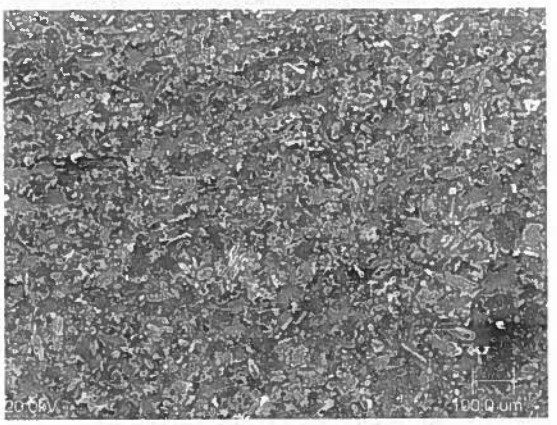

Fig. 29. Matrix. Corrosion in oxides; 100x

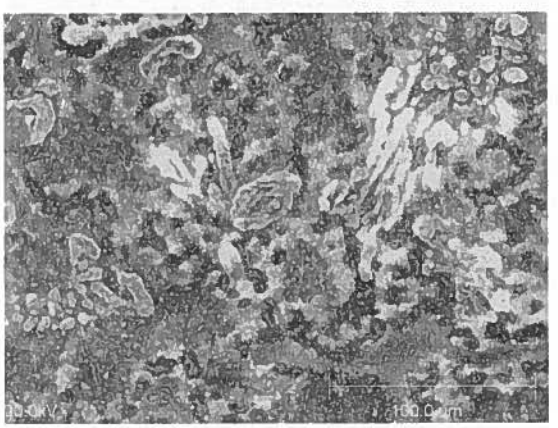

Fig. 30. Matrix. Corrosion in oxides; 500x

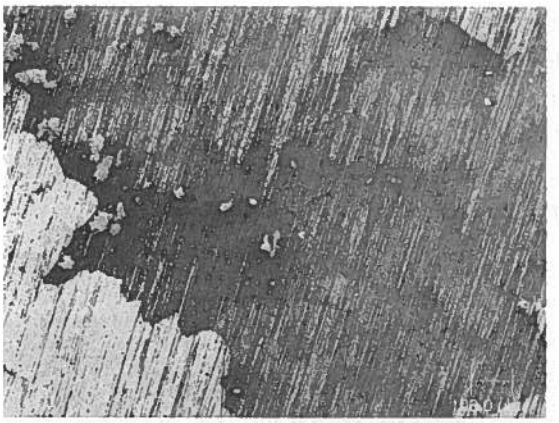

Fig. 31. Ni_3Al/TiC composite (5 vol.% TiC). Corrosion in oxides; 100x

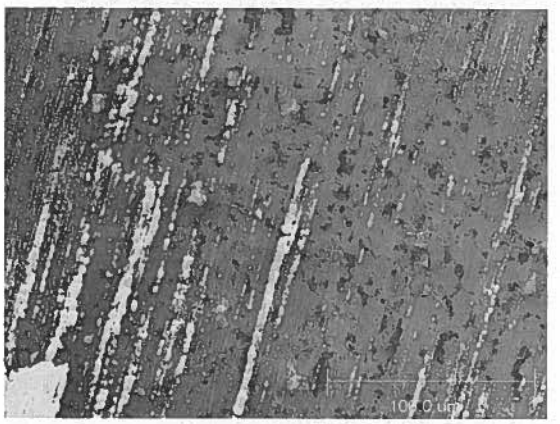

Fig. 32. Ni_3Al/TiC composite (5 vol.% TiC). Corrosion in oxides; 500x

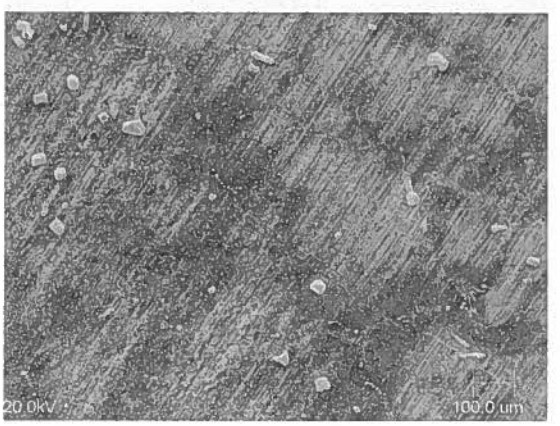

Fig. 33. Ni_3Al/TiC composite (10 vol.% TiC). Corrosion in oxides; 100x

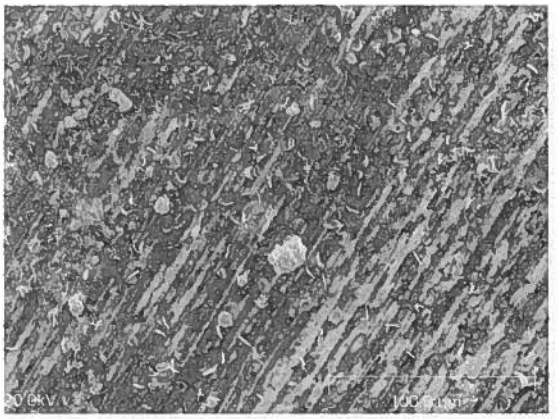

Fig. 34. Ni_3Al/TiC composite (10 vol.% TiC). Corrosion in oxides: 100x

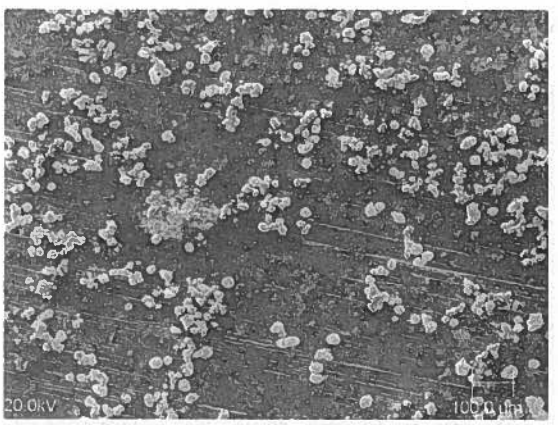

Fig. 35. Ni_3Al/(TiB, TiB_2) composite (5 vol.% Ti, TiB_2). Corrosion in oxides; 100x

Fig. 36. Ni_3Al/(TiB, TiB_2) composite (5 vol.% Ti, TiB_2). Corrosion in oxides; 500x

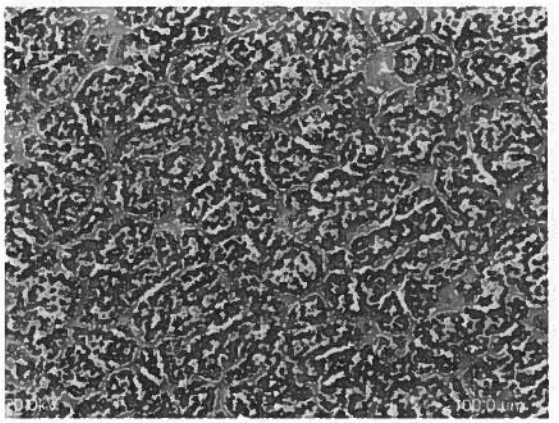

Fig. 37. $Ni_3Al/(TiB, TiB_2)$ composite (10 vol.% Ti, TiB_2). Corrosion in oxides; 100x

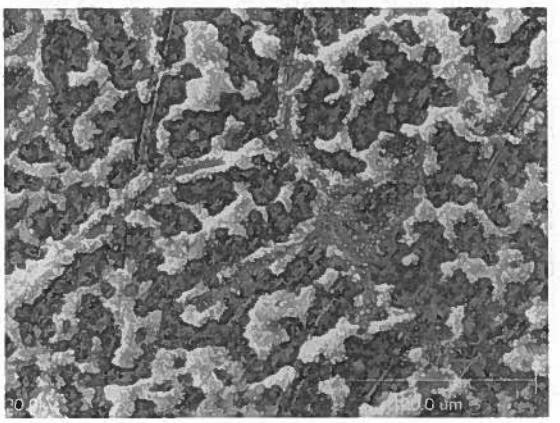

Fig. 38. $Ni_3Al/(TiB, TiB_2)$ composite (10 vol.% Ti, TiB_2). Corrosion in oxides; 500x

Similar as in the case of gas corrosion in oxides, the topography images of matrix and composites (Fig. 39a - e) show degradation of the surface of these materials when subjected to the effect of hydrogen sulphide at a temperature of 1073 K.

In spite of so great differences in surface topographies, the increments of weight in a time unit and per unit surface are similar for all the investigated materials. Thus, introducing titanium carbides or borides to Ni_3Al matrix does not deteriorate in a more significant way the gas corrosion resistance at high temperatures (1073 K). This is additionally proved by the same range of values of the corrosion constant obtained for the investigated matrix and composites.

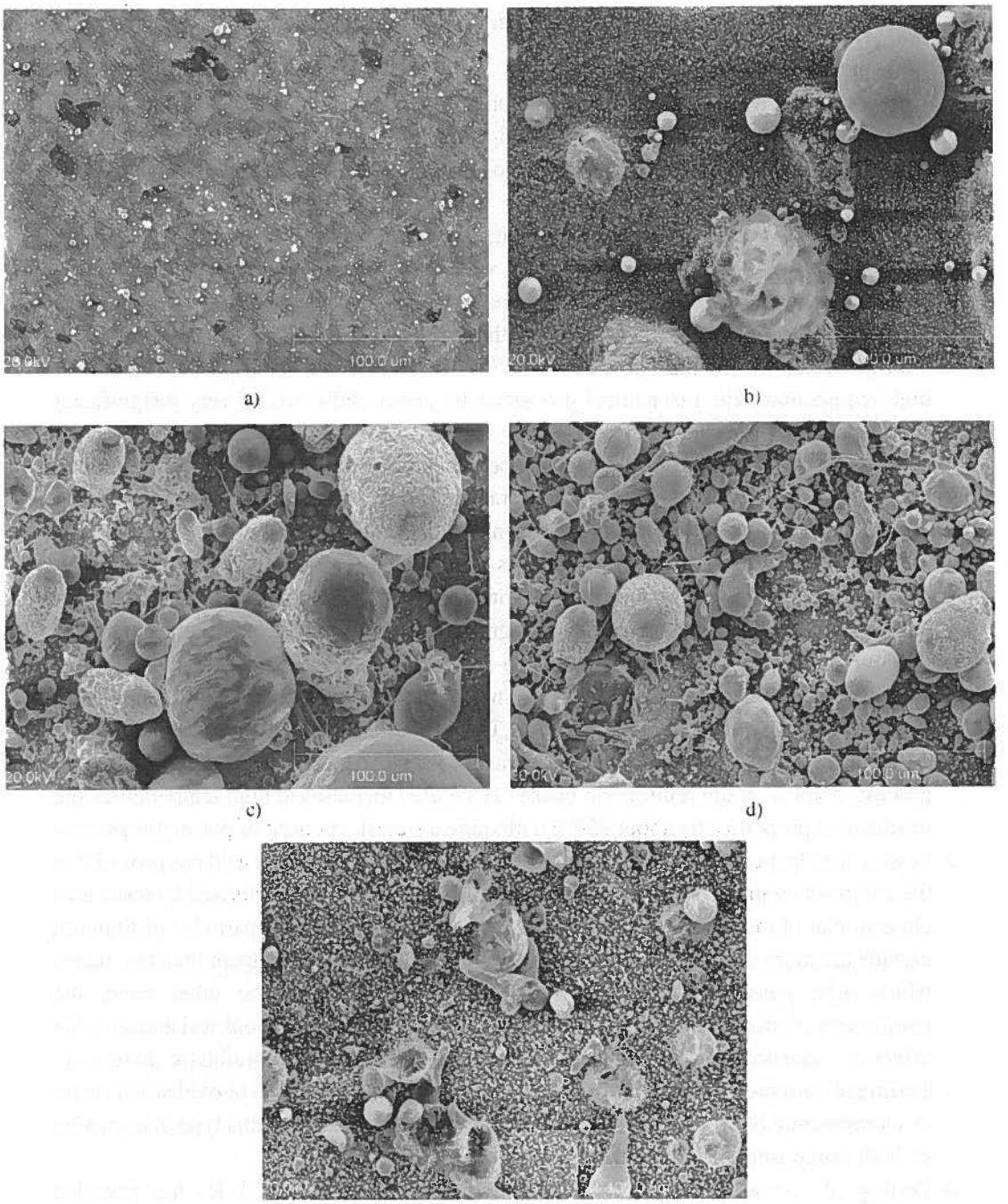

Fig. 39. Topography images obtained as a result of corrosion in H_2S: a) matrix and composites b) Ni_3Al/TiC (5 vol.% TiC), c) Ni_3Al/TiC (10 vol.% TiC), d) $Ni_3Al/(TiB,TiB_2)$ (5 vol.% TiB,TiB_2) and e) $Ni_3Al/(TiB,TiB_2)$ (10 vol.% TiB,TiB_2); 500x

Results

The results of investigation of the utilisation properties of composites "in situ", based on an intermetallic phase of Ni_3Al enriched with low additions of boron (0,05 wt.%), including mainly the mechanical, tribological and corrosion resistance properties, enabled the following conclusions to be formulated:

- The stress-strain curves plotted from static tests of uniaxial compression and tension within the range of low loads (I range) are similar for deformation temperatures of 293 and 1273 K, while within the strain range of 0,1 $\varepsilon > 1$ (II range) the tests conducted at high temperatures gave higher values of the yield stress.
- The, generated by "in situ" process, 5 vol.% of the TiC reinforcing phase increases at high temperatures the mechanical properties by about 200% with a very insignificant drop of plastic properties.
- In terms of the stability of mechanical properties, the, fabricated by the above described methods, composites are suitable for operation at high temperatures.
- The practical results of SHSB synthesis using briquettes containing titanium, aluminium and boron differ from the theoretical ones because the matrix appears to additionally contain a nickel-rich phase. During the synthesis two types of borides i.e.TiB and TiB_2, characterised by hard to differentiate topographies were formed. The volume content of titanium borides was consistent with the theoretically assumed one, but the shape, dimensions and distribution of particles in the matrix differed from the theoretically calculated one. Composites of $Ni_3Al/(TiB,TiB_2)$ containing 5 and 10 vol.% of TiB,TiB_2 were brittle but characterised by high abrasion resistance. The, generated by "in situ" process, 5 vol.% of the reinforcing phase (TiB,TiB2) increases at high temperatures the mechanical properties by about 250% with quite a significant drop of plastic properties.
- Testing the electrochemical corrosion resistance in diluted sulphuric acid has proved that the composite reinforced with particles of titanium carbide is characterised by resistance close to that of the matrix. It has been determined, moreover, that particles of titanium carbide are more susceptible to destruction while affected by the reagent than the matrix which after passivation remains practically unchanged. On the other hand, the composites reinforced with titanium borides do not possess sufficient resistance to the effect of electrocorrosion. Both matrix and titanium borides are gradually dissolved.
- Testing of corrosion resistance in a gas chamber filled with a mixture of oxides and steam at a temperature of 1073 K has revealed a comparable resistance to this type of corrosion of both composite and its matrix.
- Testing of corrosion resistance in hot hydrogen sulphide (1073 K) has revealed insufficient corrosion resistance of both matrix and composite to the effect of H2S. Weight increments in corrosion process are similar but surfaces suffer considerable degradation.

REFERENCES

[1] L.A. Dobrzański: Metaloznawstwo z podstawami nauki o materiałach. Wyd.N-T, Warszawa 1998.
[2] S. Katarzyński, S. Kocańda, M. Zakrzewski:Badanie własności mechanicznych metali. Wyd. N-T, Warszawa 1969.
[3] J.H. Hollomon: Trans. AIME, **162**, 268, (1945).
[4] D.C. Ludwigson: Met.Trans. **2**, 2825, (1971).
[5] E. Fraś, S. Wierzbiński, A.A. Janas: Polska metalurgia w latach 1998-2002 Komitet Metalurgii PAN, Kraków, 2, 337 (2002).
[6] E. Fraś, A. Janas, A. Kolbus, S. Wierzbiński: PTMK – Kompozyty (Composites) R. **2**, 4, 171 (2002).
[7] E. Fraś, A. Janas, S. Wierzbiński: Proc. of Committee of Metallurgy of the Polish Academy of Sciences, 47 Kraków, 2002.
[8] E. Fraś, S. Wierzbiński, A. Janas, H.F. Lopez: Archives of Metallurgy, 46, 4, 407 (2001).
[9] M.F. Ashby, D.R.H. Jones: Materiały inżynierskie **2**, WNT W-wa (1996)

The study was made under Research Project KBN no. 7 **T08B 048 19**

REVIEWED BY: JANUSZ GRYZIECKI
Received: 7 December 2003.

A R C H I V E S O F M E T A L L U R G Y A N D M A T E R I A L S
Volume 49 2004 Issue 1

BOGUSŁAW ONDERKA*, TADEUSZ POMIANEK**, JOLANTA ROMANOWSKA***, GRZEGORZ WNUK***, JAN WYPARTOWICZ****

SOLUBILITY OF LEAD IN LIQUID IRON AND THE ASSESSMENT OF Fe-Pb SYSTEM

ROZPUSZCZALNOŚĆ OŁOWIU W CIEKŁYM ŻELAZIE I OBLICZENIE WYKRESU FAZOWEGO Fe-Pb

The solubility of lead in liquid iron was measured over the temperature range 1873-1953 K by simultaneous equilibration of molten iron samples with saturated lead vapour as well as liquid lead. The results were used in assessment of the G i b b s energy function for liquid Fe-Pb phase. The calculations were made with the use of ThermoCalc system. The excess G i b b s energy of liquid solution was presented by means of R e d l i c h - K i s t e r equation. The equilibrium lines of Fe-Pb phase diagram were also calculated, taking into account four phases: liquid solution, solid Pb and solid Fe (fcc and bcc).

Wyznaczono rozpuszczalność ołowiu w ciekłym żelazie w zakresie temperatur 1873-1953 K poprzez doprowadzenie próbki ciekłego żelaza do równowagi zarówno z ciekłym ołowiem, jak i nasyconą parą ołowiu. Wyniki zostały użyte do obliczenia funkcji energii swobodnej G i b b s a dla ciekłej fazy Fe-Pb. Obliczenia zostały wykonane przy pomocy systemu ThermoCalc. Nadmiarowa energia swobodna G i b b s a fazy ciekłej została wyrażona przy pomocy równania R e d l i c h a - K i s t e r a. Obliczono również linie równowag wykresu fazowego Fe-Pb, uwzględniając cztery fazy: ciekły roztwór, stały Pb oraz stały Fe (fcc i bcc).

1. Introduction

Despite the common opinion that iron and lead do not dissolve one in the other, the information on their mutual solubility in liquid phase is important from the viewpoint of characterisation of several multicomponent systems, containing lead and iron. Thermodynamic description of such systems of importance in copper metallurgy as Cu-Pb-Fe,

* INSTYTUT METALURGII I INŻYNIERII MATERIAŁOWEJ IM. A. KRUPKOWSKIEGO PAN, 30-059 KRAKÓW. UL. REYMONTA 25
** WYŻSZA SZKOŁA INFORMATYKI I ZARZĄDZANIA, 35–225 RZESZÓW, UL. SUCHARSKIEGO 2
*** POLITECHNIKA RZESZOWSKA, 35-959 RZESZÓW, UL. W. POLA 2
**** AKADEMIA GÓRNICZO-HUTNICZA, 30-059 KRAKÓW, AL. MICKIEWICZA 30

Cu--Pb-Fe-As and Cu-Pb-Fe-S requires also the data on activities of components in Fe-Pb liquid solutions. These data cannot be obtained through extrapolation from multicomponent systems. Due to extremely narrow concentration range of Fe-Pb liquid solution at temperatures below 2000 K none of the experimental methods of activity determination can be applied. Thus, solubility lines are the only available data, which permit the thermodynamic assessment for liquid solution to be made. However, the data on component's solubility are scarce and new experimental results are of considerable value.

The aim of the present work is to provide new experimental data, which may help in proper description of the solubility line. For that purpose the direct equilibration method of liquid iron with both gaseous and liquid lead was applied.

The experimental works on the constitution of the Fe-Pb system have been checked for consistency by CALPHAD type assessment of constitutional data, performed in the present study, together with own experiments comprising lead solubility in liquid iron.

2. Literature data

The system Fe-Pb was studied by several techniques at various temperatures. The first data on Fe-Pb system [1902Sta] and [1907Isa] have shown that the liquid metals are practically mutually insoluble. Also, no diffusion of Pb into Fe was reported at 1273 K [1930Age] and 1273-1573 K [1934Jon]. First results of a solid solubility of Fe in Pb were given by Tammann and Olsen [1930Tam] as $2\text{-}3 \cdot 10^{-4}$ wt.% Fe. The existence of $FePb_2$ compound (88.12 wt.% Pb), suggested by [1932Dan] was not confirmed by later works [1946Now], [1947Sch].

Hansen and Anderko [1958Han] compiled all available information and proposed a phase diagram for Fe-Pb system in which liquid iron and lead are mutually virtually insoluble. Later investigations revealed that mutual solubility is measurable.

Two different methods: direct equilibration of Fe and Pb and equilibration of liquid Fe with Pb vapour were applied by Lord and Parlee [1960Lor] to measure the solubility of lead in liquid iron in 1823-1973 K temperature range.

Miller and Elliot [1960Mil] determined both the solubilities of lead in liquid iron at 1823 K and iron in liquid lead at 1575-1739 K. Their results for Pb solubility are considerably higher than those mentioned earlier. Araki [1963Ara] obtained similar results and found that solubility of Pb in solid iron was $2.7 \cdot 10^{-4}$ at.% at monotectic temperature (ca. 1803 K).

The solubility of Pb in liquid Fe over temperature range 1823-1973 K was also determined experimentally by Morozov and Ageev [1971Mor] and it was found to be higher in comparison to the data of [1960Lor].

Stevenson and Wulff [1961Ste] surveyed earlier results and re-investigated the solubility of iron in liquid lead over temperature range 973-1573 K by liquid sampling method. Their data agrees with the results published by Shepard and Parkman [1950She] for 973-1173 K range and by Weeks [1963Wee]. The latter found a solubility of $8.5 \cdot 10^{-4}$ at.% Fe at 873 K. Ali - Khan [1982Ali] used similar technique to determine iron solubility over temperature range 1253-1373 K.

Shepard and Parkman [1950She] observed a bend at 1177 K in solubility vs. temperature curve connected with bcc-Fe → fcc-Fe transformation and estimated changes of the enthalpy of dissolution of bcc-Fe and fcc-Fe in molten lead.

The slope of the solubility vs. temperature curves of none of the reported results agrees reasonably well with a rule suggested by Kubaschewski [1981Kub] which says that the quotient of the excess heat and entropy of solution should be equal to about 3400 K. She had drawn a compromise curve corresponding to the relationship:

$$\lg (at.\%Pb) = -\ 13400 \cdot T^{-1} + 6.16 \qquad (1)$$

which might be used for the extrapolation to higher temperatures.

Generally, it may be concluded, that the solubilities of lead in liquid iron are about one order of magnitude smaller than these of iron in liquid lead at comparable temperatures. For example $X_{Pb(Fe)} = 0.0008$ at 1823 K [1960Lor], while $X_{Fe(Pb)} = 0.008$ at 1824 K [1960Mil].

Basing on the same set of experimental results two assessments of Fe-Pb system were reported up to now in the literature: Hämäläinen et al. [1990Ham] and Wypartowicz [1995Wyp].

Burton [1991Bur] has compiled the available experimental data. Since then no experimental work on mutual solubility in the system Fe-Pb was reported. Sharma and Srivastava [1997Sha] in their evaluation of Fe-Pb-Zn ternary system reproduce the Fe-Pb phase diagram after Hämäläinen [1990Ham].

3. Experimental technique – equilibrium saturation method

In the present work the solubility of lead in liquid iron was determined over the temperature range 1873-1953 K by equilibrium saturation technique [1994Mid]. Diagram of a graphite cell, which is the main part of experimental arrangement, is presented in Fig. 1. Small alumina crucibles contained the weighed portions of lead (1 crucible), iron (2 crucibles) and lead together with iron (3 crucibles). They were placed on two levels inside the graphite block, which played the role of container. The leaks in graphite block allowed only for very slow lead vapour outflow, which permits to assume that the solubility experiments were carried out under equilibrium vapour pressure of lead. Additionally, good thermal conductivity of graphite block assured a stable temperature zone for all 6 alumina crucibles. The following materials were used in the experiments: iron 99.98%, delivered by Aldrich (USA) and lead 99.999%, delivered by Alfa Aesar (A Johnson Matthey Company).

The whole arrangement was contained inside the vacuum induction furnace and evacuated down to $2 \cdot 10^{-4}$ mbar. Then the system was filled with purified argon. Its pressure was set higher than equilibrium pressure of lead at the temperature of the experiment. The heating of the furnace up to required temperature took few minutes. The temperature inside the graphite block was measured by means of the PtRh30/PtRh6 thermocouple. At a given

temperature a series of runs of various exposition periods was carried out. After the termination of the run the furnace was switched off and the samples froze immediately.

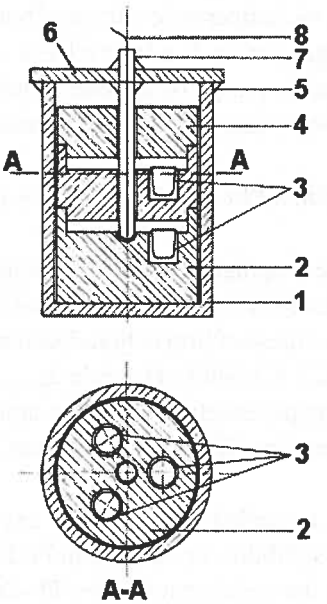

Fig. 1. Apparatus for equilibrium saturation method 1. alundum crucible, 2. graphite block, 3. alundum crucible with the sample, 4. graphite heater, 5. sealing bond, 6. alundum cover, 7. alundum thermocouple tube, 8. (PtRh6-PtRh30) thermocouple

The concentration of lead in chosen iron samples (10-12 g) was determined analytically, using atomic absorption technique (Institute of Iron Metallurgy, Gliwice, Poland). Samples were dissolved in HCl-HNO_3 concentrated solution, and spectrometer OPS ICP 3520 produced by ARL was applied. The analyzed spectral line was 220.35 nm. The concentration of lead in the samples was also determined from the increase of sample mass. The samples before and after experiment were weighed with an accuracy of 10^{-4} g.

4. Results

The experimental results of lead concentration in liquid iron are collected in Table 1. Figs 2, 3 and 4 present the change of lead content with the time of experimental run duration. It may be observed that for shorter times the obtained values of lead content were lower than maximum values. It means that the equilibrium saturation was not attained yet. Similarly, for much longer times the decrease in lead concentration was observed. Thus, for each temperature of experiment there exists the duration time, corresponding to maximum lead concentration. These maximum values of lead concentration were considered as equilibrium solubility.

TABLE 1

Experimental results of lead solubility in liquid iron

τ [h]	Equilibration with gaseous Pb		Equilibration with liquid and gaseous Pb	
	From mass balance	From analysis	From mass balance	From analysis
Lead concentration $X_{Pb} \cdot 10^3$ at 1873 K				
0.33	–	0.704	–	–
0.5	0.700	–	–	–
1.0	0.978 1.170	– 0.865	– 0.909	– 1.190
1.5	–	–	0.906	0.946
2.0	0.806	0.720	–	–
3.0	– 0.446	– –	0.646 0.494	– –
Lead concentration $X_{Pb} \cdot 10^3$ at 1923 K				
0.17	–	1.003	–	0.759
0.33	0.899 0.976	– 1.054	0.802 0.878	1.027 –
0.5	0.843 0.878	– 0.892	– 0.953	– –
0.75	0.673	–	0.647	0.675
1.0	0.956	0.783	–	–
1.5	0.447 –	0.594 –	0.261 0.513	– 0.594
Lead concentration $X_P^b \cdot 10^3$ at 1953 K				
0.13	–	0.68	–	0.60
0.17	0.979 –	– –	0.851 0.919	– –
0.25	0.937	0.973	1.360	0.81
0.33	1.30	0.892	–	–

The scatter of experimental results in Figs. 2-4 is considerably high. It may be attributed to kinetic conditions of penetration of liquid lead and lead vapour into the samples of liquid iron. From this point of view the best conditions for equilibration would be achieved, if either liquid or gaseous lead was passed through the sample of liquid iron. Such experiment seems to be very difficult in practical implementation. However, it may also be seen that the equilibration of iron with gaseous and liquid lead has given the same results within the accuracy limit of analysis. It was also found that the lead concentrations deduced from mass balance were not far from the results of analysis.

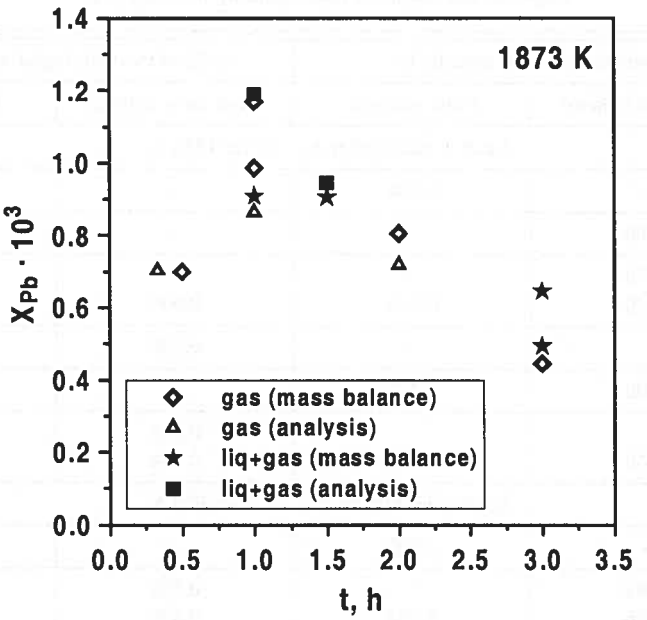

Fig. 2. The results of experimental determination of lead solubility in liquid iron at 1873 K

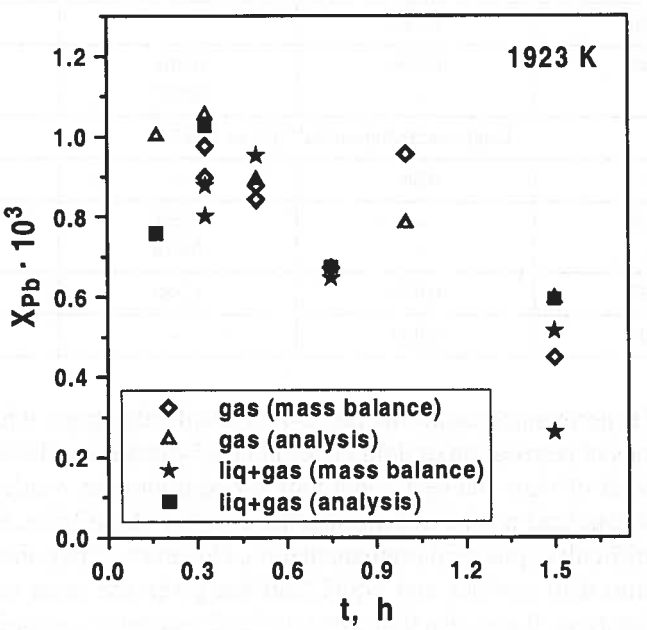

Fig. 3. The results of experimental determination of lead solubility in liquid iron at 1923 K

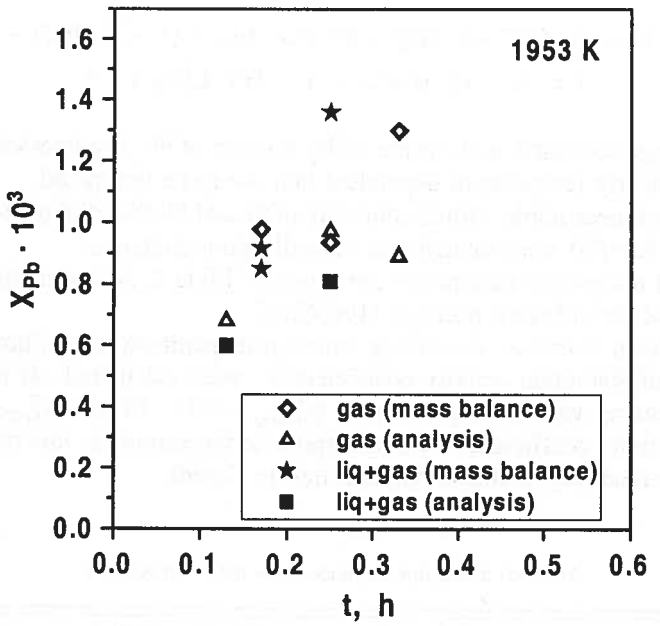

Fig. 4. The results of experimental determination of lead solubility in liquid iron at 1953 K

5. Assessment of Fe-Pb System

Optimisation of Fe-Pb system in the present work was based on the data of:
- [1960Lor], [1960Mil], [1963Ara], [1971Mor] and the present work – regarding lead solubility in liquid iron;
- [1960Mil], [1961Ste], [1982Ali] – regarding iron solubility in liquid lead.

It is reasonable to assume that the equilibrium temperatures for the γ (fcc) ↔ δ (bcc) and α (bcc) ↔ γ (fcc) iron transformations are not appreciably influenced by the presence of liquid lead because of the very low solubility of lead in solid iron.

In the thermodynamic modelling Gibbs energy function is assessed for each of the four phases: liquid, solid Pb and solid Fe (fcc and bcc) appearing in the Fe-Pb system. The Gibbs energy function $G_i^{0,\phi}(T) = G_i^{\phi}(T) - H_i^{SER}$ for the pure element i (i = Fe, Pb) in the ϕ phase (ϕ = liquid or solid bcc-Fe, fcc-Fe and fcc-Pb) is described by the equation:

$$G^{0,\phi}(T) = a + b \cdot T \cdot \ln T + d \cdot T^2 + e \cdot T^3 + f \cdot T^{-1} + g \cdot T^7 + h \cdot T^{-9}, \qquad (2)$$

where H_i^{SER} is the molar enthalpy of the stable element reference (SER) at 298.15 K and 1 bar, and T is the absolute temperature. The G i b b s energy functions for Fe and Pb are taken from the SGTE compilation by D i n s d a l e [1991Din]. The Gibbs energies of the solid and liquid phases in the Fe-Pb system were assumed to be pressure independent.

The liquid solution phase is described by the disordered substitutional solution model and its molar G i b b s energy is expressed by following equation:

$$G^{\phi} = (1-x)\cdot G^{0,\phi}_{Fe} + x\cdot G^{0,\phi}_{Pb} + R\cdot T\,[x\cdot \ln x + (1-x)\cdot \ln(1-x)] + x\cdot(1-x)\cdot [L^{0,\phi}_{Fe,Pb} + (1-2x)\cdot L^{1,\phi}_{Fe,Pb} + ...] \quad (3)$$

in which R is the gas constant, and x is the molar fraction of Pb. The interaction parameters $L^{i,\phi}_{Fe,Pb}$ may be linearly temperature dependent and are to be optimized.

Because of not measurable mutual solubility of Fe and Pb the solid phases bcc (bcc-Fe) and fcc (fcc-Fe, fcc-Pb) were treated like virtually pure elements.

The assessed interaction parameters are given in Table 2. All calculations were done with the ThermoCalc software package [1985Sun].

From the above formulas describing interaction parameters in liquid solution the limiting values of Raoultian activity coefficient γ^0 were calculated. At the temperature 1923 K the following values were obtained: $\gamma^0_{Pb(Fe)} = 9.12\cdot 10^2$ and $\gamma^0_{Fe(Pb)} = 1.22\cdot 10^2$.

Very high activity coefficients well correspond to the extremely low stability of liquid solution and the tendency to decomposition into to liquids.

TABLE 2

Assessed interaction parameters for the Fe-Pb system

Parameters [J/mol of atoms], validity 0 to 6000 °C
$L^{0,liquid}_{Fe,Pb} = 110921.9 - 9.3667\cdot T$
$L^{1,liquid}_{Fe,Pb} = 29234.6 - 6.8498\cdot T$

6. Discussion

The experimental determination of lead solubility in liquid iron meets serious problems connected with high temperature of experiments, low values of solubility as well as required high purity of materials. The technique employed in the present work may be classified as quasi-static one. Due to the small outflow of lead vapour from the compartment with samples, the true equilibrium in the system can be hardly obtained, and the experiment is carried out under stationary conditions. This may be seen from the plots: apparent lead solubility vs. time of experiment, presented in Figs. 2-4, where the highest temperature of experiments corresponded to the shortest time necessary to attain the maximum value of solubility. Next, due to the limited amount of lead in the system, the measured solubility begun to decrease with the duration of experiment. As the horizontal fragment of solubility vs. time plot was not obtained, we decided to assume the highest measured lead solubility as a true equilibrium value.

The results of the optimisation obtained in the present work were applied in the calculation of equilibrium lines of Fe-Pb phase diagram by means of the ThermoCalc system. The result is presented in Fig. 5–7.

Fig 5. demonstrates the fragment of lead solubility line, calculated in the present work in comparison with experimental data from the present work and the earlier publications of Morozov and Ageev [1973Mor], Araki [1963Ara], Lord and Parlee

[1960Lor] and Miller and Elliot [1960Mil]. Our results as well as the calculated solubility line fall between the experimental points of [1960Lor] and [1973Mor]. The results obtained by [1963Ara] are apparently too low, while the solubility reported by [1960Mil] for the temperature 1823 K seems too high. The results of [1973Mor] are close to solubility line suggested by Kubaschewski [1981Kub]. However, the experimental technique of [1973Mor] made use of silica glass cell, which might result in iron surface contamination (even through the gas phase) and iron as well as lead silicate formation.

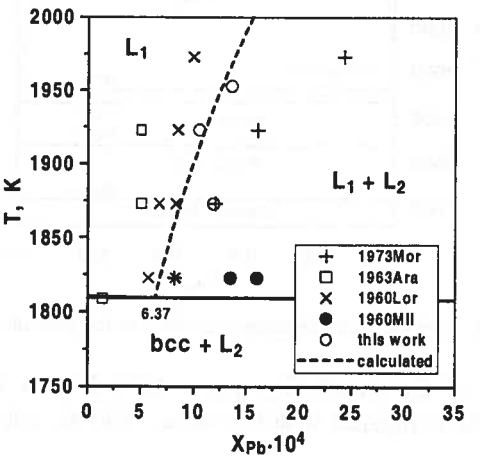

Fig. 5. Solubility of lead in liquid iron

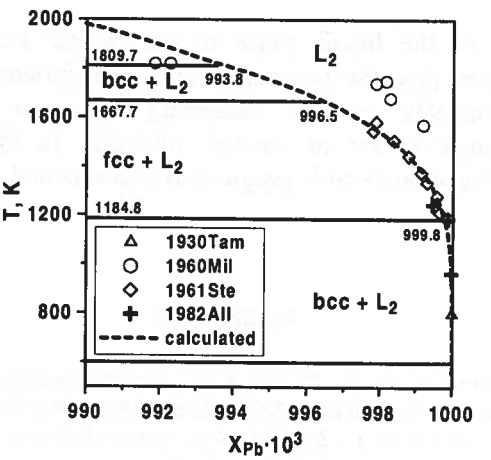

Fig. 6. Solubility of iron in liquid lead

In the lead-rich side of the phase diagram (Fig. 6) the calculated liquidus line in the range of γ phase stability agrees well with experimental results of [1961Ste]. For higher temperatures there are no reliable experimental data which might be used in verification of

calculated phase diagram. In the set of results of [1960Mil] the solubility of bcc-Fe and fcc-Fe in liquid lead do not correlate with the solubility of liquid iron.

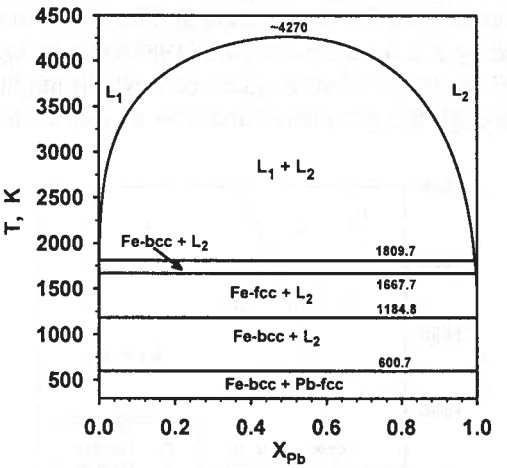

Fig. 7. Fe-Pb phase diagram calculated in the present work

The critical point of the miscibility gap ~4270 K was obtained in the present calculation. This may be compared with the value 3900 K, calculated by [1995Wyp].

7. Conclusions

The optimisation of the liquid phase in the system Fe-Pb and calculation of phase diagram seems to give the reasonably good background for further description of multicomponent metallic systems, containing both iron and lead. Taking into account results obtained so far on mutual solubility in this system, and related experimental difficulties, considerable progress in experimental accuracy is not expected in the near future.

REFERENCES

[1] [1902Sta], A. Stavenhagen, E. Schuchard, Ber.deut.chem.Ges. **35**, 910 (1902).
[2] [1907Isa], E. Isaac, G. Tammann, Z.anorg.Chem. **55**, 58-59 (1907).
[3] [1930Age], N.W. Ageev, M.I. Zamotorin, Ann.Inst.Polytech. Leningrad, Sec.Math.Phys.Sci. **31**, 15-28 (1928); abstract in J.Inst.Metals **44**, (1930) 556.
[4] [1930Tam], G. Tammann, W. Olsen, Z.anorg.Chem. **186**, 277-279 (1930).
[5] [1932Dan], E.J. Daniels, J.Inst.Metals **49**, 179-180 (1932).
[6] [1934Jon], W.D. Jones, J.Iron Steel Inst. **130**, 436 (1934).
[7] [1946Now], H. Nowotny, K. Schubert, Z.Metallkd. **37**, 22 (1946).
[8] [1947Sch], E. Scheil, Z.Metallkd., **38** 320, (1947).
[9] [1948Red], O. Redlich, A. Kister, Ind.Eng.Chem. **40**, 345 (1948).

[10] [1950She], O.C. Shepard, R. Parkman, U.S. At.Energy Comm. ORO-38 (1950).
[11] [1958Han], M. Hansen, K. Anderko, *Constitution of Binary Alloys*, New York, McGraw-Hill 1958.
[12] [1960Lor], A.E. Lord, N.A. Parlee, Trans.Metall.Soc. AIME **218**, 644 (1960).
[13] [1960Mil], K.O. Miller, J.F. Elliot, TMS-AIME **218**, 900-910 (1960).
[14] [1961Ste], D.A. Stevenson, J. Wulff, Trans.Metall.Soc. AIME **221**, 271 (1961).
[15] [1963Ara], T. Araki, Trans.Natl.Res.Inst.Met. (Tokyo) **5**, 91 (1963).
[16] [1963Wee], J.R. Weeks, NASA Spec.Publ. NASA-SP-**41**, 21 (1963).
[17] [1971Mor], A.N. Morozov, I.A. Ageev, Russ.Metall. **4**, 78 (1971).
[18] [1991Bur], Burton, J.Phase Equil. **12** 200-202 (1991).
[19] [1981Kub], O. Kubaschewski, High Temp.High Press. **13**, 435 (1981)
[20] [1982Ali], I. Ali-Khan, *Solubility of Iron in Liquid Lead, in Material Behavior and Physical Chemistry in Liquid Metal System*, Plenum Press, New York 237-242, (1982).
[21] [1985Sun], B. Sundman, B. Jansson, J-O. Andersson, CALPHAD **9**, 153-190 (1985).
[22] [1990Ham] M. Hämäläinen, R. Luoma, P. Taskinen; *Thermodynamic Analysis of the System Iron-Lead-Zinc*, Report TKK-V-B55, Helsinki University of Technology, Otaniemi 1990.
[23] [1994Mid], J. Midura-Romanowska, T. Pomianek, J.Chem.Termodynamics **26**, 507-513 (1994).
[24] [1995Wyp], J. Wypartowicz, *Interpretation of Thermodynamic Properties of Liquid Solutions in Cu-Pb-Fe-As System*, Scientific Reports of Silesian Technical Univ., ser. Metallurgy, 48, Gliwice 1995 (in Polish).
[25] [1997Sha], R.C. Sharma, M. Srivastava, J. Phase Equil. **18**, 481 (1997).

REVIEWED BY: KRZYSZTOF FITZNER
Received: 10 December 2003.

A R C H I V E S O F M E T A L L U R G Y A N D M A T E R I A L S
Volume 49 2004 Issue 1

WŁADYSŁAW GĄSIOR*, ZBIGNIEW MOSER*, JANUSZ PSTRUŚ*

MEASUREMENTS OF THE SURFACE TENSION AND DENSITY OF TIN BASED Sn-Ag-Cu-Sb LIQUID ALLOYS

POMIARY NAPIĘCIA POWIERZCHNIOWEGO I GĘSTOŚCI CIEKŁYCH STOPÓW Sn-Ag-Cu-Sb NA OSNOWIE CYNY

The maximum bubble pressure method for the determination of the surface tension and dilatometric technique for density measurements were applied in the studies of liquid quaternary Sn-Ag-Cu-Sb alloys close to the ternary eutectic (Sn-Ag-Cu). The investigations of the density were conducted in the temperature range from 513 K to 1186 K and these of the surface tension from 513 K to 1177 K. The experiments were carried out for the liquid alloy of composition close to the ternary eutectic (Sn3.3Ag0.76Cu) and for four quaternary liquid alloys (Sn-3.3Ag-0.76Cu) + Sb alloys (X_{Sb} = 0.03, 0.06, 0.09, 0.12 molar fractions). It has been found that both surface tension and density show linear dependence on temperature. The relations describing the dependence of the surface tension and density on concentration were determined. The surface tension, density and molar volume isotherms calculated at 673 K and 1273 K have shown that the antimony addition to the ternary alloy (Sn-3.3Ag-0.76Cu) decreases the surface tension and the density while increase of the molar volume is observed. The maximal decrease of surface tension is slightly higher than 50 mN/m and that for density is about 0.15 g*cm^3. The observed increase of molar volume is about 2.5 cm^3 at the maximal Sb addition equal to 0.12 mole fraction.

Stosując metodę maksymalnego ciśnienia w pęcherzykach gazowych dla pomiaru napięcia powierzchniowego oraz technikę dylatometryczną dla pomiaru gęstości wykonano badania dla ciekłych stopów czteroskładnikowych Sn-Ag-Cu-Sb bliskich eutektyce potrójnej Sn-Ag-Cu. Pomiary gęstości przeprowadzono w zakresie temperatur 513 K do 1186 K, a dla napięcia powierzchniowego od 513 K do 1177 K. Pomiary wykonano dla ciekłych stopów o składzie wyjściowym (Sn-3.3Ag-0.76Cu) i dla czterech stopów (Sn-3.3Ag-0.76Cu) + Sb (X_{Sb} = 0.03, 0.06, 0.09 i 0.12 ułamka molowego). W pracy wykazano, że zarówno napięcie powierzchniowe jak i gęstość cechują się liniową zależnością od temperatury. Wyznaczono także zależności napięcia powierzchniowego od stężenia. Izotermy napięcia powierzchniowego, gęstości i objętości molowej obliczone dla temperatur 673 K i 1273 K wykazały, że dodatek antymonu do stopu (Sn-3.3Ag-0.76Cu) obniża napięcie powierzchniowe i gęstość natomiast podwyższa objętość molowa. Maksymalne obniżenie napięcia powierzchniowego jest nieco wyższe od 50 mN/m, a dla

* INSTYTUT METALURGII I INŻYNIERII MATERIAŁOWEJ IM. A. KRUPKOWSKIEGO PAN, 30-059 KRAKÓW, UL. REYMONTA 25

gęstości wynosi około 0.15 g/cm^3. Wzrost objętości molowej wynosi około 2.5 cm^3 przy maksymalnym dodatku antymonu 0.12 ułamka molowego.

1. Introduction

Undertaken more than 40 years ago at the Institute of Metallurgy and Materials Science the extensive thermodynamic studies on liquid and solid alloys by various experimental techniques were directed towards the use in phase diagram calculations and next for correlation with physical properties and the structure. In other studies the thermodynamic properties of molten salts were combined with physical properties, mainly surface tension and density [1,2,3] to calculate the activity and concentration in the surface phase when passing from the bulk to the surface phase. The observed tendency all over the world is to use the results of the basic research towards application. Due to this trend, in 1997 we have directed our attention on Pb-free soldering materials. To elaborate a substitute for Sn-Pb solders with materials without lead it is necessary to resolve various problems. Our plans were to combine thermodynamic data in the form of optimised parameters needed both for modelling of physical properties and for calculations of phase diagrams. It should be mentioned that often phase equilibria of new Pb-free systems are not known. On the other hand, modeling of physical properties needs experimental data for testing. Among the various data important for soldering materials the surface tension and interfacial tension play an important role as responsible for wettability of the substrate by the solder.

In the course of our studies we have initiated systematic measurements of the surface tension and density by the maximum bubble pressure method and dilatometric method on pure metals Sn, Ag, Bi, Sb, In, Cu and Zn, binary low-melting eutectics and on ternary alloys based on $(Sn\text{-}Ag)_{eut}$, suggested for practical application. The obtained results were extended to include phase equilibria calculations in co-operation with Tohoku University in Japan and presented in Ref. [4]. When the addition of another component to the binary or higher order liquid alloys decreases the surface tension and interfacial tension, it simultaneously improves wettability. Hence, measurements of the surface tension can be useful for the prediction of the effect of modifying elements on solder properties.

In 2000, the Institute of Metallurgy and Materials Science started co-operation with two industrial institutes, the Institute of Non-Ferrous Metals in Gliwice and the Tele and Radio Research Institute in Warsaw as well as with Warsaw University of Technology. In addition, in 2002 we joined COST 531 Program which is partly correlated with the activity of Associated Phase Diagram and Thermodynamics Committee oriented on data bases comprising thermodynamic and physical properties of Pb-free soldering materials. The joint efforts are focused towards the production of multicomponent Pb-free solder of low Ag content in Poland. Multicomponent alloys are required to modify not only the physical properties and melting temperatures, but simultaneously the mechanical and electrical properties in order to propose the right material as close as possible to traditional Sn-Pb solders.

Our studies are oriented on two groups of materials always starting with eutectic or close to eutectic Sn-Ag-Cu alloys. In the first study, based on co-operation with the mentioned industrial institutes there is examined addition of Bi and next Sb in quinary alloys on the surface tension obtained by the maximum bubble pressure method together with meniscographic measurements of interfacial tension and with mechanical and electrical properties. It has been shown, in our previous studies [5, 6] that the surface tension obtained by the maximum bubble method is higher than the interfacial tension obtained by the meniscographic method due to the interfacial tension contribution to the measurement at the sample-flux interface.

The second group of alloys was examined within COST 531 Program in co-operation with Tohoku University. The influence of Sb and In within surface tension and density studies on ternary eutectic or close to eutectic Sn-Ag-Cu alloys will be examined. In this group of alloys we have studied the surface tension and density of liquid Sn-Sb alloys in the entire range of concentrations [7], next on Sn-Ag-Sb, combining the mentioned physical properties with the results of experimental determination of phase diagram and thermodynamic calculations; the resulting optimized thermodynamic parameters were used for modeling of the surface tension [8]. It seems interesting to continue studies on multicomponent alloys with Sb additions since they are considered to substitute the Pb-Sn solders due to sufficiently good wetting properties, strength, thermal fatigue resistance and creep strength.

Until now, in both groups of alloys the modelling by the B u t l e r ' s method [9] is used as discussed in earlier publications. In Ref. [10, 5, 6, 11, 12] a qualitative agreement was observed between the experimental and the calculated surface tensions from B u t l e r ' s model, however in each case the calculations have shown a curvilinear dependence of the surface tension vs. temperature, which is in disagreement with the experiments. As reported in our studies on Ag-Bi [12] where Bi activities obtained by solid electrolyte technique were combined with surface tension, it was concluded that some terms in the B u t l e r ' s model should be corrected. One of the possibilities is the assumption that parameters L (assumed equal to 1.091 for close packed structures) and ((parameter corresponding to the ratio of the coordination number Z in the liquid phase to that in the bulk phase) are constant during calculations. It seems that more experimental data must be collected to introduce the required corrections. It should be added that until now our experience with B u t l e r ' s model is limited only to binary and ternary alloys.

The extension to higher order systems needs experimental data of the surface tension and excess G i b b s energies of components of the investigated multicomponent alloys obtained from separate thermodynamic studies or for instance from the Calphad method. Such data are not available in literature, and therefore, as the first step of B u t l e r ' s modelling of the surface tension of quaternary alloys Sn-Ag-Cu-Sb in this study, there are presented experimental surface tension and density data for liquid alloys, limited only to small additions of Sb; for excess G i b b s energies of components we are taking into account only data from respective binaries and two ternaries; namely Sn-Ag-Cu [13] and Sn-Ag-Sb [14]. It is the main aim of this publication which in agreement with our contribution to the COST 531 PROGRAM will be continued for higher Sb concentrations in parallel with extension of B u t l e r ' s model for multicomponent systems.

2. Experimental

The surface tension of Sn-Ag-Cu-Sb liquid alloys was measured by the maximum bubble pressure method based on the following relation:

$$\sigma = \frac{1}{2} r_c \Delta p \qquad [N \cdot m^{-1}], \tag{1}$$

where: σ is surface tension, r_c is the capillary radius and Δp is the pressure difference described by the following equations:

$$\Delta p = p_g - p_a \qquad [N \cdot m^{-1}] \tag{2}$$

$$\Delta p = g(\rho_m h_m - \rho_a h_a) \qquad [N \cdot m^{-2}] \tag{3}$$

necessary to form the gas bubble at the end of capillary and detach it. The meaning of the symbols in Eqs 2 and 3 is as follows: p_g – the gas pressure, p_a – the hydrostatic pressure of liquid alloy, g – the acceleration of gravity, ρ_a and ρ_m – the density of the investigated liquid alloy and manometric liquid, h_a – the immersion depth of the capillary and h_m – the height of the manometer liquid. The surface tension calculated from Eq.1 is an approximation. The exact values of surface tensions were calculated using the procedure proposed by S u g d e n [15]. The scheme of the apparatus for the surface tension measurements is shown in Fig.1.

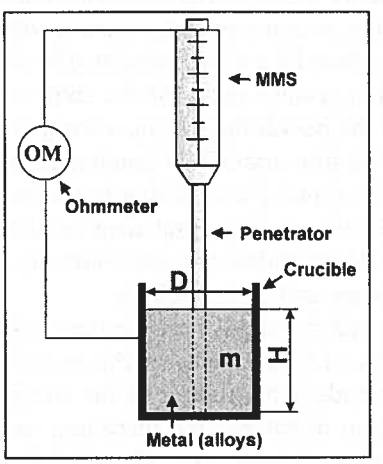

Fig. 1. Scheme of the equipment for the density measurements by the dilatometric method

Densities of liquid alloys were measured by the dilatometric method based on the measurement of the height of constant mass of liquid alloy in a graphite crucible having inside diameter D. The density and molar volume were calculated from the following equations:

$$\rho = \frac{\mathbf{m}}{\mathbf{V}} \qquad [\mathrm{g \cdot cm^{-3}}] \tag{4}$$

$$\mathbf{V} = \frac{\pi \mathbf{D^2 H}}{\mathbf{4}} \qquad [\mathrm{cm^3}], \tag{5}$$

where: ρ – the density of alloy, m – the weight of alloy, V – the volume of the alloy, D – the inside crucible diameter and H – the height of the alloy in the crucible. The correction of the thermal expansion of the crucible was made at each measurement temperature. The scheme of the apparatus for density measurements is presented in Fig. 2. The molar volume V_m of the liquid Sb-Sn alloys was calculated using the known equation:

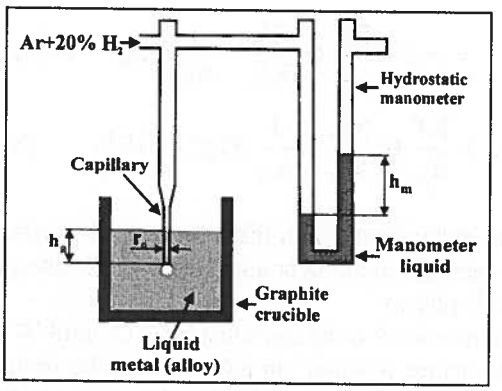

Fig. 2. Scheme of the equipment for the surface tension measurements by the maximum bubble pressure method

$$\mathbf{V_m} = \frac{\mathbf{M_{Sn}\,X_{Sn} + M_{Ag}\,X_{Ag} + M_{Cu}\,X_{Cu} + M_{Sb}\,X_{Sb}}}{\rho}, \qquad [\mathrm{cm^3 \cdot mol^{-1}}] \tag{6}$$

where: M_{Sn}, M_{Sb}, $M_C{}^u$ and M_{Ag} are the atomic weighs and X_{Sn}, X_{Sb} ,X_{Cu} and X_{Ag} are the mole fractions of Sn, Sb ,Cu and Ag, ρ is the density of the alloy

At the first step the ternary alloys were prepared by melting in a graphite crucible the appropriate amounts of tin (99.999% at.), silver (99.995% at.) and copper (99.995% at.) to produce the ternary Sn-Ag-Cu. Next the alloy was analyzed and it was found that the composition was close to the ternary eutectic and had the following composition: Sn3.3%Ag0.76%Cu (in atomic percent). At the second stage the antimony (99.999%at.) was added to the sample directly before measurements and the quaternary alloy was homogenised and mixed at a constant temperature for some hours. The protective atmosphere of high purity gas mixture of Ar-20 % vol. H_2 was used during alloy preparations and the measurements of both surface tension and density. The thermocouple of Pt-PtRh10 was applied to the measurement of temperature. The capillaries, in the surface tension measurements, and the penetrator in the density measurements were made from molybdenum.

3. Modeling of the surface tension

Considering the equilibrium between a bulk phase and a surface monoatomic layer (monolayer), regarded as an individual phase, B u t l e r [9] derived the relation allowing to calculate the surface tension of the alloys from thermodynamic properties. In the case of Ag-Cu-Sn-Sb liquid alloys the relation has the following form:

$$\sigma = \sigma_{Ag} + \frac{RT}{A_{Ag}} \ln \frac{X_{Ag}^{S}}{X_{Ag}^{B}} + \frac{1}{A_{Ag}} (G_{Ag}^{E,S} - G_{Ag}^{E,B})$$

$$= \sigma_{Cu} + \frac{RT}{A_{Cu}} \ln \frac{X_{Cu}^{S}}{X_{Cu}^{B}} + \frac{1}{A_{Cu}} (G_{Cu}^{E,S} - G_{Cu}^{E,B})$$

$$= \sigma_{Sn} + \frac{RT}{A_{Sn}} \ln \frac{X_{Sn}^{S}}{X_{Sn}^{B}} + \frac{1}{A_{Sn}} (G_{Sn}^{E,S} - G_{Sn}^{E,B})$$

$$= \sigma_{Sb} + \frac{RT}{A_{Sb}} \ln \frac{X_{Sb}^{S}}{X_{Sb}^{B}} + \frac{1}{A_{Sb}} (G_{Sb}^{E,S} - G_{Sb}^{E,B}) \qquad [N \cdot m^{-1}]. \tag{7}$$

Equation (7) relates the surface tension of the solution with surface tension of pure metals, the surface area of the metallic monolayer and excess Gibbs energies of the components in the surface and the bulk phases.

Symbols in Eq.7 are as follows: R is the gas constant in ($J \cdot mol^{-1}K^{-1}$), T is the temperature in (K), (σ_i and A_i are the surface tensions (in $mN \cdot m$) and the molar surface area (in m^2) in a monolayer of pure liquid metals (i = Ag, Cu, Sn, Sb), X_i^S, and X_i^B are the mole fractions of the components and $G_i^{E,S}$ and $G_i^{E,B}$ are the partial excess G i b b s energies of the component i in the surface and the bulk phase, respectively

The molar monoatomic surface area A_i of metal i is calculated from the equation:

$$A_i = LN^{1/3}V_i^{2/3} \qquad [m^2], \tag{8}$$

where: N is A v o g a d r o ' s number, and V_i is the molar volume of pure liquid i in (m^3), L is usually set to be 1.091 for liquid metals assuming close packed structure [16].

Finally, the relationship between excess G i b b s energy of the component i in bulk and in the surface phase is assumed to be equal as follows:

$$G_i^{E,S} = \beta G_i^{E,B} \qquad [J \cdot mol^{-1}]. \tag{9}$$

In Eq. 9 β is the parameter corresponding to the ratio of the coordination number Z in the surface phase to that in the bulk phase Z^S/Z^B, and is assumed to be equal to 0.83 for liquid metals [17, 18]. R e d l i c h - K i s t e r model [19] for the binary systems with the ternary interaction parameters (Eq.10) was used for calculations of the partial excess G i b b s energies of Ag, Cu, Sn and Sb in the quaternary Ag-Cu-Sn-Sb liquid alloys according to the equation presented by S u n d m a n [20] (Eq. 11):

$$G^E = \sum_{i=1}^{n-1}\sum_{j=i+1}^{n} X_i X_j \sum_{1}^{m} A_1 (X_i - X_j) + \sum_{i=1}^{n-2}\sum_{j=i+1}^{n-1}\sum_{k=j+2}^{n} X_i X_j X_k (B_i X_i + B_j X_j + B_k X_k)$$

$[J \cdot mole^{-1}]$ [10]

$$G_i^E = G^E + \left(\frac{dG^E}{dX_i}\right) - \sum_{1}^{k} X_i \left(\frac{dG^E}{dX_i}\right) \qquad [J \cdot mole^{-1}], \qquad [11]$$

where G^E is the excess G i b b s energy of the liquid Ag-Cu-Sn-Sb alloy, X_i is the mole fraction of metal, A_i and B_i are binary and ternary optimised thermodynamic parameters and G_i^E is the excess *Gibbs* energy of the component *i*.

4. Results and discussion

Applying the dilatometric and the maximum bubble pressure methods the density and the surface tension were measured for Sn3.3Ag0.76Cu alloy and four quaternary Sn-Ag-Cu-Sb liquid alloys with the concentration 0.03, 0.06, 0.09 and 0.12 mole fraction of antimony and in the temperature range form 513 K to 1186 K in the case of the density and from 513 K to 1177 K in the case of the surface tension. The experimental data of both surface tension and density were described for each concentration by the linear dependence on the temperature. The equations are reported in Table 1 for the density and in Table 2 for the surface tension together with the calculated errors of density, surface tension at 673K and 1173 K and of the linear equation parameters (A and B) [21]. The temperature dependences of density are shown graphically in Fig. 3.

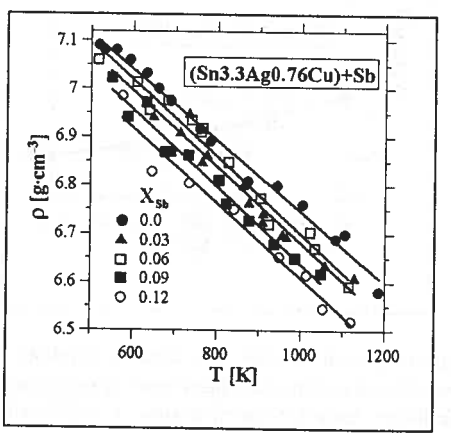

Fig. 3. The temperature dependences of the density of (Sn3.3Ag0.76Cu) and (Sn3.3Ag0.76Cu) + Sb liquid alloys. Symbols represent the experimental values determined by the dilatometric method and continuous lines show the values calculated from equation in Table 1

The density isotherms of the investigated Sn3.3Ag0.76Cu+Sb liquid alloys were calculated at 673K and 1273 K and described by the following parabolic relations dependent on concentration:

$$\rho = \rho_t + BX_{Sb} + CX_{Sb}^2 = 6.9863 - 0.6839X_{Sb} - 2.9967X_{Sb}^2 \qquad 673K \qquad [12]$$

$$\rho = \rho_t + BX_{Sb} + CX_{Sb}^2 = 6.5459 - 1.7752X_{Sb} + 4.5587X_{Sb}^2 \qquad 1273K \qquad [13]$$

In the foregoing relations ρ is the density of the quaternary alloys, ρ_t is the density of the ternary Sn-Ag-Cu alloy and X_{Sb} is the mole fraction of Sb in the quaternary Sn3.3Ag0.76Cu + Sb alloys. The equations [12] and [13] are valid in the experimental concentration range. The numerical parameters B and C of equations [12, 13] were calculated using the least squares method. Values of the density (continuous line) calculated from Eqs 12 and 13 and those from experiments (symbols) are presented in Fig. 4. The general conclusion is that the addition of antimony decreases the density of Sn-Ag-Cu alloys and that the higher addition of antimony to the Sn-Ag-Cu liquid alloys involves higher decreasing of the density of the quaternary alloys. It may be caused by the lower density of Sb than that of the ternary Sn-Ag-Cu alloys. The maximal decrease of the density in comparison to the Sn-Ag-Cu alloys is observed at the highest concentration of Sb in the Sn-Ag-Cu-Sb alloys and it is equal to about 0.13 gcm^{-3} at 673K and 0.15 gcm^{-3} at 1273 K. The dashed lines in Fig. 4 show the linear changes of the density when plotting the density of the ternary Sn-Ag-Cu liquid alloys to the pure antimony.

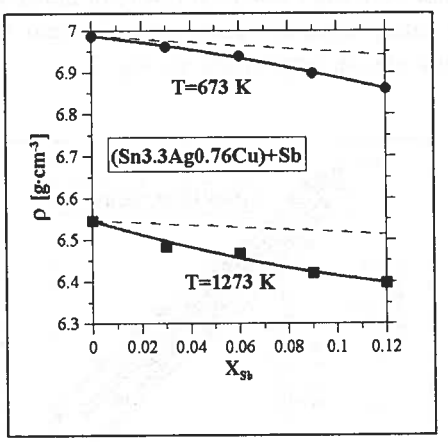

Fig. 4. Isotherms of the density calculated at 673K and 1273 K. Symbols show the values calculated from Equations in Table 1. Continuous lines are values calculated from the temperature-concentration relations [7] and [8] and dashed lines show the linear changes between density of (Sn3.3Ag0.76Cu) alloy and pure antimony

The calculated molar volume of the liquid Sn3.3Ag0.76Cu + Sb alloys from Eqs. 6, 12, 13 and those in Table 1 are shown in Fig. 5. The addition of the antimony to the investigated Sn-Ag-Cu liquid alloy increases the molar volume of the investigated

Sn3.3Ag0.76Cu + Sb quaternary alloys and the increase is higher at higher temperatures. At 1273 K the difference between the ternary Sn-Ag-Cu and the quaternary Sn3.3Ag0.76Cu + Sb alloys is about 0.5 cm^3 and at 673K it is 0.35 cm^3. The dashed lines in Fig. 5 show the linear changes between the molar volume of the ternary Sn-Ag-Cu liquid alloys and pure antimony.

TABLE 1

Temperature dependences of the density of the (Sn3.3Ag0.76Cu) and (Sn3.3Ag0.76Cu) + Sb liquid alloys together with errors calculated for density at 873 K and 1273 K and for parameters of A and B of linear equations

X_{Sb}	$\rho = A+BT$ $g \cdot cm^{-3}$	ρ_{873K} $g \cdot cm^{-3}$	ρ_{1273K} $g \cdot cm^{-3}$	Err(A) $g \cdot cm^{-3}$	Err(B) $g \cdot cm^{-3} \cdot K^{-1}$
0.000	=7.4803-0.000734T	6.839±0.036	6.546±0.044	±0.038	±0.000046
0.030	=7.4963-0.000796T	6.801±0.053	6.483±0.065	±0.070	±0.000084
0.060	=7.4658-0.000784T	6.781±0.053	6.467±0.069	±0.096	±0.000109
0.090	=7.4335-0.000795T	6.739±0.050	6.421±0.067	±0.073	±0.000092
0.120	=7.3822-0.000774T	6.707±0.077	6.397±0.098	±0.129	±0.000146

It should be noted that in comparison with (Sn3.3Ag0.76Cu) alloy in previous publication [22] for Sn3.8Ag0.57Cu the relation of density on temperature is as follows: $\rho = 7.4529-0.000662T$.

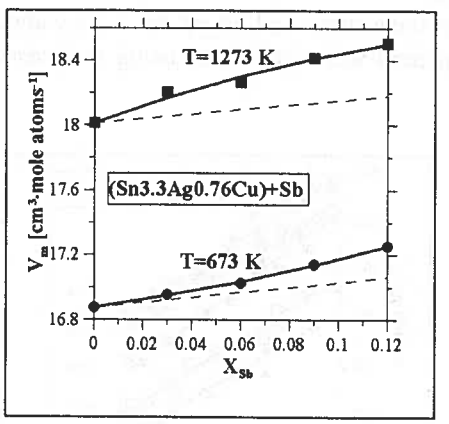

Fig. 5. Isotherms of the molar volume of (Sn3.3Ag0.76Cu) and (Sn3.3Ag0.76Cu) + Sb liquid alloys calculated at 673K and 1273 K. Symbols show the values calculated using Equation [6] and density calculated from Equations in Table 1. Dashed lines show the values calculated according with the additive rule between Sn3.3Ag0.76Cu and pure antimony while thick continuous lines illustrate the values calculated using Equations [6, 7] and [8]

The experimental values of the surface tension for the Sn3.3Ag0.76Cu + Sb liquid alloys (symbols) are shown in Fig. 5 together with those calculated from the least squares equations in Table 2 (lines). The deviations of experimental values from the least squares lines are not higher than 7 $mNcm^{-1}$. Calculated from equations in Table 2 isotherms of the surface tension at 673 K and 1273 K were described, similar as in the case of the density by the following parabolic relations dependent on the antimony concentration:

TABLE 2

Temperature dependences of the density of the (Sn3.3Ag0.76Cu) and (Sn3.3Ag0.76Cu) + Sb liquid alloys together with the surface tension and errors calculated for surface tension at 873 K and 1273 K and errors for A and B linear equations parameters

X_{Sb}	$\sigma = A + BT$ $mN \cdot m^{-1}$	σ_{873K} $mN \cdot m^{-1}$	σ_{1273K} $mN \cdot m^{-1}$	Err(A) $mN \cdot m^{-1}$	Err(B) $mN \cdot m^{-1} \cdot K^{-1}$
0.000	=582.1-0.0867T	506.4±6.6	471.7±7.2	±5.8	±0.0068
0.030	=571.5-0.0847T	497.5±4.4	463.6±5.1	±5.3	±0.0060
0.060	=575.1-0.1016T	486.5±6.9	445.8±7.9	±6.8	±0.0083
0.090	=540.3-0.0860T	465.2±6.9	430.8±7.7	±6.7	±0.0078
0.120	=523.4-0.0805T	453.1±7.6	420.8±8.6	±9.6	±0.0106

It should be noted that in comparison with (Sn3.3Ag0.76Cu) alloy in previous publication [22] for Sn3.8Ag0.57Cu the relation of surface tension on temperature is as follows: $\sigma = 586.5 - 0.0819T$.

$$\sigma = \sigma_t + BX_{Sb} + CX_{Sb}^2 = 523.73 - 227.59X_{Sb} - 2006.26X_{Sb}^2 \quad [14]$$

$$\sigma = \sigma_t + BX_{Sb} + CX_{Sb}^2 = 471.72 - 392.92X_{Sb} - 363.87X_{Sb}^2. \quad [15]$$

In the above-mentioned equations σ is the surface tension of Sn3.3Ag0.76Cu + Sb alloys, σ_t is the surface tension of the ternary Sn3.3Ag0.76Cu alloy and X_{Sb} is the mole fraction of antimony. B and C parameters were calculated using the least squares method.

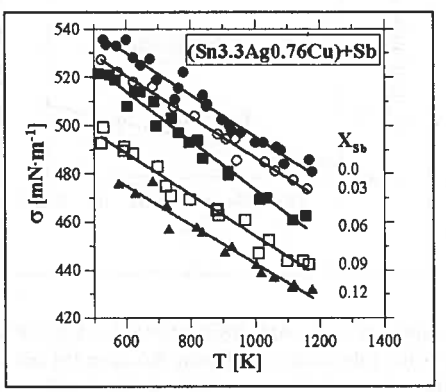

Fig. 6. The temperature depences of the surface tension of (Sn3.3Ag0.76Cu) and (Sn3.3Ag0.7Cu) + Sb liquid alloys. Symbols represent the experimental values obtained in this study using the maximum bubble pressure method and continuous lines show the values calculated from Equations in Table 2

The experimental and the calculated at 673K and 1273 K from the B u t l e r ' s model isotherms of the surface tension for the Sn3.3Ag0.76Cu + Sb alloys are shown in Fig. 7. The binary and the ternary optimized thermodynamic parameters were taken from the

following papers: for Ag-Cu, Ag-Sn and Ag-Cu-Sn from Ref. 13, for Ag-Sb and Ag-Sn-Sb from Ref.14, for Cu-Sn from Ref. 22, for Cu-Sb from Ref. 23, and for Sn-Sb from Ref 24. The remaining ternary parameters were assumed to be zero. The calculations were undertaken in the first case basing only on the binary thermodynamic parameters and in the second case including the ternary interaction parameters worked out by [13] for Sn-Ag-Cu system and [14] for the Sn-Ag-Sb system. When calculating the surface tension of the Sn-Ag-Cu-Sb alloys using only the binary thermodynamic parameters the obtained values are higher only by about 1 mNm^{-1} than those calculated using the binary and the ternary interaction parameters as presented in Fig. 7. One can suppose that the use of the ternary parameters of the other systems (Ag-Cu-Sb and Cu-Sb-Sn) will not change practically the surface tension calculated from B u t l e r ' s model for the alloys investigated in this work (Fig. 7). The isotherms calculated from Eqs 9 and 10 are drawn with thick solid lines and those obtained using B u t l e r ' s model with dotted lines.
The surface tension calculated from Butlers model is higher than that obtained from the experiment (Eqs 9, 10) both at 673K or 1273 K.

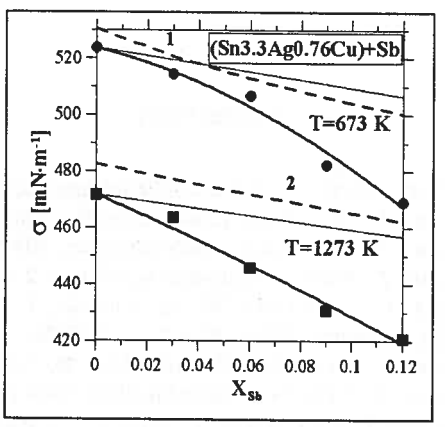

Fig. 7. Isotherms of the surface tension of (Sn3.3Ag0.76Cu) and (Sn3.3Ag0.76Cu) + Sb liquid alloys calculated at 673K and 1273K from Butler's model (dotted lines 1,2) compared with experimental data (symbols) while thick lines ilustrate surface tension calculated from Equations [9] and [10]. Thin continuous lines represent linear changes from surface tension of (Sn3.3Ag0.76Cu) liquid alloys to pure antimony

The highest deviations are observed for the highest Sb concentration (X_{Sb} = 0.12) and they are equal to nearly 30 $mN \cdot m^{-1}$ at 673K and 40 $mN \cdot m^{-1}$ at 1273 K. The common feature of the surface tension calculated from B u t l e r ' s model and of the experimental data is the decreasing tendency with the increase of the concentration of antimony.

5. Summary

Applying the dilatometric and the maximal bubble pressure methods the density and the surface tension were measured for the Sn3.3Ag0.76Cu and four Sn3.3Ag0.76Cu + Sb

liquid alloys having the concentration 0.03, 0.06, 0.09 and 0.12 mole fraction of antimony. It has been observed that the density and the surface tension decrease linearly with the increase of the temperature. The calculated at 673 K and 1273 K isotherms of the density and molar volume have shown the decreasing tendency of the density and the increase of the molar volume with the increase of the concentration of antimony. This tendency is more evident at higher temperatures.

The isotherms of the surface tension at 673 K and 1273 K obtained from the Butler's model show a similar tendency as those from the experimental results, namely the decreasing tendency which increases with the amount of antimony in the alloys. This tendency is more evident in the case of experimental data. It is expected that the agreement between modelling and experimental results would be better if all ternary and quaternary parameters were taken into account. Considering the fact that the addition of Sb to the alloy of composition close to the ternary eutectic Sn-Ag-Cu decreases the surface tension what means the improvement of the wettability, it is suggested to continue the studies on Sn-Ag-Cu-Sb as the addition of Sb improves also strength, thermal fatigue resistance and creep strength.

REFERENCES

[1] Z. Moser, M. Kucharski, K. Rzyman, J.Electrochem.Soc.**125**, 692-697(1978).
[2] Z. Moser, W. Gąsior, K. Rzyman, J.Electrochem.Soc. **126**, 1467-1470 (1979).
[3] Z. Moser, W. Gąsior, K. Rzyman, J.Electrochem.Soc. **129**, 502-506 (1982).
[4] Z. Moser, W. Gąsior, J. Pstruś, Inżynieria Materiałowa **2**, 65-68 (2002).
[5] Z. Moser, W. Gąsior, J. Pstruś, W. Zakulski, I. Ohnuma, X. J. Liu, Y. Inohana, K. Ishida, J. Electron. Mater. **30**, 1120-1128 (2001).
[6] Z. Moser, W. Gąsior, J. Pstruś: J. Electron. Mater. **30**, 1104-1111 (2001).
[7] W. Gasior, Z. Moser, J. Pstruś, J. Phase Equilibria, 2004 (in print)
[8] Z. Moser, W. Gąsior, J. Pstruś, X.J. Liu, I. Ohnuma, K. Ishida, TMS 2003, 132 Annual Meeting & Exhibition, San Diego, USA, February 3-5, 2003, Technical program, p.350.
[9] J. A. V. Butler, Proc. Roy. Soc. **A 135**, 348-375 (1932).
[10] W. Gąsior, Z. Moser, J. Pstruś, J. Phase Equilibria **22**, 20-25 (2001).
[11] Z. Moser, W. Gąsior, J. Pstruś, J.Phase Equilibria **22**, 254-258 (2001).
[12] W. Gąsior, Z. Moser, J. Pstruś, B. Krzyżak, K. Fitzner, J.Phase Equilibria **24**, 21-39 (2003).
[13] K.-W. Moon, W. J. Bettinger, U. R. Kattner, F. S. Biancaniello, C. A. Handwerker, J.Electron. Mater. **29**, 1122-1236 (2000).
[14] Ch.-S. Oh, J.-H. Shim, B.-J. Lee, D. N. Lee, J. Alloys and Compounds **238**, 154-166 (1966).
[15] S. Sugden, J. Chem. Soc. **124**, 858-68 (1924).
[16] T. Tanaka, T. Iida, Steel Research **65**, 21-28 (1994).
[17] T. Tanaka, K. Hack, T. Iida, S. Hara, Z. Metallkde **87**, 380-389 (1996).
[18] T. Tanaka, K. Hack, S. Hara, MRS Bulletin **24**, 45-50 (1999).
[19] O. Redlich, A. T. Kister, Ind. Eng. Chem. **24**, 345-348 (1948).
[20] B. Sundman, J. Agren, J.Phys.Chem.Solids **42**, 297-310 (1981).
[21] W. Volk: *Applied Statistics for Engineers*, 2-nd Edition, McGraw-Hill Book Comp., 1969.
[22] Z. Moser, W. Gąsior, J. Pstruś, J. Electron. Mater. **31**, 1225-1229 (2002).

[23] J.-H. Shim, C.-S. Oh, B.-J. Lee, D. N. Lee, Z. Metalkd. **87**, 205-212 (1996).
[24] R. Hultgren, P. Desai, D. T. Hawkins, M. Gleiser, K. K. Kelley, *Selected Values of the Thermodynamic Properties of Binary Alloys*, American Society for Metals, Metals Park, Ohio 44073, 1973.
[25] B. Jönsson, J. Ågren, Mater. Scien. Tech. **2**, 913-916 (1986).

REVIEWED BY: JAN WYPARTOWICZ
Received: 2 December 2003.

A R C H I V E S O F M E T A L L U R G Y A N D M A T E R I A L S
Volume 49 2004 Issue 1

LIDIA BURZYŃSKA*, IRENA HARAŃCZYK*, AGATA CIUMAN-KRZEMIEŃ*

RECOVERY OF SILVER FROM AgCl BY USING THE CELL Zn | H_2SO_4, AgCl | Ag

ODZYSK SREBRA Z AgCl PRZY UŻYCIU OGNIWA Zn | H_2SO_4, AgCl | Ag

Recovery of Ag from AgCl by its direct reduction was investigated in the cell Zn | H_2SO_4, AgCl | Ag, where AgCl did not directly contact with the reducing metal. Observed sudden drop of the current and of the Ag | AgCl electrode potential indicated the end of the reduction process. An equation describing dependence of the current intensity in the cell Zn | H_2SO_4, AgCl | Ag on reduced time was derived and discussed. Current efficiency and reduction degree were also determined. Influence of the concentration of sulfuric acid on the rate of the process and on the size of the reduced silver grains was studied.

Badano proces odzysku srebra metodą katodowej redukcji AgCl przy użyciu ogniwa Zn | H_2SO_4, AgCl | Ag. Stwierdzono, że zakończeniu procesu redukcji odpowiada nagły spadek mierzonych wartości natężenia prądu oraz potencjału katody Ag | AgCl. Wyprowadzono równanie empiryczne opisujące zależność natężenia prądu od czasu zredukowanego. Wyznaczono katodową wydajność prądu oraz stopień redukcji. Przedyskutowano wpływ stężenia kwasu na szybkość procesu oraz na wielkość ziaren otrzymanego proszku srebra.

1. Introduction

Cementation process is one of the most useful methods of the metals recovery from waste solutions. Reduction process is carried out directly by using metal more electronegative than being recovered one [1]. If the solutions are diluted than it is necessary at the beginning to precipitate a compound of the recovered metal, which exhibits low solubility. In this system cementation process is usually carried out by mixing difficultly soluble compound with scraps or a dust of the metal used for cementation. Product of this reaction is enriched in the metal being recovered and it needs further rafination. In this stage, pirometallurgical processes are used very often. Since this technology of metals

* WYDZIAŁ METALI NIEŻELAZNYCH, AKADEMIA GÓRNICZO-HUTNICZA. 30-059 KRAKÓW, AL. MICKIEWICZA 30

recovery from dilute solutions is complicated, a new method was elaborated. It makes possible to obtain high purity product in one – stage process [2]. In this method, the reduction is carried out in the cell which contains silver – silver chloride electrode (AgCl is located on silver plate or other conduction matrix) and the metal (zinc, aluminium or iron scraps) is used for cementation[1]. The electrodes are immersed in the electrolyte. Connection of electrodes with amperometer gives the possibility of continuous registration of the running process. The circuit can also be used to measure the potential and the changes of the potential values can be followed with time. Since Ag | AgCl is electrode of the second order, the process is characterized by current and potential stability. It can be observed that a sudden drop of the current, and of the Ag | AgCl electrode potential, shows that the reduction process is finished. At this moment only evolution of hydrogen on silver takes place. Sudden drop of the measured values provides the way of precise determination of the end of reduction process, which is very economical.

Investigations of the product of reduction reaction of difficultly soluble compound suggested that it exhibits plenty of properties different from powders produced by traditional methods (electrolysis [3], spraying [4], crushing [5]). The most important advantages are the following: it is fine – grained (a few μm), it has very good pressing properties (the possibility of making composites by pressing two or more independently produced powders or by coreduction of a mixture of difficulty soluble salts of these metals followed by pressing them [6, 7, 8]).

The continuation of the research on optimalization of parameters of this process seems to be advisable. It is necessary to know the mechanism of difficulty soluble compounds reduction reaction under different conditions.

Cathodic polarization curves in galvanostatic and potentiostatic experiments were registered by using powder silver – silver chloride electrode and unsoluble anode in the different electrolytes [9]. Within wide range of the parameters (different concentration of chloride and sulfate solutions) a linear function of the potential of Ag | AgCl electrode with the logarithm of the current density ($E = f(\log i)$) was observed. The slope of this dependence is consistent with the transfer of one electron participating in reduction reaction. These facts indicate that the kinetics of reduction reaction of AgCl is in the activation regime [10].

The aim of this work is an attempt of determination of the mechanism of cathodic reduction of difficultly soluble compound (AgCl) in the cell $Zn \mid H_2SO_4$, $AgCl \mid Ag$ in different concentration of sulfuric acid solution from measured current and potential values, and by comparing them with earlier determined polarization curves [11].

2. Experimental

Experiments with reduction of AgCl kinetics were carried out in the cell (Fig. 1). The electrodes were placed in the glass vessel containing 2 dm^3 of the electrolyte. The zinc

[1] In the cell $Zn \mid H_2SO_4$, $AgCl \mid Ag$ run the following principal reactions:
- cathodic reaction $2Ag^+ + 2\bar{e} \rightarrow 2Ag$
- anodic reaction $Zn - 2\bar{e} \rightarrow Zn^{2+}$.

cylinder was used as the anode. A horizontally situated silver plate was placed in graphite, covered with a layer of precipitated AgCl, and was applied as the cathode. Geometric surface of the cathode was equal to 16.62 cm^2. The electrodes were short circuited. Luggin's capillary tube was introduced over the layer of AgCl powder in order to measure the potential of the cathode during the experiments. The potential of the cathode was measured with respect to the saturated calomel electrode (SCE), while subsequently the measured results were converted with respect to a normal hydrogen electrode. Additionally, the current intensity was measured by using independent digital multimeter. An accuracy of measurements of potential and current intensity was ± 1 mV and ± 1 mA. All registered data were collected in the same time. The end of the reduction of Ag^+ process was determined by sudden drop of the measured values. Sulfuric acid of different concentrations (0.5 mol/dm^3, 0.375 mol/dm^3, 0.25 mol/dm^3, 0.15 mol/dm^3, 0.05 mol/dm^3, 0.0375 mol/dm^3 and 0.025 mol/dm^3) was applied. The electrolyte was continuously mixed by using magnetic stirrer. The measurements were carried out at temperature 20 ± 1 °C. Solutions were prepared from reagents of analytical purity and distilled water. AgCl samples of the known mass were precipitated by HCl solution, from exactly measured volumes of $AgNO_3$ solutions of known concentration. Mass of specimens was equal to 3 g (mass of silver contained in AgCl). Muriatic acid was added slowly to hot silver nitrate solution with continuous mixing. About 50 % of muriatic acid excess was used in relation to the stechiometry of AgCl. Precipitated AgCl was filtered, washed with distilled water and wet deposit was placed on the silver plate.

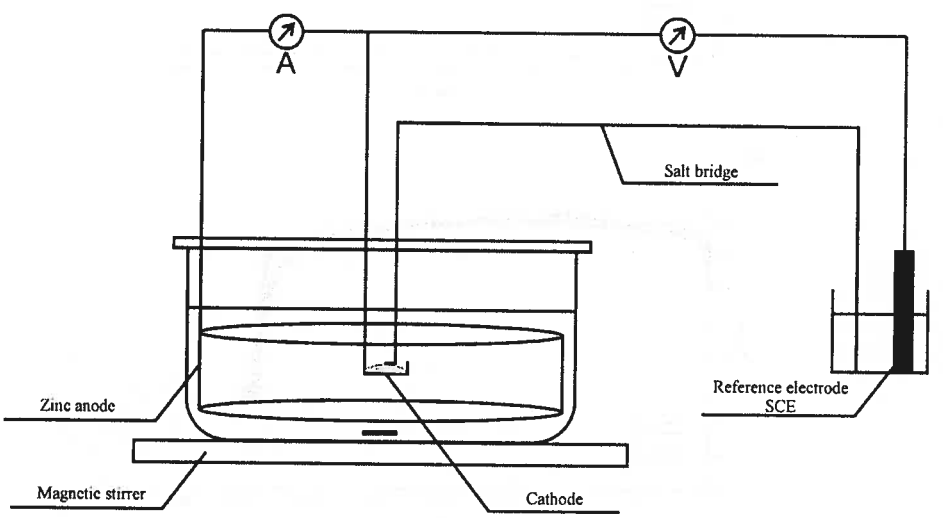

Fig. 1. Diagram of measurement circuit

Obtained silver powder was washed with hot ammonia solution in order to remove the rest of non – reduced AgCl.

3. Results and discussion

3.1. Dependence current intensity on time

Results of current intensity measured in the cell Zn | H_2SO_4, AgCl | Ag as a function of time are presented in Figs 2 a and b for two different sulfuric acid concentrations. Obtained results are characterized by good reproducibility. At the beginning of the reduction reaction it can be seen (Figs 2 a and b) that negligible increase of the current intensity occurs. It was interpreted as a result of the increase of the actual surface of powder electrode [12]. Next, the current intensity remains almost constant and the plateau is observed. At the next stage of the reduction process current intensity decreases slowly and at the end of this reaction sudden drop of the measured value is observed. At this moment current intensity is equal to

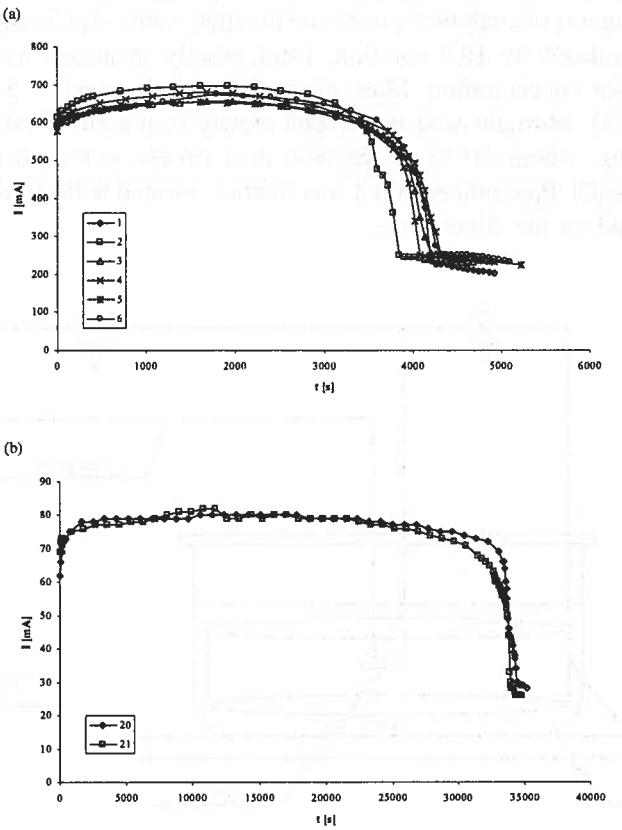

Fig. 2. Relation between current intensity I and reduction time t; (a) 0.5 mol/dm^3 H_2SO_4; (b) 0.0375 mol/dm^3 H_2SO_4; the numbers in the legend correspond to succeeeding measurements

the rate of hydrogen reduction on silver. Because the current intensity was not constant in overall time interval, the rate of reduction process was described by integration of the

dependence $I = f(t)$. Obtained value of charge Q flowing through the circuit was divided by reduction time, t_r, of AgCl (t_r – time corresponding to sudden change of current intensity to value of hydrogen reduction on silver). The value of current intensity determined in this way is an average one, I_{av}. It depends in an important manner on acid concentration.

Independently on average values I_{av} determined above, empirical dependence between current intensity and time was deduced. However, taking into account that current intensity and reduction time depend on acid concentration, in order to put forward one generalized equation for all acid concentrations, reduced time t/t_r was used. The following equation was obtained:

$$I = a + b\left(\frac{t}{t_r}\right)^c, \tag{1}$$

where a, b, c – constant values.

This equation fulfills the following boundary conditions:

- for $t = 0$ current intensity is equal to coefficient a; then $a = I(0)$, which means that this coefficient is equal to the rate of reduction AgCl in initial moment,
- for $t = t_r$ current intensity I is equal to the rate of hydrogen reduction on silver, thus $I = I_{H_2}$; it is now possible to calculate the value of coefficient b:

$$I_{H_2} = I(0) + b\left(\frac{t_r}{t_r}\right)^c \tag{2}$$

that is

$$b = I_{H_2} - I(0) \tag{3}$$

The value of the coefficient b corresponds to the difference of the rate of hydrogen evolution on silver and the rate of reduction reaction of AgCl in the initial moment. The value of coefficient c is characterized by fixed acid concentration.

Dependence of current intensity I on reduced time t/t_r for measured as well as calculated (eq. (1)) values is presented in Figs 3 a and b. Plateau in the calculated curve agrees well with average current intensity values obtained from integration of experimental values of I as a function of time. These values are given for comparison in Table 1.

It seems that good agreement between the values given in Table 1 proves that the coefficient a in equation (1) has a physical meaning. It is equal to the average current intensity value.

It is seen from Figs 3 a and b, that average current intensity value I_a^v is lower then the current value corresponding to the plateau shown on experimental curves. This plateau corresponds to the maximum of the process rate. The average value for all plateau obtained for several independent measurements at fixed acid concentrations was taken as I_{max}. The values of I_{max} depend on the acid concentration. With increasing acid concentration I_{max} increases and, additionally, decreases the range of plateau.

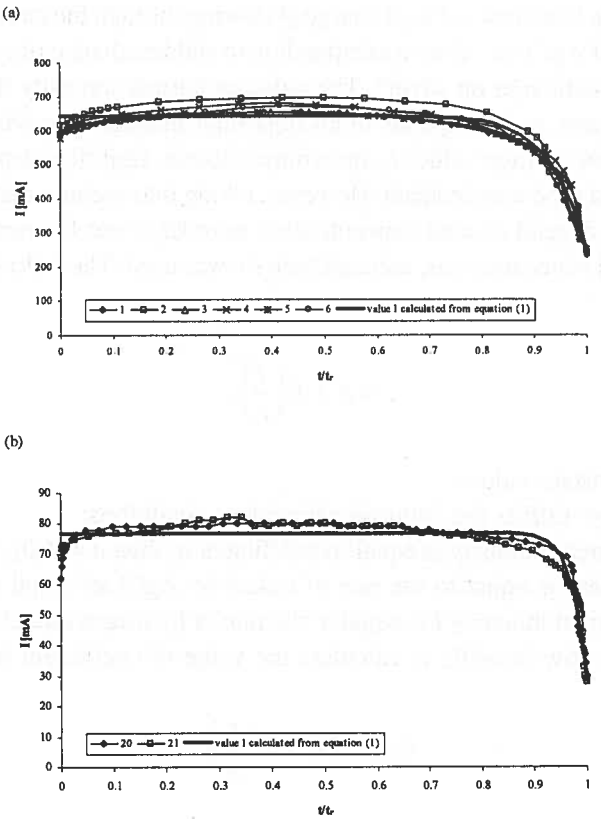

Fig. 3. Relation between current intensity I and reduced time t/t_r for measured as well as calculated (eq. 1) values of I; (a) 0.5 mol/dm^3 H_2SO_4; (b) 0.0375 mol/dm^3 H_2SO_4; the numbers in the legend correspond to succeeding measurements

TABLE 1

Influence of H_2SO_4 concentration on average current intensity I_{av} and current intensity values I calculated from equation (1)

H_2SO_4 concentration [mol/dm^3]	I_{av} (from integration)	I values calculated from equation (1) corresponding to plateau
0.5000	623 ± 15	642 ± 13
0.3750	485 ± 3	485 ± 13
0.2500	390 ± 4	394 ± 4
0.1500	240 ± 5	234 ± 10
0.0500	109.5 ± 0.5	111 ± 1
0.0375	76.5 ± 0.5	77 ± 0
0.0250	58 ± 2	57 ± 1

3.2. Dependence of cathodic potential on time

Curves' shape of cathode potential in the function of the time is similar to curves $I = f(t)$ (Fig. 2). For example, dependence of cathode potential on time for two different acid concentrations was presented in Figs 4 a and b. Based on these curves the end of the reduction process can be deduced. The end of the process corresponds to a sudden drop of the potential to the value of that of hydrogen reduction on silver.

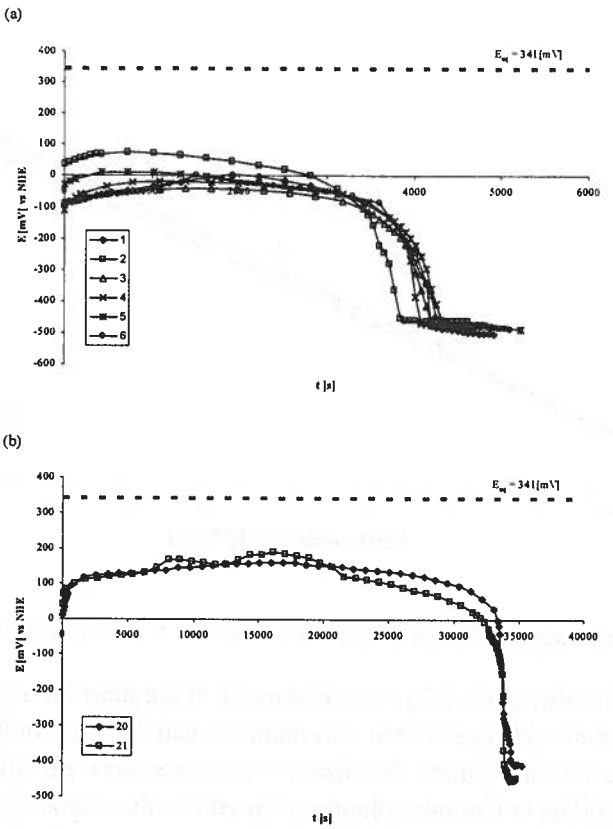

Fig. 4. Relation between cathodic potential E and reduction time t; (a) 0.5 mol/dm^3 H_2SO_4; (b) 0.0375 mol/dm^3 H_2SO_4; the numbers in the legend correspond to succeding measurements

The value of the reversible potential was compared to the reduction potentials and is also presented in Figs 4 a and b. The value of reversible potential was determined during independent measurements, and it did not depend on acid concentration.

Displacement of experimental curves in comparison with reversible potential – over-potential – was so large (in the case of 0.5 mol/dm^3 and 0.0375 mol/dm^3 H_2SO_4 solutions they were approximately equal to 250 mV and 150 mV, respectively) that it suggested activation control of the process. Overpotential increased with increasing acid concent-

ration. It should be also taken into account that the increasing acid concentration influences the electrolyte conductivity and it decreases the internal resistance of the system. This hypothesis was confirmed by the dependence of the current intensity on the electrolyte conductivity (Fig. 5). During the reduction process, the conductivity of the electrolyte was changing because of decreasing H^+ concentration and increasing Zn^{+2} ions concentration. Additionally, the acid concentration influences the rate of the zinc electrode dissolution.

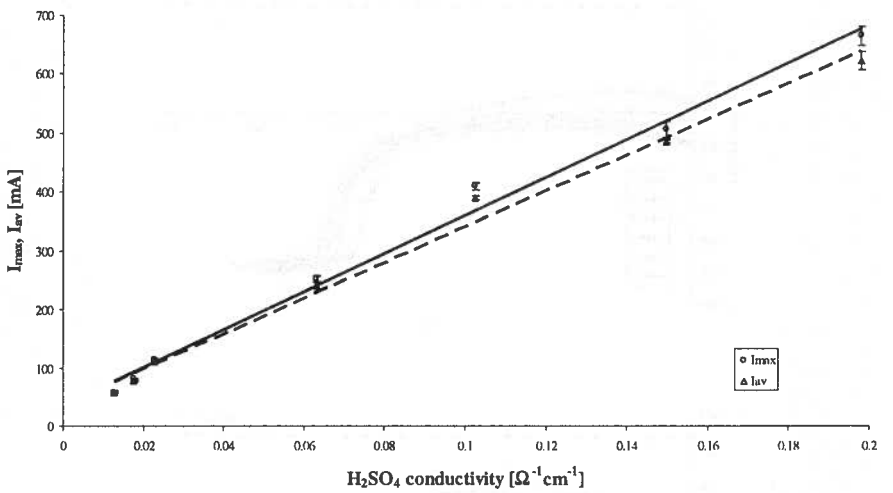

Fig. 5. Maximum current intensity I_{max} and average current intensity I_{av} as a function of H_2SO_4 conductivity

On the basis of earlier study [13] it was deduced that the substitution of chloride anions by sulfate anions and the change of their concentration had the effect only on the change of internal resistance of the system. Polarization measurements performed for different concentrations of sulfate or chloride solutions showed that the mechanism of the process is identical. Furthermore, the values of potentials of silver – silver chloride electrode measured in the cell Ag, AgCl | H_2SO_4 pointed out to the absence of functional dependence between the potential and sulfuric acid concentration (Fig. 6). It seems that above observations justify the presentation of the dependence between cathode potential E_{max} and logarithm of the cathodic current density in the cell Zn | H_2SO_4, AgCl | Ag, determined during measurements for different acid concentration solutions, in the same figure (Fig. 7). The results obtained in polarization measurements were also added in Fig. 7. It can be seen that these two straight lines are parallel to each other, but the displacement is observed. It seems that in the case of the cell in which the external current is absent, current and potential values are controlled by the electrolytic conductivity. In the case of polarization

measurements the rate of the process (i.e. current intensity) is imposed by the external current source. It is probably the reason of curves' displacement.

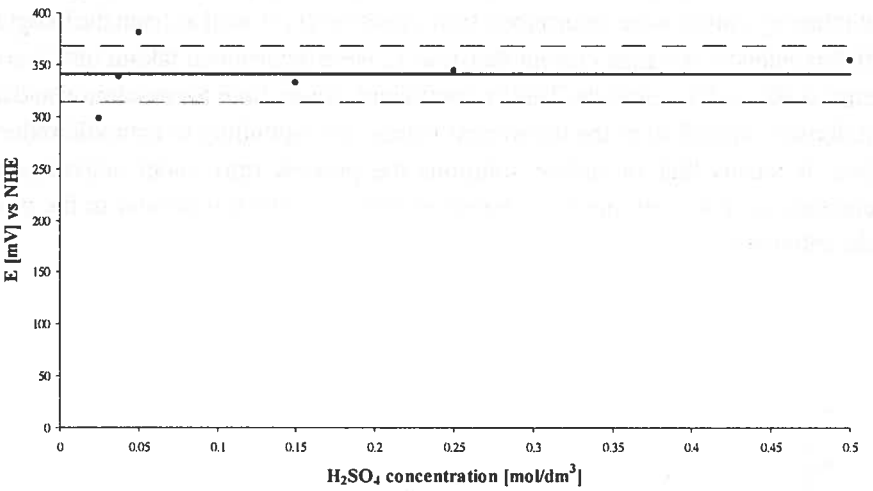

Fig. 6. Electrode Ag, AgCl | H_2SO_4 potential values measured under equilibrium condition as a function of H_2SO_4 concentration

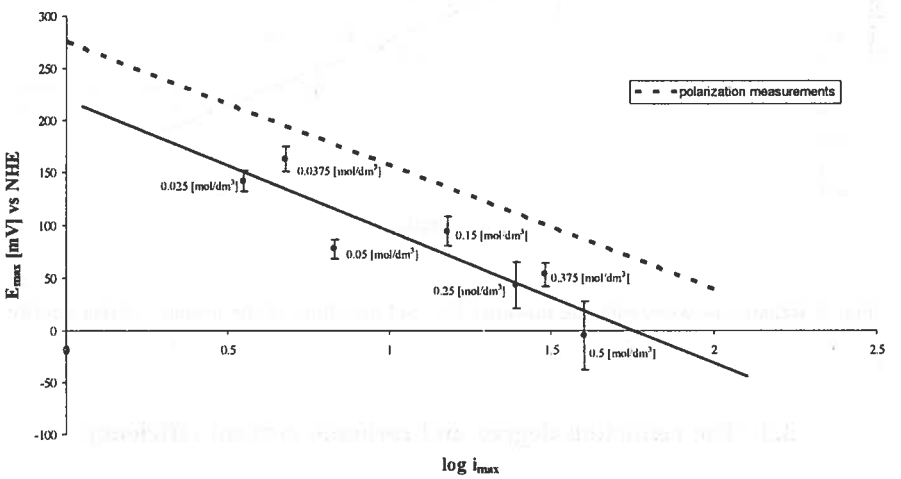

Fig. 7. Relation between cathodic potential E_{max} and logarithm of the maximum current density

The results obtained in the cell for different H_2SO_4 concentrations can be ascribed as follows:

$$E_{max} = (220 \pm 32) - (126 \pm 27)\log i_{max}. \quad (4)$$

The correlation coefficient of this straight line is equal to 0.8101. The values of current density in equation (4) correspond to the maximum values.

Additionally, the graph of cathodic potential E_{max} on log i_{av} was made (Fig. 8). Average current intensity values were determined from equation (1) as well as from the integration of $I = f(t)$ dependence. Average current densities i_{av} were determined taking into account the geometric surface of the cathode. Tafel's coefficient values, both for maximum and average current density, agreed with the theoretical values corresponding to cathodic reduction of Ag^+ ions. It means that in sulfate solutions the process runs under activation control independently on concentrations (in measured regime), which is similar to the process in chloride solutions.

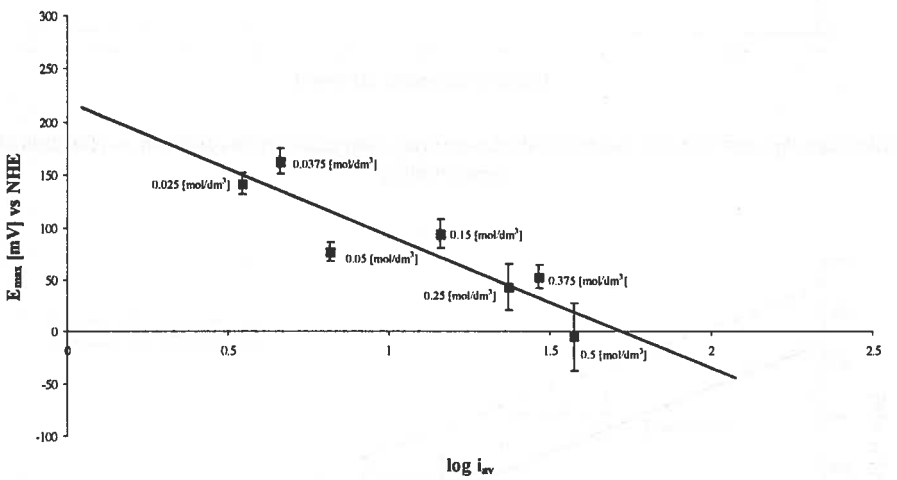

Fig. 8. Relation between cathodic potential E_{max} and logarithm of the average current density

3.3. The reduction degree and cathodic current efficiency

In Table 2 the values of the current efficiency and the reduction degree of the obtained product are gathered. Both, the reduction degree and the current efficiency are very high. No influence of the acid concentration on these values is observed. However, it should be mentioned that for the lower acid concentration the time of reduction process (t_r, Table 2) was longer. Thus, for practical purpose more concentrated solutions should be used.

TABLE 2

Reduction degree of silver from AgCl and cathodic current efficiency

No.	H_2SO_4 concentration $[mol/dm^3]$	mass of Ag in AgCl $m^0_{Ag}[g]$	Ag mass after reduction process $m_{Ag}[g]$	reduction time $t_r[s]$	amount of coulombs $Q=\int_0^t Idt[C]$	Ag mass according to Faraday's law $M_{Ag}=k_{Ag}\cdot Q[g]$	reduction degree $X=\frac{m_{Ag}}{m^0_{Ag}}\cdot 100[\%]$	cathodic current efficiency $\eta_k=\frac{m_{Ag}}{M_{Ag}}\cdot 100[\%]$	current intensity	
									$I_{max}[mA]$	$I_{av}=\frac{Q}{t_r}[mA]$
1	0.5000	2.8736	2.8406	4200	2571.51	2.8775	98.85	98.72	655	612
2	0.5000	2.8006	2.7824	3840	2508.33	2.8068	99.35	99.13	696	653
3	0.5000	2.8293	2.8101	4200	2571.87	2.8779	99.32	97.64	656	612
4	0.5000	2.8192	2.7731	4080	2571.78	2.8778	98.37	96.36	680	630
5	0.5000	2.8960	2.7408	4320	2642.73	2.9572	94.64	92.68	654	612
6	0.5000	2.8704	2.8131	4320	2667.63	2.9851	98.00	94.24	674	618
7	0.3750	2.8408	2.7657	5160	2520.03	2.8199	97.36	98.08	511	488
8	0.3750	2.8601	2.8137	5340	2569.59	2.8754	98.38	97.86	520	481
9	0.3750	2.8637	2.7948	5280	2563.23	2.8683	97.59	97.44	520	485
10	0.2500	2.8768	2.8499	6840	2688.57	3.0085	99.07	94.73	415	393
11	0.2500	2.8636	2.8400	6960	2666.70	2.9840	99.18	95.17	404	383
12	0.2500	2.8152	2.7172	6660	2607.33	2.9176	96.52	93.13	415	391
13	0.2500	2.8431	2.1736	6780	2657.31	2.9735	76.45	73.10	417	392
14	0.1500	2.7940	2.7612	10500	2538.90	2.8410	98.83	97.19	257	242
15	0.1500	2.9835	2.8652	11760	2718.39	3.0419	96.03	94.19	244	231
16	0.1500	2.9061	2.8214	10740	2623.47	2.9357	97.09	96.11	259	244
17	0.1500	2.8419	2.7693	10500	2556.81	2.8611	97.45	96.79	256	244
18	0.0500	2.8505	2.5150	24780	2691.69	3.0120	88.23	83.50	115	109
19	0.0500	2.8381	2.4872	24240	2666.67	2.9840	87.63	83.35	116	110
20	0.0375	2.8850	2.8455	34440	2646.60	2.9615	98.63	96.08	80	77
21	0.0375	2.8122	2.7856	34080	2594.13	2.9028	99.05	95.96	82	76
22	0.0250	2.8410	2.7498	43440	2625.27	2.9377	96.79	93.60	65	60
23	0.0250	2.7940	2.7376	46080	2592.51	2.9010	97.98	94.37	65	56

m^0_{Ag} – silver mass in the initial AgCl powder
Q – area under curve I = f(t) calculated trapezium method

3.4. Scanning analysis of silver powder

Grain size of silver powder obtained as a result of reduction of Ag^+ ions depends on the initial acid concentration. The microphotographs of silver powder obtained from acid solutions of different concentrations are presented in Fig. 9. The values of average chords of silver powder grains were determined. In 0.5 mol/dm^3, 0.15 mol/dm^3 and 0.025 mol/dm^3 H_2SO_4 solutions the values of average chords were 0.86 ± 0.22 μm, 1.48 ± 0.41 μm and 1.39 ± 0.44 μm, respectively. The finest grains were obtained in 0.5 mol/dm^3 sulfuric acid solutions.

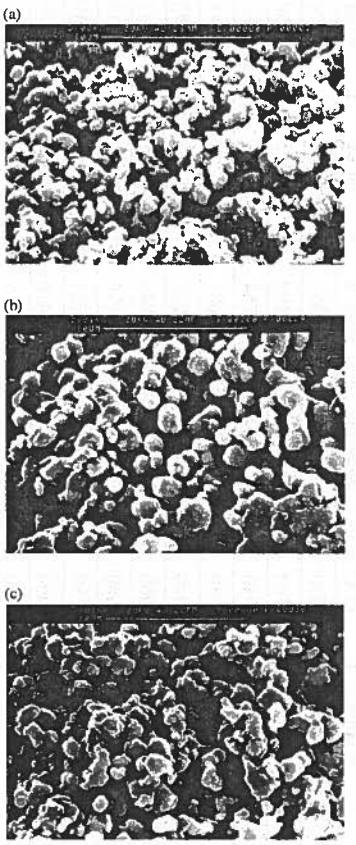

Fig. 9. Microphotographs of silver powder obtained from acid solutions of different concentrations; (a) 0.5 mol/dm^3 H_2SO_4; (b) 0.15 mol/dm^3 H_2SO_4; (c) 0.025 mol/dm^3 H_2SO_4

4. Conclusions

1) The reduction of Ag^+ ions process carried out in the cell $Zn|H_2SO_4, AgCl|Ag$ runs under activation control.

2) Independently on sulfuric acid concentration the reduction degree of Ag^+ ions is high.
3) Independently on sulfuric acid concentration the cathodic current efficiency is high.
4) Silver powder obtained from 0.5 mol/dm^3 H_2SO_4 solutions is characterized by the finest grains.
5) The optimum parameters of the process are those of the working cell in 0.5 mol/dm^3 H_2SO_4 solution (the finest grains, the shortest reduction time, high reduction degree, high cathodic current efficiency).

REFERENCES

[1] F. Łętowski, Podstawy hydrometalurgii, WNT. Warszawa (1975).
[2] J. Sędzimir, I. Harańczyk, Z. Bogacz, Polish patent 153647 (10.03.1992).
[3] A. R. Despic, Y. Dagle, Y. O. M. Bockris, J. Electrochem. Soc. **115**, 5 (1968).
[4] W. Rutkowski, Projektowanie, własności wyrobów spiekanych z proszków i włókien, PWN. Warszawa (1997).
[5] A. Lawley, Rapidly solidified powder processes – atomization models and mechanisms, Drexel University, Philadelphia, Pensylvania, USA (1990).
[6] J. Sędzimir, I. Harańczyk, W. Dziadur, Arch. of Met. **34**, 217 (1989).
[7] I. Harańczyk, S. Gacek, Metale Szlachetne 2000, Fundacja Met. Nieżel. Tradycja i Rozwój, p. 34, Niedzica 2000.
[8] I. Harańczyk, S. Gacek, J. Karwan-Baczewska, Powder Metallurgy **45**, 359 (2003).
[9] J. Sędzimir, I. Harańczyk, Arch. of Met. **39** 9 (1994).
[10] G. Kortüm, Elektrochemia, PWN. Warszawa (1975).
[11] J. Sędzimir, I. Harańczyk, Proceedings of the Second International Conference on Hydrometallurgy, Changsha, China, October 1992, p. 523.
[12] J. Sędzimir, Hydrometallurgy **64**, 161 (2002).
[13] I. Harańczyk, J. Sędzimir, Arch. of Met. **36**, 185 (1991).

REVIEWED BY: KRZYSZTOF FITZNER
Received: 10 November 2003.